

Modeling and Characterization of the Interaction of Electromagnetic Wave with Nanocomposites and Nanostructured Materials

Guest Editor: Christian Brosseau





Modeling and Characterization of the Interaction of Electromagnetic Wave with Nanocomposites and Nanostructured Materials

Journal of Nanomaterials

Modeling and Characterization of the Interaction of Electromagnetic Wave with Nanocomposites and Nanostructured Materials

Guest Editor: Christian Brosseau



Copyright © 2007 Hindawi Publishing Corporation. All rights reserved.

This is a special issue published in volume 2007 of “Journal of Nanomaterials.” All articles are open access articles distributed under the Creative Commons Attribution License, which permits unrestricted use, distribution, and reproduction in any medium, provided the original work is properly cited.

Editor-in-Chief

Michael Z. Hu, Oak Ridge National Laboratory, USA

Advisory Board

James Adair, USA
C. Brinker, USA
Taeghwan Hyeon, South Korea

Nathan Lewis, USA
Alon McCormick, USA
Gary Messing, USA

Z. L. Wang, USA
Alan Weimer, USA
Jackie Ying, USA

Associate Editors

John Bartlett, Australia
Michael Harris, USA
Do Kyung Kim, South Korea

S. J. Liao, China
Jun Liu, USA
S. Mathur, Germany

Michael S. Wong, USA
M. Yoshimura, Japan

Editorial Board

Donald A. Bansleben, USA
C. Brosseau, France
Siu Wai Chan, USA
G. Chen, USA
Sang-Hee Cho, South Korea
C. Cui, China
Ali Eftekhari, Iran
Claude Estournes, France
Alan Fuchs, USA
Lian Gao, China
Hongchen Gu, China
Justin Holmes, Ireland

David Hui, USA
Rakesh K. Joshi, USA
Li Jun, Singapore
Alan Lau, Hong Kong
B. I. Lee, USA
J. -Y. Liu, USA
Songwei Lu, USA
Ed Ma, USA
P. Panine, France
Donglu Shi, USA
Bohua Sun, South Africa
Xiaogong Wang, China

E. G. Wang, China
Y. Wang, USA
C. P. Wong, USA
Ping Xiao, UK
Zhili Xiao, USA
N. Xu, China
Doron Yadlovker, Israel
Peidong Yang, USA
Zhenzhong Yang, China
Kui Yu, Canada

Contents

Modeling and Characterization of the Interaction of Electromagnetic Wave with Nanocomposites and Nanostructured Materials, Christian Brosseau

Volume 2007, Article ID 74545, 2 pages

Electromagnetic Field Behavior in Dispersive Isotropic Negative Phase Velocity/Negative Refractive Index Guided Wave Structures Compatible with Millimeter-Wave Monolithic Integrated Circuits,

Clifford M. Krowne and Maurice Daniel

Volume 2007, Article ID 54568, 11 pages

3D-Simulation of Topology-Induced Changes of Effective Permeability and Permittivity in Composite Materials, B. Hallouet and R. Pelster

Volume 2007, Article ID 80814, 8 pages

Plasmonic Nanolayer Composites: Coupled Plasmon Polaritons, Effective-Medium Response, and Subdiffraction Light Manipulation, Justin Elser, Alexander A. Goyyadinov, Ivan Avrutsky,

Ildar Salakhutdinov, and Viktor A. Podolskiy

Volume 2007, Article ID 79469, 8 pages

On the Dielectric and Magnetic Properties of Nanocomposites, B. Hallouet, B. Wetzel, and R. Pelster

Volume 2007, Article ID 34527, 11 pages

Dielectric Polarization and Particle Shape Effects, Ari Sihvola

Volume 2007, Article ID 45090, 9 pages

Broadband Ferromagnetic Resonance Measurements in Ni/ZnO and Ni_y-Fe₂O₃ Nanocomposites,

Vincent Castel, Jamal Ben Youssef, and Christian Brosseau

Volume 2007, Article ID 27437, 16 pages

Dielectric Resonator Method for Measuring the Electrical Conductivity of Carbon Nanotubes from Microwave to Millimeter Frequencies, James Baker-Jarvis, Michael D. Janezic, and John H. Lehman

Volume 2007, Article ID 24242, 4 pages

Electromagnetic Modelling of Raman Enhancement from Nanoscale Structures as a Means to Predict the Efficacy of SERS Substrates, Richard J. C. Brown, Jian Wang, and Martin J. T. Milton

Volume 2007, Article ID 12086, 10 pages

The AC and DC Conductivity of Nanocomposites, David S. McLachlan and Godfrey Sauti

Volume 2007, Article ID 30389, 9 pages

Editorial

Modeling and Characterization of the Interaction of Electromagnetic Wave with Nanocomposites and Nanostructured Materials

Christian Brosseau

Département de Physique, Université de Bretagne Occidentale, 29238 Brest Cedex 3, France

Received 17 December 2007; Accepted 17 December 2007

Copyright © 2007 Christian Brosseau. This is an open access article distributed under the Creative Commons Attribution License, which permits unrestricted use, distribution, and reproduction in any medium, provided the original work is properly cited.

Nanostructured materials represent a size limit of the miniaturization trend of current technology. Interest in nanophases has expanded as investigators have recognized that many of the properties of finely divided matter strongly depend on the interfacial properties of the constituents by virtue of the high fraction of the overall material which is in the vicinity of an interface as well as of the confinement of electrons, excitons, and photons in small volumes. One of the interesting and important issues in predicting and understanding nanostructures and their functional behaviors is whether the properties of matter evolve gradually from bulk, as system size is reduced, and what determines this evolution behavior.

The electromagnetic characterization of nanomaterials can be considered a major part of the emerging field of nanotechnology. The potentially profound implications both for the transport properties and optics are only beginning to be explored. In that respect, multicomponent magnetic nanophases are of significant technological interest, that is, they can be considered as prospective granular magnetic films for tunable or nonreciprocal millimeter wave devices for monolithic microwave integrated circuit applications. This has also stimulated studies of the magnetoelectric effect, that is, the polarization of a material in an applied field or an induced magnetization in an external electric field.

The practical importance and industrial interest in these materials demand optimization of several types of properties in these materials. These properties include polarization, magnetization, and stability of the materials to mechanical, electrical, and magnetic fields applied during processing and operation. One of the fundamental goals of this field should be the understanding of the relationships of these properties on the composition, particle size and boundaries variations, defect structure and separation of the residual pores, but in most cases they are not well-understood.

In classical electrodynamics, the response of a material to electric and magnetic fields is characterized by two fundamental quantities: the permittivity ϵ and the magnetic permeability μ . In spite of the advances made, there is still no general agreement on interpretation of the experimental data of ϵ and μ of nanostructured materials since these quantities depend sensitively on the microstructural properties such as grain size, particle shape, and grain boundaries type.

Another related issue is the modeling of the polarization and magnetization mechanisms for these nanophases. In the effective medium approaches derived from continuum electromagnetism, only the volume fraction, or the particle number density, appears, while it is now well accepted that for dispersed two-phase nanostructures, appropriate descriptors of the interfaces should also appear. Therefore, collective magnetic and electromagnetic behaviors in nanosystems are challenging in terms of both experimental observation and development of theoretical analyses.

This special issue is dedicated to diverse topics related to electromagnetism of nanostructured materials. The contributors to this issue have endeavored to be selective, choosing and documenting those results to have the highest relevance and reliability. There was no attempt to be exhaustive and comprehensive. The careful selection of the topics included, however, suggests that the most attractive feature of these nanostructures is that their dielectric and magnetic properties can be varied over a wide range by the choice of the shape, size, and connectivity of the constituents in the structure. This issue contains nine survey contributions describing several active areas in this field of research. A relatively small number of contributions can only skim the surface of the exciting developments in this area. Our goal is only to illustrate the current status in the understanding of the electromagnetic properties of heterostructures. Clearly, the interplay between processing, structure, and macroscopic

properties is an important engineering and scientific concern. Both the editor and contributors of this volume would feel well rewarded if this issue helps relieve some of the problems of finding useful information on the morphological and electromagnetic properties of nanostructures.

Christian Brosseau

Research Article

Electromagnetic Field Behavior in Dispersive Isotropic Negative Phase Velocity/Negative Refractive Index Guided Wave Structures Compatible with Millimeter-Wave Monolithic Integrated Circuits

Clifford M. Krowne¹ and Maurice Daniel²

¹ Microwave Technology Branch, Electronics Science and Technology Division, US Naval Research Laboratory, Washington, DC 20375-5347, USA

² Electronics Science and Technology Branch, Sensors and Technology Division, DCS Corporation, 1330 Braddock Place, Alexandria, VA 22314, USA

Received 8 February 2007; Accepted 26 June 2007

Recommended by Christian Brosseau

A microstrip configuration has been loaded with a dispersive isotropic left-handed medium (LHM) substrate and studied regarding its high frequency millimeter-wave behavior near 100 GHz. This has been accomplished using a full-wave integral-equation anisotropic Green's function code configured to run for isotropy. Never before seen electromagnetic field distributions are produced, unlike anything found in normal media devices, using this *ab initio* solver. These distributions are made in the cross-sectional dimension, with the field propagating in the perpendicular direction. It is discovered that the LHM distributions are so radically different from ordinary media used as a substrate that completely new electronic devices based upon the new physics become a real possibility. The distinctive dispersion diagram for the dispersive medium, consisting of unit cells with split ring resonator-rod combinations, is provided over the upper millimeter-wave frequency regime.

Copyright © 2007 C. M. Krowne and M. Daniel. This is an open access article distributed under the Creative Commons Attribution License, which permits unrestricted use, distribution, and reproduction in any medium, provided the original work is properly cited.

1. INTRODUCTION

Tremendous interest in the last few years has occurred with the experimental realization of macroscopic demonstrations of left-handed media, predicted or at least suggested in the literature several decades ago [1]. Attention has followed on the focusing characteristics and related issues of left-handed media (LHM), with appropriate arrangements to accomplish such behavior, as shown by literature publications [2–25]. But no attention has been directed toward what intrinsic left-handed media could do in propagating devices used in integrated circuit configurations. This is not to say that some work has not happened on applications using backward wave production or LHM properties in specialized microwave devices which rely on reduced dimension negative phase velocity behavior [26–34]. (Also see references contained in [35, 36] for other focusing and backward wave devices.) And much of that work has looked at macroscopic realizations, which may be amenable in the future, with current efforts

on metamaterials, to advancing microwave integrated circuit component technology utilizing left-handed media.

We are particularly interested here in new physical properties being the result of using material which is intrinsically left-handed, or also variously referred to in the literature as negative phase velocity material (NPVM or NPV) or negative refractive index material (NRIM or NIM). There may be substantial interest in understanding the effects of left-handed media in guided wave structures since advances in integrated circuit technology, passive components, control components, and active devices have increasingly been utilizing layers and arrangements of many differing materials. From heterostructures in active devices to complex materials like chiral, ferroelectric, and ferromagnetic materials, in passive and control components, this trend has been rising. Efforts on metamaterials are sure to further this trend.

A hint at the remarkably different field distributions has been disclosed recently using LHM substrates in guided wave devices [37]. Dispersion diagram description of the physics

is provided in [35], and this diagram shows the effect of the RHM/LHM interface seen in the cross-sectional view on the propagation normal to the cross-section. Bands of pure phase propagation and bands of evanescent propagation occur. Also, negative phase velocity behavior of the LHM interacts with the RHM to generate regions of both ordinary wave propagation as well as backward wave propagation in the negative phase velocity sense relative to the guided wave power flow. In [35], only the low end band is displayed in field distribution plots at 5 GHz. But the plots shown are instructive for the new physics they demonstrate: unusual field line or circulation characteristics for the electric or magnetic fields, startling intensity variation of the fields, counter intuitive charge arrangement on the guiding metal strip, and interesting visual display of opposed Poynting vectors in adjoining RHM and LHM regions for power flow down the device.

Attention to the new possibilities for electronic devices is given in [36, 38] when using LHM/NPV substrates. There, distributions up to 40 GHz are provided, somewhat over the beginning of the millimeter-wave frequency band. However, nowhere have we made available the remarkable field distributions found at the higher millimeter wavelengths, and so in this paper, we would like to show for the first time what the fields look like at nearly $10^{11} = 100$ GHz (we will actually draw our attention to $f = 80$ GHz as a starting point). A new technique that we have developed of lifting out the lower magnitude fields in order to visualize their directions in arrow distribution plots will be utilized here for the first time (Section 5). This is particularly important in distribution plots where the field magnitudes may vary over many orders of magnitude. A number of field distribution plotting methods will be employed in this paper: arrow plots based upon linear representation of the field magnitude, arrow plots for both electric and magnetic fields based upon scaled representation of the field magnitude, line plots showing electric field behavior emanating from the strip and off of it, line plots showing magnetic field behavior circulating around the guiding strip and off of it, and magnitude plots of both the electric and magnetic fields.

Sections 2 and 3 provide short discussions of left-handed material properties (Section 2) and Green's function technique (Section 3) used to solve the material physics/field problem. Once these preliminaries are out of the way, the eigenvalues and dispersion diagram (Section 4) and the field distributions (Section 5) are determined.

2. LEFT-HANDED MATERIAL CHARACTERISTICS

It is expected that the left-handed medium characteristic to alter the electromagnetic field based upon its new properties contained in its tensors describing permittivity and permeability will not only lead to new structures enlisting just this new material, but eventually allow the creation of multi-layered devices containing various substances including left-handed media. Here we report on the new physics associated with left-handed media in guided wave propagating structures which are applicable to microwave and millimeter-

wave integrated circuits, although the focus here is primarily on the millimeter-wave region. Here we address the use of the left-handed media with its general bianisotropic crystalline properties reduced to scalars, that is, with anisotropic permittivity $\bar{\bar{\epsilon}}$ tensor set equal to the isotropic permittivity value $\epsilon\bar{1}$, and anisotropic permeability $\bar{\bar{\mu}}$ tensor set equal to the isotropic permeability value $\mu\bar{1}$. Consideration of the anisotropic or bianisotropic crystalline case is examined elsewhere [39]. Suffice it to say here that just as in the case of optical or lower frequency focusing, isotropy is what allows proper organization of all the wave fronts (or rays in the geometric optics limit). But in a guided wave structure, what may be the most critical issue is the assumption of isotropy in many applications to allow arbitrary field contouring or sculpting, although it is now known that particular anisotropies can lead to remarkable field asymmetries of potential use in electronic devices [40]. Individual unit cell construction and repetitive cells in all directions can lead to isotropy, as well as materials with intrinsic isotropic crystalline properties. The scalar relative permittivity and permeability ϵ and μ seen in the literature have frequency dependences $\epsilon(\omega)$ and $\mu(\omega)$. Left-handed material is obtained when $\text{Re}[\epsilon(\omega)] < 0$ and $\text{Re}[\mu(\omega)] < 0$ simultaneously. Whether this is a narrow- or wideband phenomenon will not be addressed here, other than to note that there may be both metaobject construction as well as intrinsic material methods to adjust the bandwidth. There is every indication today that these two implementation categories may provide enough design possibilities to make such bandwidth adjustment realistic. So, whether one uses nonresonant objects, resonant objects, microscopic properties of crystals, or nanoscale materials, there is no reason to doubt that the frequency region $\Delta\omega$ over which the desired behavior occurs may be viewed as being subject to the choice of the physicist or engineer for some intended use.

So, in order to study what the field distributions would do for a LHM substrate in a certain configuration at a particular frequency, we need to set $\text{Re}[\epsilon(\omega)] = -\epsilon_r$ and $\text{Re}[\mu(\omega)] = -\mu_r$, where $\epsilon_r =$ real positive constant and $\mu_r =$ real positive constant. Fundamental mode is sought, which has an eigenvalue even as $\omega \rightarrow 0$ ($f \rightarrow 0$). This is the simplest problem one can solve for in our inhomogeneous boundary condition problem. Hope for obtaining wideband behavior is now supported by recent results showing that negative refraction can be obtained by using heterostructures of intrinsic crystals with negligible dispersion [39, 41–43]. The narrowest behavior occurs with resonant structures like split ring resonator-rod combinations. Even for these structures, which are characterizable by $\epsilon(\omega) = 1 - (\omega_{pe}^2 - \omega_{e0}^2)/(\omega^2 - \omega_{e0}^2 + i\omega L_\epsilon)$ and $\mu(\omega) = 1 - F\omega^2/(\omega^2 - \omega_{m0}^2 + i\omega L_\mu)$ (these forms are widely quoted in the literature, with, for example, the permeability being derivable from [44]), because ω_{pe} , ω_{e0} , and F are subject to the designer's control, one can always, for a desired setting for ϵ and μ at a particular frequency ω , solve the two equations implicit in these depictions for the three unknowns, with a rich multiplicity of solutions. Finally, photonic crystals which provide the negative refraction using ordinary RHM crystals with RHM inclusions, may have

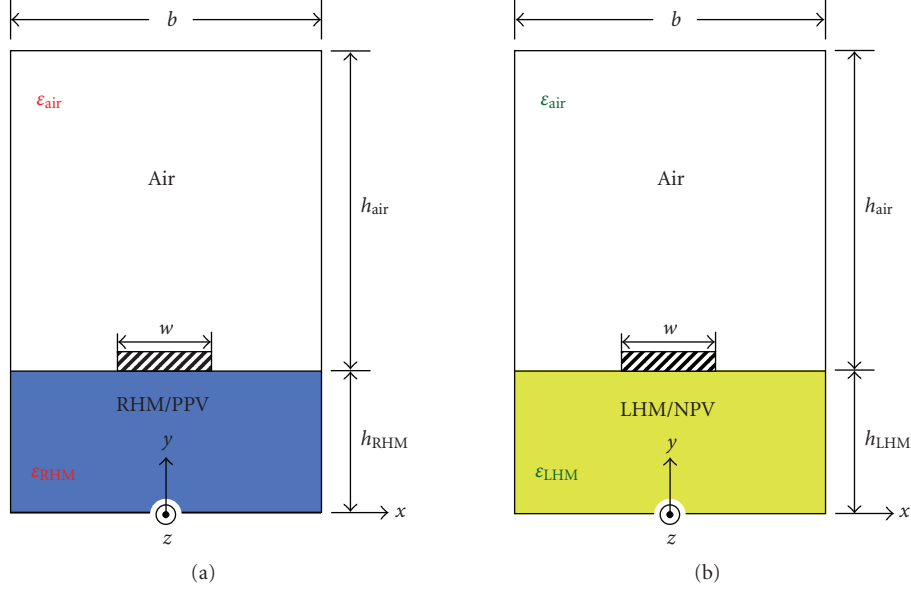


FIGURE 1: Cross-section of a microstrip structure with (a) a substrate using right-handed material (RHM/PPV) or (b) a substrate using left-handed material (LHM/NPV).

bandwidths somewhere between nondispersive and highly dispersive (as in the resonant structures).

3. GREEN'S FUNCTION FOR LEFT-HANDED GUIDED WAVE STRUCTURE

Green's function for the problem is a self-consistent one for a driving surface current vector Dirac delta function applied at the guiding microstrip metal, $\mathbf{J} = j_x \delta(x - x_0) \hat{x} + j_z \delta(x - x_0) \hat{z}$ with $x_0 = 0$ point on the strip. Figure 1(a) shows a cross-section of the structure with a right-handed material (RHM/PPV-ordinary material; PPV = positive phase velocity) used for the substrate, and Figure 1(b) shows a cross-section of the structure with a left-handed material (LHM/NPV). The Green's function is a dyadic, constructed as a 2×2 array relating tangential x - and z -components of surface current density to tangential electric field components. This function is used to solve for the propagation constant (see [45] for a recent use of this type of Green's function). Determination of the field components is done in a second stage of processing, which in effect creates a large rectangular Green's function array, of size 6×2 , in order to generate all electromagnetic field components, including those in the y -direction normal to the structure layers. The governing equation of the problem can be stated as

$$\frac{d\psi}{dy} = i\omega \mathbf{R} \psi, \quad \psi = [E_x \ E_z \ H_x \ H_z]^T, \quad (1)$$

where the system 4×4 matrix \mathbf{R} depends on the Green's function and on the physical properties of the materials. This equation gives the tangential transverse a field component variation (column vector ψ) perpendicular to the surface in the y -direction. Auxiliary equations give the two remaining field components, E_y and H_y .

The self-consistent problem is solved by expanding the surface currents on the guiding microstrip metal in the infinite expansions $J_x = \sum_{i=1}^{n_x} a_{xi} j_{xi}(x)$ and $J_z = \sum_{i=1}^{n_z} a_{zi} j_{zi}(x)$, and then requiring the determinant of the resulting system of equations to be zero. At this step of the problem, only the surface current basis functions $j_{xi}(x)$ and $j_{zi}(x)$ need to be provided and the complex propagation constant $\gamma = \alpha + j\beta$ is returned by the computer code. Of course, the summation limits n_x and n_z must be truncated at an appropriate value when convergence is acceptable.

Acquisition of the electromagnetic fields necessitates obtaining the basis function expansion coefficients a_{xi} and a_{zi} , explicitly constructing the actual driving surface current density on the microstrip metal, finding the resulting top or bottom boundary fields, and then utilizing operators to pull up or down through the structure layers, generating the electric and magnetic fields throughout in the process. The entire solution method uses the constraint that the vertical side walls of the device are perfect electric walls (perfect metallic conductors), which can be shown to discretize the eigenvalues in the x -direction. These are the Fourier transform variables for the spectral domain, and an infinite set of them forms a complete set for the problem. Only a finite number of them are used, with their maximum number being denoted by n .

4. DISPERSION DIAGRAMS OF LHM AND RHM DEVICES

To gain some idea of the general trend of the propagation constant, a dispersion diagram is graphed in Figure 2 for an ordinary medium substrate in the millimeter-wave frequency regime for a device with air above the substrate and right-handed medium (RHM/PPV, PPV) below the strip with $\text{Re}[\epsilon(\omega)] = \epsilon_r = 2.5$, and $\text{Re}[\mu(\omega)] = \mu_r = 2.3$, substrate

thickness $h_s = 0.5$ mm, microstrip width $w = 0.5$ mm, air region thickness $h_a = 5.0$ mm, and vertical wall separation $b = 5.0$ mm. Also, $\text{Im}[\varepsilon(\omega)] = \varepsilon_i = 0$ and $\text{Im}[\mu(\omega)] = \mu_i = 0$ making the medium lossless. (We also consider the microstrip metal lossless, although modifications for its loss can be made [45], as well as for medium loss in the substrate [45].) There are two γ roots possible for even symmetry of the J_z surface current component. They are mirror images of each other, with one corresponding to a z -directed wave and the other to a $-z$ -directed wave propagating in the reverse longitudinal direction. The figure only shows the positive going wave solution (solid yellow curve) for the fundamental mode, and we see that $\gamma = \alpha + j\beta = j\beta$, meaning that pure phase behavior occurs in the RHM/PPV structure. The dispersion diagram was produced with $n_x = n_z = 1$ and $n = 200$, although we have found solutions up to $n_x = n_z = 9$ and $n = 900$, with the change in the numerical value being in the fourth decimal place. Because we are putting our attention deep into the millimeter-wavelength regime, plots will be later done at frequency $f = 80$ GHz, which for the RHM/PPV structure has $\bar{\beta} = \beta/k_0 = 2.200$.

For a left-handed medium LHM/NPV substrate, instead of choosing $\text{Re}[\varepsilon(\omega)] = -\varepsilon_r = -2.5$, $\text{Re}[\mu(\omega)] = -\mu_r = -2.5$, and $\text{Im}[\varepsilon(\omega)] = -\varepsilon_i = 0$, $\text{Im}[\mu(\omega)] = -\mu_i = 0$ [35], with the geometric parameters being the same as for the RHM/PPV structure, we will consider a metamaterial model of the LHM/NPV substrate consisting of split ring resonators [44] with rods [46] (SRRs). Such a metamaterial will introduce explicit material dispersion into the problem, in addition to the dispersion already in the problem due to the guided configuration. For the rods, which we assume are continuous ($f_{e0} = 0$), their radius is chosen to be $r_e = 6.313 \mu\text{m}$, with a lattice spacing of $a = 0.690 \mu\text{m}$. These values are associated with an effective plasma frequency $f_{pe} = 149.67$ GHz and electric damping factor $L_e = 0.1305$ GHz (using aluminum). For the SRRs, the sheets' split on cylinder's model is used as an approximation to the split rings, with cylinder radius $r_m = 0.2761$ mm, and the concentric cylinder distance separation $d = 0.1668$ mm. Using the lattice spacing selected above yields $F = 0.5027$. These values are associated with a magnetic resonance frequency $f_{m0} = 74.03$ GHz, crossover frequency where effective permeability $\mu_{\text{eff}} = 0$ of $f_{mco} = 105$ GHz, and magnetic damping factor $L_\mu = 0.0853$ GHz (using aluminum). Thus, the dispersive material equations for the SRRs are completely determined:

$$\varepsilon(\omega) = 1 - \frac{\omega_{pe}^2 - \omega_{e0}^2}{\omega^2 - \omega_{e0}^2 + i\omega L_e} = 1 - \frac{\omega_{pe}^2}{\omega^2 + i\omega L_e}, \quad (2)$$

$$\mu(\omega) = 1 - \frac{F\omega^2}{\omega^2 - \omega_{m0}^2 + i\omega L_\mu}.$$

For the LHM/NPV structure, in the limiting case of $L_e \rightarrow 0$ and $L_\mu \rightarrow 0$, two γ solutions exist which have $\alpha = 0$, and $\bar{\beta} = \beta/k_0 = 1.177647$ and 1.786090 (quoted values for n_x and $n_z = 1$ and $n = 200$). One corresponds to a forward wave for nondispersive intrinsic LHMs ($\bar{\beta} = \beta/k_0 = 1.78609$), where the product of the integrated Poynting vector (net power through the cross section) and phase vector in the

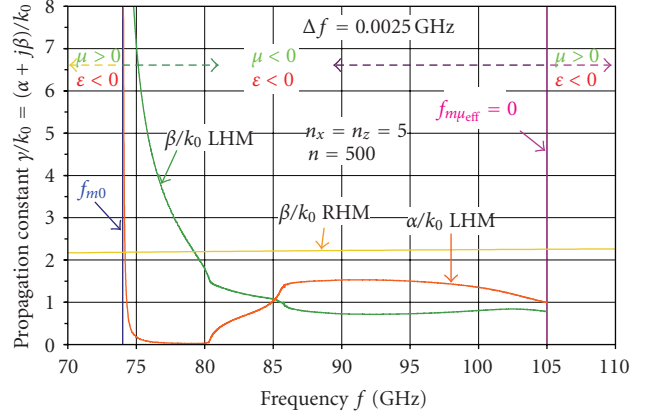


FIGURE 2: Complex propagation constant γ/k_0 versus frequency f over the range 70–105 GHz for the fundamental modes of an microstrip configuration for an RHM/PPV substrate and for a LHM/NPV substrate with SRR inclusions.

z -direction is $\oint \mathbf{P}_z \cdot \beta \hat{z} dA > 0$ (dA is the differential cross-sectional element) or equivalently $\mathbf{v}_{gl} \cdot \mathbf{v}_{pl} > 0$. The other solution is a backward wave for nondispersive intrinsic LHMs ($\bar{\beta} = \beta/k_0 = 1.177647$), where the product of the integrated Poynting vector and the phase vector in the z -direction is $\oint \mathbf{P}_z \cdot \beta \hat{z} dA < 0$ or equivalently $\mathbf{v}_{gl} \cdot \mathbf{v}_{pl} < 0$. Here, \mathbf{v}_{gl} and \mathbf{v}_{pl} are, respectively, the group and phase longitudinal velocities. These modes are referred to as fundamental modes in the sense that as $f \rightarrow 0$, a solution exists (we had earlier looked at this type of mode for the RHM/PPV substrate).

As damping loss is turned on and becomes finite, only the forward guided wave will exist, and the backward guided wave will cease to exist. The fundamental mode for the upper root is shown in Figure 2, not extending beyond either 74 GHz on the low end or 105 GHz on the high end because $\text{sg}[\varepsilon(\omega)] \text{sg}[\mu(\omega)] = -1$, and that product causes evanescent propagation to occur where β is extremely tiny. Below f_{m0} and above f_{mco} , $\mu > 0$ and $\varepsilon < 0$. However, between these critical frequency points, $\text{sg}[\varepsilon(\omega)] \text{sg}[\mu(\omega)] = +1$ and the wave propagates with $\mu < 0$ and $\varepsilon < 0$. Out of the range plotted, above the electric crossover frequency f_{eco} (near f_{pe} for low loss) where effective permeability $\varepsilon_{\text{eff}} = 0$, $\text{sg}[\varepsilon(\omega)] \text{sg}[\mu(\omega)] = +1$ will occur again, with $\mu > 0$ and $\varepsilon > 0$ this time, being completely reversed from the region between f_{m0} and f_{mco} .

The dispersion curves for the LHM/NPV substrate are plotted in Figure 2 using $n_x = n_z = 5$ and $n = 500$ with frequency increments of $\Delta f = 0.0025$ GHz between eigenvalue points (only small differences with solutions at $n_x = n_z = 9$, $n = 900$, $n_x = n_z = 1$, and $n = 100$ have been found, on the order of less than a few tenths of a percent). At 80 GHz, $\bar{\gamma} = (\bar{\alpha}, \bar{\beta}) = (0.0320222, 1.79365)$ for $n_x = n_z = 1$ and $n = 100$, whereas for $n_x = n_z = 9$ and $n = 900$, $\bar{\gamma} = (0.0322745, 1.79116)$. These values used the parameter settings mentioned above, except $L_e = 0.1305$ GHz and $L_\mu = 0.0853$ GHz, corresponding to about a fifty percent increase in loss width, providing a more conservative estimate of propagation loss due to the metamaterial which could occur

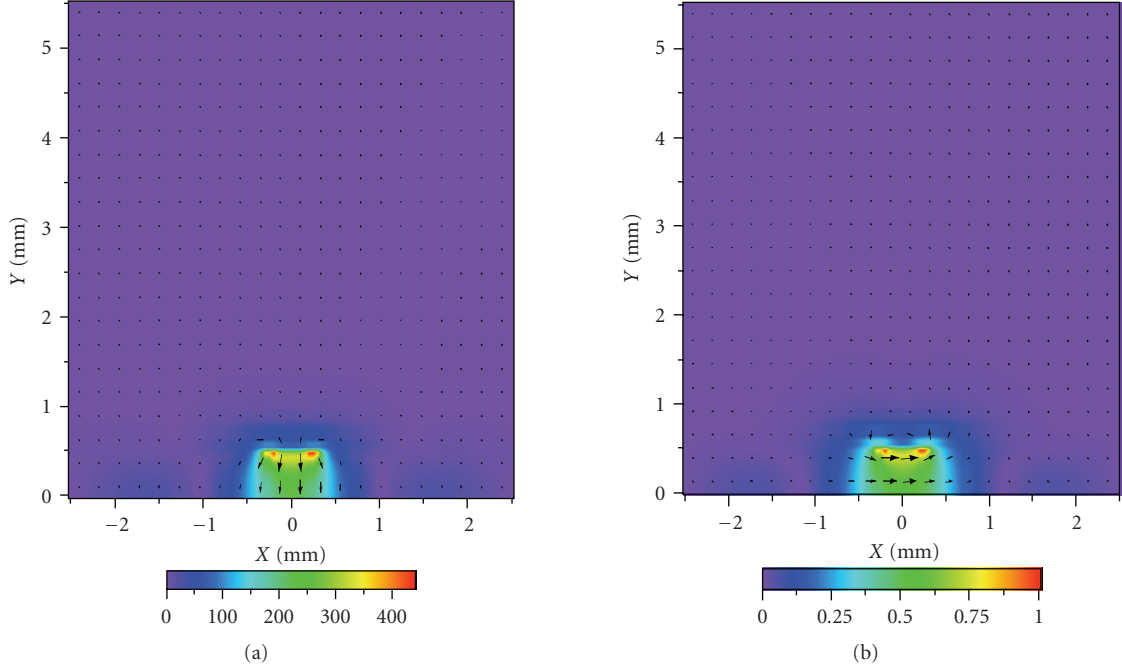


FIGURE 3: For an ordinary RHM/PPV substrate at 80 GHz, we have (a) electric field distributions in a color plot for magnitude E with an overlaid plot for vector \mathbf{E}_t in arrow form unscaled; (b) magnetic field distributions in a color plot for magnitude H with an overlaid plot for vector \mathbf{H}_t in arrow form unscaled.

from imperfect metal or lower conductivity metal. Permittivity and permeability at 80 GHz are $\epsilon = (-2.5156, 5.77348 \times 10^{-3})$ and $\mu = (-2.4817, 2.5713 \times 10^{-2})$, corresponding to loss tangents (ϵ_i/ϵ_r or μ_i/μ_r) of 2.28×10^{-3} and 1.04×10^{-2} . The reason why α rises and β falls after this frequency in Figure 2 is that both ϵ and μ are becoming ever more positive, providing much less left-handed material advantage, with the relative rates of change of ϵ and μ determining the details of the curves. Of course, once the frequency f_{mco} is hit, any effective propagation ceases.

5. ELECTROMAGNETIC FIELD DISTRIBUTIONS FOR LEFT-HANDED DEVICES

In order to correctly perceive the intensity of the fields, $E^2 = \sum_{i=1}^3 E_i^2 = E_t^2 + E_z^2$ and $H^2 = \sum_{i=1}^3 H_i^2 = H_t^2 + H_z^2$ are calculated and plotted as E and H using a color linear scale. These field magnitudes are related to the overall energy content when premultiplied by the appropriate dispersive permittivity and permeability derivatives [1, 47]—something that can be added to the model here by specifying additional microscopic physics of the LHM/NPV. This issue will be addressed in more detail elsewhere. What is important to realize here is that there is no conceptual difficulty in accomplishing that task. Care must be exercised in obtaining the linear color plot. Too small a grid results in a boxy appearance to the color distribution, making it very hard to interpret. Thus, we seek on the order of 10^4 grid points by partitioning each layer into 45 laminations and the vertical-to-vertical wall separation into 90 laminations, giving an 8372 grid points total

from the spectral domain code. (Calculations have been done with as many as 2.5×10^4 grid points.) A Fortner algorithm is used to produce the finished color plots [48].

5.1. RHM/PPV comparison structure

Once we have identified the $\bar{\beta}$ value and know the point in the diagram about which we wish to operate, we can proceed on to making a field distribution plot. Figures 3(a) and 3(b), respectively, show, for the comparison RHM/PPV structure, the E and H magnitude plots for $\bar{\beta} = \beta/k_0 = 2.200$, with unscaled linear arrow plots of electric vector \mathbf{E}_t and magnetic vector \mathbf{H}_t overlaid on them. (Surface current coefficients are $a_{x1} = (0, -0.0637503)$ and $a_{z1} = (1, 0)$.) The arrow overlays allow us to assess the actual cross-sectional magnitudes of the fields locally, as well as their directions, whereas the color distribution allows us to see continuously the entire magnitude of the fields. Field arrows are created in a $N \times M$ grid of points, $N \leq M$, usually $N = M - 1$, with $M = 22$ here. A number of basic features are seen in the plots. Variation of the magnitude has several periods in the x -direction associated with the effective wavelength in the RHM/PPV substrate. The electric field arrows emanating from the microstrip metal located about the device center line $x = 0$ mm, $y = 0.5$ mm, are directed out of the metal, consistent with a single charge residing on it, although it is in general nonuniformly distributed as expected for a conventional structure such as this. Magnetic field arrows circulate about the metal strip in one direction (Figure 3(b)), breaking up into extra fine structure below the interface, but those near the metal strip continue into the substrate just under the strip in regions of extremely

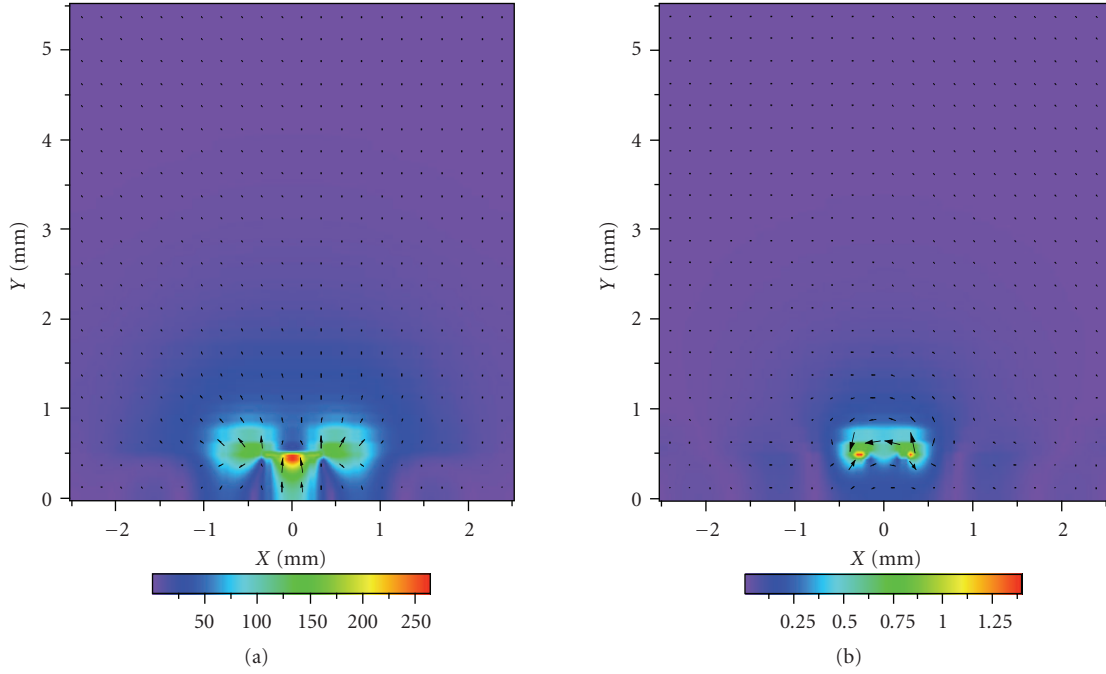


FIGURE 4: For an LHM/NPV substrate at 80 GHz, we have for the lower eigenvalue β (a) electric field distributions in a color plot for magnitude E with an overlaid plot for vector \mathbf{E}_t in arrow form unscaled; (b) magnetic field distributions in a color plot for magnitude H with an overlaid plot for vector \mathbf{H}_t in arrow form unscaled.

intense fields with singularities occurring based upon the edge condition. Even in the highly singular region near the metal strip which possesses delta function charge distributions near its edges, the discontinuity in the transverse \mathbf{H}_t field is related to the surface current \mathbf{J} to within 10% or better by the cross product $\mathbf{H}_t \times \hat{\mathbf{n}}$, where $\hat{\mathbf{n}} = \hat{\mathbf{y}}$ = normal to the interface. Outside of the metal strip interface region, field arrows crossing the interface obey the necessary boundary conditions from within a few percent to small fractions of a percent (these observations also hold for the LHM substrate case).

5.2. LHM/NPV structure

At $f = 80$ GHz for the LHM/NPV substrate case, Figures 4(a) and 4(b), respectively, show the electric E and magnetic H magnitude distributions for the lower root, backward wave LHM/NPV solution (valid for $L_\epsilon \rightarrow 0$, $L_\mu \rightarrow 0$), with unscaled linear arrow plots of electric vector \mathbf{E}_t and magnetic vector \mathbf{H}_t overlaid on them. (Surface current coefficients are $a_{x1} = (0, -0.128419)$ and $a_{z1} = (1, 0)$.) We see from these plots that the electric field E resides both around the guiding strip as well as under it in the LHM/NPV substrate. Magnetic field H is more localized near the strip metal. The upper forward wave LHM/NPV solution (valid for $L_\epsilon \neq 0$, $L_\mu \neq 0$) shown in Figures 5(a) and 5(b) demonstrates a more complicated distribution, with much more of it under the strip inside the LHM/NPV. (Surface current coefficients are $a_{x1} = (0, -0.142740)$ and $a_{z1} = (1, 0)$.) A number of striking differences are noted by comparing these results to

the ordinary substrate medium case in Figure 3 (RHM/PPV structure). Firstly, the E and H intensity distributions differ in appearance significantly for the LHM/NPV substrate structure compared to the relatively simple field pattern of the RHM/PPV structure. Secondly, in Figure 4(a), the electric field arrows \mathbf{E}_t do not point into (or out of) the metal strip but point roughly (this interpretation is modified by examining the field line distribution patterns to be discussed below in reference to Figure 6 for the LHM/NPV structure) in one direction above and below the strip, indicating that this branch still has a single charge (as was found for the RHM/PPV case in Figure 4) due to the reversed effect of the displacement electric field continuity condition normal to the interface. Thirdly, in Figure 4(a), electric field \mathbf{E}_t arrows, away from the metal strip near the interface, point in opposite directions as they cross the interface in terms of their normal components. Fourthly, in Figure 4(b), magnetic field \mathbf{H}_t arrows circulate around the strip in one direction above the interface and in the opposite direction below it, and the magnetic field arrows \mathbf{H}_t when crossing the interface point in opposite directions in terms of their y -components. Fifthly, in Figure 5(a), the electric field arrows \mathbf{E}_t point roughly (again this interpretation is modified later by the field line distribution patterns to be presented below in Figure 5) into (or out of) the metal guiding strip indicating a situation only possible if an infinitesimal dipolar charge arrangement exists in the vertical sense [35].

Of course, in addition to these noted differences between RHM/PPV and LHM/NPV substrates on guided wave behavior, the two solutions have significantly different field line

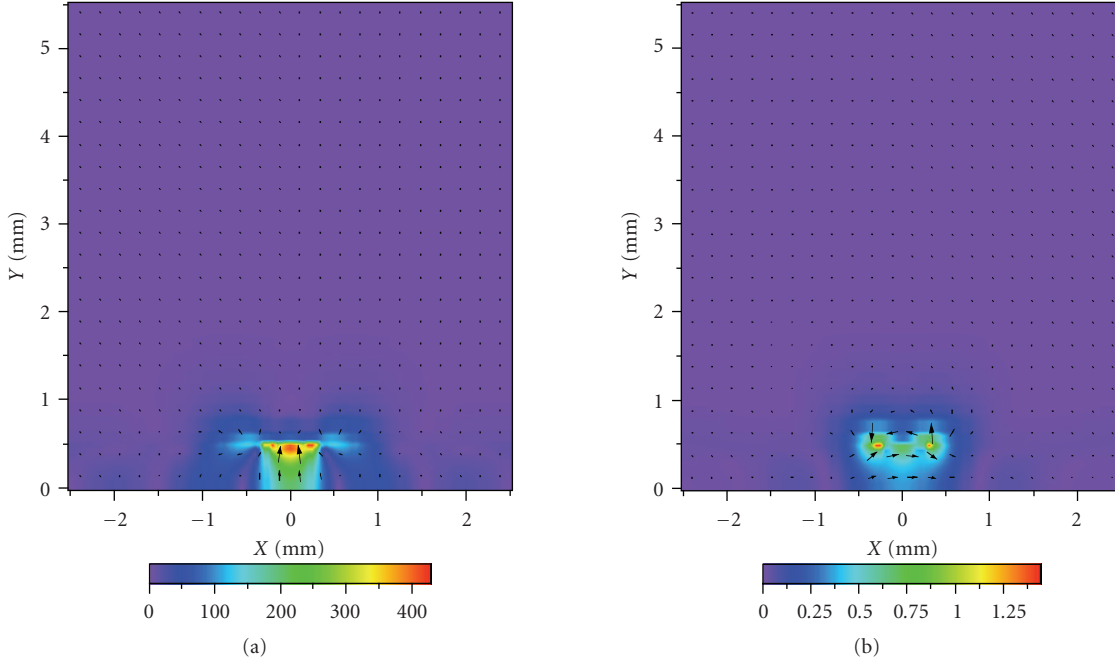


FIGURE 5: For an LHM/NPV substrate at 80 GHz, we have for the upper eigenvalue β (a) electric field distributions in a color plot for magnitude E with an overlaid plot for vector \mathbf{E}_t in arrow form unscaled; (b) magnetic field distributions in a color plot for magnitude H with an overlaid plot for vector \mathbf{H}_t in arrow form unscaled.

distribution patterns as seen in Figure 6 for the LHM/NPV structure. This is clear from the nearly circular circulating magnetic lines (first three) around the strip for the higher β value forward wave (see Figure 6(b)) compared to the broadly extended magnetic field lines for the lower β value backward wave (see Figure 6(a)). (This is evident by looking at the region above the substrate.) The electric field lines exhibit a dense pattern near the strip for the higher β value somewhat contained in a “shell,” compared to that of the lower β value mini-“shell” which barely shows this pattern emerging (examine the region just above the metal strip in the air zone). For the lower β value (see Figure 6(a)), there is a positive charge on the bottom half of the strip in the LHM/NPV (field lines enter into the strip) as well as on the ends (field lines exit from the last quarter length of the total strip length on either side of the strip) of the top part of the strip. But the mini-“shell” has its \mathbf{E}_t field lines emanating from the inner edges of the positive top charge at the boundary between this positive charge and an inside region of the top strip which is negatively charged. Upper β solution has its “shell” extending about 20% beyond the strip width, with the \mathbf{E}_t field lines emanating from the “shell” surface with the lines terminating nearest the strip center, originating near the intersection of the “shell” surface and the interface. Outside of the “shell” in both Figures 6(a) and 6(b), the electric field lines \mathbf{E}_t revert back to the simpler case of them seemingly to arise from a single uniform charge on both sides of the strip. Because the “shell” is not seen at considerably lower frequencies, this seems to imply that at higher frequencies the structure is trying to become more like an ordinary media layered

device. Finally, we note that both the electric \mathbf{E}_t and magnetic \mathbf{H}_t field line patterns are much more intricate for the higher β value in comparison to the lower β value beneath the interface in the LHM/NPV substrate.

To better visualize the directions of the fields throughout the device area, unconstrained by the need to follow selected field lines, but to retain those useful features in such field line plots, we have developed scaled arrow plots which lift the tiny magnitude field values from the background. One of the simplest methods to lift the fields in the background from numerical obscurity to visibility is to perform a log scaling such as

$$E_i = \begin{cases} \frac{E_i}{E_{i,\min}} \log_{10} \left(\left| \frac{E_i}{E_{i,\min}} \right| \right), & |E_i| > E_{i,\min}, \\ 0 & |E_i| \leq E_{i,\min}, \end{cases} \quad (3)$$

$$H_i = \begin{cases} \frac{H_i}{H_{i,\min}} \log_{10} \left(\left| \frac{H_i}{H_{i,\min}} \right| \right), & |H_i| > H_{i,\min}, \\ 0 & |H_i| \leq H_{i,\min}, \end{cases}$$

where $E_{i,\min}$ and $H_{i,\min}$ are positive magnitude cutoffs, and the argument presented to the \log_{10} operator is always positive whereas the sign of the field component is preserved in the prefactor. The problem with this scaling approach, though, is that it can damage the angle between the x - and

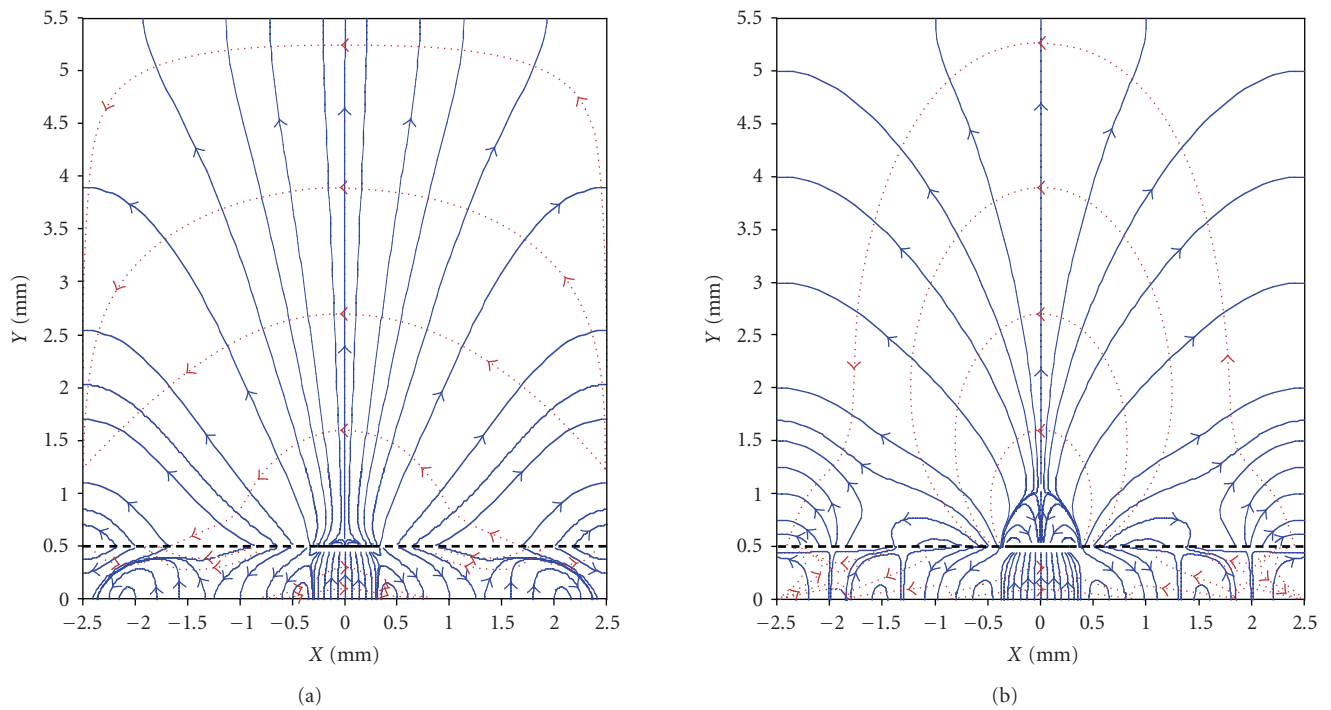


FIGURE 6: Electromagnetic field line distribution plots showing electric \mathbf{E}_t (blue dotted line) and magnetic \mathbf{H}_t (red dashed line) fields at 80 GHz for an LHM/NPV substrate in the fundamental mode for (a) the lower $\beta/k_0 = 1.177647$ and (b) the upper $\alpha/k_0 = 0.032022175$, $\beta/k_0 = 1.7936490$ eigenvalue solutions.

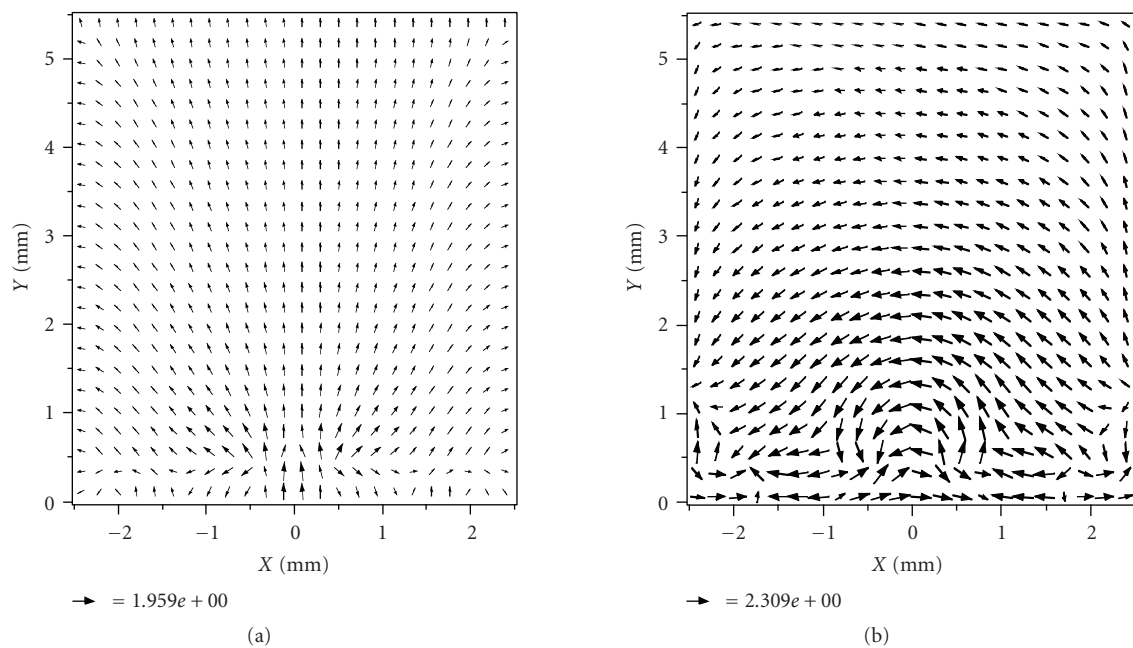


FIGURE 7: Arrow field distribution plots for the LHM/NPV structure at 80 GHz for (a) electric field \mathbf{E}_t and (b) magnetic field \mathbf{H}_t for the lower $\beta/k_0 = 1.1776$ eigenvalue solution using a trigonometric scaling method.

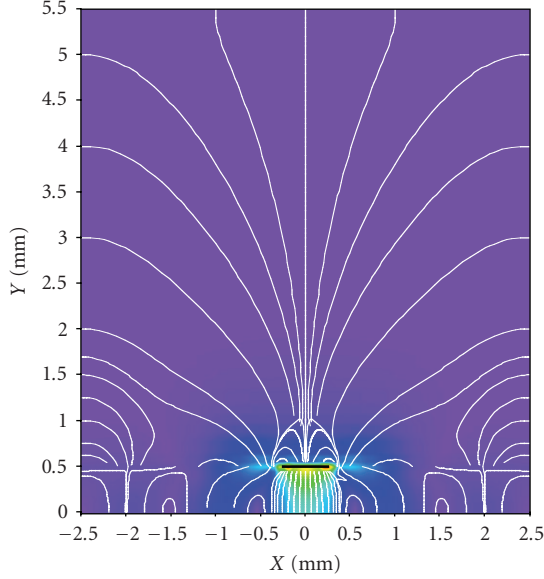


FIGURE 8: For an LHM/NPV substrate at 80 GHz, for the upper eigenvalue β , the electric field distribution in a color plot for magnitude E with an overlaid line distribution plot for E_t is shown.

y -components of the fields. Therefore, we have instead created an inverse trigonometric method,

$$\begin{aligned} E_i &= \frac{E_i}{E_t} \left[\left| \tan^{-1} \left(\frac{E_i}{E_{av}} \right) \right| + 0.75 \right], \\ H_i &= \frac{H_i}{H_t} \left[\left| \tan^{-1} \left(\frac{H_i}{H_{av}} \right) \right| + 0.75 \right]. \end{aligned} \quad (4)$$

Here,

$$\begin{aligned} E_t^2 &= E_x^2 + E_y^2, \\ H_t^2 &= H_x^2 + H_y^2. \end{aligned} \quad (5)$$

Ratio factor on the left is merely the cosine of the field angular offset from the x -axis, that is, $\cos \theta_E = E_i/E_t$ and $\cos \theta_H = H_i/H_t$. Figures 7(a) and 7(b), respectively, plot the electric and magnetic field distributions for the lower β LHM/NPV solution, with $E_{av} = 100$ V/m and $H_{av} = 0.01$ amps/m.

Lastly, in Figure 8 is provided the electric field E magnitude distribution for the LHM/NPV structure, overlaid with electric field lines E_t for the upper eigenvalue at 80 GHz. This figure combines some of the information from Figures 5(a) and 6(b), in such a way to assist visualization and understanding of the field behavior, allowing one to see the directional information at a glance while being able to assess the strength of the field.

6. CONCLUSION

In conclusion, we have shown completely new field distributions in a guided wave microstrip-like device structure containing left-handed material (LHM), otherwise referred to also as negative phase velocity material (NPV or NPVM)

in the power/phase sense. The results are valid for intrinsic LH crystalline materials, LH metamaterials, or LH heterostructure or layered crystalline materials. These field distributions show new physics, and although that is what has drawn our attention, such structures which are compatible with integrated circuit and solid state technology may open up many future possibilities. Unusual field distributions based upon new physics suggest the chance of completely new devices for future electronics besides the amendment of present devices which act as control components, active devices, and passive transmission structures. New devices could include millimeter-wave couplers, filters, phase shifters, isolators, and circulators, to mention a few.

We have also learned from the dispersion diagram for a SRR type of metamaterial LHM substrate that although the resonance nature of the unit cell can be extremely lossy at resonance, away from resonance there is a region of low enough loss to suggest realistic use in millimeter-wave integrated circuits.

REFERENCES

- [1] V. G. Veselago, "Electrodynamics of media with simultaneous negative electric permittivity and magnetic permeability," in *Advances in Electromagnetics of Complex Media and Metamaterials*, S. Zouhdi, A. H. Sihvola, and M. Arsalane, Eds., NATO Science, pp. 83–97, Kluwer Academic Publishers, Dordrecht, The Netherlands, 2002.
- [2] P. F. Loschialpo, D. L. Smith, D. W. Forester, F. J. Rachford, and J. Schelleng, "Electromagnetic waves focused by a negative-index planar lens," *Physical Review E*, vol. 67, no. 2, Article ID 025602, 4 pages, 2003.
- [3] F. J. Rachford, D. L. Smith, P. F. Loschialpo, and D. W. Forester, "Calculations and measurements of wire and/or split-ring negative index media," *Physical Review E*, vol. 66, no. 3, Article ID 036613, 5 pages, 2002.
- [4] W. T. Lu, J. B. Sokoloff, and S. Sridhar, "Refraction of electromagnetic energy for wave packets incident on a negative-index medium is always negative," *Physical Review E*, vol. 69, no. 2, Article ID 026604, 5 pages, 2004.
- [5] A. Lakhtakia and J. A. Sherwin, "Orthorhombic materials and perfect lenses," *International Journal of Infrared and Millimeter Waves*, vol. 24, no. 1, pp. 19–23, 2003.
- [6] A. Lakhtakia, "Handedness reversal of circular Bragg phenomenon due to negative real permittivity and permeability," *Optics Express*, vol. 11, no. 7, pp. 716–722, 2003.
- [7] R. B. Gregor, C. G. Parazzoli, K. Li, and M. H. Tanielian, "Origin of dissipative losses in negative index of refraction materials," *Applied Physics Letters*, vol. 82, no. 14, pp. 2356–2358, 2003.
- [8] S. Foteinopoulou, E. N. Economou, and C. M. Soukoulis, "Refraction in media with a negative refractive index," *Physical Review Letters*, vol. 90, no. 10, Article ID 107402, 4 pages, 2003.
- [9] D. R. Smith and D. Schurig, "Electromagnetic wave propagation in media with indefinite permittivity and permeability tensors," *Physical Review Letters*, vol. 90, no. 7, Article ID 077405, 4 pages, 2003.
- [10] A. A. Houck, J. B. Brock, and I. L. Chuang, "Experimental observations of a left-handed material that obeys Snell's law," *Physical Review Letters*, vol. 90, no. 13, Article ID 137401, 4 pages, 2003.

- [11] C. G. Parazzoli, R. B. Greegor, K. Li, B. E. C. Koltenbah, and M. Tanielian, "Experimental verification and simulation of negative index of refraction using Snell's law," *Physical Review Letters*, vol. 90, no. 10, Article ID 107401, 4 pages, 2003.
- [12] J. Pacheco Jr., T. M. Grzegorzczuk, B.-I. Wu, Y. Zhang, and J. A. Kong, "Power propagation in homogeneous isotropic frequency-dispersive left-handed media," *Physical Review Letters*, vol. 89, no. 25, Article ID 257401, 4 pages, 2002.
- [13] A. Lakhtakia, M. W. McCall, and W. S. Weiglhofer, "Brief overview of recent developments on negative phase-velocity mediums (alias left-handed materials)," *AEU—International Journal of Electronics and Communications*, vol. 56, no. 6, pp. 407–410, 2002.
- [14] R. Ruppin, "Surface polaritons of a left-handed material slab," *Journal of Physics Condensed Matter*, vol. 13, no. 9, pp. 1811–1818, 2001.
- [15] G. W. 't Hooft, "Comment on 'negative refraction makes a perfect lens'" *Physical Review Letters*, vol. 87, no. 24, Article ID 249701, 1 pages, 2001.
- [16] J. Pendry, "Pendry replies," *Physical Review Letters*, vol. 87, no. 24, Article ID 249702, 1 pages, 2001.
- [17] J. M. Williams, "Some problems with negative refraction," *Physical Review Letters*, vol. 87, no. 24, Article ID 249703, 1 pages, 2001.
- [18] J. Pendry, "Pendry replies," *Physical Review Letters*, vol. 87, no. 24, Article ID 249704, 1 pages, 2001.
- [19] G. Dewar, "Candidates for $\mu < 0$, $\epsilon < 0$ nanostructures," *International Journal of Modern Physics B*, vol. 15, no. 24–25, pp. 3258–3265, 2001.
- [20] Z. M. Zhang and C. J. Fu, "Unusual photon tunneling in the presence of a layer with a negative refractive index," *Applied Physics Letters*, vol. 80, no. 6, pp. 1097–1099, 2002.
- [21] A. Lakhtakia, "On perfect lenses and nihility," *International Journal of Infrared and Millimeter Waves*, vol. 23, no. 3, pp. 339–343, 2002.
- [22] E. Shamonina, V. A. Kalinin, K. H. Ringhofer, and L. Solymar, "Imaging, compression and Poynting vector streamlines for negative permittivity materials," *Electronics Letters*, vol. 37, no. 20, pp. 1243–1244, 2001.
- [23] J. Paul, C. Christopoulos, and D. W. P. Thomas, "Time-domain modelling of negative refractive index material," *Electronics Letters*, vol. 37, no. 14, pp. 912–913, 2001.
- [24] T. Weiland, R. Schuhmann, R. B. Greegor, et al., "Ab initio numerical simulation of left-handed metamaterials: comparison of calculations and experiments," *Journal of Applied Physics*, vol. 90, no. 10, pp. 5419–5424, 2001.
- [25] C. Caloz, C.-C. Chang, and T. Itoh, "Full-wave verification of the fundamental properties of left-handed materials in waveguide configurations," *Journal of Applied Physics*, vol. 90, no. 11, pp. 5483–5486, 2001.
- [26] A. Grbic and G. V. Eleftheriades, "Dispersion analysis of a microstrip-based negative refractive index periodic structure," *IEEE Microwave and Wireless Components Letters*, vol. 13, no. 4, pp. 155–157, 2003.
- [27] G. V. Eleftheriades, A. K. Iyer, and P. C. Kremer, "Planar negative refractive index media using periodically L-C loaded transmission lines," *IEEE Transactions on Microwave Theory and Techniques*, vol. 50, no. 12, pp. 2702–2712, 2002.
- [28] A. Grbic and G. V. Eleftheriades, "Experimental verification of backward-wave radiation from a negative refractive index metamaterial," *Journal of Applied Physics*, vol. 92, no. 10, pp. 5930–5935, 2002.
- [29] A. Alu and N. Engheta, "Radiation from a traveling-wave current sheet at the interface between a conventional material and a metamaterial with negative permittivity and permeability," *Microwave and Optical Technology Letters*, vol. 35, no. 6, pp. 460–463, 2002.
- [30] N. Engheta, "An idea for thin subwavelength cavity resonators using metamaterials with negative permittivity and permeability," *IEEE Antennas and Wireless Propagation Letters*, vol. 1, no. 1, pp. 10–13, 2002.
- [31] C. Caloz, A. Sanada, L. Liu, and T. Itoh, "A broadband left-handed (LH) coupled-line backward coupler with arbitrary coupling level," in *IEEE MTT-S International Microwave Symposium Digest*, vol. 1, pp. 317–320, Philadelphia, Pa, USA, June 2003.
- [32] I.-H. Lin, C. Caloz, and T. Itoh, "A branch-line coupler with two arbitrary operating frequencies using left-handed transmission lines," in *IEEE MTT-S International Microwave Symposium Digest*, vol. 1, pp. 325–328, Philadelphia, Pa, USA, June 2003.
- [33] H. Okabe, C. Caloz, and T. Itoh, "A compact enhanced-bandwidth hybrid ring using a left-handed transmission line section," in *IEEE MTT-S International Microwave Symposium Digest*, vol. 1, pp. 329–332, Philadelphia, Pa, USA, June 2003.
- [34] N. Engheta, "Ideas for potential applications of metamaterials with negative permittivity and permeability," in *Advances in Electromagnetics of Complex Media and Metamaterials*, S. Zouhdi, A. H. Sihvola, and M. Arsalane, Eds., NATO Science, pp. 19–37, Kluwer Academic Publishers, Dordrecht, The Netherlands, 2002.
- [35] C. M. Krowne, "Physics of propagation in left-handed guided wave structures at microwave and millimeter wave frequencies," *Physical Review Letters*, vol. 92, no. 5, Article ID 053901, 4 pages, 2004.
- [36] C. M. Krowne and M. Daniel, "Electronic aspects of propagation in left-handed guided wave structures: electromagnetic-media interactions," in *IEEE MTT-S International Microwave Symposium Digest*, vol. 1, pp. 309–312, Philadelphia, Pa, USA, June 2003.
- [37] C. M. Krowne, "Physics and electronics of left-handed guided wave devices," *Bulletin of the American Physical Society*, vol. 48, part 1, p. 580, 2003.
- [38] C. M. Krowne, "Electromagnetic-field theory and numerically generated results for propagation in left-handed guided-wave single-microstrip structures," *IEEE Transactions on Microwave Theory and Techniques*, vol. 51, no. 12, pp. 2269–2283, 2003.
- [39] C. M. Krowne, "Negative refractive Bi—crystal with broken symmetry leading to unusual fields in guided wave heterostructures," *Bulletin of the American Physical Society*, vol. 49, part 2, p. 928, 2004.
- [40] C. M. Krowne, "Left-handed material anisotropy effect on guided wave electromagnetic fields," *Journal of Applied Physics*, vol. 99, no. 4, Article ID 044914, 19 pages, 2006.
- [41] Y. Zhang, B. Fluegel, and A. Mascarenhas, "Total negative refraction in real crystals for ballistic electrons and light," *Physical Review Letters*, vol. 91, no. 15, Article ID 157404, 4 pages, 2003.
- [42] C. M. Krowne, "Negative-refractive bicrystal with broken symmetry produces asymmetric electromagnetic fields in guided-wave heterostructures," *Physical Review Letters*, vol. 93, no. 5, Article ID 053902, 2004.
- [43] A. Lakhtakia and C. M. Krowne, "Restricted equivalence of paired epsilon-negative and mu-negative layers to a negative

- phase-velocity material (alias left-handed material),” *Optik*, vol. 114, no. 7, pp. 305–307, 2003.
- [44] J. B. Pendry, A. J. Holden, D. J. Robbins, and W. J. Stewart, “Magnetism from conductors and enhanced nonlinear phenomena,” *IEEE Transactions on Microwave Theory and Techniques*, vol. 47, no. 11, pp. 2075–2084, 1999.
- [45] C. M. Krowne, “Dyadic Green’s function modifications for obtaining attenuation in microstrip transmission layered structures with complex media,” *IEEE Transactions on Microwave Theory and Techniques*, vol. 50, no. 1, pp. 112–122, 2002.
- [46] J. B. Pendry, A. J. Holden, W. J. Stewart, and I. Youngs, “Extremely low frequency plasmons in metallic mesostructures,” *Physical Review Letters*, vol. 76, no. 25, pp. 4773–4776, 1996.
- [47] L. D. Landau, E. M. Lifshitz, and L. P. Pitaevskii, *Electrodynamics of Continuous Media*, Pergamon Press, Oxford, UK, 1984.
- [48] Fortner Research LLC. Commercial plotting software, 1996.

Research Article

3D-Simulation of Topology-Induced Changes of Effective Permeability and Permittivity in Composite Materials

B. Hallouet and R. Pelster

Fachrichtung 7.2, Experimentalphysik, Universität des Saarlandes, Postfach 151150, 66041 Saarbrücken, Germany

Received 15 February 2007; Revised 11 May 2007; Accepted 4 June 2007

Recommended by Christian Brosseau

We have performed 3D simulations of complex effective permittivity and permeability for random binary mixtures of cubic particles below the percolation threshold. We compare two topological classes that correspond to different spatial particle arrangements: cermet topology and aggregate topology. At a low filling factor of $f = 10\%$, where most particles are surrounded by matrix material, the respective effective material parameters are indistinguishable. At higher concentrations, a systematic difference emerges: cermet topology is characterized by lower effective permittivity and permeability values. A distinction between topological classes might thus be a useful concept for the analysis of real systems, especially in cases where no exact effective-medium model is available.

Copyright © 2007 B. Hallouet and R. Pelster. This is an open access article distributed under the Creative Commons Attribution License, which permits unrestricted use, distribution, and reproduction in any medium, provided the original work is properly cited.

1. INTRODUCTION

Composite materials have a lot of technical applications, and especially magnetic nanocomposites have been studied recently [1–3]. The fundamental question is how the properties of their components and their microstructure contribute to the effective properties of the new material. Besides a multiplicity of approximative mixture formulas, there are some analytical solutions of the so-called effective-medium problem (see, e.g., [4–8]). Also 2D and 3D computer simulations allow to predict the effective material parameters for various particle arrangements and shape (see, e.g., [9–17]). The inherent structure-dependence is beyond controversy and in the strict sense every microstructure can give rise to a different mixture rule. Therefore, the analysis of nanocomposites, for example, of nanoparticles dispersed in a host material, represents a challenge: due to the difficulty to control a spatial particle arrangement on a nm scale, the exact microstructure is often unknown. Nevertheless, we are still interested either in predicting the properties of the composite or in studying the dispersed nanoparticles that do not necessarily behave like bulk material (the latter case represents the so-called inverse problem, where measured effective quantities are used to evaluate the properties of a component). For both cases, at least approximative procedures are required. In view of this fact, we raise a fundamental question regarding

the concept of topological classes. More precisely, we want to find out to what extent it is useful to distinguish between two topological classes.

In the following, we consider composite materials consisting of 2 phases that we call “matrix” and “particles” (indices “ m ” and “ p ”). In order to attribute an effective permittivity and an effective permeability to these mixtures, the structural inhomogeneities have to be sufficiently small compared to the wavelength of an applied electromagnetic field. According to their definition as volume averaged quantities [18, 19], the effective material parameters are independent of the size of the inclusions, but depend on the volume filling factor of the particles $f = V_p/V_{\text{total}}$ as well as on the properties of the two components,

$$\frac{\epsilon_{\text{eff}}}{\epsilon_m} = \mathcal{F}\left(f, \frac{\epsilon_p}{\epsilon_m}\right), \quad (1)$$

whereas the function \mathcal{F} depends on the microstructure. The same holds for the magnetic permeability, presupposed that the field excitation is unchanged (consider, e.g., a sample in a homogeneous electric or magnetic field):

$$\frac{\mu_{\text{eff}}}{\mu_m} = \mathcal{F}\left(f, \frac{\mu_p}{\mu_m}\right). \quad (2)$$

According to a formalism developed by Bergman, Fuchs, and Milton, it is even possible to separate the influence of

microstructure, characterized by a spectral density function g , from that of the components, characterized by their material parameters [20]: the effective permittivity can be written as

$$\frac{\epsilon_{\text{eff}}}{\epsilon_m} = 1 + f \left\{ \frac{C}{t} + \int_0^1 \frac{g_f(n)}{t+n} dn \right\} \quad (3)$$

with $t = 1/(\epsilon_p/\epsilon_m - 1)$ and C being the strength of percolation describing the contribution of infinite clusters. Although there is no method to determine $g_f(n)$ from first principles, the theoretical consequences are quite clear: every new microstructure requires a new calculation of the effective properties. The implications for the analysis of real systems are not so explicit. Do experimental physicists need a different mixture formula for every real sample system? And how should they select one when no detailed information about the microstructure is available? In such cases, where it is impossible to choose an “exact” model, topological criteria are applied to find the best approximation for the system under study.

Generally, two topological classes are considered in the description of binary composite materials [18]. On the one hand the so-called matrix inclusion topology (cermet topology, separated grain structure), where a discontinuous phase (e.g., particles below the percolation threshold f_c) is dispersed in a continuous host matrix, all regions of which are perfectly interconnected (e.g., a polymer or a liquid, see Figures 1(a) or 3(a)). Here matrix and filler are not topologically equivalent. For example, an exact analytical solution for an arbitrary spatial configuration of well-separated spheres has been formulated in [6]. Based on this, 3D computer simulations were performed [21] showing that two of the well-known effective medium formulas for randomly dispersed particles describe the limits of very narrow and very broad particle-size distributions (see Figure 2): for monodisperse spheres Maxwell-Garnet formula holds:

$$\epsilon_{\text{eff}} = \epsilon_m \cdot \left(1 + f \cdot \frac{\epsilon_p - \epsilon_m}{\epsilon_m + (1-f) \cdot 1/3 \cdot (\epsilon_p - \epsilon_m)} \right), \quad (4)$$

while for polydisperse systems with a sufficiently broad size-distribution the Hanai-Bruggeman formula applies:

$$\left(\frac{\epsilon_{\text{eff}} - \epsilon_p}{\epsilon_m - \epsilon_p} \right) \cdot \left(\frac{\epsilon_m}{\epsilon_{\text{eff}}} \right)^{1/3} = (1-f). \quad (5)$$

The latter is often successfully applied to describe experimental data, since most real systems are polydisperse (see, e.g., [22]). But of course, depending on the degree of agglomeration, real systems can show more complicated non-random spatial arrangements so that the above mixture rules are no longer valid (see, e.g., [23]).

On the other hand, there is the so-called aggregate topology, where both phases are topologically equivalent (see Figures 1(b) or 3(b)). This equivalence reflects in the symmetry of the corresponding mixture formula: interchanging both phases, $\epsilon_p \leftrightarrow \epsilon_m$ and $f \leftrightarrow (1-f)$, does not affect the result: $\epsilon_{\text{eff}}(\epsilon_p, \epsilon_m, f) = \epsilon_{\text{eff}}(\epsilon_m, \epsilon_p, 1-f)$. An example is, for example,

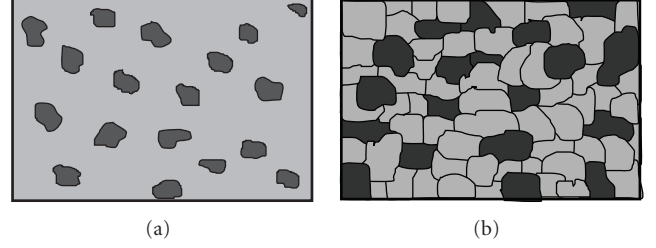


FIGURE 1: (a) Matrix inclusion topology (cermet topology, separated grain structure) describing discrete particles that are dispersed in a continuous host phase. (b) Aggregate topology, where two topologically equivalent phases are mixed (compact powders consisting of two types of particles, polymer mixtures, interpenetrating network structures, etc.) For an idealized system, see Figure 3.

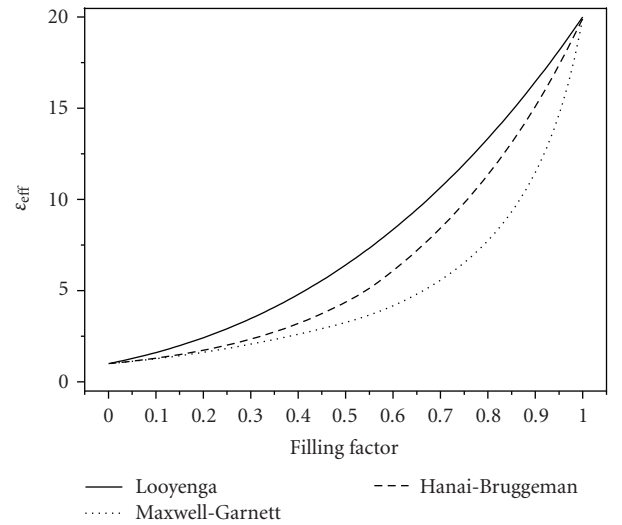


FIGURE 2: Effective permittivity versus volume filling factor for a binary mixture with $\epsilon_p = 20$ and $\epsilon_m = 1$: examples for matrix inclusion topology (model of Maxwell-Garnet, (4), and Hanai-Bruggeman, (5)) and aggregate topology (model of Looyenga, (6)).

the formula of Landau, Lifshitz, and Looyenga (see Figure 2)

$$\epsilon_{\text{eff}}^{1/3} = f \epsilon_{\text{eff}}^{1/3} + (1-f) \epsilon_m^{1/3}. \quad (6)$$

The aggregate topology is, for example, appropriate for compact powders, heterogeneous polymer mixtures, and interpenetrating network structures [19]. In a range of filling factors, where both phases are above their percolation threshold, they exhibit a high degree of interconnection and form some kind of interwoven network. In this case, even particles in a continuous host phase can be approximated fairly well by the aggregate topology. For example, in a recent study, experimental data for granular material (pulverized samples, i.e., air-particle mixtures) was compared with 6 effective media formulas, 3 of them belonging to the cermet topology, and 3 to the aggregate topology, and the above Looyenga-equation performed best [24]. In Figure 2, we compare the above mixture formulas. The model of Looyenga yields higher effective

values, but it is not clear whether this is a fundamental feature of the aggregate topology: there is a multiplicity of approximative formulas for both topologies [25, 26], the respective range of validity is sometimes difficult to assess, and we have just made an arbitrary choice of 3 models.

Summarizing, there is some experimental evidence that depending on the concentration range, a topological discrimination might be a useful concept: above the percolation threshold formulas of the “aggregate type” perform well, while below this threshold formulas of the “cermet type” can yield good approximations (at least for systems of well separated particles). But it is difficult to assess whether this difference is of fundamental nature and whether it persists when we compare nonpercolating systems with an identical particle concentration.

In this article, we thus want to shed some light on the difference between both topologies. We focus on composite materials at filling factors below the percolation threshold, where in both cases the dispersed phase does not form a continuous network. For this purpose, we have performed computer simulations of 3D systems containing dispersed cubic particles as sketched in Figure 3. With monodisperse particles of this shape, it is possible to realize both topologies just by varying their spatial arrangement. For a given concentration, the respective microstructures look rather similar (and they would be hardly distinguishable without indicating the cubic grid in the sketch of the aggregate topology): there are just particles in a matrix. We would like to know whether, despite this similarity, the effective properties differ considerably. Only in this case the concept of topological classes might help to discriminate between effective medium models and to select the best approximation for the analysis of experimental data.

2. SIMULATION

2.1. Method

Filling a resonator with a material leads to a change of its complex resonance frequency, an effect that can be used to determine the effective material parameters of a composite:

$$\nu = \frac{\nu_0}{\sqrt{(\epsilon\mu)_{\text{eff}}}}, \tag{7}$$

with ν_0 being the resonance frequency of the empty resonator and ν that of the material-filled resonator (these are complex frequencies, whereas the imaginary part reflects losses [27]). The simulation is based on the discretization of the Maxwell laws in such a resonator with dimensions $LX * LY * LZ$. Resonator and field distribution of the fundamental mode are sketched in Figure 4. The simulation code was developed by Stölze and Leinders [9–11], who used it to simulate an aggregate topology. It allows to calculate the complex effective permittivity ϵ_{eff} and permeability μ_{eff} of a 3D binary mixture in the following way.

The resonator is filled randomly with N cubes of side length a [$N = (LX/a) * (LY/a) * (LZ/a)$], either particles or matrix material, according to the respective volume fraction (see Figure 5). Such an inhomogeneous filling leads to a

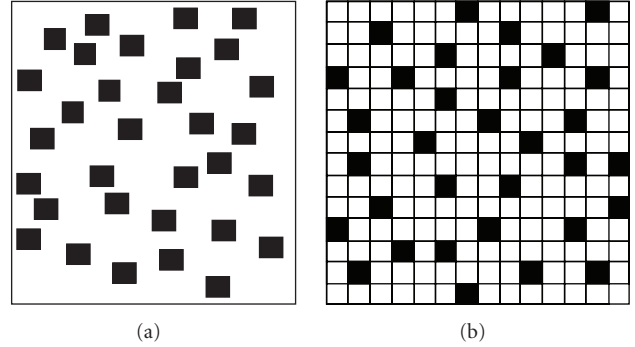


FIGURE 3: Sketch of an isotropic composite material containing randomly dispersed cubic particles: (a) Matrix inclusion topology, where the particle positions are arbitrary (only particle overlap is excluded). (b) Aggregate topology, where the particles are randomly dispersed on a cubic grid (a random mixture of cubes of material “p” and “m”).

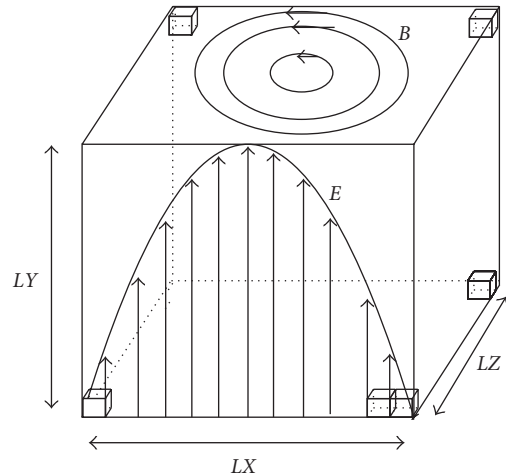


FIGURE 4: Distribution of electric and magnetic fields inside a resonator of size $LX * LY * LZ$ (for an empty resonator in the fundamental mode). When the resonator is filled with cubes of matrix material or particles, this leads to local changes of the field distribution and to a change of resonance frequency.

local perturbation of the fields compared to the well-known analytical solution for an homogeneous filling. The local distribution of electric and magnetic fields in the resonator is calculated following an approach developed by Weiland (see [9–11]). As displayed in Figure 6, a tripod of electric field is assigned at the edges of each cube forming the cubic grid G . A reciprocal grid G^* , shifted by a half diagonal from the first grid G , contains the magnetic field vectors so that they penetrate the surfaces of the cube. The discretisation of the Maxwell equations on these grids leads to an eigenvalue equation that is solved via an algorithm developed by Stölze (for more information we refer to [9–11]). So the field vectors as well as the complex resonance frequency are determined. The latter information allows us to calculate the

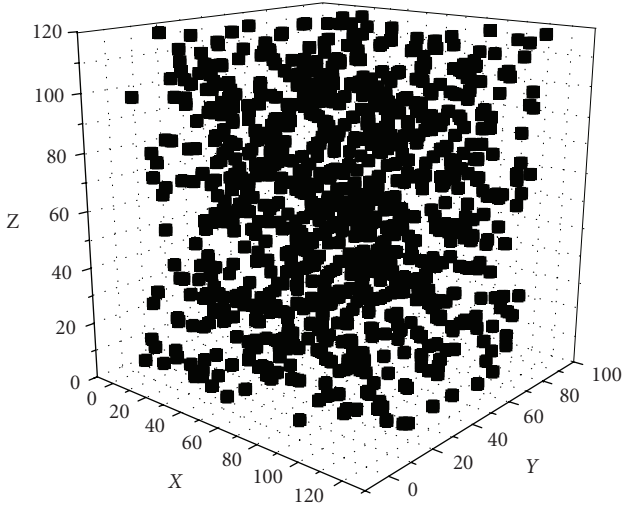


FIGURE 5: Spatial distribution of the particles for a filling factor of 0.56% (size of the resonator: $120a * 90a * 120a$). Different random distributions yield the same effective permittivities or permeabilities within a maximum deviation of 0.5%.

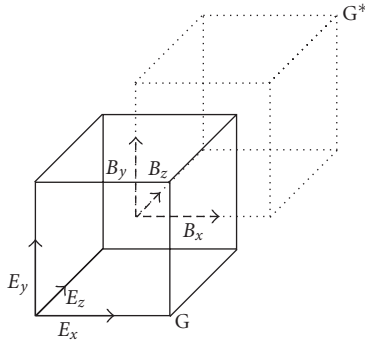
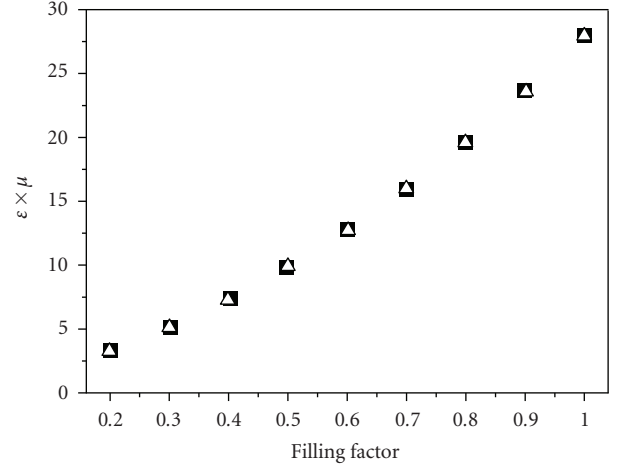


FIGURE 6: Representation of field vectors inside the resonator. The electric field is calculated along the first grid G (of side length a), the magnetic field along the reciprocal grid G^* which is shifted by half a cube diagonal from the first grid.

product $(\epsilon\mu)_{\text{eff}}$ from the complex resonance frequencies of the empty and the filled resonator according to (7).

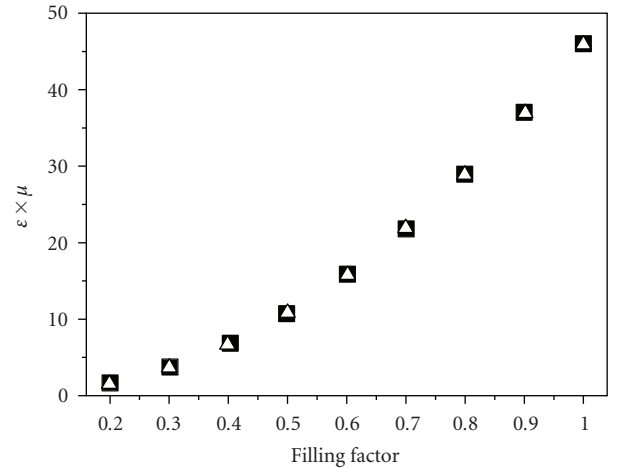
In order to obtain ϵ_{eff} and μ_{eff} separately, two simulation runs are necessary. In the first one, a nonmagnetic system ($\mu_p = \mu_m = 1$) is considered yielding ϵ_{eff} . In the second run, μ_{eff} is evaluated for a purely magnetic material ($\epsilon_p = \epsilon_m = 1$). In Figure 7, we show that the product of these values, $\epsilon_{\text{eff}} \cdot \mu_{\text{eff}}$, equals the value of $(\epsilon\mu)_{\text{eff}}$ that results from a single run (where $\mu_p \neq 1$ and $\epsilon_p \neq 1$). Two final remarks are necessary.

- (i) Since effective permeability and permeability are a function of ϵ_p/ϵ_m and μ_p/μ_m , we can set $\epsilon_m = \mu_m = 1$ in all simulations without loss of generality (see (1) and (2)). A high contrast between matrix and particles results in higher effective material parameters, so that structure-induced changes can be monitored more easily. In the following, we therefore choose particle parameters $|\epsilon_p| \gg 1$ or $|\mu_p| \gg 1$.



■ $\text{Re}(\epsilon \times \mu)_{\text{eff}}$
 △ $\text{Re}(\epsilon_{\text{eff}} \times \mu_{\text{eff}})$

(a)



■ $\text{Im}(\epsilon \times \mu)_{\text{eff}}$
 △ $\text{Im}(\epsilon_{\text{eff}} \times \mu_{\text{eff}})$

(b)

FIGURE 7: Real (a) and imaginary (b) parts of the product of permittivity and permeability for a binary mixture simulated in two different ways. Filled cubes: $(\epsilon \cdot \mu)_{\text{eff}}$ resulting from one simulation run with $\epsilon_p = 10 - 4i$, $\epsilon_m = 1$, $\mu_p = 4 - 3i$, and $\mu_m = 1$. Open triangles: $\epsilon_{\text{eff}} \cdot \mu_{\text{eff}}$ calculated from two simulation runs, a dielectric one ($\epsilon_p = 10 - 4i$, $\epsilon_m = \mu_p = \mu_m = 1$ yielding ϵ_{eff}) and a magnetic one ($\mu_p = 4 - 3i$, $\mu_m = \epsilon_p = \epsilon_m = 1$ yielding μ_{eff}). Obviously, $(\epsilon \cdot \mu)_{\text{eff}} = \epsilon_{\text{eff}} \cdot \mu_{\text{eff}}$ holds.

- (ii) Due to the resonator geometry, the effective permittivity is evaluated for an electric field parallel to a symmetry axis of the cubic grid ($E \parallel y$, see Figure 4), while the circumferential magnetic field yields a different volume average. For this reason, different functions \mathcal{F} describe the magnetic and dielectric responses (see (1) and (2) as well as [11]).

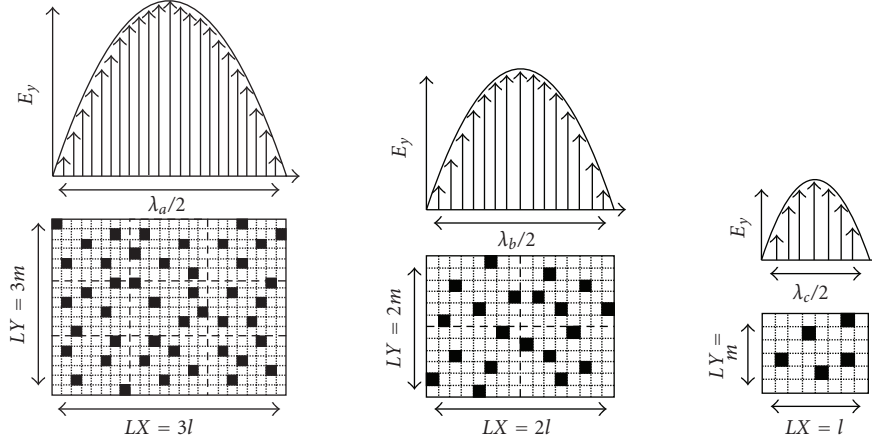


FIGURE 8: Testing for size effects by varying the resonators dimensions with respect to the particle size (aggregate topology).

In this work, we have used the original code of Stölzle and Leinders, that the authors kindly put at our disposal (we made only some minor technical modifications). Implemented on a modern personal computer (64-bit processor, 2.2 GHz, 4 GB RAM), it allows to simulate much bigger systems than those shown in the original work (having a size of $40a \times 30a \times 40a$ [9–11]). We are now able to simulate systems up to a size of $120a \times 90a \times 120a$ in a reasonable time [28], that is, on average it takes several hours to calculate an effective permittivity or permeability (the evaluation of permeability requires less CPU time). As a consequence, we can study more complex systems and we are no longer restricted to the pure aggregate topology, as we shall show in the following.

2.2. Numerical test for size effects

A freely propagating wave exhibits a constant frequency, but the wavelength depends on the dielectric and magnetic properties of the medium. In a resonator, the situation is different. The wavelength is fixed and the resonance frequency changes depending on the filler medium (7). Here we consider the fundamental mode of a rectangular waveguide resonator with $LX = LZ$, so that $\lambda/2 = LX$ holds (see Figure 4). As long as the structural inhomogeneities are small compared to the wavelength, the effective material parameters of a composite depend on the microstructure but not on the absolute size d of the inclusions (1)–(3). In addition, the discretization of the resonator, that is, the grid size a , has to be sufficiently fine in order to assure a precise calculation of field distribution and resonance frequency. Therefore,

$$2 \cdot LX = \lambda_{\text{res}} \gg d, a \quad (8)$$

has to hold in order to guarantee that the effective parameters are well defined and to exclude finite size effects of the simulation.

We check this for the aggregate topology and we start with a situation where particle dimension and grid size are identical quantities, $a = d$. For this purpose, we keep $d = a$

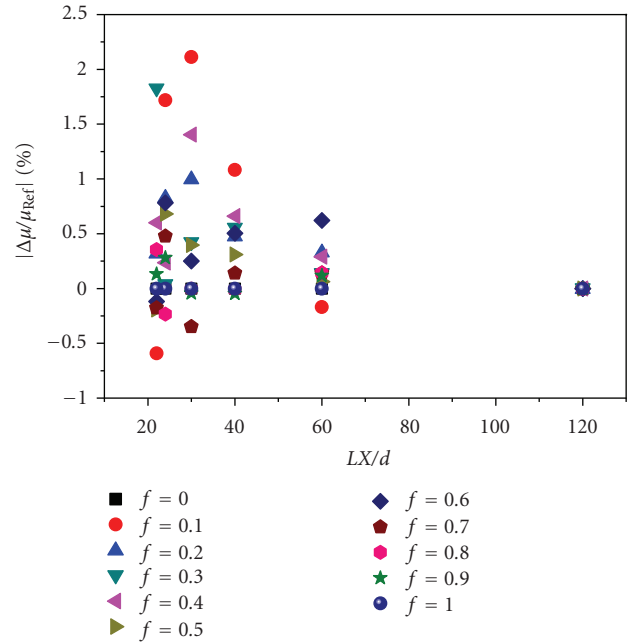


FIGURE 9: Variation of the absolute value of permeability as a function of system size or wavelength, $Lx/d = \lambda/(2d)$ for different filling factors $0 \leq f \leq 1$ (aggregate topology with $d = a$, see Figure 8). The respective effective permeability of the largest system, $LX * LY * LZ = 120a * 90a * 120a$, is taken as reference value (simulation parameters: $\mu_p = 20 - 12i$, $\mu_m = 1$, $\epsilon_p = \epsilon_m = 1$).

constant and change the size of the resonator and thus the wavelength as indicated in Figure 8. We start with a maximum resonator size of $LX * LY * LZ = 120a * 90a * 120a$ and simulate the effective permeability of a binary mixture ($\mu_p = 20 - 12i$, $\mu_m = 1$, $\epsilon_p = \epsilon_m = 1$). This value is taken as a reference value. Then we repeat the same procedure for a two-time smaller resonator ($60a * 45a * 60a$), a three-times smaller resonator, and so on. In Figure 9, we display the relative deviation of the effective permeability as a function of the

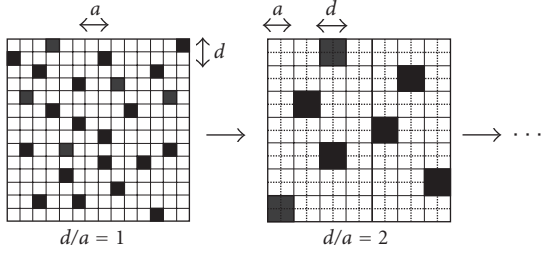


FIGURE 10: Testing for finite size effects by varying the ratio of particle size over grid size, d/a , while the size of the resonator is kept constant (aggregate topology). According to Figure 9 and (9) the finest discretization that can be realized corresponds to $d = 6 \cdot a$.

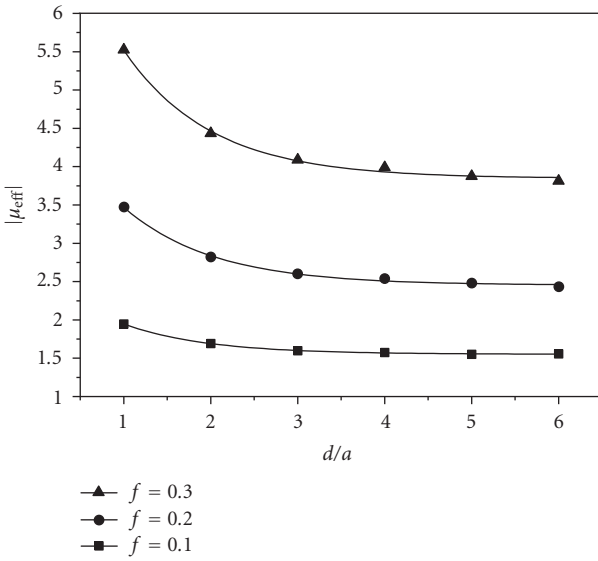


FIGURE 11: Variation of the absolute value of permeability as a function of the ratio of particle size to grid size for an aggregate topology (see Figure 10). The system size is approximately constant, $LX \cdot LY \cdot LZ \approx 120a \cdot 90a \cdot 120a$. $d/a = 1$ corresponds to a coarse and $d/a = 6$ to a fine discretization of the particles (simulation parameters: $\mu_p = 20 - 12i$, $\mu_m = 1$, $\epsilon_p = \epsilon_m = 1$). The lines are a guide to the eyes (fit functions of the form $|\mu_{\text{eff}}| = \alpha + \beta \cdot \exp(-\gamma \cdot d/a)$). For $d/a \geq 4$, the discretization is sufficiently fine so that the calculated effective permeability reaches a saturation value.

relative resonator dimension Lx/d for filling factors between 0 and 1. The largest deviations (up to 2%) occur for small systems or big particles. Therefore, the permeability does not depend on the particle size (or at least only in a marginal way) as long as

$$\frac{LX}{d} = \frac{\lambda_{\text{res}}}{2d} \geq 20 \quad (9)$$

holds.

In the next step, we have to adjust the grid size a with respect to the particle size d in order to make sure that the electromagnetic fields inside the particles are calculated with

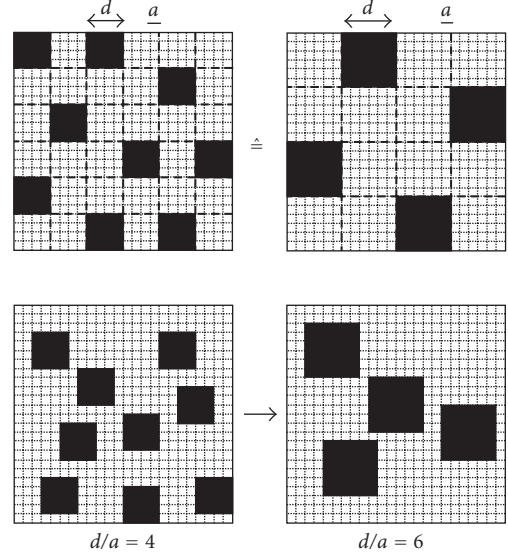


FIGURE 12: In order to monitor a topological transition from aggregate to cermet topology, random binary mixtures at constant volume filling factor but with different spatial particle arrangement are compared. Upper row: aggregate topology for increasing ratio of particle size d to grid size a . Lower row: intermediate topologies, where the same particles are arbitrarily dispersed on the grid. The limit $a/d \rightarrow 0$ corresponds to the cermet topology, where the particles can be located everywhere in 3D space.

a sufficiently high accuracy. For this purpose, we now keep the resonator approximately constant ($LX \cdot LY \cdot LZ \approx 120a \cdot 90a \cdot 120a$) and vary the ratio d/a as indicated in Figure 10. While the electromagnetic fields are calculated on a fine grid of size a (about $1.3 \cdot 10^6$ cubic cells of size a^3), the particles are randomly distributed on a coarse grid of size $d = n \cdot a$, so that we always maintain the aggregate topology. We do this from $d/a = 1$ up to the finest discretization $d/a = 6$. This upper limit corresponds to the largest particle size that still fulfills (9). The high number of cells of size d^3 filled with material m or p guarantees a good statistics for the simulation of a random mixture. For example, at $d/a = 4$, we have more than 20000 material cubes, at $d/a = 6$ still more than 8200. The results of the respective simulations are displayed in Figure 11. For low ratios of d/a , there is a systematic decrease of the effective permeability. For

$$d \geq 4a, \quad (10)$$

the discretization is sufficiently fine and the calculated permeability values approach a saturation value (from $d/a = 5$ to $d/a = 6$ they change by less than 2% for $f = 0.2$ and $f = 0.3$, while there is no change for $f = 0.1$). Summarizing, we are able to simulate particles with side lengths from $d = 4a$ up to $d = 6a$ without the appearance of any finite size effect and with a precision of the order of 2% (including systematic errors and repeatability of different random distributions).

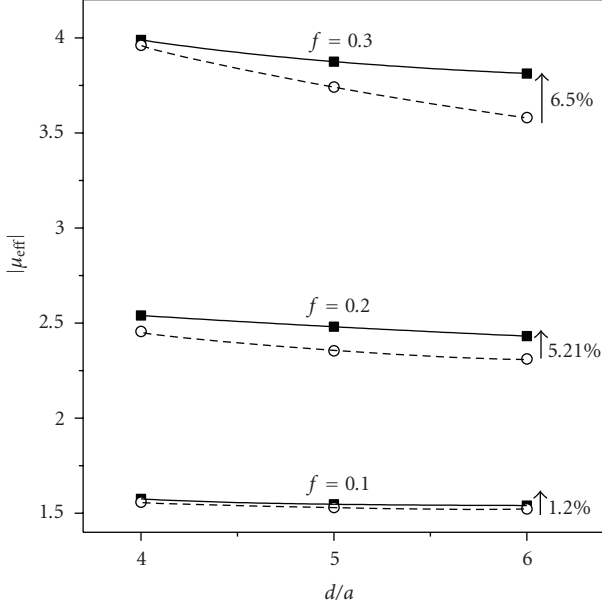


FIGURE 13: Absolute value of effective permeability vs ratio d/a for different volume filling factors. Filled cubes: aggregate topology. Open circles: intermediate topologies as sketched in Figure 12. Simulation parameters: $\mu_p = 20 - i \cdot 12$, $\mu_m = \varepsilon_p = \varepsilon_m = 1$. The lines are a guide to the eyes. The arrows indicate the relative differences at $d/a = 6$.

3. SIMULATING A TRANSITION FROM AGGREGATE TO CERMET TOPOLOGY

Until now we have only studied the aggregate topology, simulating random binary mixtures as shown in the upper row of Figure 12. We can realize this type of microstructure for different ratios of particle size d to grid size a whereas the effective properties remain unchanged. This was simply achieved by assigning only particle positions on a coarse grid of size $d = n \cdot a$. Now we can lift this restriction so that we obtain new spatial arrangements as sketched in the lower row of Figure 12. Cubic particles of side length $d = n \cdot a$ are randomly distributed in a grid of size a . With increasing ratio of d/a , the distance between two particles can become arbitrary small in comparison with their size. The limit $a/d \rightarrow 0$ corresponds to the cermet topology sketched in Figure 3(b). Compared to the particle size d , the grid is so fine that the matrix can be considered as a continuous phase hosting the dispersed discrete particles.

The topological transition can thus be monitored as follows. We keep the volume filling factor f constant and for each ratio d/a , we compare the effective material parameters of the aggregate and of the respective intermediate topology (upper and lower rows in Figure 12). We do this for $d/a \geq 4$, where finite size effects are sufficiently small. With increasing ratio d/a , the aggregate topology remains unchanged while the intermediate topologies approach the cermet topology.

We start with a binary mixture containing magnetic particles with losses. As before we set $\mu_p = 20 - i \cdot 12$ and $\mu_m = \varepsilon_p = \varepsilon_m = 1$. Figure 13 displays the absolute value

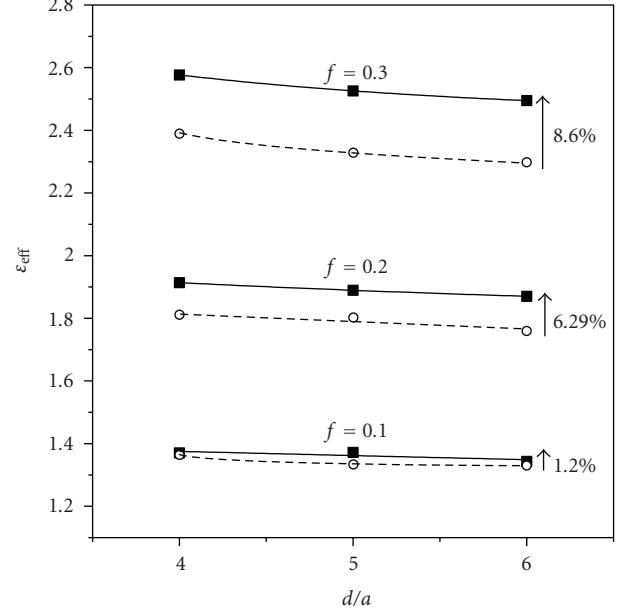


FIGURE 14: Effective permittivity versus ratio d/a for different volume filling factors. Filled cubes: aggregate topology. Open circles: intermediate topologies as sketched in Figure 12. Simulation parameters: $\varepsilon_p = 10$, $\varepsilon_m = \mu_p = \mu_m = 1$. The lines are a guide to the eyes. The arrows indicate the relative differences at $d/a = 6$.

of the effective permeability as a function of d/a for particle concentrations from 10% to 30%, that is, below the percolation threshold. The aggregate topology shows the plateau values already presented in Figure 11. The behaviour of the intermediate topologies depends on the particle concentration: at low filling factor of $f = 10\%$, the results equal those for the aggregate topology (within the accuracy of the simulation). At higher concentrations systematic deviations are observed. The effective permeability values are lower by about 5% at $f = 20\%$ and by 6.5% at $f = 30\%$. Since there is only a weak dependency on d/a at $f = 10\%$ and $f = 20\%$, the simulated values can be taken as a good approximation of the cermet topology. At $f = 30\%$, however, $|\mu_{\text{eff}}|$ does not attain a plateau value, so that we can expect even smaller values for the limiting case of the cermet topology.

Next let us check how loss-free particles behave. This time we choose a purely dielectric system with $\varepsilon_p = 10$ and set $\varepsilon_m = \mu_p = \mu_m = 1$. The effective permittivity is displayed in Figure 14. Once again, the aggregate topology exhibits higher effective material parameters, while the deviation increases with increasing particle concentration: there is no difference at the lowest concentration, but for $f = 20\%$ and $f = 30\%$ the deviations are of the same order of magnitude as in the previous case (compare Figures 13 and 14).

4. CONCLUSION

We have performed 3D simulations of loss-free and lossy random binary mixtures on a cubic grid in order to study the transition from aggregate to cermet topology (see Figure 12).

At a low filling factor of $f = 10\%$, where most particles are surrounded by matrix material, no differences in the effective material parameters are observed. At higher concentrations of $f = 20\%$ and $f = 30\%$, both permeability and permittivity vary in a systematic way during the transition. This is an effect of the changing spatial distribution of the particles. Aggregate topology, where the particle positions are random but more restricted, is characterized by the highest effective material parameters. Cermet topology, where arbitrary interparticle distances are possible, exhibits the smallest effective permittivity and permeability values. In this concentration range below the percolation threshold, the concept of topological classes might be of use. Additional simulations are needed in order to quantify the observed effects and to find out whether they persist at smaller dielectric or magnetic contrasts.

ACKNOWLEDGMENT

The authors are grateful to the authors of [9–11] who kindly put their original numerical code at our disposal.

REFERENCES

- [1] R. Ramprasad, P. Zurcher, M. Petras, M. Miller, and P. Renaud, "Magnetic properties of metallic ferromagnetic nanoparticle composites," *Journal of Applied Physics*, vol. 96, no. 1, pp. 519–529, 2004.
- [2] M. Dikeakos, L. D. Tung, T. Veres, A. Stancu, L. Spinu, and F. Normandin, "Fabrication and characterization of tunable magnetic nanocomposite materials," *Materials Research Society Symposium Proceedings*, vol. 734, pp. 315–320, 2003.
- [3] V. B.regar, "Advantages of ferromagnetic nanoparticle composites in microwave absorbers," *IEEE Transactions on Magnetics*, vol. 40, no. 3, pp. 1679–1684, 2004.
- [4] K. Günther and D. Heinrich, "Dielektrizitätskonstante, Permeabilität, elektrische Leitfähigkeit, Wärmeleitfähigkeit und Diffusionskonstante von Gemischen mit kugelförmigen Teilchen (gitterförmige und statistische Anordnung)," *Zeitschrift für Physik*, vol. 185, no. 4, pp. 345–374, 1965.
- [5] D. R. McKenzie, R. C. McPhedran, and G. H. Derrick, "The conductivity of lattices of spheres. II. The body centred and face centred cubic lattices," *Proceedings of the Royal Society of London A*, vol. 362, no. 1709, pp. 211–232, 1978.
- [6] L. Fu, P. B. Macedo, and L. Resca, "Analytic approach to the interfacial polarization of heterogeneous systems," *Physical Review B*, vol. 47, no. 20, pp. 13818–13829, 1993.
- [7] N. Harfield, "Conductivity of a periodic particle composite with spheroidal inclusions," *The European Physical Journal—Applied Physics*, vol. 6, no. 1, pp. 13–21, 1999.
- [8] N. Harfield, "Bulk permittivity of a composite with coated spheroidal filler particles," *Journal of Materials Science*, vol. 35, no. 23, pp. 5809–5816, 2000.
- [9] S. Stölzle, A. Enders, and G. Nimtz, "Numerical simulation of random composite dielectrics," *Journal de Physique I*, vol. 2, no. 4, pp. 401–408, 1992.
- [10] S. Stölzle, A. Enders, and G. Nimtz, "Numerical simulation of random composite dielectrics. II. Simulations including dissipation," *Journal de Physique I*, vol. 2, no. 9, pp. 1765–1777, 1992.
- [11] H. Leinders and A. Enders, "Computer simulations of dielectric and magnetic composite media including dissipation," *Journal de Physique I*, vol. 5, no. 5, pp. 555–564, 1995.
- [12] E. Tuncer and E. Tuncer, "On complex permittivity of dilute random binary dielectric mixtures in two-dimensions," *Turkish Journal of Physics*, vol. 23, pp. 101–105, 2003.
- [13] E. Tuncer, B. Nettelblad, and S. M. Gubański, "Non-debye dielectric relaxation in binary dielectric mixtures (50–50): randomness and regularity in mixture topology," *Journal of Applied Physics*, vol. 92, no. 8, pp. 4612–4624, 2002.
- [14] C. Brosseau and A. Beroual, "Computational electromagnetics and the rational design of new dielectric heterostructures," *Progress in Materials Science*, vol. 48, no. 5, pp. 373–456, 2003.
- [15] C. Brosseau and A. Beroual, "Dielectric properties of periodic heterostructures: a computational electrostatics approach," *The European Physical Journal—Applied Physics*, vol. 6, no. 1, pp. 23–31, 1999.
- [16] V. Myroshnychenko and C. Brosseau, "Finite-element method for calculation of the effective permittivity of random inhomogeneous media," *Physical Review E*, vol. 71, no. 1, Article ID 016701, 16 pages, 2005.
- [17] F. Wu and K. W. Whites, "Quasi-static effective permittivity of periodic composites containing complex shaped dielectric particles," *IEEE Transactions on Antennas and Propagation*, vol. 49, no. 8, pp. 1174–1182, 2001.
- [18] J. Monecke, "Microstructure dependence of material properties of composites," *Physica Status Solidi (B)*, vol. 154, no. 2, pp. 805–813, 1989.
- [19] G. Bánhegyi, "Comparison of electrical mixture rules for composites," *Colloid & Polymer Science*, vol. 264, no. 12, pp. 1030–1050, 1986.
- [20] V. M. Shalaev, "Electromagnetic properties of small-particle composites," *Physics Reports*, vol. 272, no. 2-3, pp. 61–137, 1996.
- [21] A. Spanoudaki and R. Pelster, "Effective dielectric properties of composite materials: the dependence on the particle size distribution," *Physical Review B*, vol. 64, no. 6, Article ID 064205, 6 pages, 2001.
- [22] R. Pelster, "Dielectric spectroscopy of confinement effects in polar materials," *Physical Review B*, vol. 59, no. 14, pp. 9214–9228, 1999.
- [23] R. Pelster and U. Simon, "Nanodispersions of conducting particles: preparation, microstructure and dielectric properties," *Colloid and Polymer Science*, vol. 277, no. 1, pp. 2–14, 1999.
- [24] S. O. Nelson, "Density-permittivity relationships for powdered and granular materials," *IEEE Transactions on Instrumentation and Measurement*, vol. 54, no. 5, pp. 2033–2040, 2005.
- [25] L. K. H. van Beek, "Dielectric behavior of heterogeneous systems," in *Progress in Dielectrics*, J. B. Birks, Ed., vol. 7, pp. 69–114, Heywood Books, London, UK, 1967.
- [26] S. S. Dukhin, "Dielectric properties of disperse systems," in *Surface Colloid Science*, E. Matijevic, Ed., vol. 3, pp. 83–165, Wiley-Interscience, New York, NY, USA, 1971.
- [27] J. D. Jackson, *Classical Electrodynamics*, John Wiley & Sons, New York, NY, USA, 1975.
- [28] B. Hallouet, "Simulationen und experimentelle Untersuchungen der dielektrischen und magnetischen Eigenschaften von Nanokompositen," Diploma Thesis, Universität des Saarlandes, Saarbrücken, Germany, 2006.

Research Article

Plasmonic Nanolayer Composites: Coupled Plasmon Polaritons, Effective-Medium Response, and Subdiffraction Light Manipulation

Justin Elser,¹ Alexander A. Govyadinov,¹ Ivan Avrutsky,² Ildar Salakhutdinov,² and Viktor A. Podolskiy¹

¹Department of Physics, Oregon State University, 301 Weniger Hall, Corvallis, OR 97331-6507, USA

²Department of Electrical and Computer Engineering, Wayne State University, Detroit, MI 48202, USA

Received 14 February 2007; Accepted 4 June 2007

Recommended by Christian Brosseau

We analyze the evolution of the modes in nanoplasmonic multilayered structures and study the transition of the optical properties of these systems to the effective-medium regime. We derive the effective-medium parameters and study the validity of our analytical results with exact numerical solutions of Maxwell equations. Finally, we explore the applications of multilayered systems for subwavelength light confinement in planar and circular waveguides.

Copyright © 2007 Justin Elser et al. This is an open access article distributed under the Creative Commons Attribution License, which permits unrestricted use, distribution, and reproduction in any medium, provided the original work is properly cited.

1. INTRODUCTION

A number of exciting applications in single-molecule imaging, spectroscopy, high-resolution lithography, and all-optical computing may benefit from light confinement and manipulation in nm-scale areas. Unfortunately, the diffraction limit prevents confinement of free-space optical radiation to dimensions smaller than $\sim \lambda_{\text{in}}/2$, with $\lambda_{\text{in}} = \lambda_0/|n| = c/(\omega|n|)$ being the wavelength inside the material, c , λ_0 , ω being speed of light, wavelength, and angular frequency of radiation in vacuum, respectively, and n being the index of refraction. Conventional resolution-improvement techniques involve either increase of operating frequency (deep UV lithography) [1, 2] or near-field operations (scanning near-field optical microscopy) [3, 4]. Another approach to increase the resolution is based on operations with high-index media. While a significant improvement of resolution can be achieved with natural materials (Si photonics) [5, 6], a further progress of subdiffraction light manipulation requires the design of *metamaterials* [7–21] with even higher refractive indices. In this work, we present an analytical and numerical analysis of perspectives of ultra-high index metamaterials based on plasmonic nanolayer structures for light manipulation in the areas smaller than $\lambda_0/10$ at UV, visible, IR, and THz frequencies.

The dielectric properties of plasmonic media are strongly affected by the dynamics of their free charges. In particular,

the permittivities of noble metals and highly doped semiconductors are negative for frequencies below their plasma frequencies (plasma frequencies of noble metals are of the order of 10 eV, yielding negative permittivities across parts of the UV, visible, and IR ranges [22, 23]). An interface between materials with negative and positive dielectric permittivities may support a special kind of electromagnetic wave, known as a surface plasmon polariton (SPP) [24]. The effective index of this wave can be related to the component of its propagating constant along the propagation direction k_z (Figure 1) and permittivities of plasmonic (metallic) and dielectric materials ϵ_m and $\epsilon_d < |\epsilon_m|$ via

$$n_{\text{SPP}} = \text{Re}\left(\frac{k_z c}{\omega}\right) = \text{Re}\left(\sqrt{\frac{\epsilon_m \epsilon_d}{\epsilon_m + \epsilon_d}}\right). \quad (1)$$

Note that since $n_{\text{SPP}}^2 > \epsilon_d, \epsilon_m$, the field of an SPP exponentially decays into both the metal and dielectric media. However, since in reality for optical frequencies $|\epsilon_m| \gg \epsilon_d$, the index of SPP wave only slightly exceeds that of the dielectric $n_d = \sqrt{\epsilon_d}$: $(n_{\text{SPP}} - n_d)/n_d \approx \epsilon_d^2/\epsilon_m^2 \ll 1$, strongly diminishing the perspectives of subdiffraction light confinement with an isolated SPP wave.

The light confinement with plasmonic layers can be significantly improved in multilayer structures. When two metal-dielectric interfaces are brought close to each other, the SPP waves propagating on individual interfaces couple

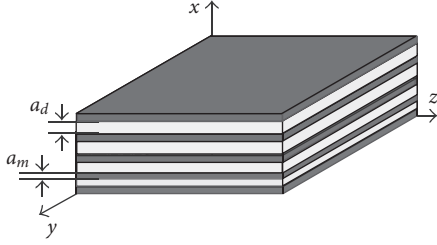


FIGURE 1: Schematic of a multilayered composite. a_m and a_d are the thicknesses of plasmonic (metallic) and dielectric composites, respectively.

together. Similar to quantum-mechanical coupling between modes of two quantum wells, which leads to the formation of symmetric and antisymmetric wavefunctions, the coupling of two SPPs yields the formation of symmetric and antisymmetric SPP combinations. This SPP coupling is accompanied by splitting between their propagation constants, increasing the effective index of one of the modes relative to that of an isolated SPP. In multilayered composites, the modes on each metal-dielectric interface couple to each other, leading to formation of *free-space-like* supermodes [25]. In the end, the multilayer metal-dielectric structure behaves like a strongly-anisotropic homogeneous metamaterial, with applications ranging from nonmagnetic negative index structures to optical links between nano- and micro-scaled systems [9, 12, 26]. The goals of this work are to provide a comprehensive study of the evolution of electromagnetic properties of plasmonic multilayer composites from an isolated SPP to effective-medium regime, to assess the perspectives of utilizing multilayer systems for nanoplasmonic applications and to present a detailed analysis of the validity of nonlocal effective-medium theory, originally proposed in [27].

2. APPROACH

To gain access into the physics behind the optical properties of nanoplasmonic structures and to verify the accuracy of our analytical results, we have employed the numerical solutions of Maxwell equations via transfer matrix method (TMM) [28, 29].

In this technique, the material is represented as a set of *homogeneous* layers. The solutions of Maxwell equations in each layer yield the set of modes; these are plane waves—propagating or evanescent—in the case of infinite layers, cylindrical waves in case of layers inside circular waveguides (optical fibers), and so forth. Boundary conditions are then used to relate the vector of amplitudes of modes in a given (j th) layer b_j to the modes in the neighboring layer. These *linear* relationships are then expressed in terms of the *transfer matrix*

$$b_{j+1} = \hat{T}_{j+1,j} b_j. \quad (2)$$

Thus, *differential* Maxwell equations are essentially reduced to *linear* equations for transfer matrices. Note that layer-specific transfer matrices can be multiplied together yielding

the single matrix which describes the *collective behavior* of the multilayer composite.

The TMM technique is in principle exact and provides a complete solution of Maxwell equations. In particular, TMM solutions can be used to find the field propagation through an arbitrary layered material, to find the dispersion characteristics of supermodes of layered systems, and to find the “microscopic” field distribution in these supermodes. The solutions of latter problems typically involve finding eigenvalues and eigenvectors for collective (composite-level) transfer matrices. However, these exact numerical solutions are extremely computationally intensive and require an increase in precision past standard machine precision for even relatively small number of layers.

3. RESULTS AND DISCUSSION

In this main section of the manuscript, we first describe the evolution of the coupled SPP modes as we increase the number of layers in the multilayer structures. We show that depending on the relationship between ϵ_m and ϵ_d , the supermodes may have positive or negative refractive indices. As the number of layers in the composite is increased, the structure of the supermodes resembles that of plane waves propagating through the homogeneous strongly anisotropic composite. We derive the analytical relationship describing the effective permittivity tensor of such a media and provide several applications of multilayer structures for nm-scale light management.

3.1. Evolution of SPP modes in multilayer structures

We start from the analysis of mode evolution as the function of the number of layers in the system. For illustrative purposes, in the remaining of the paper, we focus on the optical response of metal-dielectric composites; we note, however, that our arguments are directly applicable to the IR (or THz) response of doped semiconductors exhibiting plasma behavior, as well as to other materials with negative permittivities, including SiC and other polar dielectrics. The potential applications at THz frequencies include biology and medical sciences, homeland security, global environmental monitoring, and ultrafast computing [30].

A single metal-dielectric interface supports an SPP. When two metal layers are brought together, the SPP modes propagating on their interfaces interact with each other, leading to the formation of symmetric and antisymmetric SPP combinations as shown in Figure 2. The interaction of isolated SPP modes also leads to the splitting between effective indices of their symmetric and antisymmetric combinations. As the separation between metal films is reduced, the splitting between modal indices grows. Eventually, the antisymmetric mode experiences a cutoff, and only symmetric mode (known as *gap plasmon* [31]) survives.

The four-interfaced “sandwich” system formed by a thin metal film inserted into dielectric space between two metal cladding regions in principle supports four SPP combinations. However, if such a film is brought close enough to one

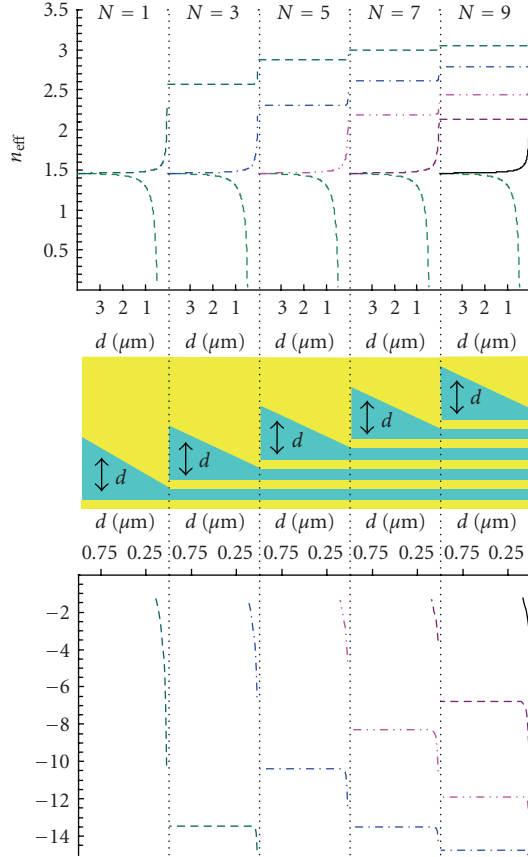


FIGURE 2: The evolution and splittings of coupled SPP modes propagating along z -direction (see Figure 1); $n = k_z c / \omega$ at $\lambda_0 = \omega / c = 1.55 \mu\text{m}$ is shown. The top part of the figure corresponds to “positive-index” structure: $\epsilon_d = 1.444^2$; $\epsilon_m = -114.5 + 11.01i$; the bottom part describes a “negative-index” one: $\epsilon_d = 1.444^2$; $\epsilon_m = -1 + 0.1i$; the inset schematically shows the xz -crosssection of the system; final layer thickness is 25 nm.

of the cladding regions, the total number of modes is reduced to three; further confinement of the structure reduces the total number of modes to two—the symmetric and antisymmetric combinations of gap plasmons. Note that the indices of these modes continue to repulse from each other, yielding a formation of the modes with effective indices exceeding the one of the isolated gap plasmon. Each additional metal strip inserted into this sandwich system will effectively lead to the formation of an additional supermode. Thus, a total number of modes hosted by the metal-dielectric multilayer system surrounded by two metallic cladding regions will be equal to the number of dielectric layers in the system (Figure 2).

A similar process of mode formation takes place in the layered metamaterial when the excitation frequency is close to the plasma frequency of its plasmonic component ($|\epsilon_m| < \epsilon_d$). While an isolated metal interface does not support an SPP in this case, two-interface system supports a single *antisymmetric* mode with *negative refraction index* [12, 32]. In a sense, the behavior of the metal-dielectric-metal system for $|\epsilon_m| < \epsilon_d$ is exactly opposite to that of $|\epsilon_m| > \epsilon_d$. The signs

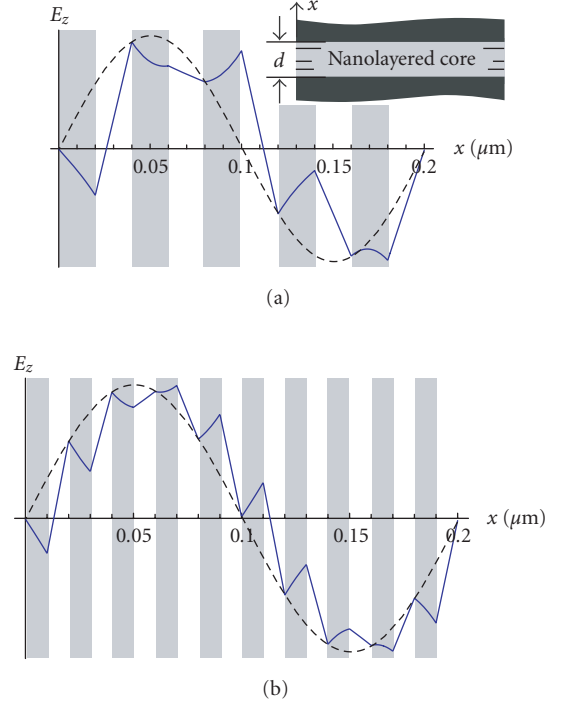


FIGURE 3: Field structure of a TM_1 mode of planar waveguide formed by metal-dielectric stack between two perfectly conducting metal claddings for a number of layers $N = 10$ (a) and $N = 20$ (b); $\epsilon_m = -100$; $\epsilon_d = 2$; $\lambda_0 = 1.55$ [27].

of their refractive indices are opposite to each other; furthermore, the cutoff of the mode in one of the systems can be related to the appearance of the mode in the other one. The multilayered composite with $|\epsilon_m| < \epsilon_d$ with N dielectric layers supports a total of N negative-index supermodes. The evolution of these supermodes is illustrated in Figure 2.

As the number of layers increases, so does the number of supermodes. At any given frequency, the composite with a very large number of layers essentially supports a continuum of modes with different modal structure. Some of these modes in the composites with 10 and 20 layers between two perfectly metallic claddings are shown in Figure 3. Note that the structure of these modes strongly resembles that of standing waves. This is obviously not surprising; the properties of nanostructured composites are expected to follow effective-medium theory (EMT) predictions.

The exact process of convergence to the effective-medium regime is of a great interest. An analytical description of this process could be used to explain the experiments with a few metal layers [25, 32] or more importantly to predict the behavior of larger multilayer composites based on experiments with few layers. Figure 4 shows the dependence of the effective modal index in the nanolayered system (Figure 1) as the function of the number of metal layers. One can see that even when the number of layers is relatively large ($\gtrsim 10$) and even when the individual layer thickness is much smaller than the wavelength, the properties of multilayer stack still significantly deviate from the EMT. As explained in [27], the origin

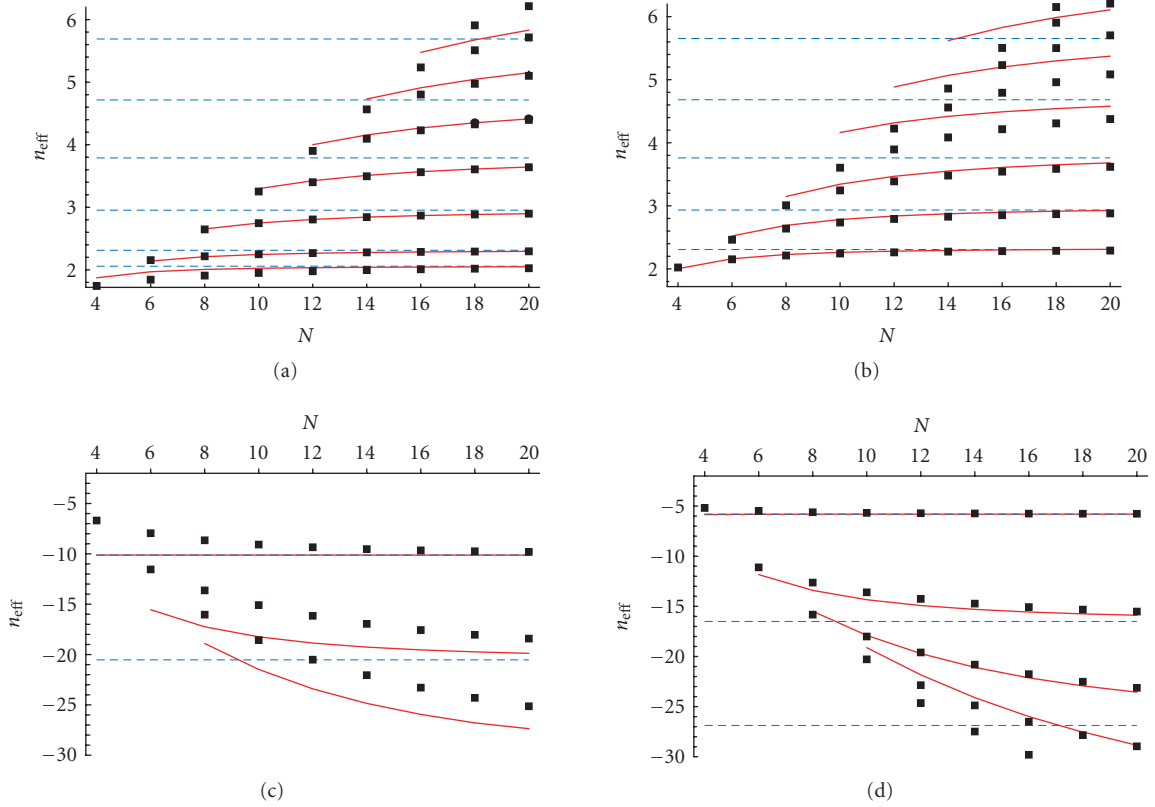


FIGURE 4: The comparison between effective modal indices of TM modes of 200-nm-thick planar waveguides with perfectly conducting (a), (c) and vacuum (b), (d) claddings plotted as a function of a number of layers in the metamaterial waveguide core N ; material parameters are $\epsilon_m = -114.5 + 11.01i$; $\epsilon_d = 1.444^2$ (Au-SiO₂ composite) (a), (b) and $\epsilon_m = -1 + 0.1i$; $\epsilon_d = 1.444^2$ (c), (d); $\lambda_0 = 1.55 \mu\text{m}$; solid lines, dashed lines, and symbols correspond to local EMT, nonlocal EMT, and TMM results, respectively; due to extremely large effective indices, $|n|$ nonlocal EMT is not applicable for higher-order modes in (c), (d).

of this relatively slow convergence lies in the strong field variation across individual layers of the system. Such a field variation leads to the strong dependence of the effective permittivity on the *modal structure* across the layers or—since the waveguide modes are typically “standing” equivalents of “propagating” bulk waves—on the direction of field propagation through the nanolayered metamaterials. The dependence of permittivity on components of wavevector, known as spatial dispersion, often appears in homogeneous media when the scale of field variation becomes comparable to interatomic distances. The onset of spatial dispersion in metamaterials can be typically related to substantial field variation on the interparticle (“meta-atom”) scale. The spatial dispersion has been recently found in GHz nanowire composites [20, 33, 34]; it was later shown that response of optical nanowire structures is substantially different from their low-frequency counterparts [11]. Using a straightforward field-matching technique [27], we arrive at the following expression for effective permittivity of nanolayered composites:

$$\begin{aligned} \epsilon_x^{\text{eff}} &= \frac{\epsilon_x^{(0)}}{1 - \delta_x(k, \omega)}, \\ \epsilon_{yz}^{\text{eff}} &= \frac{\epsilon_{yz}^{(0)}}{1 - \delta_{yz}(k, \omega)}, \end{aligned} \quad (3)$$

where

$$\begin{aligned} \epsilon_x^{(0)} &= \frac{(a_m + a_d)\epsilon_m\epsilon_d}{a_d\epsilon_m + a_m\epsilon_d}, \\ \epsilon_{yz}^{(0)} &= \frac{a_m\epsilon_m + a_d\epsilon_d}{a_m + a_d}, \end{aligned} \quad (4)$$

and the nonlocal corrections are given by

$$\begin{aligned} \delta_x &= \frac{a_m^2 a_d^2 (\epsilon_d - \epsilon_m)^2 \epsilon_x^{(0)2}}{12(a_m + a_d)^2 \epsilon_m^2 \epsilon_d^2} \left(\epsilon_{yz}^{(0)} \frac{\omega^2}{c^2} - \frac{k_x^2 (\epsilon_m + \epsilon_d)^2}{\epsilon_{yz}^{(0)2}} \right), \\ \delta_{yz} &= \frac{a_m^2 a_d^2 (\epsilon_d - \epsilon_m)^2 \omega^2}{12(a_m + a_d)^2 \epsilon_{yz}^{(0)} c^2}. \end{aligned} \quad (5)$$

Note that the choice of ω/c and k_x to describe the nonlocality in (5) as opposed to k_y or k_z is somewhat arbitrary since in the EMT regime, the components of the wavevector are related to each other via

$$\begin{aligned} \frac{\omega^2}{c^2} &= \frac{k_x^2}{\epsilon_{yz}^{\text{eff}}} + \frac{k_y^2 + k_z^2}{\epsilon_x^{\text{eff}}} \quad (\text{TM}), \\ \frac{\omega^2}{c^2} &= \frac{k_x^2 + k_y^2 + k_z^2}{\epsilon_{yz}^{\text{eff}}} \quad (\text{TE}). \end{aligned} \quad (6)$$

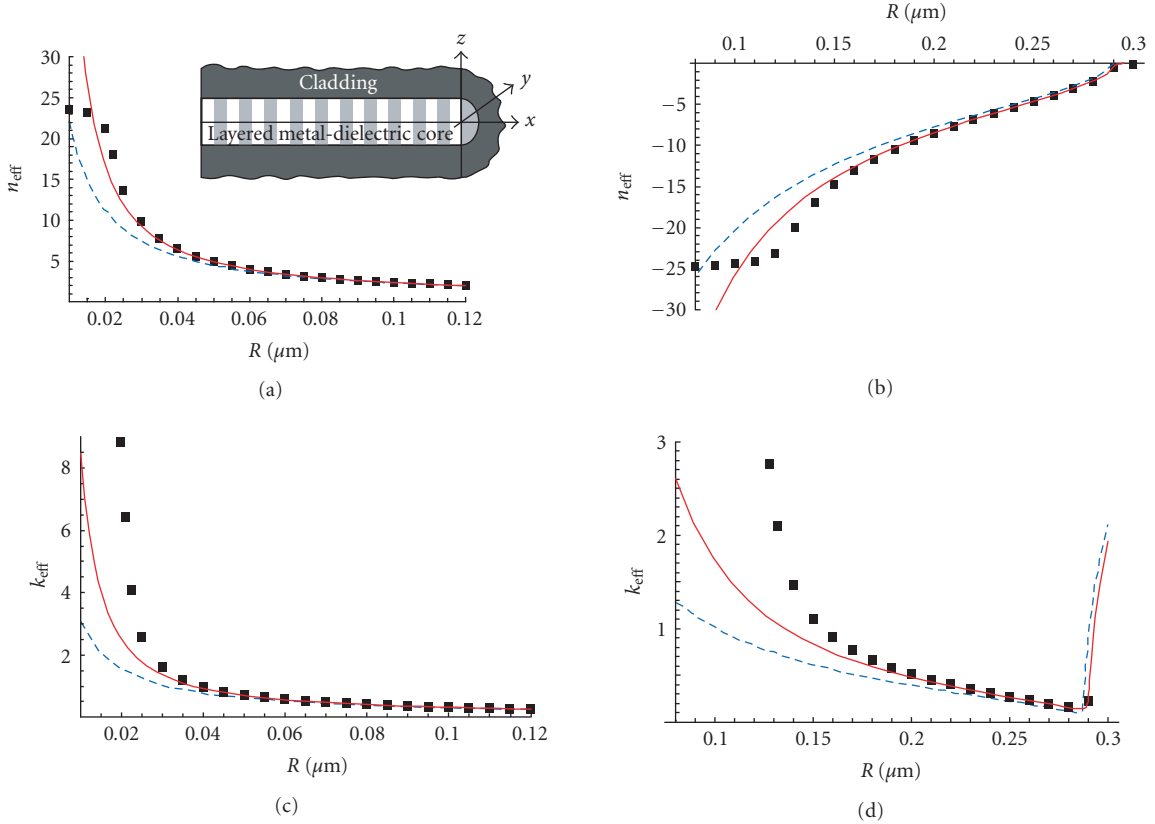


FIGURE 5: The comparison between effective refractive indices $n_{\text{eff}} = \text{Re}(k_x c/\omega)$ (a), (b) and extinction coefficients $k_{\text{eff}} = \text{Im}(k_x c/\omega)$ (c), (d) of TM_{01} modes in cylindrical waveguides with multilayer cores and perfectly conducting claddings (inset); dashed lines, solid lines and dots correspond to results of local EMT, nonlocal EMT, and exact solution of the dispersion equation [28] respectively. The multilayered core is composed of 15-nm layers with (a), (c) $\epsilon_m = -1 + 0.1i$; $\epsilon_d = 1.444^2$, and (b), (d) $\epsilon_m = -114.5 + 11.01i$; $\epsilon_d = 1.444^2$ (Au-SiO₂ structure); $\lambda_0 = 1.55 \mu\text{m}$; similar agreement between nonlocal EMT and exact dispersion equation is achieved for cylindrical systems with air claddings; note that the signs of refractive indices are opposite to those for planar mode propagation (see Figure 4).

In this section, we assume the propagation along the z -axis ($k_y = 0$) with waveguide modes in x -direction; for perfectly conducting waveguide walls, $k_x = \pi m/d$ with d being waveguide thickness and m being integer mode number. For waveguide with realistic walls, k_x could be found using “local” EMT approximation (4) or in self-consistent manner using (4), ..., (6).

We stress that the validity of EMT response requires the typical scale of field variation to be much larger than any structural size of the system. For nanolayered composite, such a requirement results in an additional condition $|k_x(a_m + a_d)| \ll 1$, which in some cases is much stricter than a commonly used criterion $(a_m + a_d)\omega/c \ll 1$. Note that the nonlocal effects mostly (see discussion below (5)) affect the x -component of material permittivity. Since our metamaterial is completely homogeneous in yz -plane, such a result is a quite expected one.

The agreement between the developed nonlocal EMT and exact solutions of Maxwell equations using TMM are shown in Figure 4. For illustrative purposes, we concentrate on TM modes; TE waves are not affected by the anisotropy, and are typically not affected by nonlocal effects. It is clearly

seen that nonlocal EMT adequately describes the behavior of the system. As expected, the agreement between EMT and exact (TMM) solutions of Maxwell equations worsens for higher-order modes where $|k_x(a + b)| \gtrsim 1$. Since the components of wavevector are related through (6), this validity condition is typically similar to $n_{\text{eff}} \gg 1$. Increasing the total thickness of the structure (decreasing k_x) or reducing the typical layer size or the number of layers restores the agreement.

The behavior of multilayers with $|\epsilon_m| < \epsilon_d$, but same sign of $\epsilon_{yz}^{(0)}$ and $\epsilon_x^{(0)}$, is an interesting one. The EMT regime of these systems does not originate from coupling of individual left-handed SPPs. As follows from our numerical solutions of Maxwell equations, reduction of layer thickness in these structures is accompanied by the increase of modal indices of SPP supermodes, so that the condition of EMT validity is never met. However, substantially thick multilayered structures with positive $\epsilon_x^{(0)}$, $\epsilon_{yz}^{(0)}$ support right-handed “volume” modes, described by the EMT.

Note that as explained above, multilayered system supports a number of modes with $n_{\text{eff}} = \text{Re}(k_x c/\omega) \gg 1$, opening the perspectives for subwavelength light manipulation in

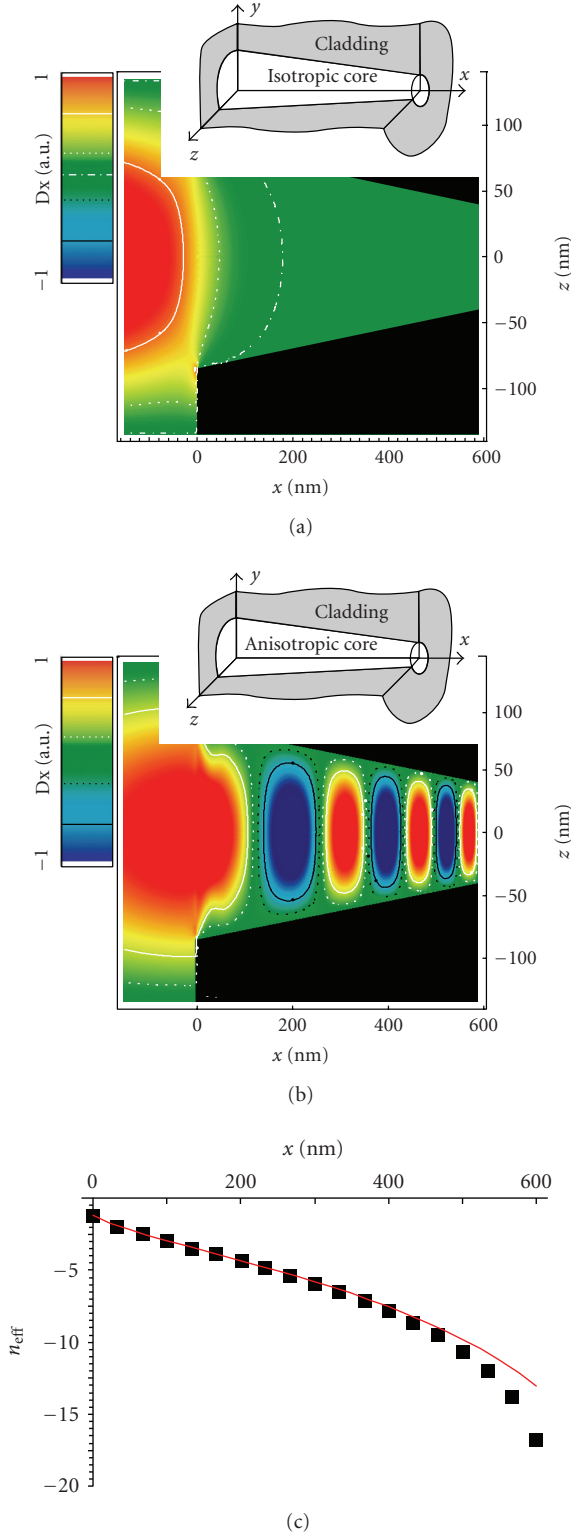


FIGURE 6: Mode propagation in conventional waveguide (a) and in anisotropy-based photonic funnel (b); material parameters $\epsilon_m = -73.02 + 1.64i$ (Ag), $\epsilon_d = 12$ (Si), $a_m = a_d = 15$ nm, and $\lambda_0 = 1.2 \mu\text{m}$, and the funnel design resembles those in [9]; panel (c), which shows the effective modal index along the funnel in (b), demonstrates the physics behind nanoscale mode compression; symbols and solid lines represent TMM results and nonlocal EMT, respectively.

planar structures with highly-confined optical modes with positive or negative refractive index [35]. The physics behind the existence of these highly confined modes can be illustrated using the following picture: the TM modes of a waveguide with strongly anisotropic dielectric core do not have a cutoff. As the waveguide size d is reduced, the effective modal index grows inversely proportional to d (see [9–11, 26] for details). Correspondingly, the internal wavelength is reduced ($\lambda_{\text{in}} \propto d$), postponing the onset of diffraction limit. Spatial dispersion, appearing in metamaterial response changes the effective-medium parameters, reducing the effective anisotropy, and eventually leading to a cutoff of waveguide modes.

3.2. Subdiffraction light propagation in nanolayer-filled waveguides

Although planar nanolayer systems are capable of guiding the light in deep subwavelength areas and may be used to realize optical packet management in 2D geometries, these materials cannot be directly coupled to optical fibers.

Ideally, two conditions must be met to achieve such a coupling between microscale optical fiber and nanoscale systems (planar waveguides, molecules, quantum dots, etc.). First, the coupler waveguide (fiber) should be able to support confined modes as waveguide radius is reduced to the nanoscale. Second, the spatial profile of a mode in the coupler waveguide should be similar to the one of the mode in optical fiber. Both these conditions are fulfilled in waveguides with strongly anisotropic cores when the axis of optical anisotropy is coaligned with direction of mode propagation.

One of the ways to achieve the required strong anisotropy of dielectric permittivity relies on multilayered nanoplasmonic structures. To coalign the optical axis with direction of mode propagation, we propose to build a waveguide with a multilayer dielectric core as shown in Figure 5 [9]. Similar to the planar structure described above, such a circular waveguide essentially does not have a cutoff radius in the “local EMT” regime, where effective modal index $n_{\text{eff}} = k_x c / \omega \propto 1/R$, postponing the appearance of diffraction limit (see [9] for details). The appearance of the cutoff can be once again related to the effective nonlocalities of metamaterial structures (Figures 5(c), 5(d)). Note however, that due to strong anisotropy of effective permittivity the positive-index modes propagating along yz -plane correspond to negative-index modes propagating along x -direction and vice versa [36].

The comparison between the effective modal index of a circular waveguide with multilayer core, calculated using exact approach [28], local, and nonlocal EMTs, is shown in Figure 5. The performance of such a system is illustrated in Figure 6, where the mode propagation in waveguide with nanolayered core is compared to the mode propagation in waveguide with conventional isotropic core. The appearance of the cutoff in isotropic system and the absence of the cutoff in tapered anisotropic waveguide (photonic funnel [9]) are clearly seen.

4. CONCLUSIONS

In conclusion, we analyzed the behavior of coupled SPP modes in multilayered metal-dielectric materials. Using exact numerical solutions of Maxwell equations, we have shown that as the number of layers increases, the optical properties of coupled SPP oscillations approach the behavior of strongly anisotropic homogeneous uniaxial media, and analyzed the validity of new analytical description of effective permittivity of such a material—nonlocal effective-medium theory. Finally, we illustrated the applications of multilayered structures for subdiffraction light propagation in planar and circular waveguides and for coupling between micro-scale and nanoscale systems. Our results, although presented here for optical response of metal-dielectric composites, are applicable to any layered structures composed from opposite-permittivity materials, including UV response of Al composites and IR and THz responses of doped semiconductors and polar dielectrics.

ACKNOWLEDGMENTS

This research was partially supported by PRF (ACS), ARO, and ONR.

REFERENCES

- [1] J. G. Goodberlet, "Patterning 100 nm features using deep-ultraviolet contact photolithography," *Applied Physics Letters*, vol. 76, no. 6, pp. 667–669, 2000.
- [2] H. Schmid, H. Biebuyck, B. Michel, and O. J. F. Martin, "Light-coupling masks for lensless, sub-wavelength optical lithography," *Applied Physics Letters*, vol. 72, no. 19, pp. 2379–2381, 1998.
- [3] A. Lewis, H. Taha, A. Strinkovski, et al., "Near-field optics: from subwavelength illumination to nanometric shadowing," *Nature Biotechnology*, vol. 21, no. 11, pp. 1378–1386, 2003.
- [4] E. Betzig, J. K. Trautman, T. D. Harris, J. S. Weiner, and R. L. Kostelak, "Breaking the diffraction barrier: optical microscopy on a nanometric scale," *Science*, vol. 251, no. 5000, pp. 1468–1470, 1991.
- [5] H. Rong, Y.-H. Kuo, S. Xu, et al., "Monolithic integrated Raman silicon laser," *Optics Express*, vol. 14, no. 15, pp. 6705–6712, 2006.
- [6] A. W. Fang, H. Park, O. Cohen, R. Jones, M. J. Paniccia, and J. E. Bowers, "Electrically pumped hybrid AlGaInAs-silicon evanescent laser," *Optics Express*, vol. 14, no. 20, pp. 9203–9210, 2006.
- [7] S. A. Maier, P. G. Kik, H. A. Atwater, et al., "Local detection of electromagnetic energy transport below the diffraction limit in metal nanoparticle plasmon waveguides," *Nature Materials*, vol. 2, no. 4, pp. 229–232, 2003.
- [8] A. Karalis, E. Lidorikis, M. Ibanescu, J. D. Joannopoulos, and M. Soljačić, "Surface-plasmon-assisted guiding of broadband slow and subwavelength light in air," *Physical Review Letters*, vol. 95, no. 6, Article ID 063901, 4 pages, 2005.
- [9] A. A. Govyadinov and V. A. Podolskiy, "Metamaterial photonic funnels for subdiffraction light compression and propagation," *Physical Review B*, vol. 73, no. 15, Article ID 155108, 5 pages, 2006.
- [10] A. A. Govyadinov and V. A. Podolskiy, "Gain-assisted slow to superluminal group velocity manipulation in nanowaveguides," *Physical Review Letters*, vol. 97, no. 22, Article ID 223902, 2006.
- [11] J. Elser, R. Wangberg, V. A. Podolskiy, and E. E. Narimanov, "Nanowire metamaterials with extreme optical anisotropy," *Applied Physics Letters*, vol. 89, no. 26, Article ID 261102, 3 pages, 2006.
- [12] A. Alù and N. Engheta, "Optical nanotransmission lines: synthesis of planar left-handed metamaterials in the infrared and visible regimes," *Journal of the Optical Society of America B*, vol. 23, no. 3, pp. 571–583, 2006.
- [13] J. B. Pendry, "Negative refraction makes a perfect lens," *Physical Review Letters*, vol. 85, no. 18, pp. 3966–3969, 2000.
- [14] N. Fang, H. Lee, C. Sun, and X. Zhang, "Sub-diffraction-limited optical imaging with a silver superlens," *Science*, vol. 308, no. 5721, pp. 534–537, 2005.
- [15] G. Shvets and Y. A. Urzhumov, "Engineering the electromagnetic properties of periodic nanostructures using electrostatic resonances," *Physical Review Letters*, vol. 93, no. 24, Article ID 243902, 4 pages, 2004.
- [16] D. O. S. Melville and R. J. Blaikie, "Super-resolution imaging through a planar silver layer," *Optics Express*, vol. 13, no. 6, pp. 2127–2134, 2005.
- [17] M. I. Stockman, "Nanofocusing of optical energy in tapered plasmonic waveguides," *Physical Review Letters*, vol. 93, no. 13, Article ID 137404, 4 pages, 2004.
- [18] J. B. Pendry, A. J. Holden, W. J. Stewart, and I. Youngs, "Extremely low frequency plasmons in metallic mesostructures," *Physical Review Letters*, vol. 76, no. 25, pp. 4773–4776, 1996.
- [19] A. K. Sarychev, R. C. McPhedran, and V. M. Shalev, "Electrodynamics of metal-dielectric composites and electromagnetic crystals," *Physical Review B*, vol. 62, no. 12, pp. 8531–8539, 2000.
- [20] P. A. Belov and C. R. Simovski, "Homogenization of electromagnetic crystals formed by uniaxial resonant scatterers," *Physical Review E*, vol. 72, no. 2, Article ID 026615, 15 pages, 2005.
- [21] M. A. Shapiro, G. Shvets, J. R. Sirigiri, and R. J. Temkin, "Spatial dispersion in metamaterials with negative dielectric permittivity and its effect on surface waves," *Optics Letters*, vol. 31, no. 13, pp. 2051–2053, 2006.
- [22] E. M. Lifshitz and L. P. Pitaevskii, *Physical Kinetics*, vol. 10 of *Course of Theoretical Physics*, Reed Educational and Professional Publishing, Oxford, UK, 1984.
- [23] With a few exceptions (Ag, Al), the response of metals in the UV and visible frequency ranges is also strongly affected by interband transitions.
- [24] L. D. Landau, E. M. Lifshitz, and L. P. Pitaevskii, *Electrodynamics of continuous media*, vol. 8 of *Course of Theoretical Physics*, Reed Educational and Professional Publishing, Oxford, UK, 2nd edition, 1984.
- [25] I. Avrutsky, I. Salakhutdinov, J. Elser, and V. A. Podolskiy, "Highly confined optical modes in nanoscale metal-dielectric multilayers," *Physical Review B*, vol. 75, no. 24, Article ID 241402, 4 pages, 2007.
- [26] V. A. Podolskiy and E. E. Narimanov, "Strongly anisotropic waveguide as a nonmagnetic left-handed system," *Physical Review B*, vol. 71, no. 20, Article ID 201101, 4 pages, 2005.
- [27] J. Elser, V. A. Podolskiy, I. Salakhutdinov, and I. Avrutsky, "Nonlocal effects in effective-medium response of nanolayered metamaterials," *Applied Physics Letters*, vol. 90, no. 19, Article ID 191109, 3 pages, 2007.
- [28] P. Yeh, A. Yariv, and C. Hong, "Electromagnetic propagation in periodic stratified media. I. General theory," *Journal of the Optical Society of America*, vol. 67, no. 4, pp. 423–438, 1977.

- [29] I. Avrutsky, "Guided modes in a uniaxial multilayer," *Journal of the Optical Society of America A*, vol. 20, no. 3, pp. 548–556, 2003.
- [30] M. Tonouchi, "Cutting-edge terahertz technology," *Nature Photonics*, vol. 1, no. 2, pp. 97–105, 2007.
- [31] D. F. P. Pile and D. K. Gramotnev, "Adiabatic and nonadiabatic nanofocusing of plasmons by tapered gap plasmon waveguides," *Applied Physics Letters*, vol. 89, no. 4, Article ID 041111, 1 page, 2006.
- [32] H. Shin and S. Fan, "All-angle negative refraction for surface plasmon waves using a metal-dielectric-metal structure," *Physical Review Letters*, vol. 96, Article ID 073907, 2006.
- [33] A. L. Pokrovsky and A. L. Efros, "Electrodynamics of metallic photonic crystals and the problem of left-handed materials," *Physical Review Letters*, vol. 89, no. 9, Article ID 93901, 4 pages, 2002.
- [34] A. L. Pokrovsky and A. L. Efros, "Nonlocal electrodynamics of two-dimensional wire mesh photonic crystals," *Physical Review B*, vol. 65, no. 4, Article ID 45110, 8 pages, 2002.
- [35] The strong overlap of nm-confined modes with metallic component of nanolayered structure leads to significant reduction of propagation length of these waves. The typical propagation length of the mode is of the order of $1 \dots 10 \mu\text{m}$. This length can be improved by using Ag instead of Au, or by selection other low-loss media. These losses can be also compensated by incorporation of gain into metamaterial structure[29].
- [36] V. A. Podolskiy and E. E. Narimanov, "Comment on: all-angle broadband negative refraction of metal waveguide arrays in the visible range: theoretical analysis and numerical demonstration," *Physical Review Letters*, vol. 98, no. 17, Article ID 179401, 2007.

Research Article

On the Dielectric and Magnetic Properties of Nanocomposites

B. Hallouet,¹ B. Wetzel,² and R. Pelster¹

¹Fachrichtung 7.2, Experimentalphysik, Universität des Saarlandes, Postfach 151150, 66041 Saarbrücken, Germany

²Institut für Verbundwerkstoffe GmbH (IVW), Erwin-Schrödinger-Straße, Gebäude 58, 67663 Kaiserslautern, Germany

Received 15 February 2007; Revised 29 June 2007; Accepted 17 October 2007

Recommended by C. Brosseau

We investigate nanocomposites, that is, dispersions of magnetite nanoparticles in an epoxy resin, by means of broadband dielectric and magnetic spectroscopy. The molecular dynamics of the polymer matrix is altered by the nanoparticles. Due to the formation of agglomerates neither permittivity nor permeability can be described with known effective medium models. We use the spectral representation (Bergman theorem) to show that a model-free evaluation of the low-frequency permeability of the nanoparticles can be achieved by combining dielectric and magnetic data. In addition, the ferromagnetic resonance is studied experimentally. It occurs near 3 GHz and is independent of the particle concentration.

Copyright © 2007 B. Hallouet et al. This is an open access article distributed under the Creative Commons Attribution License, which permits unrestricted use, distribution, and reproduction in any medium, provided the original work is properly cited.

1. INTRODUCTION

Composite materials, consisting of magnetic nanoparticles dispersed in a polymer matrix, offer the possibility to combine the properties of their components. On the one hand, the processability and mechanical quality of the matrix is an advantage compared to ferrites. On the other hand, despite a restricted particle concentration, a sufficiently high permeability has to be achieved, especially in the high frequency range around 1 GHz. For these reasons, such composites are extensively studied, both experimentally and theoretically [1–3]. Applications are possible in various areas (magnetic sensors and transducers, electromagnetic impedance matching, microwave heating, etc.).

A composite can be considered as a so-called effective medium with homogeneous material properties (effective permittivity ϵ_{eff} and effective permeability μ_{eff}) as long as the wavelength of an applied electric field E and a magnetic field H is large compared to the length scale of its structural inhomogeneities, that is, large compared to particle diameters and interparticle distances. Then the measured effective material parameters are defined in terms of volume averaged fields, $\langle \epsilon_{\text{eff}} E(r) \rangle = \langle \epsilon(r) E(r) \rangle$ and $\langle \mu_{\text{eff}} H(r) \rangle = \langle \mu(r) H(r) \rangle$, respectively. Here, the brackets denote the volume average, $\langle \dots \rangle = 1/V \cdot \int \dots dV$, and $\epsilon(r)$ and $\mu(r)$ the local material parameters. (This is a linear analysis where the electromagnetic response of the material does not depend on the

field strengths). Performing the average for each component, these definitions read [4, 5]

$$\epsilon_{\text{eff}} = \frac{(1-f)\epsilon_m \langle E \rangle_m + f\epsilon_p \langle E \rangle_p}{(1-f)\langle E \rangle_m + f\langle E \rangle_p}, \quad (1)$$

$$\mu_{\text{eff}} = \frac{(1-f)\mu_m \langle H \rangle_m + f\mu_p \langle H \rangle_p}{(1-f)\langle H \rangle_m + f\langle H \rangle_p}, \quad (2)$$

where $\langle \dots \rangle_i$ denotes the volume average in matrix ($i = m$) and particles ($i = p$) with corresponding material parameters ϵ_i and μ_i . $f = V_p/V$ is the volume filling factor of the dispersed particles. The above equations illustrate two main features.

(i) The effective material parameters do not depend only on the properties of the components and their mixing ratio. The microstructure, in our case, shape and size distribution of particles as well as their spatial arrangement, directly influences the field distribution and thus ϵ_{eff} and μ_{eff} . Therefore, analytical exact mixture rules are only available for rather simple geometries (for monodisperse arrays of spheres and spheroids, see, e.g., [6–9]). But of course, computer simulations of two and three dimensional systems allow calculation of the effective material parameters for various particle arrangements and shapes (see, e.g., [10–18]). For example, Fu et al. have found an analytically exact solution in 3D space, a complex set of equations, describing an arbitrary distribution of nontouching spheres [19]. For a given particle

TABLE 1: Properties of the components.

Component	DER332	DETA	Fe ₃ O ₄
Producer	DOW	DOW	Sigma-Aldrich
State (298.15 K/343.15 K)	Crystalline/liquid	Liquid	Powder
Density (g/cm ³)	1.16	0.9482	5.1

arrangement, this allows numerical calculation of the effective permittivity [20]. Such simulations of effective properties are helpful, but they do not resolve the problem of how to analyze experimental data, when the microstructure is not completely known, for example, due to a partial agglomeration of particles. There is a multiplicity of approximate effective-medium formulas [21, 22], but in most cases, the details of the underlying microstructure are not explicitly specified. Thus it is often not clear how to choose the one that is appropriate for the system under study. Especially the attempt to evaluate the properties of the dispersed component is impossible or, at least, subject to big errors (note that heterogeneity not only affects the absolute values of effective permittivity but also influences the characteristic frequencies of polarization processes [23] and of molecular relaxation dynamics [24], that are observable in dielectric spectroscopy).

(ii) For a given microstructure, the same formal relationship holds for permittivity and permeability: (1) transforms into (2), when E is replaced by H as well as ϵ by μ . Since the fields behave in an analogous way at the internal interfaces (the tangential components E_t and H_t are continuous whereas for the normal components, $\epsilon_p E_{\perp,p} = \epsilon_m E_{\perp,m}$ and $\mu_p H_{\perp,p} = \mu_m H_{\perp,m}$ hold), the same mixture rules apply for ϵ_{eff} and μ_{eff} .

For the effective permittivity, there exists a so-called spectral representation, that was developed by Bergman, Fuchs, and Milton (for a review see [25]). They were able to separate the influence of microstructure, characterized by a spectral density function, from that of the components, characterized by their permittivities [25]:

$$\frac{\epsilon_{\text{eff}}}{\epsilon_m} = 1 + f \left\{ \frac{C}{t_\epsilon} + \int_0^1 \frac{g_f(n)}{t_\epsilon + n} dn \right\} \quad \text{with } t_\epsilon = \frac{1}{\epsilon_p/\epsilon_m - 1}. \quad (3)$$

The constant C is the strength of percolation describing the contribution of an infinite cluster. The spectral density $g_f(n) \geq 0$ characterizes the actual microstructure at a given filling factor f (for a single particle n would correspond to the depolarization factor; in a complex system of interacting particles, it is a variable in the range $0 \leq n \leq 1$). There are two sum rules that determine the 0th and the 1st moment of the function $g_f(n)$:

$$\int_0^1 g_f(n) dn = 1 - C, \quad (4)$$

for all mixtures (i.e., g_f is normalized), and additionally,

$$\int_0^1 n g_f(n) dn = \frac{1}{3} \cdot (1 - f), \quad (5)$$

for isotropic systems.¹ In the following, we restrict ourselves to isotropic composites below the percolation threshold ($C = 0$ in (3) and (4)). Due to the above formal analogy between effective permittivity and permeability, the same spectral density function also describes the magnetic properties of a composite:

$$\frac{\mu_{\text{eff}}}{\mu_m} = 1 + f \int_0^1 \frac{g_f(n)}{t_\mu + n} dn \quad \text{with } t_\mu = \frac{1}{(\mu_p/\mu_m) - 1}. \quad (6)$$

Spectral representation does not provide a method for determining $g_f(n)$ from first principles [25], and thus it does not allow derivation of mixture formulas. But it can be very helpful for the analysis of experimental data, even in cases where the microstructure is unknown. For example, when the measured effective properties vary considerably as a function of frequency, the spectral density g_f can be evaluated using model functions for the intrinsic material parameters [28–30]. In the following, we are going to show that it is possible to evaluate the material parameters of the dispersed component as well as to detect and to quantify effects that the effective medium theory does not predict (changes of the components properties at interfaces, see below). Here, we study a model system consisting of magnetic nanoparticles (magnetite) dispersed in a polymer matrix. We have measured permittivity and permeability for different particle concentrations using dielectric spectroscopy in the frequency range from 5 Hz to 1 GHz and magnetic measurements from 5 MHz to 6 GHz.

2. EXPERIMENTAL

2.1. Samples

The composites studied are an epoxide system filled with magnetic nanoparticles. This epoxide system is composed of a resin, Diglycidylether of Bisphenol A (DER332, DOW Plastics (Rheinmünster, Germany)), and a hardener, Diethylenetriamin (DETA, DOW Plastics (Rheinmünster, Germany)). The magnetic nanoparticles, which have a mean diameter between 20 and 30 nm, are magnetite (Fe₃O₄) purchased from Sigma-Aldrich (Munich, Germany). The main characteristics of the components are listed in Table 1.

¹ These lower moments are obtained via a series expansion of $\epsilon_{\text{eff}}/\epsilon_m$ around $\epsilon_p/\epsilon_m = 1$, that is, considering the limiting case of a nearly homogeneous composite, where the electric field is uniform (for details, we refer to [26, 27]).

The sample preparation was done in two steps. At first, a concentrated epoxide/nanoparticle masterbatch with a particle content of 14.1 vol% was produced at the IVW (Institut für Verbundwerkstoffe). Then this masterbatch was further processed to obtain solid samples with different particle concentrations.

Nanoparticles in powders adhere to each other due to interactive forces between the particles, resulting in nanoparticle agglomerates with dimensions of several micrometers. In order to obtain a material with good mechanical properties, it is necessary to disintegrate the agglomerates and to distribute them homogeneously in the polymer matrix. In this study, two working principles, traditionally used for lacquer processing (dissolver and bead mill) were combined in one. After incorporating the powdery nanoparticles into the liquid resin, the resulting mixture was homogenized by a dissolver aggregate (a dissolver provides high shear forces by the rotation of a metal disc in the liquid mixture). Entrapped air was removed by vacuum. Then the magnetite was further dispersed using a torus mill. It applies high shear forces to the mixture via a rotating metal disc while hard zirconia beads with diameters between 1.2 and 1.7 mm move within the mixture. These beads generate collision effects and shear forces providing a grinding effect that further decreases the size of nanoparticle agglomerates. The beads were removed from the mixture after the dispersion process. The above processing of nanocomposites was performed under controlled conditions, that is, at constant energy input and constant temperature. The chosen particle content of the masterbatch (14.1 vol%) is close to the processing limit. At higher concentrations, the system becomes too viscous, resulting in an unstable and discontinuous flow during processing. Then dispersing the nanoparticles and wetting them with polymer becomes more and more difficult, and processing may result in a reduced homogeneity of the mixture.

In the next step, we have prepared solid samples with a specific particle concentration: at first, both the initial masterbatch and the pure resin were maintained for one hour under vacuum in order to remove entrapped air. This was done at a high temperature of 313.15 K to avoid crystallization and to diminish the viscosity of the resin. Then the masterbatch was diluted with pure resin whereas both components were mixed for 30 minutes and evacuated for one hour. This mixture was cured after adding the corresponding quantity of DETA (mass ratio resin/hardener 100 : 14). In this last phase, the material was mixed for five minutes, cooled down rapidly to room temperature in order to slow down the polymerization process, and evacuated for three minutes. The polymerization took place in a mould at room temperature. After 48 hours, the post-cure was performed at 393 K during one hour [31]. The resulting series of samples with varying nanoparticle content from $f = 2\%$ to $f = 10\%$ are listed in Table 2.

2.2. Measurement techniques

We have used dielectric and magnetic spectroscopy to determine the complex permittivity $\epsilon = \epsilon' - i\epsilon''$ and the magnetic permeability $\mu = \mu' - i\mu''$ of our samples at room temperature.

TABLE 2: Volume filling factor and mass filling factor of the samples studied.

Filling factor f (% vol)	Filling factor \times (% mass)
0	0
2	8.6
4	16.1
6	22.7
8	28.6
10	33.8

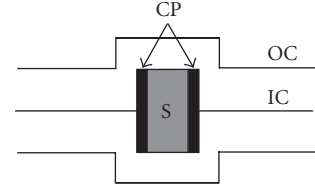


FIGURE 1: Condenser cell as a part of a transmission line (dielectric measurements). S: sample, CP: capacitor plates, IC/OC: inner/outer conductor of the transmission line

The complex permittivity has been measured using a broadband transmission method covering the frequency range from 5 Hz to 1 GHz with one experimental setup [32]. The sample is placed between two circular capacitor plates that are connected to the inner conductor of a coaxial transmission line (see Figure 1). For this purpose, cylindrical discs with a diameter of $\Phi = 13$ mm and a thickness d between 1 and 2 mm have been machined from the composite material (using a turning lathe). From the measured transmission coefficient, the permittivity is calculated. The respective geometrical tolerances of sample diameter and thickness ($\pm 20 \mu\text{m}$) result in an uncertainty of $\Delta_{\text{rel}}|\epsilon| \simeq \Delta_{\text{rel}}(\Phi^2/d) \simeq 2\%$ (for details, see [32]).

The complex permeability has been measured using an impedance analyzer (Agilent HP 8424a) in the frequency range from 5 MHz up to 110 MHz and a network analyzer (HP 8510B) between 110 MHz and 6 GHz. In both cases, the sample is inserted at the short-circuited termination of a calibrated coaxial transmission line (see Figure 2). For this purpose, cylindrical samples with outer diameter $\varphi_2 = 7$ mm and inner diameter $\varphi_1 = 3.04$ mm have been machined from the original cured composite. At low frequencies, the termination impedance of the coaxial line is measured, $Z = R + i\omega L$, with R being the resistance of the inner conductor and $L = (\mu_0/2\pi)\mu \ln(\varphi_2/\varphi_1)d$ being the inductance ($\mu_0 = 4\pi \cdot 10^{-7}$ H/m). Two measurements, with and without the sample, are sufficient to determine the complex permeability:

$$\mu = \frac{Z_{\text{sample}} - Z_{\text{empty}}}{i\omega(\mu_0/2\pi) \ln(\varphi_2/\varphi_1)d} + 1, \quad (7)$$

where ω is the circular frequency and d is the thickness of the sample [33]. The geometrical tolerances of inner and outer sample diameters ($\pm 20 \mu\text{m}$) result in an uncertainty of $\Delta_{\text{rel}}|\mu| \simeq 2\%$.

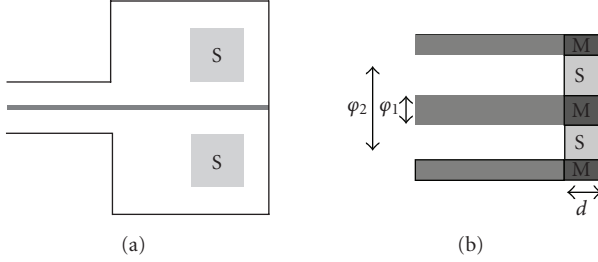


FIGURE 2: Measurement cell for the determination of the complex permeability in the low frequency range (a) and in the high frequency range (b) (impedance and reflection measurements, respectively). S: sample, M: metal, φ_1/φ_2 : inner/outer diameter of the sample, d: thickness of the sample.

In the high frequency range, the reflection coefficient Γ is measured, which is directly connected to the measured impedance $Z = Z_{\text{sample}}$ or $Z = Z_{\text{empty}}$ and the impedance of the cable, $Z_c = 50 \Omega$:

$$\Gamma_{\text{meas}} = \frac{Z - Z_c}{Z + Z_c}. \quad (8)$$

3. DIELECTRIC MEASUREMENTS

At room temperature, that is, below the glass transition temperature of the polymer matrix ($T_G = 404 \text{ K}$ [34]), we have performed dielectric measurements on the samples listed in Table 2. Figure 3 shows real and imaginary parts of the effective permittivity as a function of frequency for different filling factors. Already the pure matrix ($f = 0\%$) shows a relaxation process near 10^5 Hz leading to a decrease of permittivity from a low frequency value $\epsilon_{\text{eff},s}$ to a high frequency value $\epsilon_{\text{eff},\infty}$ above 1 GHz (Figure 4). The peak in ϵ'' seems to be an overlap of several processes. Local heterogeneity, for example, can give rise to such a distribution of relaxation times. The origin of this relaxation has to be clarified by further temperature dependent measurements. With increasing amount of nanoparticles, the process becomes more pronounced. In order to quantify this, we have fitted the curves with the empirical Havriliak-Negami model [35, 36]:

$$\epsilon_{\text{eff}}(\omega) = \epsilon_{\text{eff},\infty} + \frac{\epsilon_{\text{eff},s} - \epsilon_{\text{eff},\infty}}{(1 + (i\omega\tau)^\alpha)^\beta}, \quad (9)$$

with τ being the relaxation time. An example is shown in Figure 4. Although the fit does not reproduce the detailed structure of the ϵ'' -peak, the overall agreement is good allowing at least to satisfactorily describe the respective low and high frequency limits of permittivity. The addition of nanoparticles yields both an increase of ϵ_∞ as well as of the relaxation strength, $\Delta\epsilon_{\text{eff}} = \epsilon_{\text{eff},s} - \epsilon_{\text{eff},\infty}$ (see Figures 3 and 4). At first sight, this can be qualitatively related to the fact that the magnetite particles are conductive. When an electric field is applied, the particles become polarized, resulting in an enhanced permittivity compared to that of the pure matrix (interfacial polarization process or Maxwell-Wagner-Sillars polarization). The measured spectra thus reflect the superposition of at least two processes: the intrinsic relaxation of the

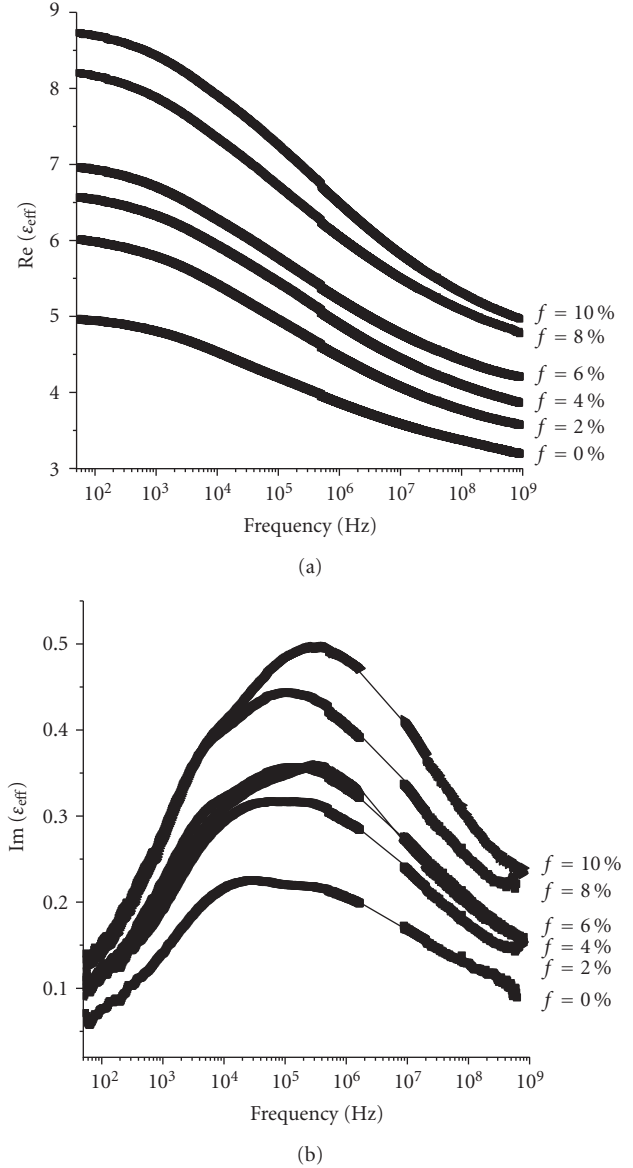


FIGURE 3: (a) Real and (b) imaginary parts of the dielectric function for an epoxy resin with Fe_3O_4 -nanoparticles at various volume filling factors.

polymer matrix and the polarization of the conductive particles. In the following, we will address two questions.

(i) Is the observed increase of permittivity only a simple polarization effect or do other processes, that effective medium theory do not predict, contribute?

(ii) To what extent does the data reflect the microstructure of the composite?

The spectral representation (3) is a useful tool to address the first question, even though the detailed microstructure is unknown. We thus start our discussion with a two phase system (matrix and particles) in the strict sense. Particles are either perfectly connected or well separated, so that there is no charge transfer. Additional interphases or contact resistances between particles are excluded (but we will come back to this point later).

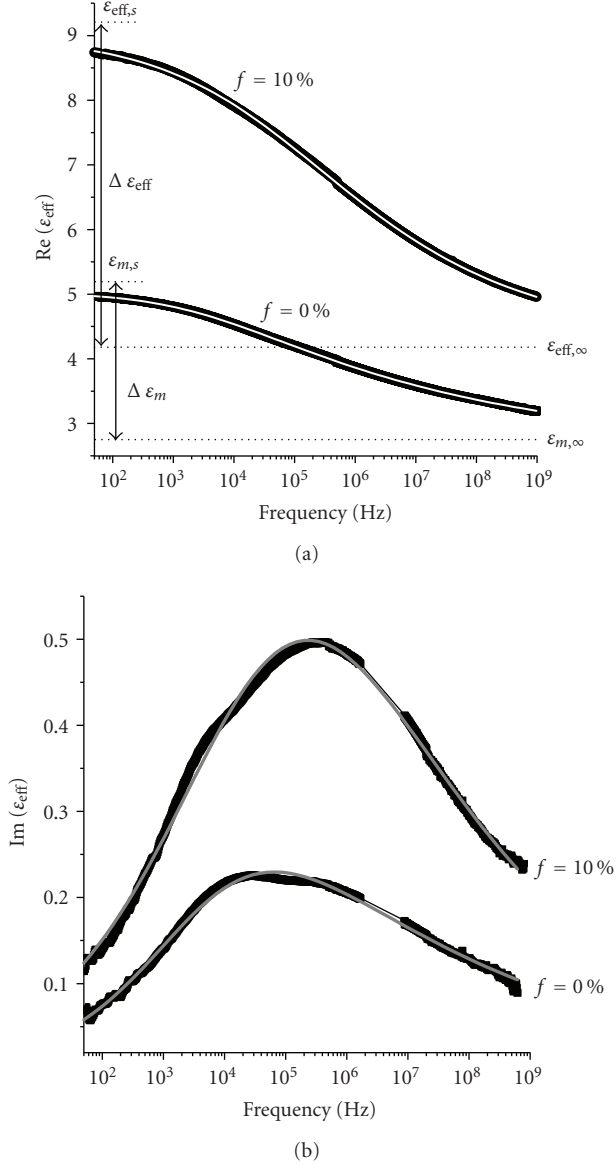


FIGURE 4: (a) Real and (b) imaginary parts of permittivity versus frequency for the pure polymer matrix as well as for a composite with $f = 10\%$. The thin lines correspond to (9). In (a), also some fitted parameters are shown (dotted lines): low-frequency permittivity $\epsilon_{\text{eff},s}$ and high-frequency permittivity $\epsilon_{\text{eff},\infty}$. The arrows indicate the respective relaxation strength, $\Delta\epsilon_{\text{eff}} = \epsilon_{\text{eff},s} - \epsilon_{\text{eff},\infty}$.

The generalized permittivity of conducting particles is given by $\epsilon_p = \epsilon' - i\sigma/(\epsilon_0\omega)$, so that the conductivity σ governs the dielectric response at low frequencies ($\epsilon_0 = 8.854 \cdot 10^{-12}$ F/m). When the nanoparticles are exposed to an electric field, they become completely polarized, that is, the average field strength inside is negligible compared to that outside (for a single sphere in an homogeneous field, e.g., $\langle E \rangle_p / \langle E_m \rangle = 3\epsilon_m / (\epsilon_p + 2\epsilon_m)$ holds). This is the case at low frequencies when

$$\left| \frac{\epsilon_p}{\epsilon_m} \right| \simeq \frac{\sigma}{\epsilon_0 \epsilon_m \omega} \gg 1, \quad (10)$$

holds, that is, in the quasistatic limit

$$\nu \ll \frac{\sigma}{2\pi\epsilon_0\epsilon_m} = \nu_g. \quad (11)$$

The DC conductivity of bulk magnetite is of the order of $\sigma \geq 300$ S/m at room temperature, for thin films with a thickness of 30 nm, it is $\sigma \geq 30$ S/m [37]. With a matrix permittivity $\epsilon_m \geq 3$ (see Figure 3), the above condition reads $\nu \ll 10^{11}$ Hz. Obviously, this is the case in our measurement range (up to 10^9 Hz). Then (3) becomes, with $|t| = |\epsilon_p/\epsilon_m - 1|^{-1} \ll 1$,

$$\frac{\epsilon_{\text{eff}}}{\epsilon_m} = 1 + f \cdot \underbrace{\int_0^1 \frac{g_f(n)}{n} dn}_{=h(f)} \quad \text{for } \nu \ll \nu_g, \quad (12)$$

where $h(f)$ is a function having real values [$h(f) \in \mathbb{R}$]. Here, we have assumed that no percolation occurs ($C = 0$). In fact, our composites do not show a DC conductivity. Therefore, $\epsilon_{\text{eff}}/\epsilon_m = h(f) \geq 1$ holds. This ratio depends on the actual microstructure, and so it is a function of the filling factor f . But it is independent of ϵ_m and ϵ_p . As a consequence, the values of $h(f)$ do not depend on frequency and are real numbers. This is a general result that reflects in all specific mixture formulas. The Maxwell-Garnett formula, for example, that describes a random distribution of monodisperse spheres [19, 20], reads, in the quasistatic limit,

$$\frac{\epsilon_{\text{eff}}^{\text{MG}}}{\epsilon_m} = \frac{1 + 2f}{1 - f} \quad \text{for } \nu \ll \nu_g, \quad (13)$$

while the Hanai-Bruggeman formula, describing randomly distributed spheres having a sufficiently broad size distribution [20], becomes

$$\frac{\epsilon_{\text{eff}}^{\text{HB}}}{\epsilon_m} = \frac{1}{(1 - f)^3} \quad \text{for } \nu \ll \nu_g. \quad (14)$$

We have calculated the ratio of the measured permittivities, $\epsilon_{\text{eff}}/\epsilon_m$, and displayed its absolute value in Figure 5. Obviously, it depends on frequency in the range where the relaxation process of the matrix polymer is active (there also, the imaginary part of $\epsilon_{\text{eff}}/\epsilon_m$ does not vanish). This means that the observed increase of relaxation strength with filling factor (Figure 6) is not solely due to the polarization of the conductive particles. Besides the two processes we have already discussed, that is, the intrinsic relaxation of the polymer matrix and the quasistatic polarization of the conductive particles, there is an additional mechanism, that is not taken into account by effective medium theory. In order to quantify this effect, we now evaluate how the effective relaxation strength should change if there were no such additional mechanism, that is, if (12) were valid. For the respective low and high frequency values, it reads

$$\begin{aligned} \epsilon_{\text{eff},s} &= h(f) \cdot \epsilon_{m,s}, \\ \epsilon_{\text{eff},\infty} &= h(f) \cdot \epsilon_{m,\infty}, \end{aligned} \quad (15)$$

and thus with $\epsilon_{\text{eff},s} = \Delta\epsilon_{\text{eff}} + \epsilon_{\text{eff},\infty}$ and $\epsilon_{m,s} = \Delta\epsilon_m + \epsilon_{m,\infty}$ (see Figure 4),

$$\Delta\epsilon_{\text{eff}}(f) = \epsilon_{\text{eff},\infty}(f) \cdot \frac{\Delta\epsilon_m}{\epsilon_{m,\infty}}. \quad (16)$$

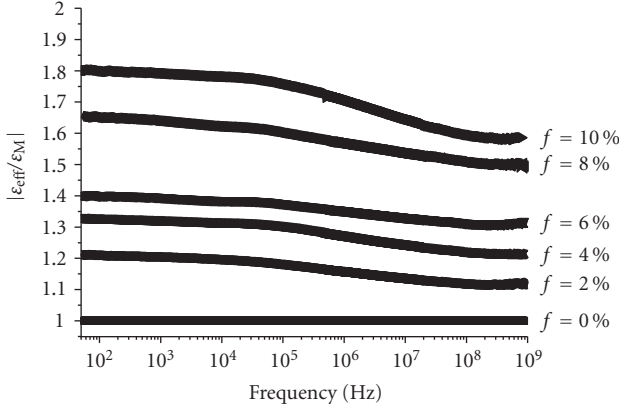


FIGURE 5: Absolute value of the ratio of effective permittivity over matrix permittivity as a function of frequency for our composites (the curves were calculated from the measured complex values shown in Figure 3). For each filling factor, effective medium theory predicts a real and frequency-independent value (see (12)). Obviously, this is not the case in the range where the relaxation of the matrix polymer is observed.

The above equation is independent of microstructure and thus holds for all composite materials, provided effective medium theory can be applied. In Figure 6, we compare the measured values of $\Delta\epsilon_{\text{eff}}$ to those calculated using (16) (inserting the experimental data for $\Delta\epsilon_m$, $\epsilon_{m,\infty}$, and $\epsilon_{\text{eff},\infty}(f)$). The experimental values are up to 38% higher (at $f = 10\%$) compared to what we may expect. Note that (3) and thus (12) to (16) presuppose that there are only two phases and that their properties remain unchanged when the components are mixed. But obviously, this basic assumption of effective medium theory is not fulfilled here. There are two possibilities.

(i) According to (16), the measured relaxation strength is proportional to the intrinsic one, $\Delta\epsilon_{\text{eff}} \propto \Delta\epsilon_m/\epsilon_{m,\infty}$. So we can understand the experimental result when we assume that the dispersion of particles alters the molecular polarizability of the polymer by enhancing the relaxation strength of the matrix compared to that of the bulk polymer. In fact, replacing, in (16),

$$\frac{\Delta\epsilon_m}{\epsilon_{m,\infty}} \longrightarrow \frac{\Delta\epsilon_m}{\epsilon_{m,\infty}} \cdot (1 + f \cdot 3.8) \quad (17)$$

allows us to describe satisfactorily well the experimental data. Such a process is possible at the interfaces between particles and the matrix, where the molecular interactions are altered (and possibly interphases form). The smaller the particles, the stronger the impact of the interfaces [38–40]. In this case, the additional increase of relaxation strength should be proportional to the surface area of the interfaces and thus proportional to f , what we in fact do observe (see Figure 6). Further experiments will show whether also the temperature dependence of the relaxation time is affected by these altered interactions.

(ii) Charge transfer between agglomerating particles, either via contact resistances (corresponding to a third phase in the mixture) or via a hopping process, can lead to an ad-

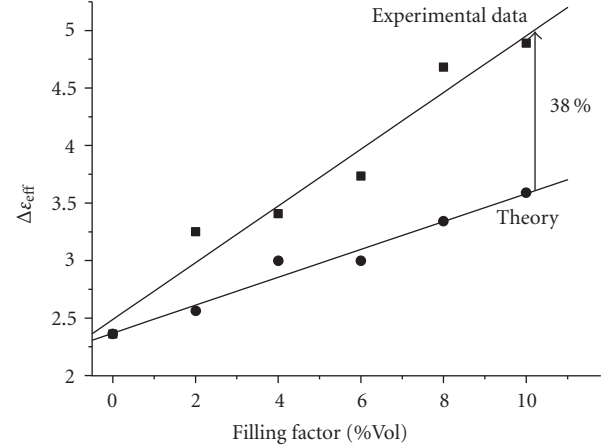


FIGURE 6: Relaxation strength $\Delta\epsilon_{\text{eff}}$ as a function of volume filling factor. Since the relaxation process is already observed at $f = 0$, it is related to the molecular dynamics of the pure matrix. The theoretical values have been calculated using (16) (inserting the measured values $\epsilon_{\text{eff},\infty}(f)$, $\Delta\epsilon_m$ and $\epsilon_{m,\infty}$).

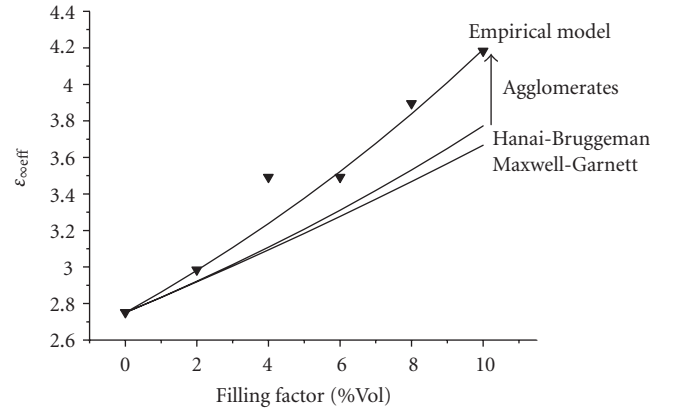


FIGURE 7: High-frequency permittivity versus volume filling factor. The solid lines correspond to the models of Maxwell-Garnett (13) and Hanai-Bruggeman (14) as well as to (18) (see text).

ditional interfacial polarization process [23, 41]. The characteristic frequency of such a process is proportional to the conductivity of the polarized object. Attributing a conductivity $\sigma_{\text{aggl}} \ll \sigma_p$ to the agglomerates, it might be located in the low frequency range and, just by chance, coincide with that of the dipolar relaxation of the polymer matrix. We consider this implausible, especially since the measured data in Figures 3(b) and 4(b) does not indicate the appearance of a new distinct peak. But the form of the relaxation peak changes on addition of nanoparticles, so that we cannot completely exclude this hypothesis. But then the two mechanisms (dipolar relaxation and agglomerate polarization) should have different activation energies, so that future temperature dependent measurements should allow us to separate the respective loss peaks.

Now, let us focus on the high-frequency permittivity, $\epsilon_{\text{eff},\infty}$, which is shown as a function of filling factor

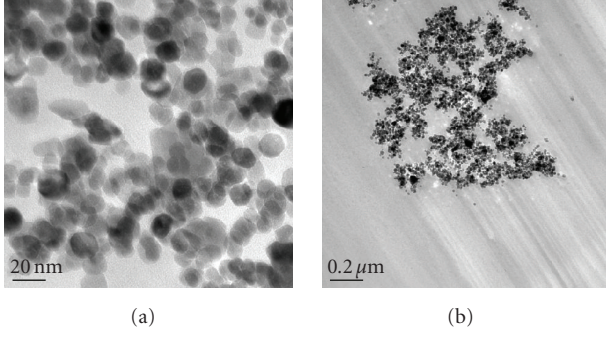


FIGURE 8: TEM-pictures of a sample with $f = 2\%$. Note the different magnifications.

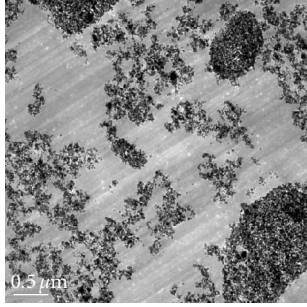


FIGURE 9: TEM-photo of a sample with $f = 10\%$.

in Figure 7. ε_∞ increases with f . We compare the experimental data with two models which apply for a statistical spatial distribution of spheres in a continuous matrix (matrix-inclusion topology or cermet topology). For monodisperse systems below the percolation threshold, the Maxwell-Garnett model applies, see (13), whereas the poly-disperse limit (i.e., spheres with a sufficiently broad size distribution) is well described by the Hanai-Bruggeman model, see (14). These formulas and their range of application have been verified by 3D computer simulations based on an analytically exact solution [19, 20].

Obviously, both models predict permittivities that are lower than those measured. This deviation is nonambiguous since, in the quasistatic limit, the effective permittivity does not depend on an unknown particle permittivity, ε_p . But we can describe the experimental data fairly well by a modified version of the Hanai-Bruggeman model, see (14), where the exponent 3 is replaced by 4 (see Figure 7):

$$\varepsilon_{\text{eff},\infty}^{\text{exp}} \simeq \frac{\varepsilon_{m,\infty}}{(1-f)^4}. \quad (18)$$

This is just an empirical description, but it will facilitate the evaluation of the magnetic measurements (see below).

In order to find out to which extent the observed enhancement is related to the microstructure of our composite, transmission electronic microscopy measurements have been performed. In Figures 8 and 9, we show TEM-pictures of two samples. Agglomerates are clearly observable, that is, there is no random spatial distribution. This leads to a higher-effective permittivity compared to simple effective-medium

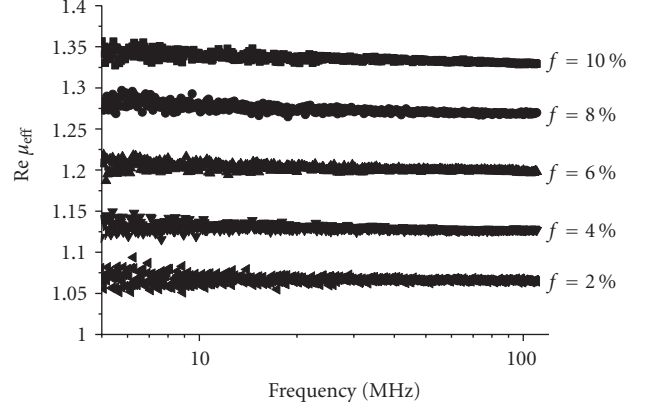


FIGURE 10: Real part of permeability versus frequency for samples with different volume filling factors. The imaginary part vanishes within the resolution of the measurement method.

models [23]. Of course, we cannot exclude that there is an additional effect, for example, an enhancement of the matrix permittivity, $\varepsilon_{m,\infty}$, due to altered interactions at the interfaces between matrix and nanoparticles, similar to what we have discussed above.

4. MAGNETIC MEASUREMENTS

Now, let us see what kind of information we can get from the magnetic measurements. These have been performed for the samples listed in Table 2. At low frequencies from 5 to 110 MHz, no losses can be observed ($\mu_{\text{eff}}'' \simeq 0$), so that we only display the real part of the effective permeability as a function of the frequency in Figure 10. The permeability increases by adding nanoparticles to our nonmagnetic matrix (see also Figure 12).

As already stated in the introduction, in the framework of effective medium theory, magnetic permeability is treated in the same way as permittivity, so that we can replace ε by μ in all formulas. But compared to the analysis of dielectric data, there are two differences in the discussion of magnetic measurements.

(i) We consider a nonmagnetic matrix, $\mu_m = 1$, and this property cannot change due to interface effects in the composite. This facilitates the analysis of the data.

(ii) The effective permeability will now depend not only on the microstructure, but also on the permeability of the dispersed particles, μ_p . Thus $\mu_{\text{eff}} = F(\mu_p, \mu_m, f)$ holds with an unknown function F . In addition, μ_p may differ from the bulk value and thus it is unknown as well. This makes an analysis more complicated.

So the question arises whether it is possible to determine μ_p although we do not dispose *a priori* of an analytical effective medium formula that is appropriate for the microstructure of our samples. For example, when we fit our data in Figure 10 using the Hanai-Bruggeman formula,

$$\left(\frac{\mu_{\text{eff}} - \mu_p}{\mu_m - \mu_p} \right) \cdot \left(\frac{\mu_m}{\mu_{\text{eff}}} \right)^{1/3} = (1-f), \quad (19)$$

we obtain a value of $\mu_p \simeq 40$ (see Figure 11). But remember that both the dielectric measurements and the TEM-pictures have shown that the particles are not randomly dispersed. Similar to what we have observed in the dielectric case, the formation of agglomerates partly contributes to the observed increase of effective permeability. This can be understood in terms of an enhanced particle interaction: in random systems, higher-multipole moments can be neglected [20], but they gain in importance in agglomerates. Therefore, the obtained value can only be considered as an upper limit, that is, we can expect $\mu_p < 40$. At first sight, it seems to be impossible to get a reliable value for μ_p without further information about the microstructure and an appropriate model to describe it. But in the following, we are going to show that the dielectric measurements described above give us all the structural information we need to evaluate the particle permeability. Instead of relying on approximate effective medium formulas, we can use the spectral representation, that is, an analytically exact formulation.

Although the spectral density, $g_f(n)$, is unknown, we have four sources of integral information to solve the problem: the two sum rules, (4) and (5), as well as the dielectric measurements in the quasistatic limit (Figure 7) and magnetic low frequency measurements (below 110 MHz, see Figure 12). Equations (6) and (12) relate the experimental data to the properties of the components and the spectral density. Using these and the above definition of the quasistatic dielectric limit, $h(f) = \lim_{|\varepsilon_p| \rightarrow \infty} (\varepsilon_{\text{eff}}/\varepsilon_m)$, we obtain

$$\begin{aligned} h(f) - \frac{\mu_{\text{eff}}(f)}{\mu_m} &= \left(1 + f \int_0^1 \frac{g_f(n)}{n} dn\right) - \left(1 + f \int_0^1 \frac{g_f(n)}{t_\mu + n} dn\right) \\ &= f \int_0^1 \frac{g_f(n)}{n} \cdot \frac{t_\mu}{n + t_\mu} dn. \end{aligned} \quad (20)$$

A Taylor expansion at $n = 1$ of the 2nd factor in the integral yields

$$\begin{aligned} \frac{t_\mu}{n + t_\mu} &= \frac{t_\mu}{1 + t_\mu} - \frac{t_\mu}{(1 + t_\mu)^2} \cdot (n - 1) + \frac{t_\mu}{(1 + t_\mu)^3} \cdot (n - 1)^2 \\ &\quad - \frac{t_\mu}{(1 + t_\mu)^4} \cdot (n - 1)^3 + \dots \end{aligned} \quad (21)$$

Inserting this result into (20) and performing the integration (using the sum rules (4) and (5) with $C = 0$), we obtain

$$\begin{aligned} \frac{\mu_{\text{eff}}(f)}{\mu_m} &= h(f) - \frac{t_\mu}{1 + t_\mu} \cdot (h(f) - 1) - \frac{t_\mu}{(1 + t_\mu)^2} \cdot [(h(f) - 1) - f] \\ &\quad - \frac{t_\mu}{(1 + t_\mu)^3} \cdot [(h(f) - 1) - 5/3 \cdot f - 1/3 \cdot f^2] + \dots \end{aligned} \quad (22)$$

The known limiting cases are easily checked; for $\mu_p/\mu_m = 1$, that is, $t_\mu = \infty$, we obtain $\mu_{\text{eff}}/\mu_m = 1$. For $\mu_p/\mu_m \rightarrow \infty$, that is,

$t_\mu \rightarrow 0$, we get once again the quasistatic limit $\mu_{\text{eff}}/\mu_m \rightarrow h(f)$. It can be easily shown that the next higher term of order $t_\mu/(1 + t_\mu)^4$ in (22) contributes at maximum 1% of $h(f)$ and thus it can be neglected. The implications of the above result, that has been obtained using spectral density analysis, are obvious.

Equation (22) allows us to evaluate t_μ and thus the particle permeability μ_p . The only quantities we need to know are the effective permeability as well as the quasistatic dielectric limit, $h(f) = \lim_{|\varepsilon_p| \rightarrow \infty} (\varepsilon_{\text{eff}}/\varepsilon_m)$. One possibility would be to insert the measured values and to solve (22) for t_μ at the respective concentration f . But there is a better way that helps to minimize the influence of statistical measurement errors as well as that of structural variations or of concentration fluctuations (remember that different samples are used to determine ε_{eff} and μ_{eff}): when the particle concentration has been varied it is advantageous to use a simple fit function to describe the measured dielectric data. From our dielectric measurements, we know that $h(f) \simeq 1/(1 - f)^4$ holds ((18) and Figure 7). Inserting this function in (22), we can directly calculate the effective permeability $\mu_{\text{eff}}(f)$ for different values of μ_p . In Figure 12, we compare this calculation with the measured low-frequency permeability. Obviously, the magnetite nanoparticles exhibit a permeability of

$$\mu_p = 7 \pm 1. \quad (23)$$

The advantage of the above evaluation procedure consists in the fact that (22) holds for an arbitrary microstructure. The only prerequisite is that the dispersed particles are conductive. In this case, a combination of dielectric and magnetic measurements enables us to determine the permeability of the dispersed particles without using any effective medium model!

At high frequencies from 110 MHz to 6 GHz, we have performed reflection measurements. The effective permeability is shown as a function of the frequency in Figure 13. Near 3 GHz, a ferromagnetic resonance can be observed. The strength of this process increases with the addition of nanoparticles, but the resonance frequency seems not to depend on the particle concentration. That is what also theoretical models predict for single-domain particles with an isotropic distribution of magnetic orientations [42]. So the situation is quite different from what is known for dielectric relaxation in dispersed particles, where the phase shift of the electric field at the interfaces induces a shift of the measurable effective relaxation frequency compared to that of the intrinsic relaxation [24]: when a complex relaxation function, $\varepsilon_p(\nu)$, is inserted into (1) or (3), the position of the effective loss peak is shifted to higher frequencies (an effect that depends on filling factor and microstructure). But note that, in the present case of ferromagnetic resonance, effective medium theory does not apply in its scalar form, even though the effective permeability of single-domain particles with an isotropic distribution of magnetic orientations is a scalar quantity [42]; close to the resonance frequency, the particle permeability is a tensor, the nondiagonal components of which do not vanish. This makes the calculation

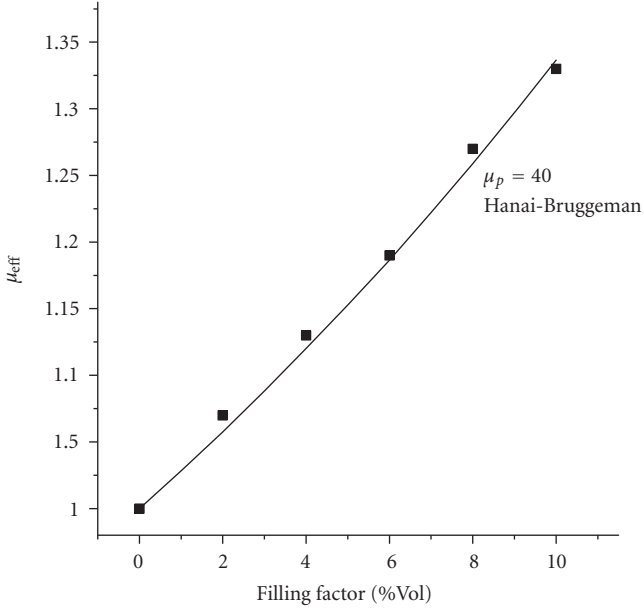


FIGURE 11: Effective permeability as a function of volume filling factor f . Symbols: experimental data (plateau values from Figure 10, i.e., at frequencies below 110 MHz). The solid line corresponds to the Hanai-Bruggeman formula, see (19), with $\mu_p = 40$ and $\mu_m = 1$. However, the dielectric data of Figure 7 shows that this model is not appropriate.

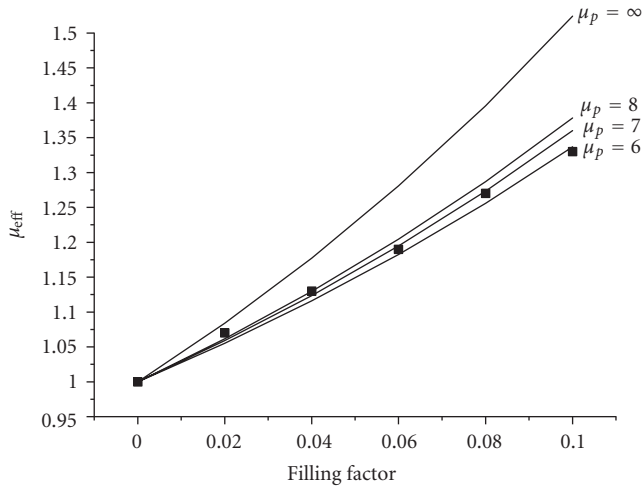


FIGURE 12: Effective permeability as a function of volume filling factor f . Symbols: experimental data (plateau values from Figure 10, i.e., at frequencies below 110 MHz). The solid lines correspond to (22) with $\mu_m = 1$ and the specified values of μ_p .

of μ_{eff} much more complicated and simple effective medium formulas should be handled with care.

5. CONCLUSION

We have prepared magnetic nanocomposites and we characterized them using broadband dielectric and magnetic spec-

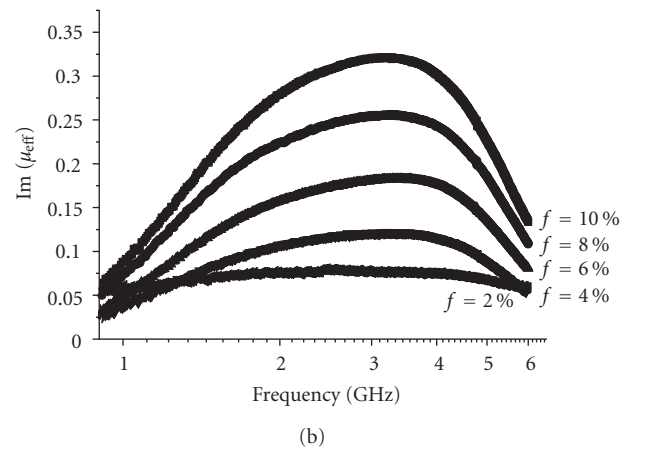
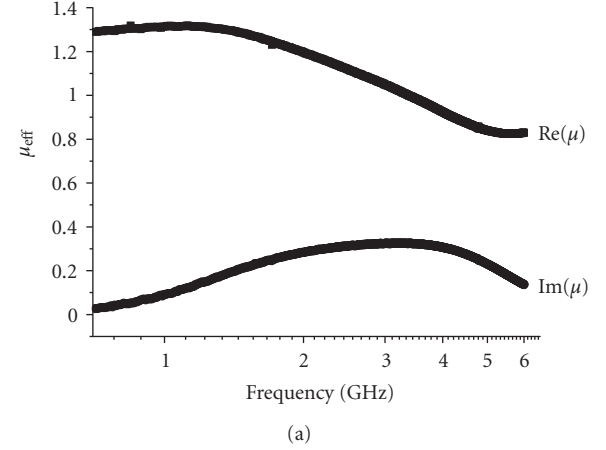


FIGURE 13: (a) Measured real and imaginary part of permeability as a function of frequency for a sample with $f = 10\%$. (b) Measured imaginary part of permeability for samples with various filling factors. Near 3 GHz, the ferromagnetic resonance is observed.

troscopy. The dispersed particles (magnetite) are conductive, so that the dielectric data corresponds to the quasistatic limit of completely polarized particles. This leads to an enhancement of permittivity that is higher than what can be expected for a spatial random distribution of particles. In fact, TEM-pictures show the presence of particle agglomerates. Moreover, the addition of nanoparticles alters the molecular dynamics of the matrix polymer at low frequencies. This effect is due to the modified interactions at the interfaces between particles and the matrix. The measured effective permeability depends both on the microstructure and on the permeability of the nanoparticles, μ_p . We have proposed a model-free procedure, that allows us to evaluate μ_p without using effective medium formulas. It applies for an arbitrary and possibly unknown microstructure and consists of combining dielectric and magnetic data using the spectral representation. In this way, we have determined a value of $\mu_p = 7 \pm 1$ for the permeability of the dispersed magnetite. At high frequencies, the ferromagnetic resonance of the nanoparticles is observed. It is independent of particle concentration and occurs near 3 GHz.

ACKNOWLEDGMENT

The authors gratefully acknowledge the help of J. Schmauch (Universität des Saarlandes), who took the TEM-pictures of our samples.

REFERENCES

- [1] R. Ramprasad, P. Zurcher, M. Petras, M. Miller, and P. Renaud, "Magnetic properties of metallic ferromagnetic nanoparticle composites," *Journal of Applied Physics*, vol. 96, no. 1, pp. 519–529, 2004.
- [2] M. Dikeakos, L. D. Tung, T. Veres, A. Stancu, L. Spinu, and F. Normandin, "Fabrication and characterization of tunable magnetic nanocomposite materials," *Materials Research Society Symposium Proceedings*, vol. 734, no. 134, pp. 315–320, 2003.
- [3] V. B.regar, "Advantages of ferromagnetic nanoparticle composites in microwave absorbers," *IEEE Transactions on Magnetics*, vol. 40, no. 3, pp. 1679–1684, 2004.
- [4] J. Monecke, "Microstructure dependence of material properties of composites," *Physica Status Solidi (B)*, vol. 154, no. 2, pp. 805–813, 1989.
- [5] G. Bánhegyi, "Comparison of electrical mixture rules for composites," *Colloid & Polymer Science*, vol. 264, no. 12, pp. 1030–1050, 1986.
- [6] K. Günther and D. Heinrich, "Dielektrizitätskonstante, Permeabilität, elektrische Leitfähigkeit, Wärmeleitfähigkeit und Diffusionskonstante von Gemischen mit kugelförmigen Teilchen (gitterförmige und statistische Anordnung)," *Zeitschrift für Physik*, vol. 185, no. 4, pp. 345–374, 1965.
- [7] D. R. McKenzie, R. C. McPhedran, and G. H. Derrick, "The conductivity of lattices of spheres. II. The body centred and face centred cubic lattices," *Proceedings of the Royal Society of London. Series A*, vol. 362, no. 1709, pp. 211–232, 1978.
- [8] N. Harfield, "Conductivity of a periodic particle composite with spheroidal inclusions," *The European Physical Journal—Applied Physics*, vol. 6, no. 1, pp. 13–21, 1999.
- [9] N. Harfield, "Bulk permittivity of a composite with coated spheroidal filler particles," *Journal of Materials Science*, vol. 35, no. 23, pp. 5809–5816, 2000.
- [10] S. Stölzle, A. Enders, and G. Nimtz, "Numerical simulation of random composite dielectrics," *Journal de Physique I*, vol. 2, pp. 401–408, 1992.
- [11] S. Stölzle, A. Enders, and G. Nimtz, "Numerical simulation of random composite dielectrics. II. Simulations including dissipation," *Journal de Physique I*, vol. 2, pp. 1765–1777, 1992.
- [12] H. Leinders and A. Enders, "Computer simulations of dielectric and magnetic composite media including dissipation," *Journal de Physique I*, vol. 5, pp. 555–564, 1995.
- [13] E. Tuncer, "On complex permittivity of dilute random binary dielectric mixtures in two-dimensions," *Turkish Journal of Physics*, vol. 27, no. 2, pp. 101–105, 2003.
- [14] E. Tuncer, B. Nettelblad, and S. M. Gubanski, "Non-Debye dielectric relaxation in binary dielectric mixtures (50-50): randomness and regularity in mixture topology," *Journal of Applied Physics*, vol. 92, no. 8, pp. 4612–4624, 2002.
- [15] C. Brosseau and A. Beroual, "Computational electromagnetics and the rational design of new dielectric heterostructures," *Progress in Materials Science*, vol. 48, no. 5, pp. 373–456, 2003.
- [16] C. Brosseau and A. Beroual, "Dielectric properties of periodic heterostructures: a computational electrostatics approach," *The European Physical Journal—Applied Physics*, vol. 6, pp. 23–31, 1999.
- [17] V. Myroshnychenko and C. Brosseau, "Finite-element method for calculation of the effective permittivity of random inhomogeneous media," *Physical Review E*, vol. 71, no. 1, Article ID 016701, 16 pages, 2005.
- [18] F. Wu and K. W. Whites, "Quasi-static effective permittivity of periodic composites containing complex shaped dielectric particles," *IEEE Transactions on Antennas and Propagations*, vol. 49, no. 8, pp. 1174–1182, 2001.
- [19] L. Fu, P. M. Macedo, and L. Resca, "Analytic approach to the interfacial polarization of heterogeneous systems," *Physical Review B*, vol. 47, no. 20, pp. 13818–13829, 1993.
- [20] A. Spanoudaki and R. Pelster, "Effective dielectric properties of composite materials: the dependence on the particle size distribution," *Physical Review B*, vol. 64, no. 6, Article ID 064205, 6 pages, 2001.
- [21] L. K. H. van Beek, "Dielectric behaviour of heterogeneous systems," in *Progress in Dielectrics*, J. B. Birks, Ed., vol. 7, pp. 69–114, Heywood, London, UK, 1967.
- [22] S. S. Dukhin, "Dielectric properties of disperse systems," in *Surface and Colloid Science*, E. Matijevic, Ed., vol. 3, pp. 83–165, Wiley-Interscience, New York, NY, USA, 1986.
- [23] R. Pelster and U. Simon, "Nanodispersions of conducting particles: preparation, microstructure and dielectric properties," *Colloid & Polymer Science*, vol. 277, no. 1, pp. 2–14, 1999.
- [24] R. Pelster, "Dielectric spectroscopy of confinement effects in polar materials," *Physical Review B*, vol. 59, no. 14, pp. 9214–9228, 1999.
- [25] V. M. Shalaev, "Electromagnetic properties of small-particle composites," *Physics Reports*, vol. 272, no. 2-3, pp. 61–137, 1996.
- [26] D. J. Bergman, "The dielectric constant of a composite material—a problem in classical physics," *Physics Reports*, vol. 43, no. 9, pp. 377–407, 1978.
- [27] D. Stoud, G. W. Milton, and B. R. De, "Analytical model for the dielectric response of brine-saturated rocks," *Physical Review B*, vol. 34, no. 8, pp. 5145–5153, 1986.
- [28] A. V. Osipov, K. N. Rozanov, N. A. Simonov, and S. N. Starostenko, "Reconstruction of intrinsic parameters of a composite from the measured frequency dependence of permeability," *Journal of Physics: Condensed Matter*, vol. 14, no. 41, pp. 9507–9523, 2002.
- [29] E. Tuncer, N. Bowler, and I. J. Youngs, "Application of the spectral density function method to a composite system," *Physica B*, vol. 373, no. 2, pp. 306–312, 2006.
- [30] C. Pecharromán and F. J. Gordillo-Vázquez, "Expansion of the spectral representation function of a composite material in a basis of legendre polynomials: experimental determination and analytic approximations," *Physical Review B*, vol. 74, Article ID 035120, 10 pages, 2006.
- [31] B. Hallouet, "Simulationen und experimentelle Untersuchungen der dielektrischen und magnetischen Eigenschaften von Nanokompositen," Diploma thesis, Universität des Saarlandes, Saarbrücken, Germany, 2006.
- [32] R. Pelster, "A novel analytic method for the broadband determination of electromagnetic impedances and material parameters," *IEEE Transactions on Microwave Theory and Techniques*, vol. 43, no. 7, pp. 1494–1501, 1995.
- [33] Agilent Technologies, "Agilent 16454A Magnetic Material Test Fixture Operation and Service Manual," Agilent Part no. 16454-90020, Fifth Edition, July 2001.

-
- [34] J. Kanzow, P. Schulze Horn, M. Kirschmann, et al., "Formation of a metal/epoxy resin interface," *Applied Surface Science*, vol. 239, no. 2, pp. 227–236, 2005.
- [35] S. Havriliak and S. Negami, "A complex plane analysis of alpha-dispersions in some polymer systems," *Journal of Polymer Science Part C*, pp. 14–99, 1966.
- [36] C. J. F. Böttcher and P. Bordewijk, *Theory of Electric Polarization: Dielectrics in Time-Dependent Fields*, vol. 2, Elsevier, Amsterdam, The Netherlands, 1978.
- [37] S. P. Sena, R. A. Lindley, H. J. Blythe, Ch. Sauer, M. Al-Kafarji, and G. A. Gehring, "Investigation of magnetite thin films produced by pulsed laser deposition," *Journal of Magnetism and Magnetic Materials*, vol. 176, no. 2, pp. 111–126, 1997.
- [38] T. J. Lewis, "Interfaces: nanometric dielectrics," *Journal of Physics D*, vol. 38, no. 2, pp. 202–212, 2005.
- [39] T. J. Lewis, "Interfaces are the dominant feature of dielectrics at the nanometric level," *IEEE Transactions on Dielectrics and Electrical Insulation*, vol. 11, no. 5, pp. 739–753, 2004.
- [40] J. K. Nelson and Y. Hu, "Nanocomposite dielectrics—properties and implications," *Journal of Physics D*, vol. 38, no. 2, pp. 213–222, 2005.
- [41] R. Pelster, A. Spanoudaki, and T. Kruse, "Microstructure and effective properties of nanocomposites: ferrofluids as tunable model systems," *Journal of Physics D*, vol. 37, no. 3, pp. 307–317, 2004.
- [42] V. B. Bregar, "Effective-medium approach to the magnetic susceptibility of composites with ferromagnetic inclusions," *Physical Review B*, vol. 71, no. 17, Article ID 174418, 8 pages, 2005.

Review Article

Dielectric Polarization and Particle Shape Effects

Ari Sihvola

Electromagnetics Laboratory, Helsinki University of Technology, P.O. Box 3000, 02015 TKK, Finland

Received 15 February 2007; Revised 30 April 2007; Accepted 30 May 2007

Recommended by Christian Brosseau

This article reviews polarizability properties of particles and clusters. Especially the effect of surface geometry is given attention. The important parameter of normalized dipolarizability is studied as function of the permittivity and the shape of the surface of the particle. For nonsymmetric particles, the quantity under interest is the average of the three polarizability dyadic eigenvalues. The normalized polarizability, although different for different shapes, has certain universal characteristics independent of the inclusion form. The canonical shapes (sphere, spheroids, ellipsoids, regular polyhedra, circular cylinder, semisphere, double sphere) are studied as well as the correlation of surface parameters with salient polarizability properties. These geometrical and surface parameters are essential in the material modeling problems in the nanoscale.

Copyright © 2007 Ari Sihvola. This is an open access article distributed under the Creative Commons Attribution License, which permits unrestricted use, distribution, and reproduction in any medium, provided the original work is properly cited.

1. INTRODUCTION

The engineering strive towards always smaller scales in the structure of matter is obvious even to people who are not working in the field of materials science. The sole terminology and use of words in popularization of technological progress may lead us to think that microelectronics is somewhat old-fashioned; nanotechnology is the theme of tomorrow if not yet today. Progress is indeed great. If measured in the exact meaning of prefixes, it is thousandfold.

This trend of looking in smaller details happens on several fronts. Scientists want to understand the structure of matter in nanoscales, engineers wish to control structures with always sharper technological tools, research program plans dream of the multiplied possibilities of material responses that this tailoring can provide, and the public expects new and unseen applications of technology along with the increased degrees of freedom.

What does the penetration of technology into smaller scales mean in terms of materials modeling? In particular, how does it affect the analysis of the electromagnetic properties of composites? The modeling of the effective properties of heterogeneous materials requires knowledge about the properties of the constituent materials and about the geometrical arrangements how these phases together compose the continuum. Classical homogenization approaches are based on a quasistatic principle. In other words, the electromagnetic field solutions are calculated using Laplace's and

Poisson's equations instead of the full Maxwell's equations. This means that the response of an individual scatterer is instantaneous. No retardation effects are needed over the size of the scatterer.

If the modeling is hence based on the assumption that the reaction of a single inclusion is like in statics and its size is considerably smaller than the wavelength of the operating electromagnetic field, the road towards smaller scales of the individual scatterers would not cause any additional problems. On the contrary, for a given electromagnetic excitation, the locally quasistatic assumption becomes more and more acceptable.

How, then, does the nanoscale modeling of heterogeneous materials differ from that of microscale or mesoscale? Certainly, many of the applied principles remain the same. And the science of materials modeling has provided us very detailed theories to predict the macroscopic dielectric characteristics of media (for a comprehensive historical review of these theories, see [1]). This is because the governing laws of electromagnetics are valid over a broad range of spatial and temporal scales. Of course, there is a limit since matter is not infinitely divisible. In the "very small nanoscale," the inclusions are clusters in which the macroscopic response is partially determined by discreteness of the building block atoms. For example, quantum confinement may affect band gap sizes in semiconductors and lasers. But in this article we are not yet manipulating individual atoms and do not take into account the granularity of matter. Let us concentrate on

such nanoscale environments where a typical object would be measured in tens of nanometers. This is much larger than the atomic dimensions which are of the order of angstroms (10^{-10} meters). The classic expression from 1959 by Richard P. Feynman, “*there’s plenty of room at the bottom,*” is astonishingly still valid in the era of nanotechnology [2].

But there is another view at the effect of scaling. Not all remain the same when the amplification in our microscope is increased and we are dealing with objects of smaller dimension. A sphere remains a sphere, be it small or large, but some of its characteristic parameters change relative to each other, even if we now neglect the discreteness that ultimately has to be faced when moving to molecular scales. Also in the continuum treatment, the specific surface area of the sphere (or of any other reasonable object for that matter) increases in direct proportion to the scale decrease: the area of the sphere surface divided by the sphere volume is inversely proportional to the radius. Then it is to be expected that the surface effects start to dominate when we are moving from the ordinary-sized material textures into the smaller-scale structures. The increased focus on surfaces of individual scatterers also means that in the modeling of composites and other heterogeneous materials composed of these type of inclusions, the interaction effects between neighboring scatterers need more attention than in connection to larger-scale modeling. Interaction forces are not scale-independent. At the same time as the surface area relative to the volume for a given particle increases, its surface-area-to-weight ratio increases with a similar pace.

In this article, the basic materials modeling questions are discussed in connection to the dielectric properties of matter. Because of the generality of the electric modeling results, many of the results are, *mutatis mutandis*, directly applicable to certain other fields of science, like magnetic, thermal, and even (at least analogously) mechanical responses of matter. In the chapters to follow, special emphasis is given to the manner how geometric and surface characteristics affect the response of clusters. Many of the results to be presented have been published in my previous special articles that concern the dielectric response of particles of various shapes. This review connects those results and discusses the surface-geometrical parameters of various particle polarizabilities that are of importance in the modeling of material effects in the nanoscale.

2. ELECTRIC RESPONSE OF A SPHERICAL SCATTERER

Many materials modeling approaches and theories are based on the principle of splitting the analysis into two parts: the whole is seen as composed of a collection of single scatterers whose response is first to be calculated (or if the mixture is composed of many different phases, the responses of all of these phases are needed), and then the global, macroscopic properties have to be computed as certain interactive sums of all the component inclusions.

Let us next focus on the first step in this process: the response of an individual, well-defined inclusion. The quasi-static response parameters of a given object can be gleaned

from the solution of the problem when the object is placed in vacuum and exposed to a uniform static electric field.

The simplest shape is a sphere. And the simplest internal structure is homogeneity. The response of a homogeneous, isotropic, dielectric sphere in a homogeneous, uniform electric field in vacuum is extraordinary simple: it is a dipolar field. And the internal field of the sphere is also uniform, directed along the exciting field and of an amplitude dependent on the permittivity. No higher-order multipoles are excited.

The relations are: the homogeneous internal field \vec{E}_i as a function of the exciting, primary field \vec{E}_e reads [3, 4]

$$\vec{E}_i = \frac{3\epsilon_0}{\epsilon + 2\epsilon_0} \vec{E}_e, \quad (1)$$

where ϵ is the (absolute) permittivity of the spherical object and ϵ_0 the free-space permittivity. Then obviously the polarization density induced within the sphere volume is $(\epsilon - \epsilon_0)\vec{E}_i$ and since the dipole moment of a scatterer is the volume integral of the polarization density (dipole moment density), the dipole moment of this sphere is

$$\vec{p} = (\epsilon - \epsilon_0) \frac{3\epsilon_0}{\epsilon + 2\epsilon_0} \vec{E}_e V, \quad (2)$$

where V is the volume of the sphere. And from this relation follows the polarizability of the sphere α , which is defined as the relation between the dipole moment and the incident field ($\vec{p} = \alpha\vec{E}_e$):

$$\alpha = 3\epsilon_0 V \frac{\epsilon - \epsilon_0}{\epsilon + 2\epsilon_0}. \quad (3)$$

This polarizability is an extremely important characteristic quantity in modeling of dielectric materials. It is true that polarizability does not tell the whole story about the response of a scatterer. In case of inclusion, shapes other than spherical,¹ also quadrupolic, octopolic, and even higher-order multipoles are created (and in the case of dynamic fields, the list of multiple moments is much longer, see [5] for a concise treatment of these). Perhaps a more accurate name for the polarizability we are now discussing would be dipolarizability.

Why is this (di)polarizability so essential? In other words, what makes the dipole moment so distinct from the other multipole moments? Part of the answer is that the effect of the multipoles on the surroundings decreases with the distance in an inverse power. And the higher is the power, the higher is the order of the multipole. Therefore, the greatest far-field effect is that of the lowest multipole. Dipole is the lowest-order multipole except monopole. And monopole is not counted since a monopole requires net charge, and we are here dealing with neutral pieces of matter which have equal amounts of positive and negative charges.

¹ And in the spherical case, too, when the exciting electric field is nonuniform, the perturbational field is not purely dipolar.

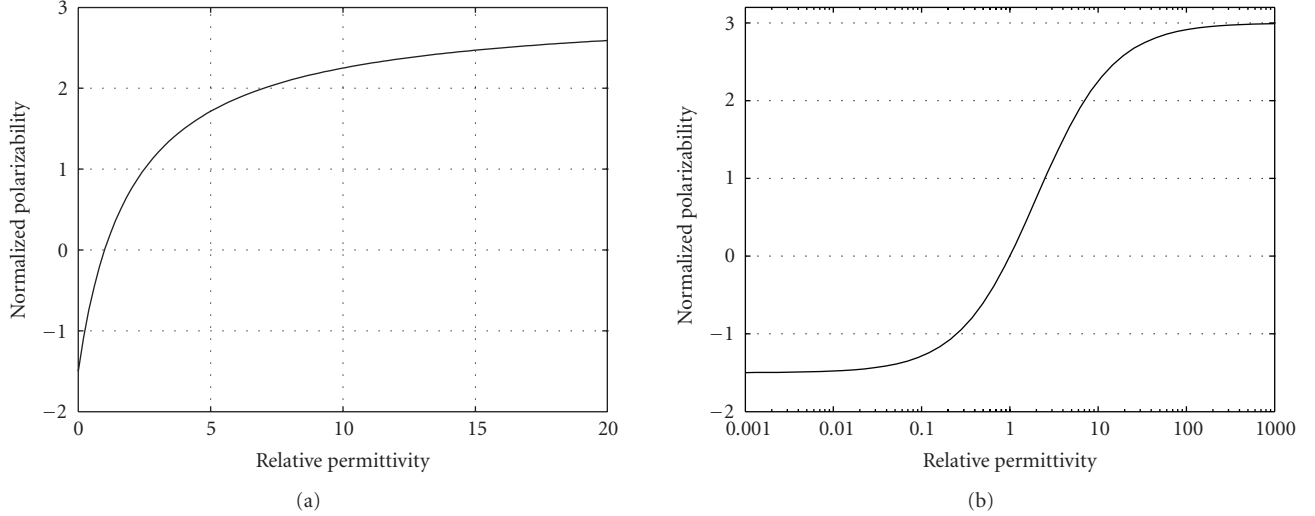


FIGURE 1: The polarizability of a dielectric sphere for positive values of the relative permittivity, with linear and logarithmic scales. Note the negative values for the polarizability for permittivities less than that of free space. The symmetry of the polarizability behavior in the two limits (high-permittivity, or “conducting” and zero-permittivity, or “insulating”) can be seen from the right-hand side curve.

Therefore, let us concentrate on the (di)polarizability α . As can be seen from (3), there is a trivial dependence of the polarizability on the volume. Obviously, the bigger the volume of the inclusions is, the larger its electrical response is. A more characteristic quantity would be a normalized polarizability α_n , which for the sphere reads

$$\alpha_n = \frac{\alpha}{\epsilon_0 V} = 3 \frac{\epsilon_r - 1}{\epsilon_r + 2}, \quad (4)$$

where the dimensionless quality of this quantity is guaranteed by the division with the free-space permittivity ϵ_0 . Note also the use of the relative permittivity of the sphere $\epsilon_r = \epsilon/\epsilon_0$.

Here is the response of matter stripped to the very essentials. It is a response quantity of the most basic three-dimensional geometrical object with one single material parameter, permittivity. And still, this response function is by no means trivial. Some of the properties of this function are very universal as we will see later.

Figure 1 displays the polarizability behavior of a dielectric sphere for positive permittivity values. The obvious limits are seen: the saturation of the normalized polarizability to the value 3 for large permittivities and to the value $-3/2$ for the zero-permittivity.

But it is not unfair to note that the polarizability function in Figure 1 seems rather monotonous and dull. However, if the permittivity is freed from the conventional limits within the domain of positive values, very interesting phenomena can be observed. To display this, Figure 2 is produced.

In Figure 2, one phenomenon overrides all other polarizability characteristics: the singularity of the function for the permittivity value $\epsilon_r = -2$, directly appreciated from (4). This is the electrostatic resonance that goes in the literature under several names, depending on the background of the authors, which can be electromagnetics, microwave engi-

neering, optics, or materials science. This is the surface plasmon or Fröhlich resonance [6].

However, the present article does not concentrate on negative-permittivity materials. Metamaterials [7] form a large class of media that embrace such negative-permittivity media and metamaterials in fact are very much in the focus of today’s research [8, 9]. In the following, let us restrict ourselves to positive permittivity values. Interesting results can be extracted about the material response also within this regime.

Let us collect some of these basic observations that are most clearly seen from the formula for the polarizability of the sphere (4), but also valid for other dielectric objects in the three-dimensionally averaged sense [10]. The normalized polarizability $\alpha(\epsilon_r)$, for the permittivity value $\epsilon_r = 1$, satisfies the following:

- (i) $\alpha = 0$ at $\epsilon_r = 1$,
- (ii) $\partial\alpha/\partial\epsilon_r = 1$ at $\epsilon_r = 1$,
- (iii) $\partial^2\alpha/\partial\epsilon_r^2 = -2/3$ at $\epsilon_r = 1$.

Indeed, the polarizability is a quite powerful tool in analyzing the dielectric response of single scatterers but also the response of dielectric mixtures as a whole. The classical homogenization principles starting from Garnett [11], following through Bruggeman [12], over to the modern refined theories take careful respect to the polarizabilities of the inclusions that make up the mixture they are modeling.

Let us next allow the geometry of the inclusion deviate from the basic spherical shape.

3. ELLIPSOIDS AND NONSYMMETRY

To gather more information about how the microgeometry and the specific surface area have effect on the material response of dielectric scatterers, let us allow the spherical

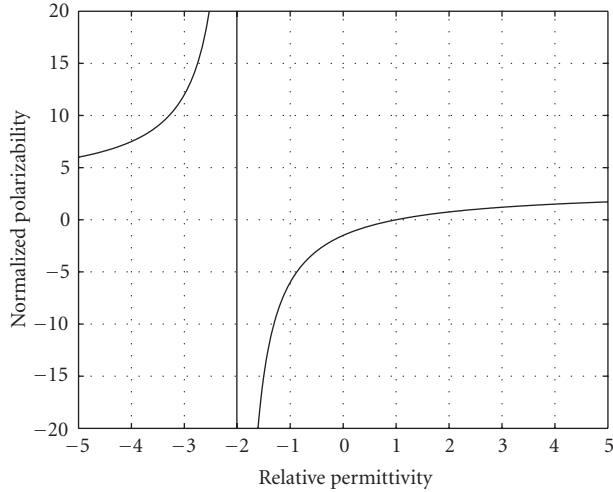


FIGURE 2: The polarizability of a dielectric sphere when the permittivity is allowed to be negative as well as positive.

form to be changed to ellipsoid. Ellipsoids are easy geometries since the dipole moment of such shaped homogeneous objects can be written in a closed form, which is a consequence of the fact that the internal field of a homogeneous ellipsoid in a constant electric field is also constant.² The amplitude of this field is naturally linear to the external field, but there also exists a straightforward dependence of this field on the permittivity of the ellipsoid and of a particular shape parameter, so-called depolarization factor.

Let the semiaxes of the ellipsoid in the three orthogonal directions be a_x, a_y, a_z . Then the internal field of the ellipsoid (with permittivity ϵ), given that the external, primary field \vec{E}_e be x -directed, is (a generalization of (1))

$$\vec{E}_i = \frac{\epsilon_0}{\epsilon_0 + N_x(\epsilon - \epsilon_0)} \vec{E}_e, \quad (5)$$

where N_x is the depolarization factor of the ellipsoid in the x direction, and can be calculated from

$$N_x = \frac{a_x a_y a_z}{2} \int_0^\infty \frac{ds}{(s + a_x^2) \sqrt{(s + a_x^2)(s + a_y^2)(s + a_z^2)}}. \quad (6)$$

For the other depolarization factor N_y (N_z), interchange a_y and a_x (a_z and a_x) in the above integral.³

The three depolarization factors for any ellipsoid satisfy

$$N_x + N_y + N_z = 1. \quad (7)$$

² Note, however, that the field *external* to the ellipsoid is no longer purely dipolar. In the vicinity of the boundary, there are multipolar disturbances whose amplitudes depend on the eccentricity of the ellipsoid.

³ A Java applet to calculate the depolarization factors and polarizability components of an arbitrary ellipsoid is located in the URL address of the Helsinki University of Technology <http://users.tkk.fi/~mpitkone/Ellipsoid/Ellipsoidi.html>

A sphere has three equal depolarization factors of $1/3$. For prolate and oblate spheroids (ellipsoids of revolution), closed-form expressions can be written for the depolarization factors [4, 13]. The limiting cases of spheroids are disk (depolarization factors $(0, 0, 1)$) and a needle (depolarization factors $(1/2, 1/2, 0)$).

From the field relation (5), the normalized polarizability components follow. In this case where the spherical symmetry is broken, the polarizabilities are different for different directions. In the x -direction, the polarizability component reads

$$\alpha_{n,x} = \frac{\epsilon_r - 1}{1 + N_x(\epsilon_r - 1)} \quad (8)$$

and the corresponding expressions for the y - and z -components are obvious. This relation allows quite strong deviations from the polarizability of the spherical shape. For a simple example, consider the limits of very large or very small permittivities. These read

- (i) $\alpha_{n,x} = 1/N_x$, for $\epsilon_r \rightarrow \infty$,
- (ii) $\alpha_{n,x} = -1/(1 - N_x)$, for $\epsilon_r \rightarrow 0$.

And obviously these may possess wild limits when the depolarization factors have the allowed ranges $0 \leq N_i \leq 1$ for any of the three components $i = x, y, z$. This hints to the possibilities that with extremely squeezed ellipsoids one might be able to create strong macroscopic effective responses, at least if the field direction is aligned with all the ellipsoids in the mixture.

In addition to the view at the special polarization properties of a mixture composed of aligned ellipsoids, the isotropic case is also very important. An isotropic mixture can be generated from nonsymmetric elements (like ellipsoids) by mixing them in random orientations in a neutral background. Then the average response of one ellipsoid is a third of the sum of its three polarizability components:

$$\alpha_{n,ave} = \frac{1}{3} \sum_{i=x,y,z} \frac{\epsilon_r - 1}{1 + N_i(\epsilon_r - 1)}. \quad (9)$$

The effect of the eccentricity (nonsphericity) of the ellipsoid is visible from Figure 3 where the average polarizability is plotted against the permittivity for different ellipsoids.

4. ARBITRARY SHAPE OF THE INCLUSION

If the inclusion has a shape other than the ellipsoid, the electrostatic solution of the particle in the external field does not have a closed-form solution. Fortunately, for such cases, very efficient computational approaches have been developed. With various finite-element and difference-method principles, many electrostatics and even electromagnetic problems can be solved with almost any desired accuracy (see, e.g., [14, 15]).

Then also the polarizabilities of these arbitrarily shaped particles can be found. For an arbitrary object, there are now new geometrical parameters that define the inclusion and which affect the polarizability, in addition with the permittivity. One of the interesting questions in connection with

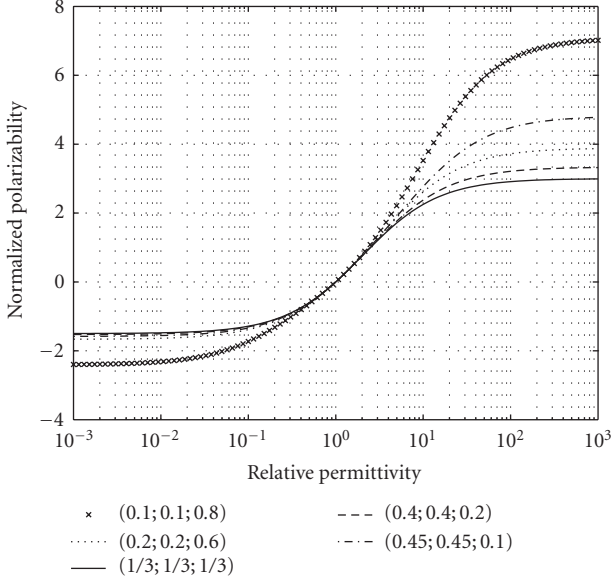


FIGURE 3: The average polarizability of a dielectric ellipsoid (one-third of the normalized polarizabilities in the three orthogonal directions) for various depolarization factor triplets.

nanostructures is how the specific geometrical and surface parameters correlate with the amplitude of the polarizability. A systematic study into this problem would require the numerical electrostatic analysis of very many different scatterer shapes. And again for those shapes that are nonsymmetric⁴, one needs to distill the trace (or the average of the components) of the polarizability dyadic, which in the end would be a fair quantity to compare with the canonical shapes.

Let us review some of the important shapes for which there does not exist a closed-form solution of the Laplace equation, or such one only exists in a form of infinite series. The parameter that tells the essentials about the response is the normalized polarizability. In the normalized form, the linear dependence on the volume of the inclusion is taken away, and the effect of geometry is mixed with the effect of permittivity.

4.1. Platonic polyhedra

Perhaps the most symmetric three-dimensional shapes after sphere are the five regular polyhedra: tetrahedron, hexahedron (cube), octahedron, dodecahedron, and icosahedron. They share with the sphere the following property: the polarizability dyadic is a multiple of the unit dyadic. In other words, the three eigenvalues of polarizability are equal. One single parameter is sufficient to describe the dipole moment

response. Of course, higher-order multipolarizabilities are also present in increasing magnitudes as the sharpness of the corners of the polyhedra increases.

The dielectric response of these regular Platonic objects have been solved with a boundary-integral-equation principle [16]. An integral equation for the potential is solved with method of moments [17] which consequently allows many characteristic properties of the scatterer to be computed. Among them, the polarizabilities of the five Platonic polyhedra have been enumerated with a very good accuracy. Also regression formulas turned out to predict the polarizabilities correct to at least four digits. These have been given in the form [16]

$$\alpha_n = \alpha_\infty (\epsilon_r - 1) \frac{\epsilon_r^3 + p_2 \epsilon_r^2 + p_1 \epsilon_r - \alpha_0}{\epsilon_r^4 + q_3 \epsilon_r^3 + q_2 \epsilon_r^2 + q_1 \epsilon_r + \alpha_\infty}, \quad (10)$$

where p_1, p_2, q_1, q_2, q_3 are numerical parameters, and α_∞ and α_0 are the computationally determined polarizability values for $\epsilon_r \rightarrow \infty$ and $\epsilon_r \rightarrow 0$, respectively. Of course, these parameters are different for all five polyhedra. At the special point $\epsilon_r = 1$, the conditions $\alpha_n = 0, \alpha'_n = 1, \alpha''_n = -2/3$ are satisfied for all five cases. See also [10] for the connection of the derivatives of the polarizability with the virial coefficients of the effective conductivity of dispersions and the classic study by Brown [18] on the effect of particle geometry on the coefficients.

Figure 4 shows the polarizabilities of the various shapes as functions of the permittivity.⁵ From these results it can be observed that the dielectric response is stronger than that of the sphere, and the response seems to be stronger for shapes with fewer faces (tetrahedron, cube) and sharper corners, which is intuitively to be expected. Sharp corners bring about field concentrations which consequently lead to larger polarization densities and to a larger dipole moment.

4.2. Circular cylinder

Another basic geometry is the circular cylinder. This shape is more difficult to analyze exhaustively for the reason that it is not isotropic. The response is dependent on the direction of the electric field. The two eigendirections are the axial direction and the transversal direction (which is degenerate as in the transverse plane, no special axis breaks the symmetry). Furthermore, the description of the full geometry of the object requires one geometrical parameter (the length-to-diameter ratio) which means that the two polarizability functions are dependent on this value and the dipolarizability response of this object is a set of two families of curves depending on the permittivity.

With a computational approach, the polarizabilities of circular cylinders of varying lengths and permittivities have

⁴ Nonsymmetric in the sense that the polarizability operator has three distinct eigenvectors; perhaps it is not proper to call such scatterers anisotropic because anisotropy is commonly associated with the direction dependence of the bulk material response.

⁵ A Java-applet to calculate the depolarization factors and polarizability components of Platonic polyhedra is located in the URL address of the Helsinki University of Technology
<http://www.tkk.fi/Yksikot/Sahkomagnetikka/kurssit/animaatiot/Polarisaatio.html>

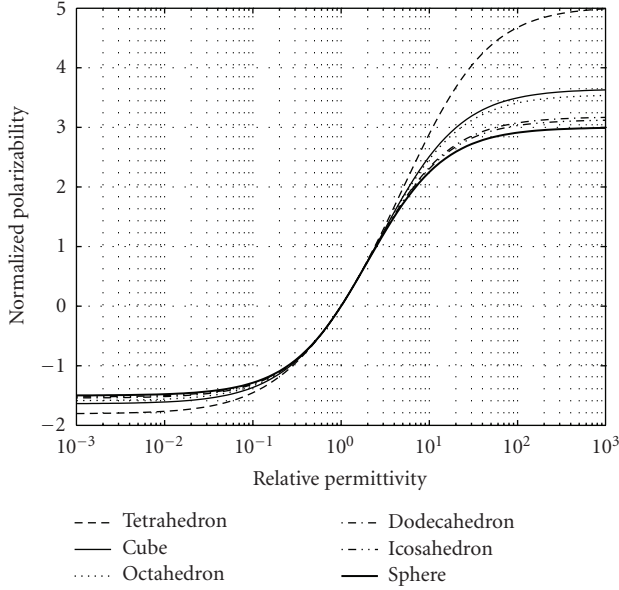


FIGURE 4: The polarizabilities of Platonic polyhedra and sphere. Note that the curve for sphere is always smallest in magnitude, and the order of increase is icosahedron, dodecahedron, octahedron, hexahedron, and tetrahedron (which has the highest curve).

been computed [19]. Again, approximative formulas give a practical algorithm to calculate the values of the polarizabilities. In [19], these formulas are given as differences to the polarizabilities of spheroids with the same length-to-width ratio as that of the cylinder under study. Spheroids are easy to calculate with exact formulas (8). Since they come close to cylinders in shape when the ratio is very large or very small, probably their electric response is also similar, and the differences vanish in the limits. Obviously, the field singularities of the wedges in the top and bottom faces of the cylinder cause the main deviation of the response from that of the spheroid. Note also [20] and the early work on the cylinder problem in the U.S. National Bureau of Standards (see references in [15]).

An illustrative example is the case of “unit cylinder.” A unit cylinder has the height equal to the diameter [21]. Its polarizability components are shown in Figure 5. There, one can observe that its effect is stronger than that of sphere (with equal volume), but not as high as that of a cube.

4.3. Semisphere

A dielectrically homogeneous semisphere (a sphere cut in half gives two semispheres) is also a canonical shape. However, the electrostatic problem where two dielectrically homogeneous domains are separated by semispherical boundaries lead to infinite series with Legendre functions. The polarizability of the semisphere cannot be written in a closed form. However, by truncating the series and inverting the associated matrix, accurate estimates for the polarizability can be enumerated [22]. This requires matrix sizes of a couple of hundred rows and columns. Furthermore, a semisphere as

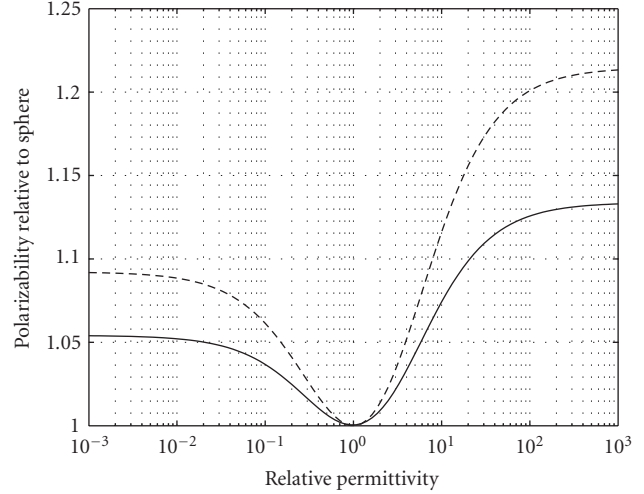


FIGURE 5: A comparison of the polarizability of a unit cylinder and cube. The unit cylinder has different response to axial and transversal excitations; here one-third of the trace of the polarizability is taken. Both curves are relative to a sphere with the corresponding volume and permittivity.

a rotationally symmetric object has to be described by two independent polarizability components. However, it is more “fundamental” than cylinder because no additional geometrical parameter is needed to describe its shape.

The axial (z) and transversal (t) polarizability curves for the semisphere resemble those for the other shapes. The limiting values for low and high permittivities are the following:

$$\begin{aligned} \alpha_{n,z} &\approx 2.1894, & \alpha_{n,t} &\approx 4.4303, & (\epsilon_r \rightarrow \infty) \\ \alpha_{n,z} &\approx -2.2152, & \alpha_{n,t} &\approx -1.3685, & (\epsilon_r \rightarrow 0). \end{aligned} \quad (11)$$

Note here the larger high-permittivity polarizability in the transversal direction compared to the longitudinal, which is explained by the elongated character in the transversal plane of the semisphere. However, in the $\epsilon_r = 0$ limit, the situation is the opposite: a larger polarizability for the axial case (larger in absolute value, as the polarizability is negative).

4.4. Double sphere

A very important object especially in the modeling of random nanomaterials is a doublet of spheres. A sphere is a common, equilibrium shape. And when a sphere in a mixture gets into the vicinity of another sphere, especially in the small scales the interaction forces may be very strong, and the doublet of spheres can be seen as a single polarizing object. Even more, two spheres can become so closely in contact that they merge and metamorphose into a cluster. Such a doublet can be described with one geometrical parameter: the distance between the center points of the spheres divided by their radius. The value 2 for this parameter divides the range into

the two cases whether the doublet is clustered or separate. Again, this object is rotationally symmetric and needs to be described by two polarizabilities, axial and transversal.

A solution of the electrostatic problem with double-sphere boundary conditions is not easy. It requires either a numerical approach or a very complicated analysis using toroidal coordinate system. Several partial results have been presented for the problem [23–25], but only recently a full solution for this problem [26] and its generalization [27] have appeared.

In both limiting cases of the double sphere (the distance of the center points of the spheres goes either to zero or very large), both of the normalized polarizability components of the double sphere approach the sphere value (4). And obviously, it deviates from the sphere value to a largest degree when the distance between the centers is around two radii (the distance for maximum deviation depends on the permittivity of the spheres). For the case of ϵ_r approaching infinity, the case of touching spheres has the following analytical properties [25, 28]:

$$\alpha_{n,z} = 6\zeta(3) \approx 7.212; \quad \alpha_{n,t} = \frac{9}{4}\zeta(3) \approx 2.705 \quad (12)$$

with the Riemann Zeta function. Here the axial polarizability (z) is for the case that the electric field excitation is parallel to the line connecting the center points of the two spheres, and if the field is perpendicular to it, the transversal (t) polarizability applies.

5. CORRELATION OF THE POLARIZABILITY WITH SURFACE PARAMETERS

From the polarizability results in the previous section for various shapes of inclusions, it is obvious that in the polarizability characteristics, sphere is a minimum geometry. In other words, with a given amount of dielectric material, in a spherical form it creates the smallest dipole moment, and every deviation from this shape increases its polarizability.⁶ Also theoretical results to prove this have appeared in the literature [28, 29]. But how does the deviation of the dielectric response from that of sphere depend on the geometrical difference between the object and sphere? This is a difficult question to answer because there are infinite number of ways how the shape of a spherical object can begin to differ from that perfect form.

But intuitively it seems reasonable that all information about the geometrical and surface details of various properties of object is encoded the polarizability curves. However, on the other hand, from a look at the curves for various objects, one might expect that the curves contain also very much redundant information. After all, they resemble

TABLE 1: Characteristic figures for the polarizability of Platonic polyhedra and sphere. Note the third derivative of α_n at $\epsilon_r = 1$; the first and second derivatives are equal for all objects.

	$\alpha_n(\epsilon_r = \infty)$	$\alpha_n(\epsilon_r = 0)$	$\alpha'_n(\epsilon_r = 0)$	$\alpha'''_n(\epsilon_r = 1)$
Tetrahedron	5.0285	-1.8063	4.1693	0.98406
Cube	3.6442	-1.6383	3.0299	0.82527
Octahedron	3.5507	-1.5871	2.7035	0.78410
Dodecahedron	3.1779	-1.5422	2.4704	0.71984
Icosahedron	3.1304	-1.5236	2.3659	0.70087
Sphere	3	-1.5	2.25	0.66667

each other very much in their global form. As was pointed out earlier, the polarizabilities of all isotropic scatterers seem to have equal values, and also equal-valued first and second derivatives at $\epsilon_r = 1$. Table 1 shows the values of the limiting polarizabilities and the derivative at $\epsilon_r = 0$ and the third derivative at $\epsilon_r = 1$ for the five polyhedra and sphere.

The results in Table 1 show also that the numerical correlations between the values of the third derivate and the limiting values at low and high permittivities are very high (of the order of 0.98 and more). Therefore, one could expect that it is possible to compress very much of the polarizability characteristics into a few characteristic numbers.

Article [30] contains a systematic study of comparing the amplitudes of the polarizabilities to certain well-defined geometrical properties of the deformed objects. For regular polyhedra, the following characteristics tell something about the object: number of faces, edges, vertices, solid angle subtended by the corners, specific surface area, and radii of the circumscribed and inscribed spheres. These have been correlated against the electrical polarizability parameters with interesting observations, among which the following is not unexpected: the polarizability of a perfect electric conductor ($\epsilon_r \rightarrow \infty$) polyhedron correlates strongly with the inverse of the solid angle of the vertex. On the other hand, the strongest correlation of the polarizability of “perfectly insulating sphere” (in other words the case $\epsilon_r = 0$) is with the normalized inscribed radius of the polyhedron.

6. DISCUSSION

A detailed knowledge of the polarizability of inclusions with basic shapes gives valuable information about the way such building blocks contribute to the effective dielectric parameters of a continuum. Many models for the macroscopic properties of matter replace the effect of the particles in the medium fully by its polarizability. It is to be admitted that for complex scatterers, this is only a part of the whole response which also contains near-field terms due to higher-order multipoles that is characterized by stronger spatial field variation close to the scatterer. Nevertheless, dipolarizability remains the dominant term in the characteristics of the inclusion.

⁶ Here polarizability has to be understood in the average three-dimensional sense. Of course, some of the polarizability components of an ellipsoid may be smaller than that of the sphere of the same permittivity and volume; however, the remaining components are so much larger that the average will override the sphere value.

The shortcoming of the direct scaling of the macroscopic polarization results down to nanoscale is that the results discussed in this paper are based on quasistatic analysis and are therefore scale-independent. The modeling principles make use of the normalized polarizabilities of particles (like (4)). This remains constant even if we decrease the size of the particle. On the other hand, the specific surface area of an inclusion increases without limit when its size becomes small. Surface effects dominate in the nanoscale. Clusters more complex than the fairly basic shapes discussed in this paper are formed.

Of course, the translation of continuum models (like this analysis of basic shapes and their responses) into smaller scales is problematic also in another respect. Even if we are not yet in the molecular and atomic level in the length scales, this nanoregion is the intermediate area between bulk matter and discrete atoms. One cannot enter into very small scales without the need of quantum physical description. This deviation from the classical physics description is hiding behind the corner and we have to remember that exact geometrical shapes start to lose meaning in the deeper domains of nanoscale. Another issue to be connected to the manner how well the shapes remind of those familiar from continuum three-dimensional world, is whether the nanoclusters are built from exact ordered crystal structure or more amorphous-like aggregates. One could expect that in the latter case the “softer” forms (spheres and ellipsoids) would be more correct approximations to reality. And because the classical mixing rules very often rely on assumptions of such scatterer shapes, we might expect that homogenization and effective medium theories have their place also in materials modeling in the nanoscale.

REFERENCES

- [1] C. Brosseau, “Modelling and simulation of dielectric heterostructures: a physical survey from an historical perspective,” *Journal of Physics D*, vol. 39, no. 7, pp. 1277–1294, 2006.
- [2] The transcript of Richard P. Feynman’s talk *There’s plenty of room at the bottom* at the annual meeting of the American Physical Society on December 29, 1959, is a classic reference in nanoscience, February 2007, <http://www.zyvex.com/nanotech/feynman.html>.
- [3] J. D. Jackson, *Classical Electrodynamics*, John Wiley & Sons, New York, NY, USA, 3rd edition, 1999.
- [4] A. Sihvola, *Electromagnetic Mixing Formulas and Applications*, IEE Publishing, London, UK, 1999.
- [5] R. E. Raab and O. L. de Lange, *Multipole Theory in Electromagnetism: Classical, Quantum, and Symmetry Aspects, with Applications*, Clarendon Press, Oxford, UK, 2005.
- [6] C. F. Bohren and D. R. Huffman, *Absorption and Scattering of Light by Small Particles*, John Wiley & Sons, New York, NY, USA, 1983.
- [7] A. Sihvola, “Electromagnetic emergence in metamaterials,” in *Advances in Electromagnetics of Complex Media and Metamaterials*, S. Zouhdi, A. Sihvola, and M. Arsalane, Eds., vol. 89 of *NATO Science Series: II: Mathematics, Physics, and Chemistry*, pp. 1–17, Kluwer Academic Publishers, Dordrecht, The Netherlands, 2003.
- [8] December 2006, <http://www.metamorphose-eu.org>.
- [9] DARPA stands for the *Defense Advanced Research Projects Agency* and is the central research and development organization for the U.S. Department of Defense (DoD), December 2006, <http://www.darpa.mil/dso/thrust/matdev/metamat.htm>.
- [10] E. J. Garboczi and J. F. Douglas, “Intrinsic conductivity of objects having arbitrary shape and conductivity,” *Physical Review E*, vol. 53, no. 6, pp. 6169–6180, 1996.
- [11] J. C. M. Garnett, “Colours in metal glasses and in metallic films,” *Philosophical Transactions of the Royal Society of London*, vol. 203, pp. 385–420, 1904.
- [12] D. A. G. Bruggeman, “Berechnung verschiedener physikalischer Konstanten von heterogenen Substanzen. I. Dielektrizitätskonstanten und Leitfähigkeiten der Mischkörper aus isotropen Substanzen,” *Annalen der Physik*, vol. 416, no. 7, pp. 636–664, 1935.
- [13] L. D. Landau and E. M. Lifshitz, *Electrodynamics of Continuous Media*, Pergamon Press, Oxford, UK, 2nd edition, 1984.
- [14] A. Mejdoubi and C. Brosseau, “Finite-element simulation of the depolarization factor of arbitrarily shaped inclusions,” *Physical Review E*, vol. 74, no. 3, Article ID 031405, 13 pages, 2006.
- [15] M. L. Mansfield, J. F. Douglas, and E. J. Garboczi, “Intrinsic viscosity and the electrical polarizability of arbitrarily shaped objects,” *Physical Review E*, vol. 64, no. 6, Article ID 061401, 16 pages, 2001.
- [16] A. Sihvola, P. Ylä-Oijala, S. Järvenpää, and J. Avelin, “Polarizabilities of platonic solids,” *IEEE Transactions on Antennas and Propagation*, vol. 52, no. 9, pp. 2226–2233, 2004.
- [17] S. Järvenpää, M. Taskinen, and P. Ylä-Oijala, “Singularity extraction technique for integral equation methods with higher order basis functions on plane triangles and tetrahedra,” *International Journal for Numerical Methods in Engineering*, vol. 58, no. 8, pp. 1149–1165, 2003.
- [18] W. F. Brown, “Solid mixture permittivities,” *The Journal of Chemical Physics*, vol. 23, no. 8, pp. 1514–1517, 1955.
- [19] J. Venermo and A. Sihvola, “Dielectric polarizability of circular cylinder,” *Journal of Electrostatics*, vol. 63, no. 2, pp. 101–117, 2005.
- [20] M. Fixman, “Variational method for classical polarizabilities,” *The Journal of Chemical Physics*, vol. 75, no. 8, pp. 4040–4047, 1981.
- [21] A. Sihvola, J. Venermo, and P. Ylä-Oijala, “Dielectric response of matter with cubic, circular-cylindrical, and spherical microstructure,” *Microwave and Optical Technology Letters*, vol. 41, no. 4, pp. 245–248, 2004.
- [22] H. Kettunen, H. Wallén, and A. Sihvola, “Polarizability of a dielectric hemisphere,” Tech. Rep. 482, Electromagnetics Laboratory, Helsinki University of Technology, Espoo, Finland, February 2007.
- [23] B. U. Felderhof and D. Palaniappan, “Longitudinal and transverse polarizability of the conducting double sphere,” *Journal of Applied Physics*, vol. 88, no. 9, pp. 4947–4952, 2000.
- [24] L. Poladian, “Long-wavelength absorption in composites,” *Physical Review B*, vol. 44, no. 5, pp. 2092–2107, 1991.
- [25] H. Wallén and A. Sihvola, “Polarizability of conducting sphere-doublets using series of images,” *Journal of Applied Physics*, vol. 96, no. 4, pp. 2330–2335, 2004.
- [26] M. Pitkonen, “Polarizability of the dielectric double-sphere,” *Journal of Mathematical Physics*, vol. 47, no. 10, Article ID 102901, 10 pages, 2006.

-
- [27] M. Pitkonen, "An explicit solution for the electric potential of the asymmetric dielectric double sphere," *Journal of Physics D*, vol. 40, no. 5, pp. 1483–1488, 2007.
- [28] M. Schiffer and G. Szegő, "Virtual mass and polarization," *Transactions of the American Mathematical Society*, vol. 67, no. 1, pp. 130–205, 1949.
- [29] D. S. Jones, "Low frequency electromagnetic radiation," *IMA Journal of Applied Mathematics*, vol. 23, no. 4, pp. 421–447, 1979.
- [30] A. Sihvola, P. Ylä-Oijala, S. Järvenpää, and J. Avelin, "Correlation between the geometrical characteristics and dielectric polarizability of polyhedra," *Applied Computational Electromagnetics Society Journal*, vol. 19, no. 1B, pp. 156–166, 2004.

Research Article

Broadband Ferromagnetic Resonance Measurements in Ni/ZnO and Ni γ -Fe₂O₃ Nanocomposites

Vincent Castel,¹ Jamal Ben Youssef,² and Christian Brosseau^{1,3}

¹Laboratoire d'Electronique et Systèmes de Télécommunications (UMR CNRS 6165), Université de Bretagne Occidentale, CS 93837, 6 avenue Le Gorgeu, 29238 Brest Cedex 3, France

²Laboratoire de Magnétisme de Bretagne (FRE CNRS 2697), Université de Bretagne Occidentale, CS 93837, 6 avenue Le Gorgeu, 29238 Brest Cedex 3, France

³Département de Physique, Université de Bretagne Occidentale, CS 93837, 6 avenue Le Gorgeu, 29238 Brest Cedex 3, France

Received 16 February 2007; Accepted 27 June 2007

Recommended by Donald A. Bansleben

A comparative study at the ambient temperature of the ferromagnetic resonance (FMR) spectra of Ni/ZnO and Ni γ -Fe₂O₃ nanocomposites (NCs) is reported. A microstrip transmission line technique was used to measure the FMR profiles and linewidths in the 8–24 GHz frequency range. The samples were placed at the center of a microstrip line where the derivative of the absorbed power was measured using a standard ac field modulation technique (10 Oe amplitude) and lock-in detection. The analysis of the FMR spectra can be interpreted as arising from aggregates of magnetic nanoparticles, each of which resonates in an effective magnetic field composed of the applied field, the average (magnetostatic) dipolar field, and the randomly oriented magnetic anisotropy field. It is found that frequency and applied magnetic field strongly influence the lineshape of the FMR spectra. Two observations are identified within the FMR spectra. On the one hand, the resonance field increased linearly with frequency as expected from uniform mode theory and yielded a Landé g factor in the range 1.48–2.05. On the other hand, there is no clear correlation between FMR linewidths and frequency. Inhomogeneity-based line-broadening mechanisms, due to the damping of surface/interface effects and interparticle interaction, affect the FMR effective linewidth.

Copyright © 2007 Vincent Castel et al. This is an open access article distributed under the Creative Commons Attribution License, which permits unrestricted use, distribution, and reproduction in any medium, provided the original work is properly cited.

1. INTRODUCTION

The recent emphasis on nanomaterials for various applications related to spintronics [1, 2], magnetic recording media [3], and magneto-optics [4, 5] has generated considerable interest in several magnetic metal-dielectric systems which have previously received very little attention. There are many instances in which we would like to control the microwave properties of nanocomposites (NCs), selecting from more than one possible magnetic component by adjusting for example parameters of exchange interaction between the individual constituents or, the magnetization-polarization coupling in multiferroic oxides through product property [6–10]. The required coupling between polarization and magnetization is difficult but has been achieved in a number of systems [11–14]. Recently, several approaches to reach this “magnetoelectricity” at microwave frequencies have been suggested and experimentally observed [2, 12, 13]. In the sub-100-nm regime, magnetic particles are single domain, that is, the size of the system is smaller than the exchange

correlation length, but the particles eventually form aggregates and apart from the dipolar interaction between the nanoparticles, other types of interactions, for example, intracuster exchange, may also become relevant. The magnetic properties of nanophases are determined both by the behavior of particles and by the spatial distribution of the aggregates which defines the magnetostatic interactions between them. The ability to probe magnetoelectric coupling on the nanoscale in NCs will open a new opportunity to develop novel high-frequency soft magnetic materials and pave the way for advances in nanoelectronics systems. A key feature of these approaches is the use of core-shell structures in which the metal nanograins are insulated by insulating layers, thus the conductivity of the system will be dramatically decreased, leading to a significantly reduced eddy current loss, while the coupling strength between neighboring magnetic aggregates can overcome the anisotropy and demagnetizing effect.

As part of a large effort to quantitatively model the electromagnetic transport properties in nanostructures, we have recently investigated on the microwave properties of NCs

TABLE 1: Selected physical properties of the powders investigated in this study.

Powder	ZnO	γ -Fe ₂ O ₃	Ni
Average particle size ^{(a),(b),(c)}	49 nm	23 nm	35 nm
Powder color	White	Brown	Gray
Specific surface area bet (m ² g ⁻¹)	22	51	15.6
Morphology	Elongated	Nearly spherical, faceted	Spherical
Crystal phase	Wurtzite	Maghemite (cubic spinel)	Fm3m (225) ccp
Density ^(a) (g cm ⁻³)	5.6	5.2	8.9

^(a) From manufacturer product literature.

^(b) Determined from specific surface area.

^(c) Checked by TEM images.

containing Ni, Co, ZnO, and γ -Fe₂O₃ nanoparticles [15–23]. For these epoxy-coated particles, the distance of closest approach between particles is expected to be large enough for the interactions to have mainly a magnetostatic character [20]. Neither widely-used phenomenological models, nor ab initio effective medium theories (EMTs) are entirely successful in describing all experimental findings concerning the electromagnetic behavior of NCs. This is mainly due to the absence of finite-size and surface effects in these modeling approaches; see, for example, [16–20]. More and more evidence, coming from various researchers employing a panoply of techniques, points to the fact that electromagnetic wave transport, polarization, and magnetization mechanisms in NCs differ from those in bulk samples. Theoretical interest is also motivated by the suggestion that surface magnetic interactions and surface disorder can greatly enhance the effective magnetic properties of nanostructures, for example, coercivity as a consequence of the reduced crystal symmetry near the surface originating from the finite size and possible existence of surface disorder [24–28]. In particular, the set of compounds Ni/ γ -Fe₂O₃ and Ni/ZnO have proven fertile to study in order to examine the interplay between magnetic metal and semiconductor oxide as γ -Fe₂O₃ is substituted into the ZnO member [20, 22], which has been seen to occur in a wide variety of granular nanostructures. These nanostructures provide an ideal playground to experimentally investigate some fundamental phenomena connected with interparticle interactions because the specific surface area of γ -Fe₂O₃ nanoparticles is more than three times that of Ni (see Table 1) causing the magnetic boundaries to strongly interact. The controllability in these systems allows a clean study of much complicated physics in a controllable fashion. Indeed, due to the large ratio of surface area to volume in nanosized objects, the behavior of surfaces and interfaces becomes a prominent factor controlling the physical and chemical properties of nanostructured materials. Reasons for this are the confinement of electrons in nanometric dimensions that gives rise to changes in the electronic distribution and thus in the optical, electromagnetic, transport, and so forth, properties and to the surface effects.

A number of experimental techniques are currently being deployed in an effort to understand the dynamic magnetic properties of individual and aggregates of nanoparticles. In this regard, the ferromagnetic resonance (FMR) investigation of magnetic nanomaterials and NCs has received

considerable attention over the years [21, 29–33]. FMR spectra, as observed in microwave spectroscopy, are a direct manifestation of the forces that determine the dynamical properties of magnetic materials [34]. The correct interpretation of FMR fundamentals can lead to an evaluation of the effective ferromagnetic resonance frequency ω_{res} and Gilbert damping coefficient α which describe the details of the gyroscopic precession of the magnetization. However, the satisfactory characterization of the FMR characteristics in granular nanostructures has proved to be a challenge. Clearly, there remain fundamental questions about how the microwave magnetic response under magnetic fields, of granular heterostructures in which the constituents can exhibit product properties, can bring information on the role of intergranular exchange effect. The fundamental questions can be stated more generally as: what is the structure of the FMR line (single Lorentzian or composite lineshape), and what changes are initiated in the FMR line by the choice of the magnetic species, composition, and clustering of nanoparticles? These aspects would be expected to have a profound significance on the observed FMR properties of granular nanostructures. In such experiments, the resonance is probed by sweeping the applied field. The resonance fields provide a measurement of the effective field seen by the uniform precession mode that is excited by a uniform rf field. The effective field, H_{eff} , contains contributions from the external field, the demagnetizing field, the exchange field, the magnetostrictive, and the magnetocrystalline energies. FMR results provide accurate measures of the static properties of magnetic composites, given by anisotropy constants, and the dynamic properties, given by the linewidth ΔH of the resonance which provides information on relaxation processes.

The impetus for this work stems from our recent investigations [21, 23], employing microwave, spin-wave, and magnetic characterizations, of the structure-magnetic permeability and permittivity relationships for granular γ -Fe₂O₃/ZnO NCs. In [21], we found that the FMR linewidth is very sensitive to details of the spatial magnetic inhomogeneities and increases continuously with the volume content of magnetic material. Different mechanisms were considered to explain the FMR linewidth: the intrinsic Gilbert damping, the broadening induced by the magnetic inhomogeneities, and the extrinsic magnetic relaxation. From these measurements, the characteristic intrinsic damping dependent on the selected material and the damping due to surface/interface effects

TABLE 2: Overview of NCs compositions: f_X denotes the volume fraction of the X species, f_p is the porosity of the samples, and f_{resin} is the volume fraction of resin. The uncertainty on f_X is typically of the order of 5%. Compaction pressure for all composites was 10^7 Nm^{-2} for two minutes.

Material designation	f_{Ni}	f_{ZnO}	f_p	f_{resin}	$f_{\gamma\text{-Fe}_2\text{O}_3}$
nNiZ1	0.49	0.08	0.28	0.15	—
nNiZ2	0.42	0.17	0.27	0.14	—
nNiZ3	0.38	0.21	0.26	0.15	—
nNiZ4	0.33	0.26	0.25	0.15	—
nNiZ5	0.29	0.30	0.26	0.15	—
nNiZ6	0.25	0.35	0.25	0.15	—
nNiZ7	0.18	0.44	0.23	0.14	—
nNiZ8	0.09	0.54	0.22	0.15	—
nNiZ9	0	0.63	0.21	0.16	—
1-nNiF	0.08	—	0.26	0.13	0.53
2-nNiF	0.17	—	0.25	0.14	0.44
3-nNiF	0.29	—	0.27	0.12	0.32
4-nNiF	0.50	—	0.26	0.15	0.09
5-nNiF	0.04	—	0.26	0.25	0.55

and interparticle interaction were estimated. More specifically, we found that the inhomogeneous linewidth (damping) due to surface/interface effects decreases with diminishing particle size, whereas the homogeneous linewidth (damping) due to interactions increases with increasing volume fraction of magnetic particles (i.e., reducing the separation between neighboring magnetic phases) in the composite.

With these considerations in mind and following the same experimental methodology in the current report we undertook a careful experimental study of the effective FMR mode's dependence and effective magnetization of granular NCs as a function on applied magnetic field and frequency, and composition. Emphasis is placed upon the understanding of properties such as the positions, linewidths, and shapes of the FMR lines. Another motivation for the present work was to look more closely at the similarity between the spectra of Ni/ $\gamma\text{-Fe}_2\text{O}_3$ and Ni/ZnO NCs to examine if common magnetization properties exist and how these commonalities may relate to the surface anisotropy contribution to the anisotropy of Ni and $\gamma\text{-Fe}_2\text{O}_3$ nanoparticles.

This paper is divided as follows. We first give a brief reprise of the experimental conditions developed in [21], and details of the materials under study. In Section 3, we present the FMR measurements and discuss the experimental results. The discussion focuses on both the frequency and magnetic field dependences of spectroscopic properties. The comparison of these results to similar analysis in $\gamma\text{-Fe}_2\text{O}_3/\text{ZnO}$ NCs is also given. Section 4 concludes the paper and indicates the direction of further developments. Certain details related to the experimental results are relegated in a couple of appendices.

2. EXPERIMENTAL PROCEDURES

2.1. Materials and sample preparation

The samples studied herein were prepared by mixing the fine particules of neat Ni, $\gamma\text{-Fe}_2\text{O}_3$, and ZnO with a stable epoxy resin widely used for low temperature experiments (Scotchcast 265) and purchased from 3M. A series of 14 powdered NC samples with volume fraction of resin in the range 12–25% (see Table 2) were prepared. The nanosized powders were obtained from Nanophase Technologies Corp., Burr Ridge, Ill, USA. The powders were used without further purification. NCs of Ni and $\gamma\text{-Fe}_2\text{O}_3$ with Ni volume fractions spanning $0 \leq f_{\text{Ni}} \leq 0.5$ range were prepared through powder pressing and characterized by conductivity and microwave frequency-domain spectroscopy (complex permittivity and magnetic permeability) [18]. The conductivity measurements indicate that the sample size is always below the skin depth for the entire range of frequencies considered (see Appendix A). Materials with nonzero conductivity display eddy (surface) current losses in addition to the FMR losses. Eddy currents shield the magnetic field from penetrating into the particles. However, following the experimental results and the discussion presented in [18], we expect eddy current contribution to the losses to be negligible. The comparison with repeated measurements and fabrication protocols for these NCs gave a possible systematic error in our volume fraction of phases of no more than 5%. The detailed fabrication procedure to achieve homogeneous composition of the samples has been already described in [16–19]. The morphology and size of the starting powders were determined by transmission electron microscopy (TEM). The purity of the phases was checked by X-ray powder diffraction (XRD) and

the crystallite sizes were determined from the line broadening of the reflections using the Scherrer formulas. The grain sizes determined from analysis of bright field cross-sectional TEM images are consistent with the ones obtained from XRD (see Table 1). The fractional volume of voids (porosity) is deduced from density measurements in conjunction with the known volume fractions of ZnO, Fe₂O₃ (or Ni), and epoxy. Two series of granular NCs will be considered: on the one hand, fine-grained composites composed of polycrystalline ferromagnetic Ni clusters in a nanocrystalline nonmagnetic (ZnO) host, and on the other hand, Ni clusters embedded in a host composed of ferrimagnetic γ -Fe₂O₃ nanoparticles.

2.2. FMR and static magnetization properties

For VSM and FMR characterizations, the sample was cut from the initial piece of composite and polished to the cubic shape of 1 mm thickness, 1 mm length, and 1 mm width. A detailed analysis for the specific choice of these dimensions is contained in Appendix B.

The details of the FMR apparatus and procedure can be found elsewhere [21]. Briefly, FMR measurements, conducted in an in-plane field geometry have been done with a commercial spectrometer at frequencies in the range from 8 GHz to 24 GHz. The samples were placed at the center of a microstrip line where the derivative of the absorbed power was measured using a standard ac field modulation technique (10 Oe amplitude) and lock-in detection (Signal Recovery 7225). The cw microwave source consisted of an Anritsu MG3694B synthesized sweeper. The amplitude of the exciting field is evaluated to be 10 mOe, which corresponds to the linear response regime. The waveguide is characterized by a transmission line of 1 mm width, and a length of 10 mm, which is designed to have 50 Ω impedance. The magnetic field was applied normally to the sample plane and was measured using a Hall probe (Lakeshore 450).

dc magnetization measurements were using a vibrating sample magnetometer (VSM), that allows a field sweep of ± 10 kOe. All measurements presented in this research were performed at ambient conditions. It should be noted that M - H patterns from different positions of the sample were collected, denoted hereafter as perpendicular (per), or in-plane, and parallel (par), respectively.

3. EXPERIMENTAL RESULTS AND DISCUSSION

3.1. Magnetization of Ni/ZnO, Ni/ γ -Fe₂O₃, and γ -Fe₂O₃/ZnO NCs

Before proceeding to discuss FMR results, a preliminary assessment of the magnetic state of the samples has been done through their magnetization (M) versus field (H) plots at 300 K. Typical hysteretic magnetizations corresponding to the Ni/ZnO (nNiZ8) sample containing 8.9 vol % Ni is shown in Figure 1, for per and par positions, with a sharp increase in magnetization at low fields followed by a linear saturating behavior. Observe that the differences between in-plane and out-of-plane hysteresis loops of the sample are small. To extract some interesting information from the

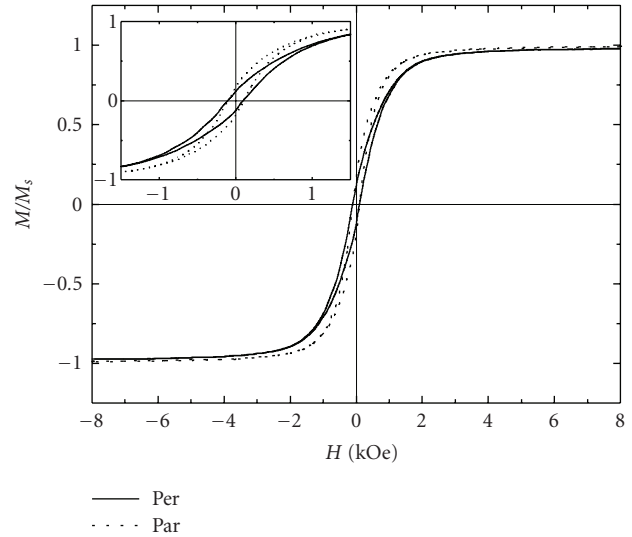


FIGURE 1: Typical M - H plot of the Ni/ZnO sample (nNiZ8) containing 8.9 vol % of Ni. Room temperature. Inset: an expanded view of the plot clearly showing hysteresis.

in-plane (per) magnetization curves $M(H)$, the saturation magnetization M_s , the coercivity H_c , and the remanent magnetization M_r normalized to M_s (squareness), M_r/M_s , were determined. In Figures 2 and 3, we show the magnitude of M_s , H_c , and M_r/M_s for all samples.

We first compare the effect of the Ni content on the magnetic properties for Ni/ZnO and Ni/ γ -Fe₂O₃ NCs. For Ni/ZnO, the M_s values increase linearly (see Figure 2(a)) with increasing Ni content. One feature of interest is illustrated in Figure 2(a) by the solid line which shows that the linear response one would expect for an unmodified Ni phase with a $4\pi M_s$ the same as that obtained for 100 vol %, that is, $4\pi M_s = 6.1$ kG [31–33], cannot be reached: only 75% of this value is found. Hence the static magnetic response observed here cannot be totally explained by the demagnetization process of noninteracting Ni particles. Therefore, this result suggests that some interaction exists between the Ni boundary structures (aggregates). The coercivity H_c (see Figure 2(b)) for Ni/ZnO NCs exceeds the value of Ni/ γ -Fe₂O₃ NCs over the entire range of Ni volume fraction explored. This decrease in coercivity for the Ni/ZnO NCs upon increasing the Ni content is not due to the internal porosity since the value of porosity is almost identical for all these kinds of samples (see Table 2). Note that the coercivity observed for the Ni/ γ -Fe₂O₃ NCs remains constant in the range of Ni volume fraction explored. While Figure 2(c) shows that the squareness ratio remains fairly constant at an average of 0.06 for the NCs with ZnO, which is significantly much smaller than the value predicted by the Wolfarth model predicting $M_r/M_s = 0.5$ for a random distribution of noninteracting uniaxial single domain particles, with coherent rotation of the magnetization. We believe that this deviation from this ideal value is due to interparticle interactions as a consequence of aggregation within the host matrix. We also observe a slow decrease of this ratio in the case of Ni/ γ -Fe₂O₃ NCs for Ni

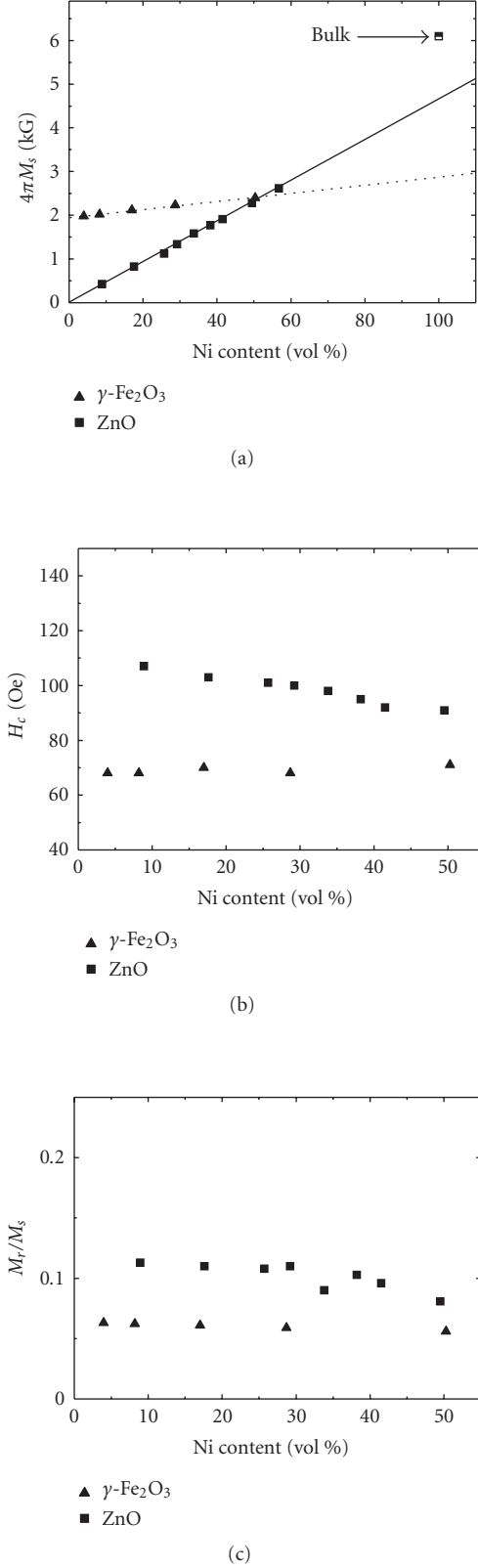


FIGURE 2: (a) Variation of the saturation magnetization $4\pi M_s$ as a function of Ni content in Ni/ZnO and Ni/γ-Fe₂O₃ samples. Room temperature. Squares (resp., triangles) denote Ni/ZnO (resp., Ni/γ-Fe₂O₃) NCs. (b) Same as in (a) for the coercivity H_c . (c) Same as in (a) for the ratio of remanent magnetization to saturation magnetization (squareness) M_r/M_s .

concentrations above 30%, albeit at a level which exceeds the squareness ratio for the NCs with ZnO.

Further insight into the characteristics of these magnetic states is obtained by comparison with our earlier study [21] of γ-Fe₂O₃/ZnO NCs. For our purpose of comparing M_s , H_c , and M_r/M_s for Ni/γ-Fe₂O₃ and γ-Fe₂O₃/ZnO NCs, the data in Figure 3 reveal that H_c remains constant and that $M_r/M_s \leq 0.15$ over the range of γ-Fe₂O₃ concentration explored. It is also interesting to note that the average saturation magnetization M_s is found to scale linearly with the γ-Fe₂O₃ content, but like the behavior of Ni in the granular ZnO matrix, only 70% of the $4\pi M_s$ value of dense γ-Fe₂O₃, that is, 5.2 kG [31–33], is obtained from the extrapolated value to the 100 vol %. Very recently, Kalarickal et al. [35] found a similar fact in a study of the static magnetic properties of ferrite (nickel zinc)-ferroelectric (barium strontium titanate) composite materials. Although there are some similarities between their samples and our samples, we believe that the differences in interpretation can be explained by different boundaries separating the particles in the samples. The ferrite particles investigated have dimensions of a few micrometers, while the aggregate sizes investigated here have significantly smaller dimensions. In addition, these boundaries differ significantly due to the amorphous (epoxy) inter-aggregate layer.

3.2. FMR in Ni/ZnO, Ni/γ-Fe₂O₃, and γ-Fe₂O₃/ZnO NCs

Figures 4(a)–4(h) display a series of typical absorption versus field derivative profiles obtained at room temperature, shown in arbitrary units, for five values of the operating frequency for a typical Ni/ZnO NC. Several comments appear warranted after a careful examination of Figure 4. First, we observed that the FMR lineshapes are quite symmetric and undistorted at the lowest Ni volume fractions in the NCs. However, the FMR profiles are more complicated for Ni volume fractions larger than 30%, especially at high frequency. Indeed, one can observe that the derivative profiles of the main resonance are distorted by the presence of higher-order spin-wave modes on the high field side. A detailed examination of the actual FMR profiles shows a secondary peak which appears at the high field tail part of the absorption curve at about 10 kOe (see Figures 4(g) and 4(h)). Second, a weakly resolved line is clearly visible on the low field side at a nominal frequency of 10 GHz. The origin of the weak signal has yet to be elucidated, but it should be remarked that a similar weak signal (at about 500 Oe) was observed in nanogranular films composed of ferromagnetic amorphous Fe nanoparticles embedded in SiO₂ glass matrices [36].

The main resonance signal is due to an FMR uniform mode which corresponds to a uniform precession of all the magnetic moments coupled to the Ni particles. In Figure 4, we see with increasing frequency the shift of the uniform mode to a higher field. The uniform mode frequency [34–38] may be obtained in the form $\omega_{\text{res}} = \gamma(H_{\text{res}} + H_{\text{int}})$, where γ is the effective gyromagnetic ratio, and H_{res} and H_{int} denote the resonance field at frequency, $\omega_{\text{res}}/2\pi$, and the internal field, respectively. The data in Figure 5 show how the resonance

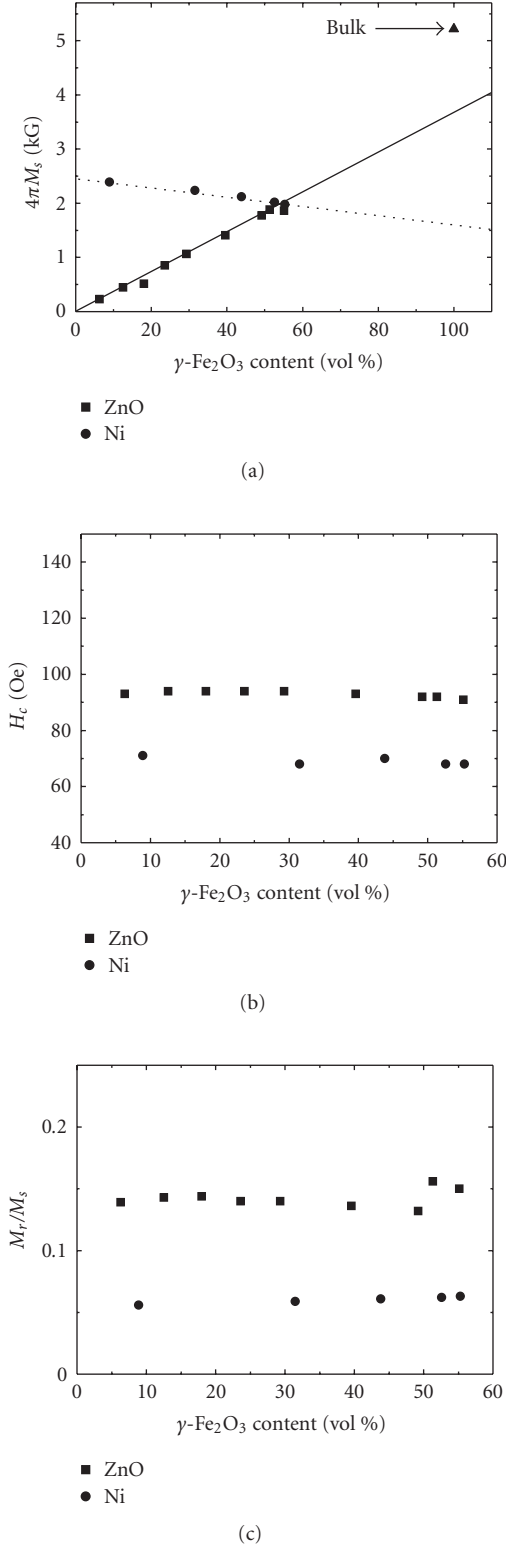


FIGURE 3: (a) Variation of the saturation magnetization $4\pi M_s$ as a function of γ -Fe₂O₃ content in Ni/γ-Fe₂O₃ and γ-Fe₂O₃/ZnO samples. The data for γ-Fe₂O₃/ZnO are from [21]. Room temperature. Squares (resp., triangles) denote γ-Fe₂O₃/ZnO (resp., Ni/γ-Fe₂O₃) NCs. The solid line shows an extrapolation of the linear $4\pi M_s$ response up to 100 vol % Ni. The dashed line is a guide for the eye; (b) Same as in (a) for the coercivity H_c ; (c) Same as in (a) for the squareness M_r/M_s .

frequency evolves with H_{res} . From the slope of the linear functional $\omega_{res}(H_{res})$, we find that γ is in the range from 1.28 to $1.76 \cdot 10^7 \text{ Oe}^{-1} \text{ s}^{-1}$ (see Figure 6(a)). The offset of the frequency data versus magnetic field serves to obtain the internal field H_i . The difference between Ni/ZnO and Ni/γ-Fe₂O₃ NCs is most clearly seen in Figure 6(b). Here, H_i is shown as a function of Ni concentration. The main effect of increasing the Ni content is to increase significantly H_i for the Ni/ZnO NCs, for example, for Ni/ZnO H_i (40 vol %) exceeds by a factor of three the corresponding value for Ni/γ-Fe₂O₃. As mentioned earlier, (long-range) magnetostatic intergranular interactions dominate the exchange (short-range) in these NCs. This explains the changes in the effective field $H_{eff} = H_{int} + 4\pi M_s$ as the Ni content is increased (Figure 6(c)).

Additional insight into the relationship between composition, magnetic species, and resonance properties can be gained by comparing the FMR absorption versus field derivative profiles for Ni/ZnO (see Figure 4) and Ni/γ-Fe₂O₃ (see Figure 7) NCs. Overall, the profiles displayed in Figure 7 are more complicated than those discussed above. The derivative profiles for the main resonance are distorted by the presence of higher spin-wave modes for all sample and frequency investigated. One sees large departures from a Lorentzian-line shape which eventually indicates complicated interaggregates dipolar interactions, particularly in samples with large volume-filling factor. However, when one looks at the uniform mode frequency, plotted in Figure 8 as a function of the resonance field, one finds a much more linear increase than before. The values of γ associated with this plot change little and are in the range from 1.56 to $1.63 \cdot 10^7 \text{ Oe}^{-1} \text{ s}^{-1}$ (see Figure 9(a)) to be compared with those previously determined in γ-Fe₂O₃/ZnO NCs which were in the range 1.70 – $1.82 \cdot 10^7 \text{ Oe}^{-1} \text{ s}^{-1}$. We can also compare the FMR absorption versus field derivative profiles for Ni/γ-Fe₂O₃ (see Figure 7) and γ-Fe₂O₃/ZnO (see [21, Figure 1]) NCs. Perhaps the most glaring difference with regard to γ-Fe₂O₃ concentration between Ni/γ-Fe₂O₃ and γ-Fe₂O₃/ZnO NCs is the influence of the internal field (see Figure 9(b)), constant and of the order of 500 Oe, on the significant increase of the effective field (Figure 9(c)) for γ-Fe₂O₃/ZnO samples while H_{eff} for the Ni/γ-Fe₂O₃ samples is a smoothly decreasing function of γ-Fe₂O₃ content. Therefore, magnetostatic interactions can be tuned by the choice of the magnetic species in these NCs.

The absorption profiles of loss versus field were obtained by integration of the raw data after baseline correction. An example (for a nominal frequency of 16 GHz) of FMR absorption curve of microwave loss versus static magnetic field is shown in Figure 10. The analysis of the FMR peak shapes cannot be realized by making the assumption that the resonance has a simple Lorentzian-line shape. However, we note that the FMR peak shape changes from a Lorentzian to a more complex shape for sufficiently large values of frequency. It is important to ask how well the simulations match the data based on least-square fitting using a pure Lorentzian profile. An example of this type of plot for an Ni/ZnO NC with 25.5 vol % is shown in the inset of Figure 10. Using this approach predicts linewidths that may be significantly different from measured values at low (<10 GHz) and high frequencies (>25 GHz). However, at intermediate frequencies,

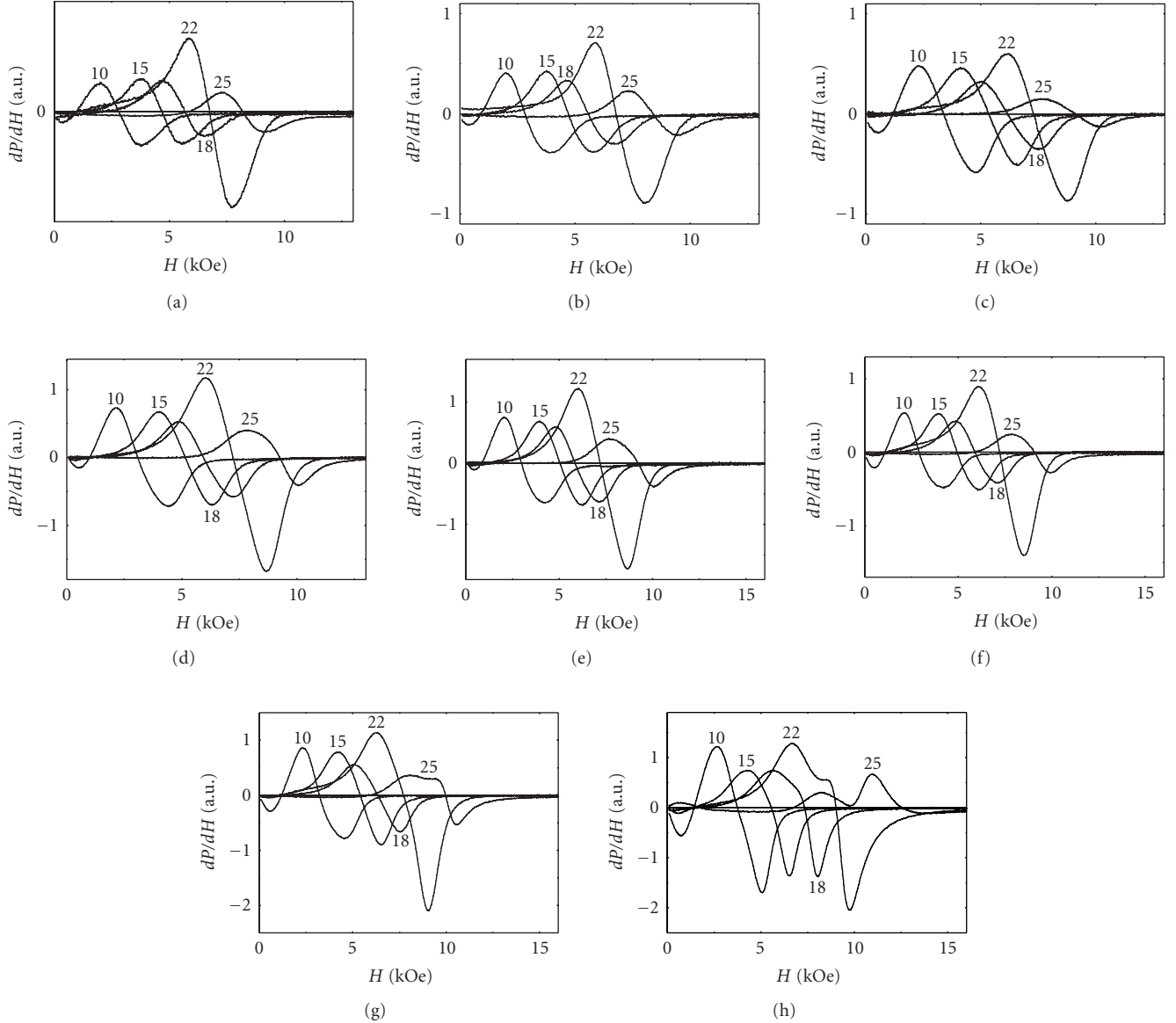


FIGURE 4: (a) Variation with magnetic field of the absorbed power derivative at different frequencies for the Ni/ZnO samples considered in the present study. Room temperature. The value of the frequency in GHz is indicated on each curve. nNiZ8 sample (Ni content is 8.9 vol %); (b) nNiZ7 sample (Ni content is 17.5 vol %); (c) nNiZ6 sample (Ni content is 25.5 vol %); (d) nNiZ5 sample (Ni content is 29.2 vol %); (e) nNiZ4 sample (Ni content is 33.4 vol %); (f) nNiZ3 sample (Ni content is 37.8 vol %); (g) nNiZ2 sample (Ni content is 41.8 vol %); (h) nNiZ1 sample (Ni content is 49.5 vol %).

for example, at a nominal frequency of 16 GHz, we find that the difference is at most $\pm 3\%$. Although FMR data taken separately could often be treated in impressive detail a consistent overall model of microwave losses has not been reached. Thus, in the discussion to follow, the FMR absorption curve has been primarily modeled in terms of a Lorentzian-line shape (at 16 GHz) and we will advance only a qualitative analysis of the FMR response.

3.3. Discussion

The issues and results outlined in the previous subsections call for further comment on: (a) the interpretation of the

peak-to-peak linewidth in terms of the Gilbert effective damping parameter α , and (b) the role of anisotropy.

Commencing with item (a), we note that one of the major challenges for describing the dynamic magnetic response of magnetic heterostructures is the characterization of the damping mechanisms. Many theoretical approaches have been applied. Smith [39] has shown how fluctuation-dissipation arguments can discriminate between alternative phenomenological damping models, for example, inhomogeneity and finite-size effects, which can complement traditional uniform magnetization descriptions of damped ferromagnetic resonance (FMR). A tensor of damping which reflects the anisotropy of the magnetic system was also derived

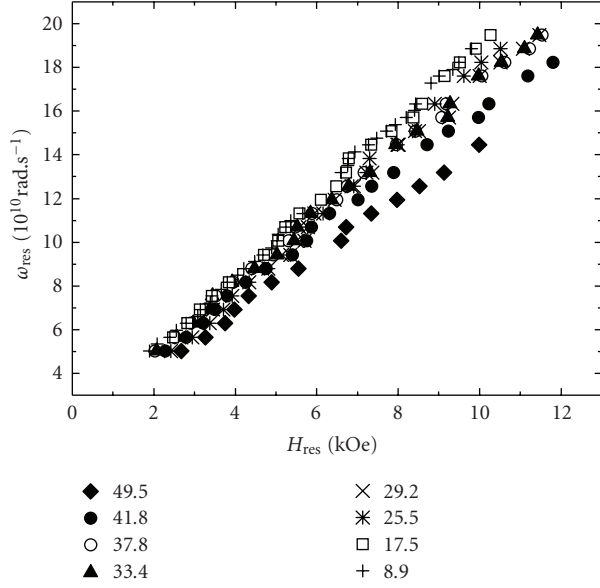


FIGURE 5: Dependence of the resonance frequency as a function of the resonance field. Room temperature. Symbols denote the volume fraction of Ni. The slope of the linear dependence is in the range 1.28 to $1.76 \cdot 10^7 \text{ Oe}^{-1} \text{ s}^{-1}$ for all samples.

by Safonov et al. [40–44]. Unfortunately, the damping processes in these materials often possess a manifestly phenomenological nature, and so many ab initio approaches, including the deterministic Landau-Lifshitz equation of motion with the Gilbert form for the magnetic damping term $\partial_t \mathbf{M} = -\gamma \mathbf{M} \times \mathbf{H}_{\text{eff}} + (\alpha/M_s) \mathbf{M} \times \partial_t \mathbf{M}$, have significant difficulties with incorporating all damping mechanisms even for a monodomain ferromagnetic material, that is, beside intrinsic damping, there is also damping due to surface an interface effects, and interparticle interactions. In this continuum theory, \mathbf{M} is the magnetization density, with magnitude $|\mathbf{M}| = M_s$ equal to the saturation magnetization, γ is the gyromagnetic ratio and is given by $\gamma = g\mu_B/\hbar$, where μ_B is the Bohr magneton moment and the Landé g factor (spectroscopic splitting factor), α is the dimensionless Gilbert-damping parameter [45–54]. \mathbf{H}_{eff} is the local (effective) magnetic field acting on \mathbf{M} , which can include magnetostatic fields of external sources, crystal anisotropy, shape-dependent dipolar interactions, and exchange interactions which govern ferromagnetic spin-wave spectral characteristics [55].

We first turn our attention to the determination of the effective linewidth ΔH determined at 16 GHz. In Figure 11 (resp., Figure 12), we compare the Ni (resp., $\gamma\text{-Fe}_2\text{O}_3$) volume fraction dependence of ΔH for the series of samples considered here. The results in these figures are for 16 GHz. The interesting information contained in Figures 11 and 12 is that there is a clear difference in the variation of ΔH with composition. In Ni/ZnO and Ni/ $\gamma\text{-Fe}_2\text{O}_3$ NCs, ΔH is in the range 1.8–2.6 kOe and increases linearly with Ni content. In Ni/ $\gamma\text{-Fe}_2\text{O}_3$ and $\gamma\text{-Fe}_2\text{O}_3$ /ZnO, ΔH was roughly on the same order, but with important differences in the rate of increase (resp., decrease) with $\gamma\text{-Fe}_2\text{O}_3$ content and the zero linewidth intercepts for $\gamma\text{-Fe}_2\text{O}_3$ /ZnO (resp., Ni/ γ -

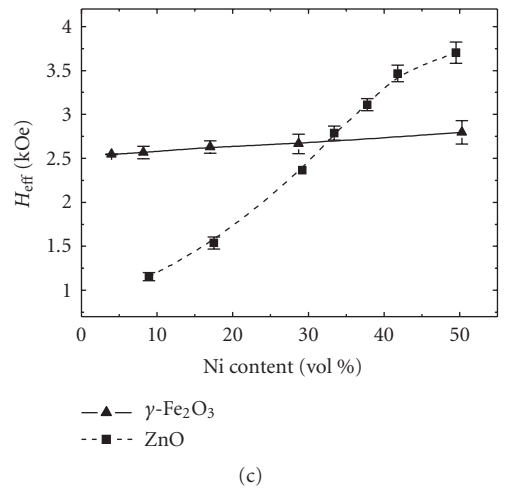
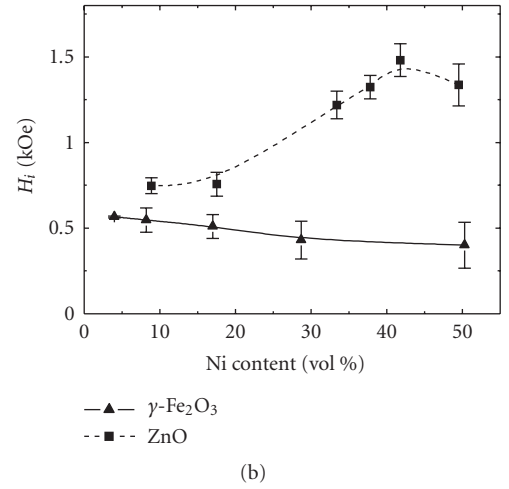
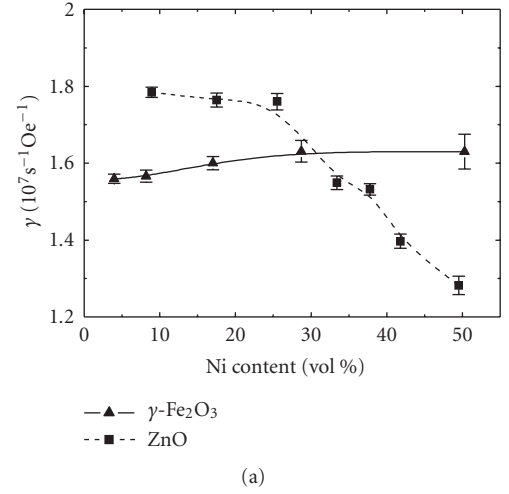


FIGURE 6: Comparison of the values of the gyromagnetic factor, γ , internal field, H_i , and, effective field, H_{eff} , for Ni/ZnO and Ni/ $\gamma\text{-Fe}_2\text{O}_3$ samples as a function of the volume fraction of Ni. Room temperature. The solid and dashed lines serve to guide the eye.

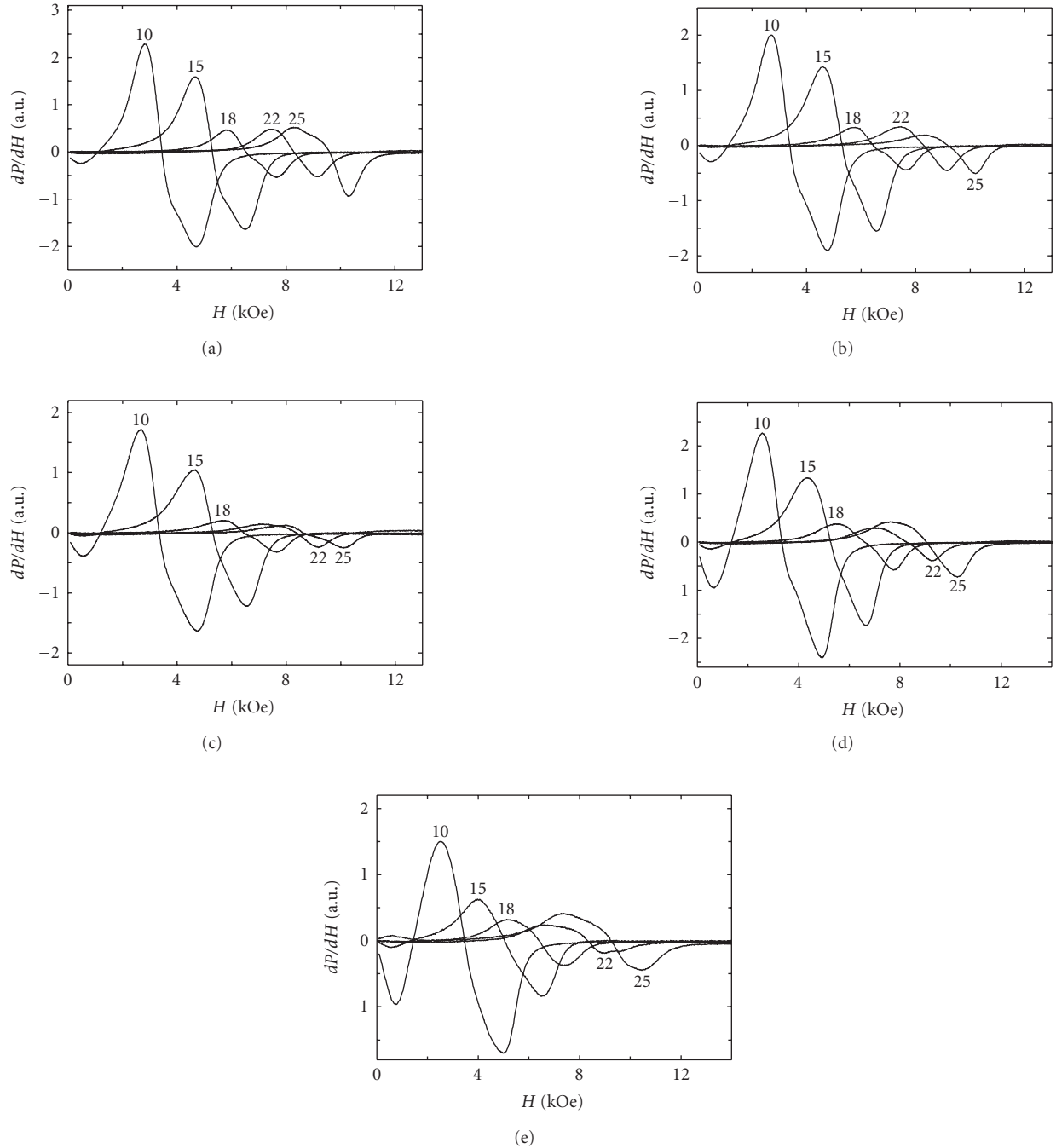


FIGURE 7: Same as in Figure 4 for Ni/ γ -Fe₂O₃ samples considered in the present study. The value of the frequency in GHz is indicated on each curve. (a) 5-nNiF sample (4 vol % Ni and 55 vol % γ -Fe₂O₃); (b) 1-nNiF sample (8.2 vol % Ni and 53 vol % γ -Fe₂O₃); (c) 2-nNiF sample (17 vol % Ni and 44 vol % γ -Fe₂O₃); (d) 3-nNiF sample (28 vol % Ni and 32 vol % γ -Fe₂O₃); (e) 4-nNiF sample (50.3 vol % Ni and 9 vol % γ -Fe₂O₃). It is worth observing that the total magnetic volume fraction contained in these samples is nearly constant \cong 60 vol %.

Fe₂O₃). The conductivity of a metal/insulator NC system can be dramatically decreased compared with conventional metallic alloys, leading to significantly reduced eddy current losses. It was emphasized by Ramprasad et al. [56] that eddy current losses of composites consisting of ferromagnetic (monodisperse) particles embedded in a nonmagnetic matrix are negligible below 10 GHz, if the particle radii are smaller than 100 nm, while composites with larger particles

display significant effective permeability degradation. However, the effect of substitution of a magnetic phase (high conductivity) by a nonmagnetic phase (low conductivity) in the γ -Fe₂O₃ surrounding matrix is not related to the composition dependent conductivity [17]. Further work is needed to determine the origin of the FMR linewidth contributions displayed in Figure 12, but in any event the slopes of opposite sign indicate that they are clearly different for γ -Fe₂O₃/ZnO

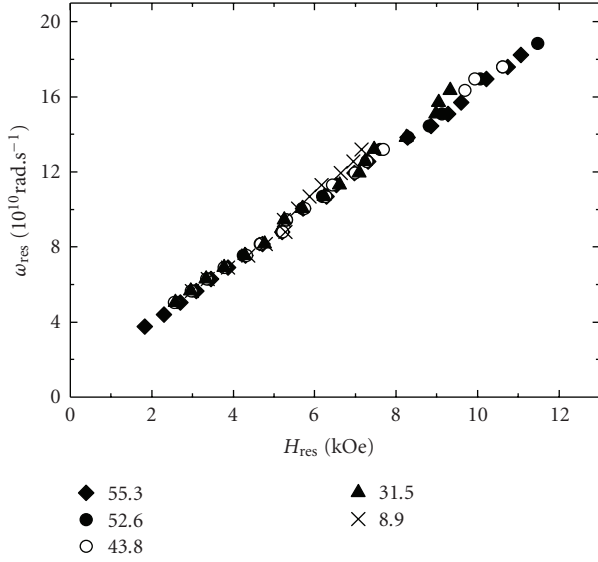


FIGURE 8: Same as in Figure 5 for Ni/ $\gamma\text{-Fe}_2\text{O}_3$ samples considered in the present study. Symbols denote the volume fraction of Ni. The slope of the linear dependence is in the range 1.56 to $1.63 \cdot 10^7 \text{ Oe}^{-1} \text{ s}^{-1}$ for all samples.

and Ni/ $\gamma\text{-Fe}_2\text{O}_3$. The apparent match in $\Delta H \cong 2 \text{ kOe}$ when the two straight lines cross each other at approximately 50% vol may be fortuitous (see Figure 12).

The effective linewidth, defined as the full width at half maximum of the absorption curve, is an important feature of the FMR modes. There are two main contributions to the linewidth: intrinsic and extrinsic. The intrinsic contribution is due to damping and is a fundamental characteristic of the magnetic material. The extrinsic contribution is due to the magnetic inhomogeneities which are contained into the material and anisotropy dispersion within the material. The peak-to-peak FMR linewidth of the uniform resonance mode ΔH is related to the damping parameter α and is given by $\Delta H = 2\alpha\omega/\sqrt{3}\gamma$, where ω is the angular frequency of the exciting field and where the coefficient of $1/\sqrt{3}$ is the correction of the difference between the full width at half maximum and the peak-to-peak linewidth for the Lorentzian-line shape. The observed effective ΔH and α are believed to be the result of inhomogeneity-related relaxation processes which increase the FMR linewidth from intrinsic values. Overall, one can say that the value effective damping parameter which is in the range 0.21–0.37 (see the inset of Figures 11 and 12) is consistent with the fact that for nanoparticles the damping parameter can exceed the bulk value for one order of magnitude or more [55–57].

As noted in Section 1, another perspective to characterize these NCs came from the study of microwave properties using spin-wave (SW) spectroscopy [23]. The relative change of SW group velocity induced by the samples was observed to depend significantly on the chemical composition and volume fraction of magnetic species contained in the NC. It was argued that the peaks in the losses have a magnetic character and are due to spin excitations of magnetic nanoparticles. It was also observed that the variation of the SW velocity in

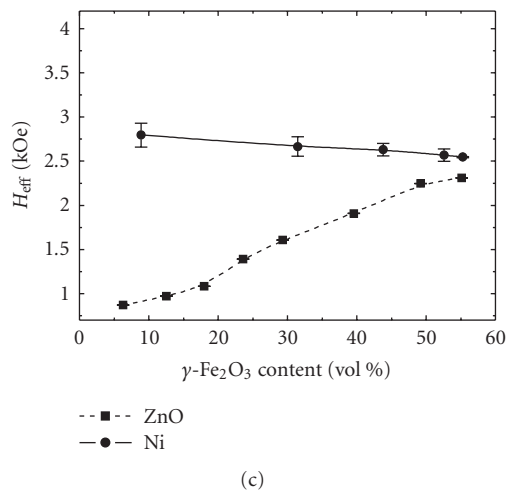
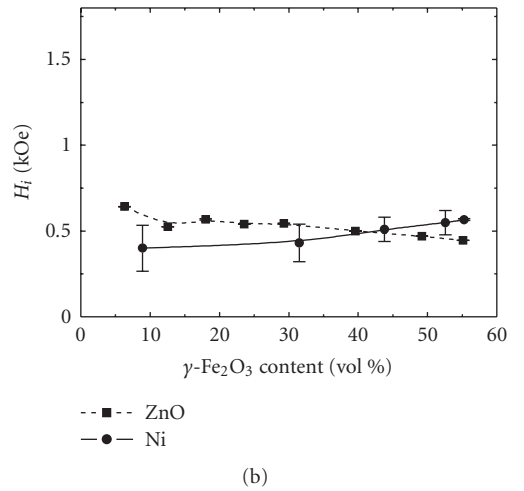
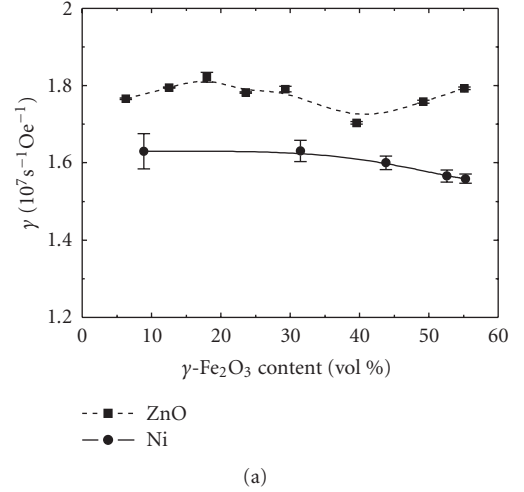


FIGURE 9: Same as in Figure 6 for Ni/ $\gamma\text{-Fe}_2\text{O}_3$ and $\gamma\text{-Fe}_2\text{O}_3/\text{ZnO}$ samples as a function of the volume fraction of $\gamma\text{-Fe}_2\text{O}_3$. The solid and dashed lines serve to guide the eye.

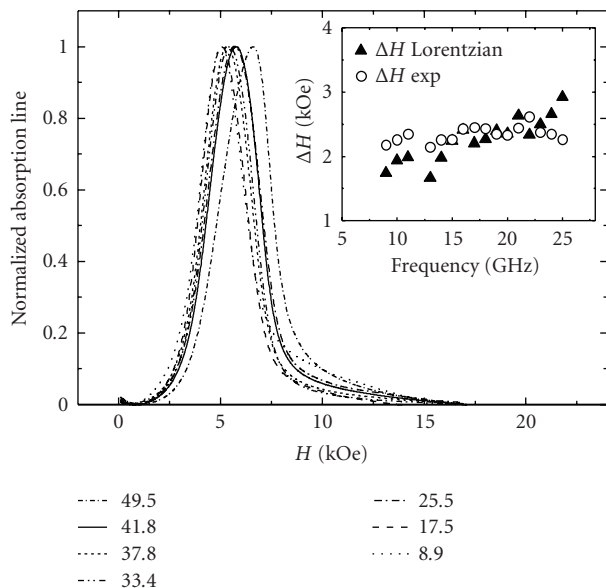


FIGURE 10: Integrated profiles for the derivative FMR profiles versus the static external magnetic field at 16 GHz for the Ni/ZnO samples considered in the present study. Room temperature. The value of the Ni content in vol % is indicated on each curve. The inset compares the peak-to-peak FMR effective linewidth obtained from the measurements (\circ) and that derived by assuming a pure Lorentzian profile (\blacktriangle).

Ni/ZnO and Ni/ γ -Fe₂O₃ showed opposite trends when the data were plotted as a function of Ni concentration.

Now concerning item (b), we make several observations related to the surface anisotropy contribution to the anisotropy of Ni and γ -Fe₂O₃ nanoparticles. Surface anisotropy becomes important only for particles with size less than, say, 100 nm. In this sub-100-nm regime, magnetic particles are single domain but the particles eventually form aggregates and apart from the dipolar interaction between the nanoparticles, other types of interactions, for example, intracluster exchange, may also become relevant. The magnetic properties of nanophases are determined both by the behavior of particles and by the spatial distribution of the aggregates which defines the magnetostatic interactions between them. As we have noticed earlier, the distance of closest approach between particles is expected to be large enough for the interactions to have mainly a magnetostatic character. It is interesting to observe that a set of bounds for the effective permeability of composites containing spherical (monodisperse) particles with a ligand shell coating was derived by Ramprasad et al. [56], showing that this physicochemical attribute of the particles may become relevant when the ligand shell thickness is large compared to the particle radius. As previously mentioned [22], it is believed that the differences observed in the gyromagnetic resonance spectra observed between the NCs are a consequence of effective magnetic anisotropy.

We would like to emphasize that the exact oxidation state and oxidation-layer thickness of Ni nanoparticles in the NCs are unknown. Because the samples have been prepared in

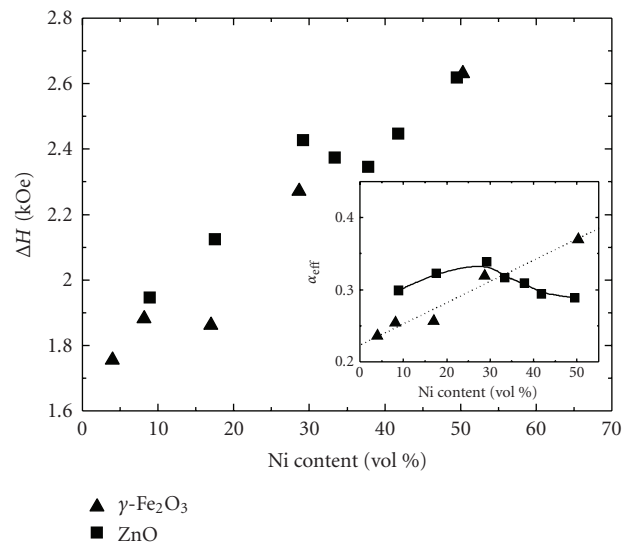


FIGURE 11: The peak-to-peak resonance effective linewidth as a function of Ni content for Ni/ZnO and Ni/ γ -Fe₂O₃ samples. The inset shows the variation of the effective Gilbert damping parameter determined for a nominal frequency of 16 GHz for Ni/ γ -Fe₂O₃ and Ni/ZnO samples as a function of Ni content. The solid and dashed lines serve to guide the eye.

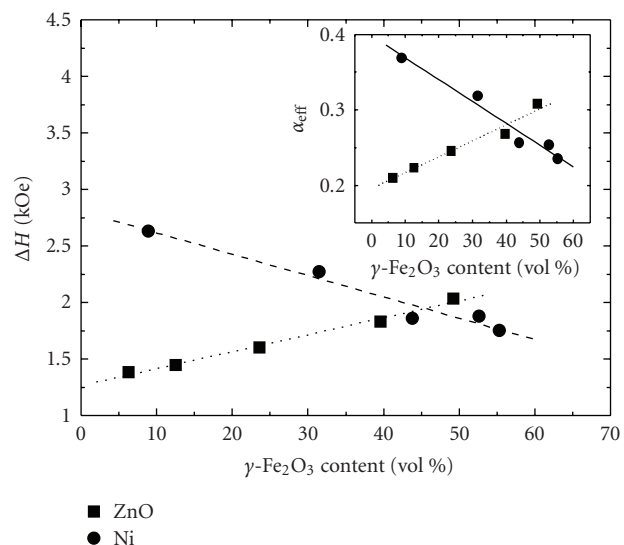


FIGURE 12: Same as in Figure 11 for Ni/ γ -Fe₂O₃ and γ -Fe₂O₃/ZnO samples as a function of γ -Fe₂O₃ content.

ambient atmosphere, surface passivation by a thin layer of nickel oxide NiO is inevitable. Due to the large surface-area-to-volume ratio, oxidation seems to be a persistent problem in core-shell nanoparticles. There have been a number of contributions to this problem, and although there is a consensus that the oxidation state of Ni has an impact on the magnetic properties, there is still ongoing debate on the role of oxide, with recent evidence from ⁵⁷Fe Mössbauer

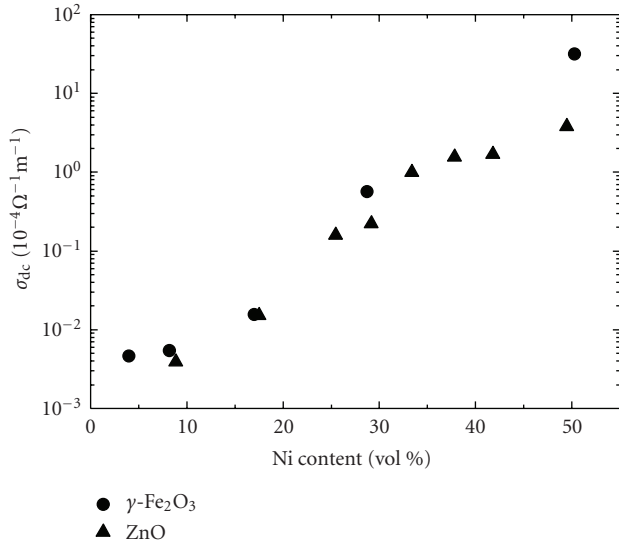


FIGURE 13: Experimental values of the dc conductivity of Ni/ZnO (▲) and Ni/ $\gamma\text{-Fe}_2\text{O}_3$ (●) NCs, measured by the four-point probe technique, as a function of Ni content. Room temperature.

spectroscopy, neutron powder diffraction and magnetization studies of the properties of mixtures of (ferromagnetic) $\gamma\text{-Fe}_2\text{O}_3$ and (antiferromagnetic) NiO nanoparticles, indicating that the mixing of $\gamma\text{-Fe}_2\text{O}_3$ nanoparticles with NiO nanoparticles results in a faster superparamagnetic relaxation and a reduced coercivity compared to a sample consisting solely of $\gamma\text{-Fe}_2\text{O}_3$ nanoparticles [57]. This point may also underline the propensity of the material or defects within the NC to provide oxidation sources for the metal nanocrystals since it influences greatly the microwave magnetic response. We further note that the development of magnetic metal nanoparticles has been limited by the fact that they oxidize in air, forming either weakly magnetic or nonmagnetic oxides, resulting in the generation of stresses [58, 59].

4. CONCLUDING REMARKS

We have presented a detailed study on the magnetization and FMR response of Ni/ZnO and Ni/ $\gamma\text{-Fe}_2\text{O}_3$ NCs. To summarize, the immediate conclusions that we can make from the experimental results presented above are as follows: (i) the analysis of the FMR spectra can be interpreted as arising from aggregates of magnetic nanoparticles, each of which resonates in an effective magnetic field composed of the applied field, the average (magnetostatic) dipolar field, and the randomly oriented magnetic anisotropy field; (ii) referring to the experimental data, it has been established that inhomogeneity-based line-broadening mechanisms, due to the damping of surface/interface effects and interparticle interaction, affect the FMR effective linewidth. The large value of the peak-to-peak linewidth cannot be taken as a representation of the intrinsic losses due to the inhomogeneous line-broadening contribution; (iii) particularly important is the fact that the FMR peak shape changes from a Lorentzian to a more complex shape showing distortions for sufficiently

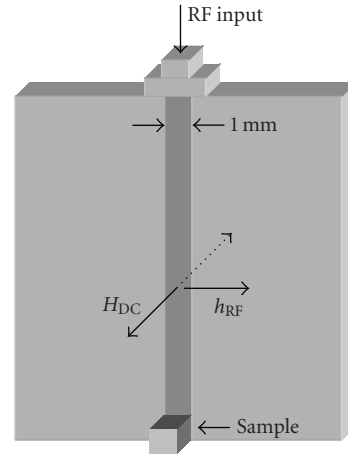


FIGURE 14: Schematic description of the microstrip line employed for the FMR measurements (in-plane field geometry). The transmission stripline (Au) of 1 mm width and a length of 10 mm is designed to have 50Ω impedance above 4 GHz. It was fabricated by UV lithography and deposited on a 5 mm thick alumina substrate with a bottom conducting ground plane.

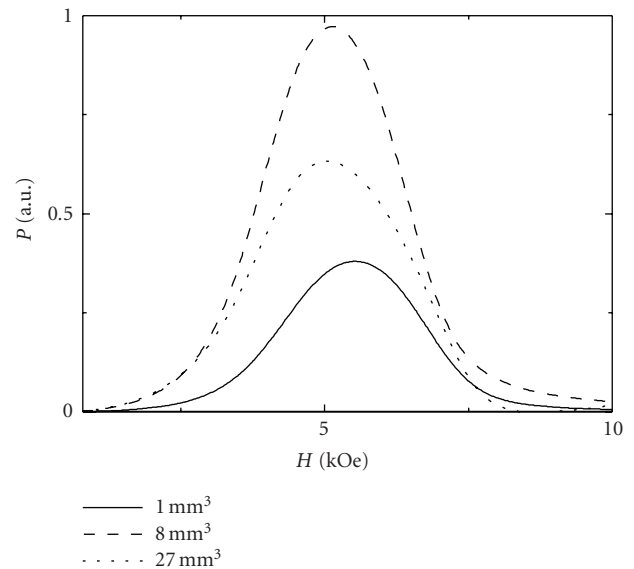


FIGURE 15: Ferromagnetic resonance profiles at 16 GHz. The graphs show the absorbed power versus applied magnetic field for a representative Ni/ZnO cubic shape sample (nNiZ6 containing 25 vol % Ni and 35 vol % ZnO) for three volumes: 1, 8, and $27 mm^3$, as indicated. Room temperature.

large values of frequency. Details of the origins of these distortions are not entirely clear; (iv) a comparison between the linewidth for granular metal and metal oxide NCs proves interesting in the FMR experiments.

It has been widely recognized that, at all length scales, the scale-relative properties of electromagnetic and magnetic systems vary with their size due to increasing edge-to-surface and surface-to-volume ratios. Thus, engineering useful NCs

will require an understanding of how the physical properties of aggregates evolve with size and shape into those of bulk NCs. As recalled earlier, an additional problem is particle oxidation arising from the large surface-area-to-volume ratio. The fundamental nature of oxidation in nanometer-sized structures has received some recent attention [60–64], however it is far from being well understood.

Before we conclude, we place our results in perspective. Challenges towards multiple functionality in NCs include design and preparation of materials that exhibit electric and magnetic fields-tunable electromagnetic wave transport properties. We are currently engaged in a systematic investigation of loss minimization of NCs for optimizing microwave applications. In a broader context, a similar analysis is planned for a series of piezoelectric-magnetostrictive NCs with a systematic variation in composition, control of internal strain, and magnetoelastically induced anisotropy due to large stress between the nanoparticles and the surrounding matrix, impurities, and porosity since it is well established that all of these preparation parameters are known to produce large linewidths. For that purpose, the consolidation of high density NCs, that is, by using hot pressing [65], or hot isostatic pressing [66, 67], is a critical step towards development of an optimal soft magnetic NC.

APPENDICES

A. EVALUATION OF CONDUCTIVITY AND SKIN EFFECT AND EDDY CURRENT ANALYSIS

In this appendix, we describe several details of the measurement of the dc conductivity, σ_{dc} , of our NCs using the four-point probe technique. In Figure 13, we show $\sigma_{dc}(f_{Ni})$ for Ni/ZnO samples. From Figure 13, we observe that the data collected at low field exhibit an exponential increase between 10 and 40 vol % Ni and a change of slope at about 40 vol % Ni. In electrodynamics [68, 69], it has been traditional to consider the skin depth as the distance δ through which the amplitude of the propagating wave decreases by a factor e^{-1} . For our low-conductivity NCs and considering the measured values of the effective electromagnetic parameters of these NCs [17, 18], we find that δ is in the 10^2 – 10^3 mm size range in the GHz frequency range, that is, much larger than the sample thickness. Thus, one can safely assume a full penetration of the microwave field into our samples. Similar measurements for the Ni/ γ -Fe₂O₃ NCs indicate that the values of $\sigma_{dc}(f_{Ni})$ are close to the values for Ni/ZnO NCs. Another important issue which has been previously discussed in [17] is the possibility of a direct observation of the intrinsic complex permittivity of the magnetic phases based on the measurement of the effective complex permittivity of the NCs and using a mean-field (effective medium) theory, for example, Bruggeman, McLachlan. At present there is no universal agreement about an effective medium theory that can self-consistently explain the various experimental measurements probing the dielectric properties of NC. We refer the interested reader to [17] for the details of the derivation. No conduction (percolation) threshold is evidenced indicating a

disconnected nanoparticles network. In these powder compact composites, the presence of insulating grains and of the amorphous epoxy resin increases the conduction barrier height and therefore is expected to decrease the overall conductivity of the samples. However, even if the volume fraction of the nanoparticles—and hence the intergrain spacing—and grain size were independently adjustable, we have not yet studied the local charge transport mechanisms.

Several comments are in order. First, in composite with uniform dispersions of magnetic nanoparticles, the conductivity of the NC is determined mainly by the interparticle distance and eddy currents, produced within the particle that are extremely small at high frequency, are limited to individual particles or aggregates. We note that Ramprasad et al. [56] have shown, in their phenomenological modeling of the properties of magnetic nanoparticle composites, that in the 0.1–10 GHz frequency range, particles with radii smaller than 100 nm are expected to encounter negligible eddy current losses. This was found true even at high particle volume fraction, when clustering of particles could result in aggregates much larger than the actual particles. Second, no signature for percolation threshold is apparent for the data collected; thus we infer from the weak f_{Ni} dependence of σ_{dc} that the Ni nanoaggregates should be separated in the ZnO matrix. It is well established by now that in ferromagnetic NCs, the shielding and dissipation due to eddy currents rapidly diminish with decreasing the particle size [70]. This has for effect to reduce the dielectric losses in metallic nanoparticles. Third, with dimensions of NCs well below the skin depth, the electromagnetic wave fully penetrates the sample and allows the contribution of the whole volume to the magnetic properties of the NCs.

B. INFLUENCE OF SAMPLE SHAPE ON INHOMOGENEOUS BROADENING

The purpose of this appendix is to briefly discuss the issue raised in Section 2.1, namely, the choice of the dimensions of our NC samples. Cubes with different nominal thickness in the millimeter size range were fabricated. The specific data shown in the experimental section (Figures 4 and 7) are for a 1 mm thick cube. Intuitively, one expects the present experimental condition to apply for sample thickness comparable or smaller than the width (1 mm) of the microstrip line (with reference to Figure 14). The samples were placed in the microstrip with the homogeneous external static magnetic field applied perpendicular to the sample and the linearly polarized microwave excitation field h_{rf} in the sample plane.

Strictly speaking, the FMR equation that was used to determine the FMR field is only valid for spherical samples [37]. It has been widely recognized that because of inhomogeneities in the demagnetization field this may affect the broadening of the FMR peak. To discriminate between sample thickness and material on the observed broadening, we varied the thickness of our cubic samples. We illustrate the influence of the sample thickness (see Figure 14) for the absorbed power change of a representative sample (nNiZ6 containing 25 vol % Ni) as a function of applied magnetic field. These absorption profiles of loss versus field were obtained

from direct integration of the raw data (measured derivative of the absorbed power versus applied magnetic field). One can see that the peak loss points in the graphs in Figure 15 are shifted up in field for the two smaller samples. The effective linewidth, taken as the full width at half maximum of the profiles in Figure 15, are 2.4 kOe (resp., 2.5 kOe and 3.1 kOe) for the 1 (resp., 2 and 3) mm thick sample. The asymmetry of the absorption profile apparent for the $2 \times 2 \times 2$ and $3 \times 3 \times 3$ mm³ samples is indicative of a departure from a Lorentzian line. Such inhomogeneously broadened line originates from a complicated interaggregate dipolar interaction due to large residual strains and porosity. On the other hand, the line shape for the 1 mm thick sample is symmetric. Increasing the thickness by a factor of three does not strongly change the FMR linewidth of the integrated power of the uniform mode itself, and indicates that H_{res} (at 16 GHz) is not appreciably affected. The fact that no increase in FMR linewidth with thickness is evidenced supports also the conclusion that eddy current losses are negligible for this sample.

This interpretation also resonates well with the recent FMR and high-frequency analysis of ferrite-ferroelectric composite materials by Kalarickal et al. [35], who studied how the shape (cubes and spheres with nominal diameters of 2 mm) of their composite samples influences the static magnetic properties. They found that cubes and spheres gave similar results for all the effective loadings of the ferrite component. Their FMR measurements were made on nominal 1 mm diameter spheres (for 100% ferrite material) or 3 mm diameter spheres (for the materials with lower loadings). Guskos et al. [71] investigated by FMR polymer composites containing as filler a binary mixture of Fe₃O₄ and Fe₃C nanoparticles (30–50 nm) dispersed in a diamagnetic carbon matrix. These authors placed a square-shaped sample of 3.5×3.5 mm² cut out from the polymer sheet in the center of a TE₁₀₂ cavity, that is, at the local maximum of the microwave magnetic component and in the nodal plane of the electric component.

ACKNOWLEDGMENT

The first author acknowledges the financial support from the Conseil Régional de Bretagne for a Ph.D. studentship.

REFERENCES

- [1] S. A. Wolf, D. D. Awschalom, R. A. Buhrman, et al., "Spintronics: a spin-based electronics vision for the future," *Science*, vol. 294, no. 5546, pp. 1488–1495, 2001.
- [2] M. Fiebig, "Revival of the magnetoelectric effect," *Journal of Physics D*, vol. 38, no. 8, pp. R123–R152, 2005.
- [3] V. Skumryev, S. Stoyanov, Y. Zhang, G. Hadjipanayis, D. Givord, and J. Nogués, "Beating the superparamagnetic limit with exchange bias," *Nature*, vol. 423, no. 6942, pp. 850–853, 2003.
- [4] R. F. Ziolo, E. P. Giannelis, B. A. Weinstein, et al., "Matrix-mediated synthesis of nanocrystalline γ -Fe₂O₃: a new optically transparent magnetic material," *Science*, vol. 257, no. 5067, pp. 219–223, 1992.
- [5] A. F. Bakuzis, K. S. Neto, P. P. Gravina, et al., "Magneto-optical properties of a highly transparent cadmium ferrite-based magnetic fluid," *Applied Physics Letters*, vol. 84, no. 13, pp. 2355–2357, 2004.
- [6] H. S. Nalwa, Ed., *Encyclopedia of Nanoscience and Nanotechnology*, American Scientific, New York, NY, USA, 2004.
- [7] E. L. Wolf, *Nanophysics and Nanotechnology*, Wiley-VCH, Weinheim, Germany, 2004.
- [8] G. Cao, *Nanostructures and Nanomaterials*, Imperial College Press, London, UK, 2004.
- [9] H. Schmid, "Magnetolectric effects in insulating magnetic materials," in *Introduction to Complex Mediums for Optics and Electromagnetics*, W. S. Wieglofer and A. Lakhtakia, Eds., pp. 167–195, SPIE Press, Bellingham, Wash, USA, 2003.
- [10] J. Wang, J. B. Neaton, H. Zheng, et al., "Epitaxial BiFeO₃ multiferroic thin film heterostructures," *Science*, vol. 299, no. 5613, pp. 1719–1722, 2003.
- [11] J. Baker-Jarvis and P. Kabos, "Dynamic constitutive relations for polarization and magnetization," *Physical Review E*, vol. 64, no. 5, Article ID 056127, 14 pages, 2001.
- [12] J. Zhai, J. Li, D. Viehland, and M. I. Bichurin, "Large magnetoelectric susceptibility: the fundamental property of piezoelectric and magnetostrictive laminated composites," *Journal of Applied Physics*, vol. 101, no. 1, Article ID 014102, 4 pages, 2007.
- [13] R. S. Devan and B. K. Chougule, "Effect of composition on coupled electric, magnetic, and dielectric properties of two phase particulate magnetoelectric composite," *Journal of Applied Physics*, vol. 101, no. 1, Article ID 014109, 6 pages, 2007.
- [14] G. B. Smith, "Nanostructured thin films," in *Introduction to Complex Mediums for Optics and Electromagnetics*, W. S. Wieglofer and A. Lakhtakia, Eds., SPIE Press, Bellingham, Wash, USA, 2003.
- [15] V. Kochergin, V. Zaporozhchenko, H. Takele, F. Faupel, and H. Föll, "Improved effective medium approach: application to metal nanocomposites," *Journal of Applied Physics*, vol. 101, no. 2, Article ID 024302, 7 pages, 2007.
- [16] C. Brosseau, J. Ben Youssef, P. Talbot, and A.-M. Konn, "Electromagnetic and magnetic properties of multicomponent metal oxides heterostructures: nanometer versus micrometer-sized particles," *Journal of Applied Physics*, vol. 93, no. 11, pp. 9243–9256, 2003.
- [17] C. Brosseau and P. Talbot, "Effective permittivity of nanocomposite powder compacts," *IEEE Transactions on Dielectrics and Electrical Insulation*, vol. 11, no. 5, pp. 819–832, 2004.
- [18] C. Brosseau and P. Talbot, "Effective magnetic permeability of Ni and Co micro- and nanoparticles embedded in a ZnO matrix," *Journal of Applied Physics*, vol. 97, no. 10, Article ID 104325, 11 pages, 2005.
- [19] S. Mallécol, C. Brosseau, P. Quéffelec, and A.-M. Konn, "Measurement of the permeability tensor in nanophases of granular metal oxides and field-induced magnetic anisotropy," *Physical Review B*, vol. 68, no. 17, Article ID 174422, 6 pages, 2003.
- [20] C. Brosseau, S. Mallécol, P. Quéffelec, and J. Ben Youssef, "Nonreciprocal electromagnetic properties of nanocomposites at microwave frequencies," *Physical Review B*, vol. 70, no. 9, Article ID 092401, 4 pages, 2004.
- [21] J. Ben Youssef and C. Brosseau, "Magnetization damping in two-component metal oxide micropowder and nanopowder compacts by broadband ferromagnetic resonance measurements," *Physical Review B*, vol. 74, no. 21, Article ID 214413, 13 pages, 2006.

- [22] C. Brosseau, S. Mallégo, P. Quéffelec, and J. Ben Youssef, "Electromagnetism and magnetization in granular two-phase nanocomposites: a comparative microwave study," *Journal of Applied Physics*, vol. 101, no. 3, Article ID 034301, 15 pages, 2007.
- [23] L. Lutsev, S. Yakovlev, and C. Brosseau, "Spin wave spectroscopy and microwave losses in granular two-phase magnetic nanocomposites," *Journal of Applied Physics*, vol. 101, no. 3, Article ID 034320, 8 pages, 2007.
- [24] Y. Wu, J. Li, Z.-Q. Zhang, and C. T. Chan, "Effective medium theory for magnetodielectric composites: beyond the long-wavelength limit," *Physical Review B*, vol. 74, no. 8, Article ID 085111, 9 pages, 2006.
- [25] S. A. Majetich and M. Sachan, "Magnetostatic interactions in magnetic nanoparticle assemblies: energy, time and length scales," *Journal of Physics D*, vol. 39, no. 21, pp. R407–R422, 2006.
- [26] J. A. A. J. Perenboom, P. Wyder, and F. Meier, "Electronic properties of small metallic particles," *Physics Reports*, vol. 78, no. 2, pp. 173–292, 1981.
- [27] M. Wu, Y. D. Zhang, S. Hui, et al., "Microwave magnetic properties of $\text{Co}_{50}/(\text{SiO})_{50}$ nanoparticles," *Applied Physics Letters*, vol. 80, no. 23, pp. 4404–4406, 2002.
- [28] K. Yamaura, D. P. Young, and R. J. Cava, "Thermally induced variable-range-hopping crossover and ferromagnetism in the layered cobalt oxide $\text{Sr}_2\text{Y}_{0.5}\text{Ca}_{0.5}\text{Co}_2\text{O}_7$," *Physical Review B*, vol. 63, no. 6, Article ID 064401, 5 Pages, 2001.
- [29] A. R. Pereira, K. L. C. Miranda, P. P. C. Sartoratto, P. C. Morais, and A. F. Bakuzis, "Ferromagnetic resonance investigation of maghemite-silica nanocomposites," *Journal of Applied Physics*, vol. 100, no. 8, Article ID 086110, 3 Pages, 2006.
- [30] H. M. Sauer, E. Cura, S. Spiekermann, and R. Hempelmann, "Nanoscaled nickel-zinc-iron oxides of spinell type as soft magnetic colloids and their ferromagnetic resonance spectrum," *Zeitschrift für Physikalische Chemie*, vol. 220, no. 2, pp. 189–198, 2006.
- [31] W. Wong, H. Li, Z. R. Zhao, and J. C. Chen, "Magnetic coercivity of Fe_3O_4 particle systems," *Journal of Applied Physics*, vol. 69, no. 8, pp. 5119–5121, 1991.
- [32] E. Tronc, D. Fiorani, M. Noguès, et al., "Surface effects in non-interacting and interacting $\gamma\text{-Fe}_2\text{O}_3$ nanoparticles," *Journal of Magnetism and Magnetic Materials*, vol. 262, no. 1, pp. 6–14, 2003.
- [33] A. E. Berkowitz, W. J. Schuele, and P. J. Flanders, "Influence of crystallite size on the magnetic properties of acicular $\gamma\text{-Fe}_2\text{O}_3$ articles," *Journal of Applied Physics*, vol. 39, no. 2, pp. 1261–1263, 1968.
- [34] M. Pardavi-Horvath and L. J. Swartzendruber, "Ferromagnetic resonance relaxation in reaction milled and annealed Fe_3O_4 nanocomposites," *IEEE Transactions on Magnetics*, vol. 35, no. 5, pp. 3502–3504, 1999.
- [35] S. S. Kalarickal, D. Ménard, J. Das, et al., "Static and high frequency magnetic and dielectric properties of ferrite-ferroelectric composite materials," *Journal of Applied Physics*, vol. 100, no. 8, Article ID 084905, 9 pages, 2006.
- [36] S. Tomita, M. Hagiwara, T. Kashiwagi, et al., "Ferromagnetic resonance study of diluted Fe nanogranular films," *Journal of Applied Physics*, vol. 95, no. 12, pp. 8194–8198, 2004.
- [37] M. Sparks, *Ferromagnetic Relaxation Theory*, McGraw-Hill, New York, NY, USA, 1964.
- [38] A. F. Kip and R. D. Arnold, "Ferromagnetic resonance at microwave frequencies in an iron single crystal," *Physical Review*, vol. 75, no. 10, pp. 1556–1560, 1949.
- [39] N. Smith, "Fluctuation-dissipation considerations for phenomenological damping models for ferromagnetic thin films," *Journal of Applied Physics*, vol. 92, no. 7, p. 3877, 2002.
- [40] V. L. Safonov, "Micromagnetic grain as a nonlinear oscillator," *Journal of Magnetism and Magnetic Materials*, vol. 195, no. 2, pp. 523–529, 1999.
- [41] V. L. Safonov, "Thermal reversal of magnetization as "random walk" dynamics of a nonlinear oscillator," *Journal of Applied Physics*, vol. 85, no. 8, pp. 4370–4372, 1999.
- [42] V. L. Safonov and H. N. Bertram, "Dynamic-thermal reversal in a fine micromagnetic grain: time dependence of coercivity," *Journal of Applied Physics*, vol. 87, no. 9, pp. 5681–5683, 2000.
- [43] V. L. Safonov and H. N. Bertram, "Magnetization dynamics and thermal fluctuations in fine grains and films," in *The Physics of Ultra-high-Density Magnetic Recording*, M. Plumer, J. van Ek, and D. Weller, Eds., p. 81, Springer, Berlin, Germany, 2001.
- [44] V. L. Safonov and H. N. Bertram, "Fluctuation-dissipation considerations and damping models for ferromagnetic materials," *Physical Review B*, vol. 71, Article ID 224402, 5 pages, 2005.
- [45] A. Aharony, *Introduction to the Theory of Ferromagnetism*, Oxford University Press, New York, NY, USA, 1996.
- [46] E. C. Stoner and E. P. Wohlfarth, "A mechanism of magnetic hysteresis in heterogeneous alloys," *Philosophical Transactions of the Royal Society of London*, vol. 240, pp. 599–642, 1948.
- [47] A. H. Morrish, *The Physical Principles of Magnetism*, John Wiley & Sons, New York, NY, USA, 1965.
- [48] T. L. Gilbert, "A Lagrangian formulation of the gyromagnetic equation of the magnetic field," *Physical Review*, vol. 100, p. 1243, 1955.
- [49] L. Landau and E. Lifshitz, "On the theory of the dispersion of magnetic permeability in ferromagnetic bodies," *Physikalische Zeitschrift der Sowjetunion*, vol. 8, pp. 153–169, 1935.
- [50] L. D. Landau, E. M. Lifshitz, and L. P. Pitaevski, *Statistical Physics*, Pergamon Press, Oxford, UK, 3rd edition, 1980.
- [51] L. D. Landau, "On the theory of phase transition," in *Collected Papers of L. D. Landau*, D. ter Haar, Ed., p. 193, Gordon and Breach, New York, NY, USA, 1967.
- [52] R. Kikuchi, "On the minimum of magnetization reversal time," *Journal of Applied Physics*, vol. 27, no. 11, pp. 1352–1357, 1956.
- [53] W. F. Brown Jr., *Micromagnetics*, Wiley-Interscience, New York, NY, USA, 1963.
- [54] H. Kronmüller and M. Fähnle, *Micromagnetism and the Microstructure of Ferromagnetic Solids*, Cambridge University Press, Cambridge, UK, 2003.
- [55] W. F. Brown Jr., *Magnetostatic Principles in Ferromagnetism*, North-Holland, Amsterdam, The Netherlands, 1962.
- [56] R. Ramprasad, P. Zurcher, M. Petras, M. Miller, and P. Renaud, "Magnetic properties of metallic ferromagnetic nanoparticle composites," *Journal of Applied Physics*, vol. 96, no. 1, pp. 519–529, 2004.
- [57] C. Frandsen, C. W. Ostefeld, M. Xu, et al., "Interparticle interactions in composites of nanoparticles of ferrimagnetic $\gamma\text{-Fe}_2\text{O}_3$ and antiferromagnetic (CoO,NiO) materials," *Physical Review B*, vol. 70, no. 13, Article ID 134416, 7 pages, 2004.
- [58] H. S. Nalwa, Ed., *Encyclopedia of Nanoscience and Nanotechnology*, American Scientific, New York, NY, USA, 2004.
- [59] H. E. Evans, "Stress effects in high temperature oxidation of metals," *International Materials Reviews*, vol. 40, no. 1, pp. 1–40, 1995.

- [60] S.-J. Cho, J.-C. Idrobo, J. Olamit, K. Liu, N. D. Browning, and S. M. Kauzlarich, "Growth mechanisms and oxidation resistance of gold-coated iron nanoparticles," *Chemistry of Materials*, vol. 17, no. 12, pp. 3181–3186, 2005.
- [61] K. S. Buchanan, A. Krichevsky, M. R. Freeman, and A. Meldrum, "Magnetization dynamics of interacting iron nanocrystals in SiO₂," *Physical Review B*, vol. 70, no. 17, Article ID 174436, 10 pages, 2004.
- [62] C. A. Ross, "Patterned magnetic recording media," *Annual Review of Materials Science*, vol. 31, pp. 203–235, 2001.
- [63] S. Sun and H. Zeng, "Size-controlled synthesis of magnetite nanoparticles," *Journal of the American Chemical Society*, vol. 124, no. 28, pp. 8204–8205, 2002.
- [64] B. Ravel, E. E. Carpenter, and V. G. Harris, "Oxidation of iron in iron/gold core/shell nanoparticles," *Journal of Applied Physics*, vol. 91, no. 10, pp. 8195–8197, 2002.
- [65] C. E. Patton, "Effect of grain size on the microwave properties of polycrystalline yttrium iron garnet," *Journal of Applied Physics*, vol. 41, no. 4, pp. 1637–1641, 1970.
- [66] H. V. Atkinson and B. A. Rickinson, *Hot Isostatic Processing*, Adam Hilger, Bristol, UK, 1991.
- [67] H. V. Atkinson and S. Davies, "Fundamental aspects of hot isostatic pressing: an overview," *Metallurgical and Materials Transactions A*, vol. 31, no. 12, pp. 2981–3000, 2000.
- [68] L. Landau, E. M. Lifshitz, and L. P. Pitaevskii, *Electrodynamics of Continuous Media*, Butterworth-Heinemann, Oxford, UK, 1984.
- [69] D. J. Jackson, *Classical Electrodynamics*, John Wiley & Sons, New York, NY, USA, 2nd edition, 1975.
- [70] J. Smit and H. P. J. Wijn, *Ferrites*, Philips Technical Library, Eindhoven, The Netherlands, 1975.
- [71] N. Guskos, E. A. Anagnostakis, V. Likodimos, et al., "Ferromagnetic resonance and ac conductivity of a polymer composite of Fe₃O₄ and Fe₃C nanoparticles dispersed in a graphite matrix," *Journal of Applied Physics*, vol. 97, no. 2, Article ID 024304, 6 pages, 2005.

Research Article

Dielectric Resonator Method for Measuring the Electrical Conductivity of Carbon Nanotubes from Microwave to Millimeter Frequencies

James Baker-Jarvis,¹ Michael D. Janezic,¹ and John H. Lehman²

¹Electromagnetics Division, National Institute of Standards and Technology (NIST), Boulder, CO 80305-3328, USA

²Optoelectronics Division, National Institute of Standards and Technology (NIST), Boulder, CO 80305-3328, USA

Received 27 February 2007; Accepted 21 June 2007

Recommended by Christian Brosseau

We describe a dielectric resonator-based measurement method for determining the electrical conductivity of carbon nanotubes at microwave to millimeter frequencies. This measurement method is not limited by the metal conductor contact resistances or impedance mismatch commonly encountered in the measurement of single nanotubes. The measurement of carbon nanotubes yielded conductivities of approximately 0.08×10^7 S/m.

Copyright © 2007 James Baker-Jarvis et al. This is an open access article distributed under the Creative Commons Attribution License, which permits unrestricted use, distribution, and reproduction in any medium, provided the original work is properly cited.

1. INTRODUCTION

The objective of this study is to develop an accurate method to measure the electrical conductivity of carbon nanotubes in the gigahertz frequency range that minimizes the effects of contact resistance and impedance mismatch. The application of the high-frequency technique we develop in this paper is new and does not require connections across metallic transmission-line conductors. It therefore bypasses a number of calibration issues that are encountered by the use of other methods.

The dielectric resonator method for loss determination has been used extensively for measurements of the surface resistance of superconducting thin films and for the measurement of metal resistivity [1–3]. The measurement method uses the TE₀₁₁ mode of a sapphire dielectric resonator, as diagrammed in Figure 1 and the resonating fixture as shown in Figure 2. This method is similar to that used by Courtney for measurements of the permittivity of rod specimens; however in this research, the permittivity is determined by measurement, and the conductor losses of the nanotubes are treated as unknown [4].

In applications where nanotubes or nanowires could be used in electrical devices, the operational frequencies would be in the microwave through millimeter bands. Therefore, the measurement of the electrical properties of nanotubes is

important. The theoretical model of the electrical conductivity of nanotubes is usually based on the work of Lüttinger [5]. Over the years, the conductivity of carbon nanotubes has been studied both experimentally and theoretically by a number of different methods [6]. Some researchers have attempted to measure carbon nanotubes individually by welding the nanotubes across microconductors that have been deposited onto transmission lines. Circuit models are then used to estimate the electrical conductivity [5, 7]. The main problem with these approaches is that there is a large impedance mismatch between the nanotube and the transmission line as well as an unknown contact resistance at the position of the weld. The method developed in this paper is not limited by these measurement artifacts. Our method yields a conductivity that is averaged over many nanotubes.

In our method, carbon nanotubes were deposited as a coating on the end-faces of the sapphire rods, and then, the resonators were fitted into a parallel-plate resonator system that allows a measurement of the quality factor (*Q*). Changes in the *Q* of the coated resonators over those of the bare resonators allow for the calculation of the surface resistance and electrical conductivity of bulk nanotube layers [1, 2].

The single-wall carbon nanotube (SWNT) samples for the present work were obtained from Southwest NanoTechnologies produced by the proprietary CoMoCAT process (S-P95-Dry). The manufacturer indicates that the material

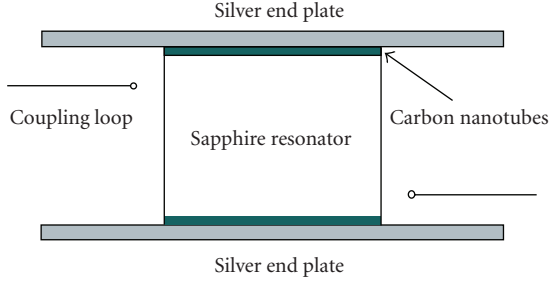


FIGURE 1: A parallel-plate and resonator with a layer of carbon nanotubes deposited on both ends.

content should consist of no more than 5% nonnanotube materials. The resonator coating was formed from the bulk SWNTs dispersed in chloroform, sonicated for 10 minutes and applied with an airbrush at 6.9 kPa [8]. The proportion of carbon nanotubes to chloroform, by mass, was approximately 1 : 100. Resonant Raman Spectroscopy (RRS) of a representative sample of the SWNT coating was performed in the backscattering configuration using 7 mW of an argon ion laser providing 488 nm (2.54 eV) excitation. A 55 mm telephoto lens was employed to both focus the beam to approximately 0.25 mm² area and to collect the Raman scattered light. The scattered light was analyzed with a 0.27 m grating spectrometer equipped with a liquid-nitrogen-cooled, charge-coupled detector and a holographic notch filter. From this we obtained a measure of purity as quantified by the ratio of intensities of “D” and “G” bands, where D/G = 0.0342.

In our procedure, the permittivity of the rod is calculated from the resonant frequency and used to calculate the conductivity of the coated ends of the resonator. Either one or both of the ends can be coated with the unknown nanotube material. Our approach assumes that the researcher has a sufficient amount of carbon nanotubes to coat the upper or lower surfaces of a resonator, or both, to a thickness of a few electrical skin depths. This thickness is sufficient to ensure that very little field penetrates to the silver end plates. When both faces of the sapphire cylinder are terminated with conducting end plates, the surface resistance and electrical conductivity can be calculated from measurements of the shift in Q relative to those of the uncoated resonator [1, 2]. The method is robust since specimens can be measured at various frequencies, from microwave to millimeter frequencies, by use of different size sapphire resonators. Another advantage of this method over other transmission-line methods is that fixture-metal losses are minimized.

In Section 2, we overview the theoretical model for conductivity determination. In Section 3, we introduce the measurement procedure; and in Section 4, we present measurement results.

2. SURFACE RESISTIVITY MODEL

This section is a short overview of the model we used to deconvolve the conductivity from measurements of the Q



FIGURE 2: A parallel-plate resonator measurement fixture.

and resonant frequency. The calculation of the conductivity is based on an electromagnetic field model that uses the Q and resonant frequency f_r of the unloaded and loaded dielectric resonator to obtain an effective conductivity. A transcendental equation for the resonant frequencies is obtained by matching the tangential components of the electric and magnetic fields across the resonator-nanotube interfaces [2]:

$$\frac{J_1(\nu_1 a) K_0(\nu_2 a)}{\nu_1 a} + \frac{K_1(\nu_2 a) J_0(\nu_1 a)}{\nu_2 a} = 0, \quad (1)$$

where a denotes the radius of the sapphire rod, $\nu_1 = \sqrt{k^2 \epsilon_{rs} - (\pi/L)^2}$, and $\nu_2 = \sqrt{(\pi/L)^2 - k^2}$, L is the height of the sapphire rod, $k = \omega/c = \omega/\sqrt{\epsilon_0 \mu_0}$, ϵ_{rs} is the permittivity of the resonator, and J, K denote Bessel and modified Bessel functions, respectively. The roots of (1) determine the permittivity of the rod given the measured resonant frequencies f_r . The measured Q is decomposed into contributions from the nanotubes Q_c and the losses in the dielectric Q_d :

$$\frac{1}{Q} = \frac{1}{Q_c} + \frac{1}{Q_d}, \quad (2)$$

where

$$Q_d = \frac{1+R}{\tan \delta}, \quad (3)$$

where $\tan \delta = \epsilon''/\epsilon'$ and

$$R = \frac{1}{\epsilon_{rs}} \left[\frac{\nu_1 J_0(\nu_1 a)}{\nu_2 K_0(\nu_2 a)} \right]^2 \frac{\int_0^a \rho K_1^2(\nu_2 \rho) d\rho}{\int_0^a \rho J_1^2(\nu_1 \rho) d\rho}. \quad (4)$$

The surface resistance can then be calculated by use of $1/Q_c = 1/Q - 1/Q_d$ with (3) and (4) from

$$R_s = 240\pi^2 \epsilon_r \left[\frac{1}{Q} - \frac{\tan(\delta)}{1+R} \right] \frac{1+R}{1+\epsilon_{rs}R} \left(\frac{L}{\lambda} \right)^3. \quad (5)$$

Once we have obtained R_s , using the knowledge that the material is nonmagnetic, we can calculate the conductivity from

$$\sigma = \frac{\pi f_r \mu_0}{R_s^2}. \quad (6)$$



FIGURE 3: A dielectric resonator with carbon nanotubes deposited on the end surfaces.

The skin depth δ_s is the distance traveled by the fields before they are damped to $1/e$ of their initial value. Estimation of the skin depth is important in order to predict how thick the carbon nanotube layers need to be in order to minimize field penetration. The skin depth is given by

$$\delta_s = \sqrt{\frac{1}{\pi f_r \mu_0 \sigma}}. \quad (7)$$

3. MEASUREMENTS

In order to investigate the frequency dependence of the conductivity, we used two cylindrical single-crystal sapphire resonators machined to have dimensional aspect ratios yielding optimal field structures at 5 and 10 GHz.

We deposited a layer of carbon nanotubes, approximately 30 to 60 μm thick on both of the ends of the sapphire resonators, as shown in Figure 3. The sapphire resonator was placed between two silver end plates in the fixture shown in Figure 2. The coupling loops excited a TE_{011} resonant mode. We measured the Q and resonant frequency of the TE_{011} mode with a network analyzer for both the coated and uncoated resonators. The losses in the carbon nanotubes produces a decrease in the Q factor. We used the Q and f_r to calculate the surface resistance from (5) and thereby the effective conductivity of the carbon nanotubes from (6).

The permittivity of the sapphire resonators were $\epsilon'_r = 9.458$ and $\tan \delta = 1 \times 10^{-6}$. One resonator operated at 4.98 GHz and had a diameter of 23.178 mm and a height of 15.452 mm. The other resonator operated at 9.95 GHz and had a diameter of 11.589 mm and a height of 7.726 mm. Millimeter frequency measurements require smaller resonators. In order for the measurements to be consistent with the model, the layer of carbon nanotubes must be a few skin depths in thickness. Using the measured thickness of 30 μm , we estimate the skin depth from our measured conductivity to be less than 10 μm . Therefore, this thickness is adequate for the fields to decay before it reaches the cavity end walls. For comparison purposes, the skin depth of fields incident

TABLE 1: The measured effective conductivity and associated uncertainties for two sets of depositions of carbon nanotubes.

Configuration	Frequency (GHz)	Conductivity (S/m)	Uncertainty
Resonator 1	9.958	1.8×10^6	$U = 2 \times 10^5$
Resonator 2	4.988	1.8×10^6	$U = 2 \times 10^5$
Resonator 1	9.958	0.8×10^6	$U = 1 \times 10^5$
Resonator 2	4.988	0.4×10^6	$U = 1 \times 10^5$

on our silver-plated fixture is approximately 0.64 μm . The results of the measured conductivity are displayed in Table 1.

The standard uncertainty is defined as $u(x_i)$, where x_i are the independent sources of uncertainty. Uncertainties that can be calculated by statistical means are called Type A. The uncertainties for the resonator were developed by a statistical approach. The combined RSS standard uncertainty is calculated as

$$u_c = \sqrt{\sum_i \left(u(x_i) \frac{\partial \theta}{\partial x_i} \right)^2}. \quad (8)$$

In this paper, the measurand is σ and we included the independent uncertainties due to the sapphire resonator dimensions, film thickness, Q determination, and resonant frequency. The uncertainties of the Q and thickness of the material dominated. The expanded uncertainty is $U(\theta) = k u_c(\theta)$, where k is the coverage factor. We have used $k = 2$. We noted a relatively large systematic uncertainty between different coatings of carbon nanotubes. The origins of this systematic uncertainty is probably due to the deposition process and possibly variations in nanotubes.

4. CONCLUSIONS

The resonator method described in this paper bypasses some of the difficulties encountered in single-strand methods. Our results yield conductivities that are slightly greater than that reported by other authors. For example, Ma 0.05×10^7 S/m reported [9]. We believe this is due in part to variations between nanotubes and the fact that our measurements are minimally influenced by metal losses. We have observed some variations of conductivity from different carbon nanotube batches probably due to variations in the carbon nanotubes, or deposition process and thickness uncertainties. In transmission lines at micro wave frequencies, losses due to metal influences can be appreciable. The resonator method has a very low uncertainty if the thickness of the coating is known accurately and if the coating is thick enough for the fields to decay before the copper cavity endplates. Most of the contributions to the uncertainties in Table 1 are due to these factors. Some limitations and restrictions of our method include the amount of nanotube material required, variations in the thickness of the carbon-nanotube layer; and the method yields an ensemble-averaged conductivity. This method should work equally well for any type of nanowire.

REFERENCES

- [1] J. Krupka, M. Klinger, M. Kuhn, et al., "Surface resistance measurements of HTS films by means of sapphire dielectric resonators," *IEEE Transactions on Applied Superconductivity*, vol. 3, no. 3, pp. 3043–3048, 1993.
- [2] Z.-Y. Shen, C. Wilker, P. Pang, W. L. Holstein, D. Face, and D. J. Kountz, "High T_c superconductor-sapphire microwave resonator with extremely high Q-values up to 90 K," *IEEE Transactions on Microwave Theory and Techniques*, vol. 40, no. 12, pp. 2424–2431, 1992.
- [3] J. Baker-Jarvis, M. D. Janezic, B. Riddle, et al., "Measuring the permittivity and permeability of lossy materials: solids, liquids, metals, building materials, and negative-index materials," Tech. Rep. 1536, National Institute of Standards and Technology, Boulder, Colo, USA, February 2005.
- [4] W. E. Courtney, "Analysis and evaluation of a method of measuring the complex permittivity and permeability of microwave insulators," *IEEE Transactions on Microwave Theory and Techniques*, vol. 18, no. 8, pp. 476–485, 1970.
- [5] P. J. Burke, "Luttinger liquid theory as a model of the gigahertz electrical properties of carbon nanotubes," *IEEE Transactions on Nanotechnology*, vol. 1, no. 3, pp. 129–144, 2002.
- [6] P. Singjai, S. Changsarn, and S. Thongtem, "Electrical resistivity of bulk multi-walled carbon nanotubes synthesized by an infusion chemical vapor deposition method," *Materials Science and Engineering A*, vol. 443, no. 1-2, pp. 42–46, 2007.
- [7] P. Chiu and I. Shih, "A study of the size effect on the temperature-dependent resistivity of bismuth nanowires with rectangular cross-sections," *Nanotechnology*, vol. 15, no. 11, pp. 1489–1492, 2004.
- [8] J. H. Lehman, C. Engtrakul, T. Gennett, and A. C. Dillon, "Single-wall carbon nanotube coating on a pyroelectric detector," *Applied Optics*, vol. 44, no. 4, pp. 483–488, 2005.
- [9] R. Z. Ma, C. L. Xu, B. Q. Wei, J. Liang, D. H. Wu, and D. J. Li, "Electrical conductivity and field emission characteristics of hot-pressed sintered carbon nanotubes," *Materials Research Bulletin*, vol. 34, no. 5, pp. 741–747, 1999.

Research Article

Electromagnetic Modelling of Raman Enhancement from Nanoscale Structures as a Means to Predict the Efficacy of SERS Substrates

Richard J. C. Brown, Jian Wang, and Martin J. T. Milton

Analytical Science Group, National Physical Laboratory, Teddington, Middlesex TW11 0LW, UK

Received 19 March 2007; Accepted 31 July 2007

Recommended by Christian Brosseau

The requirement to optimise the balance between signal enhancement and reproducibility in surface enhanced Raman spectroscopy (SERS) is stimulating the development of novel substrates for enhancing Raman signals. This paper describes the application of finite element electromagnetic modelling to predict the Raman enhancement produced from a variety of SERS substrates with differently sized, spaced, and shaped morphologies with nanometre dimensions. For the first time, a theoretical comparison between four major generic types of SERS substrate (including metal nanoparticles, structured surfaces, and sharp tips) has been performed and the results are presented and discussed. The results of the modelling are consistent with published experimental data from similar substrates.

Copyright © 2007 Richard J. C. Brown et al. This is an open access article distributed under the Creative Commons Attribution License, which permits unrestricted use, distribution, and reproduction in any medium, provided the original work is properly cited.

1. INTRODUCTION

Recent developments in techniques for the detection of single molecules have opened up new opportunities for research in analytical chemistry and the life sciences [1–3]. One technique that has a wide range of potential applications is surface enhanced Raman spectroscopy (SERS) [4–7]. SERS is a noninvasive technique that can detect and characterise both simple organic [8, 9], and complex biological molecules [10, 11] at ultralow, and even single molecular concentrations. The sensitivity of SERS is particularly important since there is a growing emphasis on trace-level detection in analytical research [12].

The basis of the SERS technique is the capacity of metallic substrates to support the propagation of surface plasmons with resonant frequencies in the visible region of the electromagnetic spectrum [13]. These surface plasmons act to enhance the native Raman signal by producing an increased electric field in the vicinity of the target molecule [14, 15]. In addition to this “electromagnetic mechanism,” Raman signals from target molecules are also enhanced by a more complex and less well-quantified “chemical” or “electronic” mechanism, although previous studies have shown that this is usually small in comparison to the electromag-

netic effect [16]. Silver and gold are the most widely used materials for SERS substrates and are most commonly used in the form of spherical particles on the nanometre scale [17, 18]. In addition to these metal nanoparticles, other substrate types (Figure 1), such as nanostructured surfaces, and the tip-surface geometries offered by scanning probe microscopies, are being used increasingly for SERS experimentation [19]. However, little work has been published that compares the fundamental characteristics of these different substrate types for enhancing Raman signals. Moreover, if candidate SERS substrates could be assessed, and optimised by modelling their electromagnetic characteristics, time and effort could be saved in laboratory preparation and experimental testing.

Much effort has been expended in modelling the mechanisms of electromagnetic scattering accurately [20, 21]. It is a complex problem because the nature of the secondary waves generated by scattering are determined not only by the characteristics of the incident wave but also by the field generated by other scatterers nearby. Therefore, for most practical situations, such as those encountered in SERS, numerical methods are employed. As the field enhancement is strongly dependent on physical parameters, such as the surface morphology, the optical constants used to perform

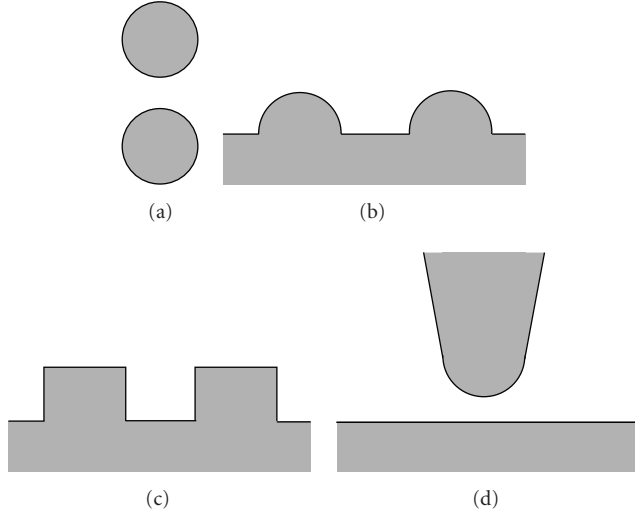


FIGURE 1: Diagrammatic representations of a section through the four generic types of SERS substrates modelled: (a) two nanoparticles, (b) structured surface with hemispherical features, (c) structured surface with cuboid features, and (d) tip surface.

the modelling, and the excitation conditions, detailed computational consideration is required to achieve robust models. Validation of these numerical results is challenging as direct experimental measurement of the field enhancement is usually not possible. However, we have previously shown that Raman enhancements from metal nanoparticles obtained experimentally agree with predictions from modelling to within one order of magnitude [16].

This paper presents the results of the predicted Raman enhancement, obtained using electromagnetic modelling, from four major generic types of SERS substrate. These generic substrates are shown diagrammatically in Figure 1.

The electric field enhancement between a pair of metal nanoparticles has received some study previously [16, 22], but the other substrates modelled here have received less attention. In this work, similar sizes and separations of features for each of the substrate types have been modelled so that the results may be compared. The results enable the relative enhancement from these commonly used substrates to be compared in detail for the first time.

2. EXPERIMENTAL

We have modelled the field distribution from four generic SERS metallic nanostructures in two dimensions. They can be considered as sections through a three-dimensional artefact at the point of maximum enhancement. For the substrates modelled here this will occur at the point of closest approach of the nanostructured features. For the two nanoparticles, this is along the line of their centres, and for a tip-surface substrate, this is in the plane passing through the centre of the point of tip. The substrates modelled are illustrated in detail in Figures 2, 3, 4, and 5. In all cases, silver substrates are considered and published optical constants for silver [23] that have been widely used for modelling studies have been

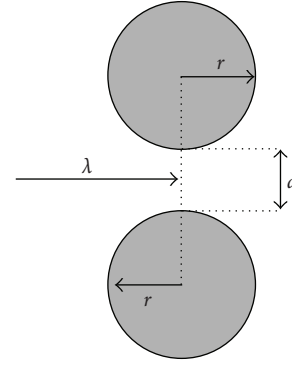


FIGURE 2: Section through two nanoparticles. The quantities varied during the modelling process were: r , the radius of the nanoparticles; d , the separation of the nanoparticles; and λ , the wavelength of the incident monochromatic radiation, which was incident normal to the line joining the centres of the nanoparticles.

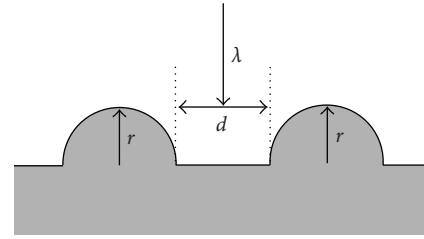


FIGURE 3: Section through the structured surface with hemispherical features. The quantities varied during the modelling process were: r , the radius of the metal hemispheres on the metal surface; d , the separation of the metal hemispheres; λ , the wavelength of the incident monochromatic radiation, which was incident normal to the metal surface.

employed. The polarisation of the incoming radiation (between 300 and 800 nm) was in the incident plane to ensure excitation of surface plasmons. In the case of the structured surfaces, and the surface in the tip-surface substrate, the modelled structures are large enough that the maximum predicted enhancement is not influenced by the size of these boundaries.

The incident electromagnetic field in the complex-field representation can be written as follows:

$$\begin{aligned} E(\mathbf{r}, t) &= E_0 \exp(ik \cdot \mathbf{r} - i\omega t), \\ H(\mathbf{r}, t) &= H_0 \exp(ik \cdot \mathbf{r} - i\omega t), \end{aligned} \quad (1)$$

where $E(\mathbf{r}, t)$ and $H(\mathbf{r}, t)$ are the electric and magnetic field components, respectively, at location \mathbf{r} and time t ; E_0 and H_0 are the electric and magnetic field amplitudes, respectively, k is the wavevector, and ω is the angular frequency of the wave. In the absence of nonlinear optical effects and when only the elastic scattering process is considered, the electromagnetic fields surrounding the scatterers must be self-consistent, leading to the following conditions:

$$\begin{aligned} E(\mathbf{r}, t) &= E_{\text{in}}(\mathbf{r}, t) + E_{\text{sc}}(\mathbf{r}, t), \\ H(\mathbf{r}, t) &= H_{\text{in}}(\mathbf{r}, t) + H_{\text{sc}}(\mathbf{r}, t), \end{aligned} \quad (2)$$

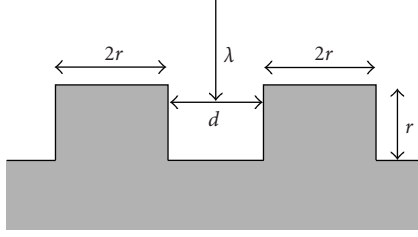


FIGURE 4: Section through the structured surface with cuboid features. The quantities varied during the modelling process were: r , the half-width, and the depth, of the metal cuboids on the metal surface; d , the separation of the metal cuboids; λ , the wavelength of the incident monochromatic radiation, which was incident normal to the metal surface. The corners of the structure have been rounded slightly, with radii of curvature of 1 nm, to make the modelled situation more realistic.

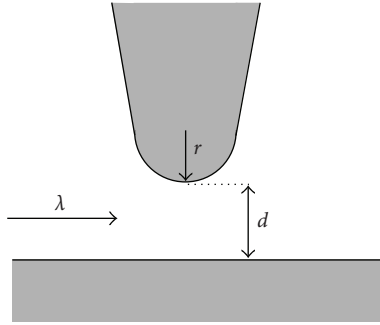


FIGURE 5: Section through the tip-surface substrate. The quantities varied during the modelling process were: r , the radius of the metal tip at its sharpest point; d , the separation of the metal tip from the surface; λ , the wavelength of the incident monochromatic radiation, which was incident parallel to the metal surface.

where the subscripts “in” and “sc” denote the incident and scattered waves, respectively. The electromagnetic waves must satisfy Maxwell’s equations within the modelling domain, and adhere to the boundary equations at the interface between the media and the scatterer, leading to the following conditions:

$$\begin{aligned} \nabla \times (\nabla \times E) - \omega^2 \epsilon \mu E &= 0, \\ \nabla \times (\nabla \times H) - \omega^2 \epsilon \mu H &= 0, \\ (E_2(\mathbf{r}) - E_1(\mathbf{r})) \times \mathbf{n} &= 0, \\ (H_2(\mathbf{r}) - H_1(\mathbf{r})) \times \mathbf{n} &= 0, \end{aligned} \quad (3)$$

where the ϵ and μ are the complex-valued permittivity and permeability and \mathbf{r} is on the boundary of the scatterer, and \mathbf{n} is a unit vector orthogonal to the boundary. The field distribution must be a solution of these equations. Finite element methods (FEM) using Comsol Multiphysics software [24] have been employed to provide numerical solutions to these equations for each substrate. Previous studies have also used FEM to model the field enhancement and spectral response in the vicinity of rough surfaces [25] and nanoparticles [26]. The FEM methodology requires the creation of a “radiation boundary condition” or “absorption boundary condition” to truncate the modelling scenario into a confined domain. The

“perfect matched layers” (PML) boundaries method [27] has been used for this simulation. This matches the optical index at the interface of the media and attenuates the wave quickly within the artificial layer so that little or no electromagnetic radiation will be reflected back into the domain of scattering. Additionally, a low-reflection boundary condition is applied at the outer PML boundary in order to minimise residual reflection. In this way, the possibility of artefacts occurring in the modelling output is minimised.

The output of the modelling process is a two-dimensional map of the electric field intensity which can be used to calculate the Raman enhancement $G_{(r,\omega)}$ using [28]:

$$G_{(r,\omega)} = \left| \frac{\hat{E}_{\text{loc}}(\omega_L)}{\hat{E}_{\text{free}}} \right|^2 \left| \frac{\hat{E}_{\text{loc}}(\omega)}{\hat{E}_{\text{free}}} \right|^2, \quad (4)$$

where ω_L and ω are the frequencies of the incident and scattered light, respectively; \hat{E}_{loc} and \hat{E}_{free} are the absolute values of the local vector potentials (normalised to the intensities of the incident and scattered light) in the presence and absence, respectively, of the substrate. When the polarisation of the scattered light is the same as that of the incident light, the expected electromagnetic enhancement of the Raman signal may be expressed to a first approximation (for example Otto [28], Pendry [29], Moskovits [13], and Kneipp [30]) as

$$G_{(r,\omega)} = \left| \frac{E_{(r,\omega)}}{E_{\text{inc}(\omega)}} \right|^4, \quad (5)$$

where $E_{(r,\omega)}$ is the total predicted electric field at position r , and $E_{\text{inc}(\omega)}$ is the electric field associated with the incoming electromagnetic radiation. The maximum value of the Raman enhancement ($G_{\text{max}(r,\omega)}$) can be calculated from any given situation. Three practical definitions of this maximum have been used in this work:

- the maximum value for $G_{(r,\omega)}$ obtained over the entire simulation area;
- the maximum value for $G_{(r,\omega)}$ obtained in a 5 nm² area in the region of closest approach of the two metallic structures of interest;
- the average value for $G_{(r,\omega)}$ obtained in a 5 nm² area in the region of closest approach of the two metallic structures of interest.

Figure 6 shows the maximum enhancement calculated according to these three definitions for two silver nanoparticles each with a radius of 25 nm and separated by 3 nm. As can be seen, the three definitions lead to values of the Raman enhancement that are comparable to better than an order of magnitude at wavelengths longer than 350 nm. At wavelengths shorter than 350 nm, the maximum Raman enhancement is often predicted to be displaced from the region of closest approach of the two metallic structures of interest, therefore definition (a) produces higher enhancement factors. In order to avoid misinterpreting cases where the maximum Raman enhancement does not occur in the region of closest approach of the two metallic structures of interest, definition (a) was chosen as the method for calculating $G_{\text{max}(r,\omega)}$ from the substrates presented here.

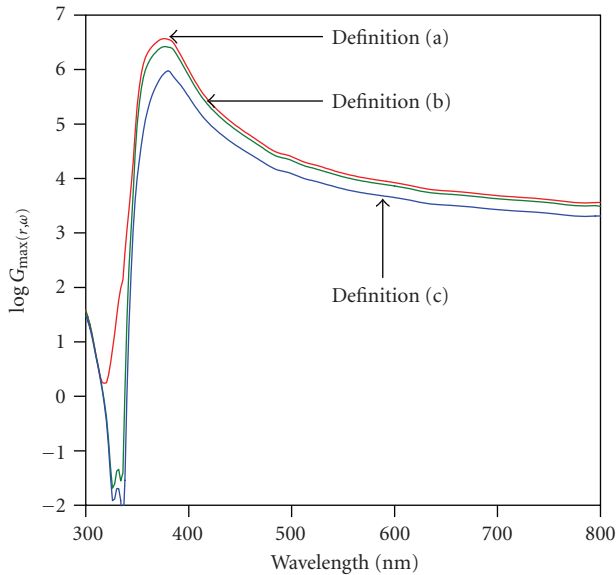


FIGURE 6: Wavelength dependence of the maximum Raman enhancement predicted using definition (a), (b), and (c) for two silver nanoparticles each with a radius of 25 nm separated by 3 nm.

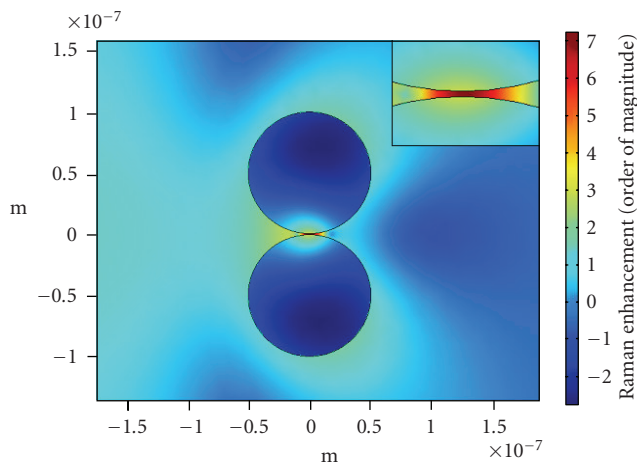


FIGURE 7: Modelled Raman enhancements around two silver nanoparticles; $r = 50$ nm, $d = 1$ nm, $\lambda = 514$ nm. The inset shows an enlarged portion around the area between the nanoparticles. The colours in red correspond to the areas of highest Raman enhancement and those in blue to the areas of lowest Raman enhancement.

Figure 7 shows an example of the distribution of predicted Raman enhancement around two silver nanoparticles.

Validation of the modelling procedure was carried out against published data; in particular, Garcia-Vidal's implementation of Maxwell's equations on adaptive meshes for the study of the interaction of light with metals surfaces [29] and with Xu et al.'s study of colloid particle shape and size on the electromagnetic enhancement factor using classic electromagnetic theory [31]. In these cases, the methodology used here produced comparable enhancement factors to those predicted by Garcia-Vidal for structured metal surfaces for incident wavelengths of light between 310 and 620 nm.

(Although these results were based on silver hemicylinders placed on a silver surface, a two-dimensional section through such a substrate, orthogonal to the cylinder axis, should be comparable to a similar section through hemispheres on a surface). The modelling used here also produces results that are comparable to Xu et al.'s predictions of enhancement factors for spherical particle substrates with separations of 1 nm and 5 nm (similar to the nanoparticles arrays being modelled in this study) to within an order of magnitude. This level of agreement with published data from two quite different studies confirms the applicability and flexibility of the modelling methodology used here for predicting Raman enhancement factors. Taking this data into consideration, the uncertainty in the predicted Raman enhancement data, within and between modelling scenarios, is approximately one order of magnitude. The uncertainty of the ratios of predicted enhancement factors within the same modelling scenario may be less than this.

3. RESULTS AND DISCUSSION

3.1. Two nanoparticles

The results of the modelling of the two nanoparticle substrate (Figure 2) is shown in Figure 8.

The principal trend in the modelled data is that predicted Raman enhancement increases as the separation of the features decreases. This relationship is strong—the difference in predicted maximum Raman enhancement from two nanoparticles 1 nm apart and 25 nm apart can be as much as six orders of magnitude. The maximum Raman enhancement predicted for these nanoparticles is of the same order of magnitude as the enhancement levels regularly observed experimentally by us and other groups [16, 32, 33]—approximately 10^9 . A comparison of the predicted results for different nanoparticle sizes in Figures 8(a), 8(b), and 8(c) shows that the maximum predicted enhancements are relatively similar. These trends are summarised in Figure 9.

Figure 9 illustrates the decrease in predicted maximum enhancement with increasing feature separation, and also shows that this relationship is relatively insensitive to feature size. It also shows that the wavelength at which the Raman maxima are predicted becomes shorter as the feature separation increases. Figure 10 shows that the average predicted enhancement between 350 and 800 nm, $G_{ave(350-800\text{ nm})}$, generally increases with feature size for any given feature separation.

3.2. Structured surfaces

Two nanostructured surfaces have been modelled; one with hemispherical features and the other with cuboid features. These are similar to substrates that can be produced by templating techniques (for the structured surfaces with hemispherical features) or e-beam lithography techniques (for the structured surfaces with cuboid features). The results of modelling the wavelength dependence of the maximum Raman enhancement for these surfaces are shown in Figures 11 and 12, respectively.

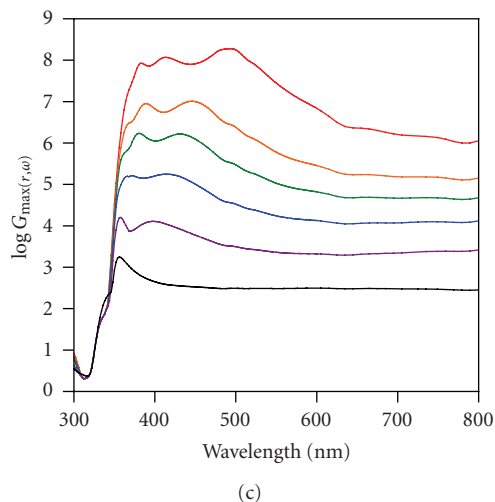
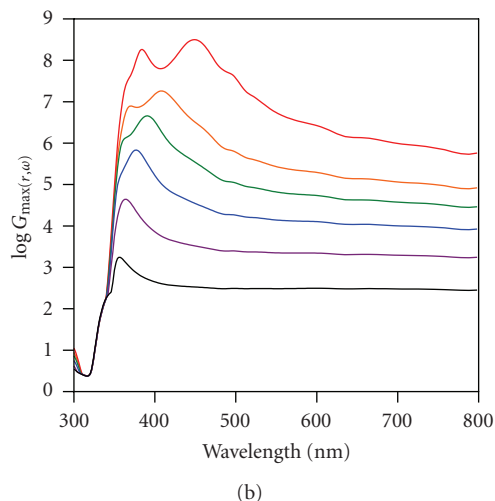
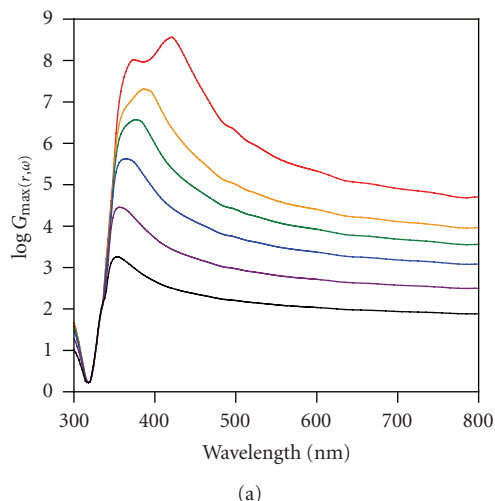


FIGURE 8: Modelled wavelength dependence of the maximum Raman enhancement from two silver nanoparticles, as shown in Figure 2, with radii r of: (a), 25 nm, (b), 50 nm, and (c), 75 nm. The separations of the two nanoparticles that have been modelled are: 1 nm (top curve), 2 nm, 3 nm, 5 nm, 10 nm, and 25 nm (bottom curve).

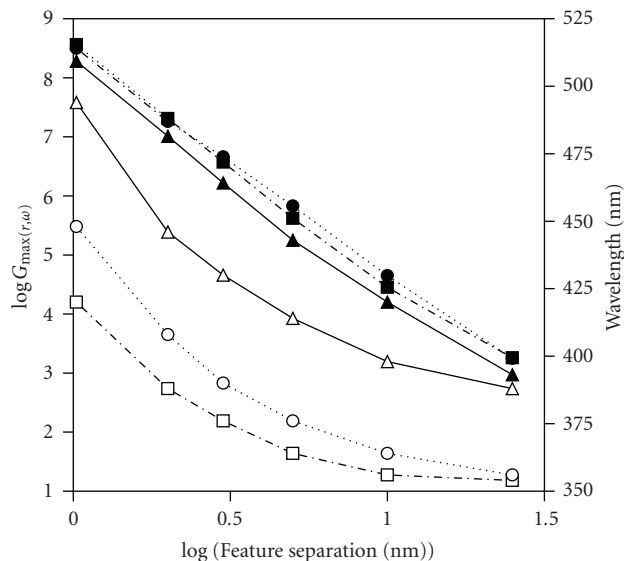


FIGURE 9: Relationship between the maximum predicted Raman enhancement and the separation of the two silver nanoparticles with radii of: 25 nm (■), 50 nm (●), and 75 nm (▲). Additionally the dependence of the wavelength at which the maximum Raman enhancement is predicted to occur on the separation of the two silver nanoparticles with radii of: 25 nm (□), 50 nm (○), and 75 nm (△).

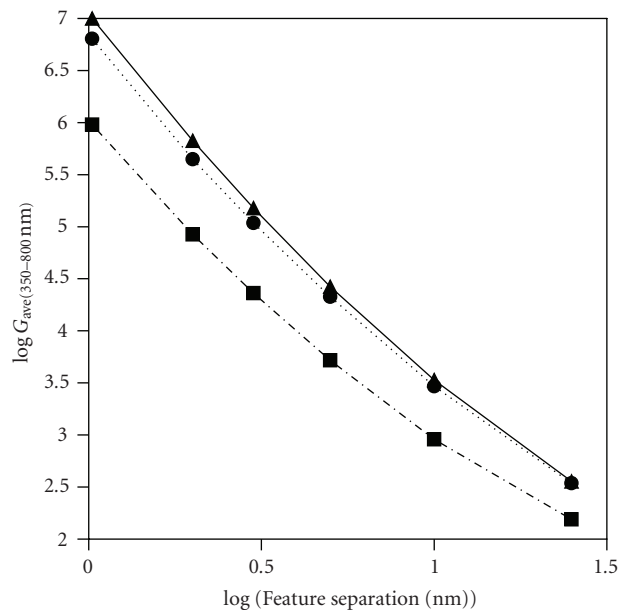


FIGURE 10: Relationship between the average predicted Raman enhancement between 350 and 800 nm and the separation of the two silver nanoparticles with radii of: 25 nm (■), 50 nm (●), and 75 nm (▲).

The results from the modelling of the surface with hemispherical features show several differences from the results for the two nanoparticles (Figure 8). In general, the enhancements observed are higher than those for the two nanoparticles at shorter wavelengths, but drop off more quickly as the wavelength increases and are generally lower than those

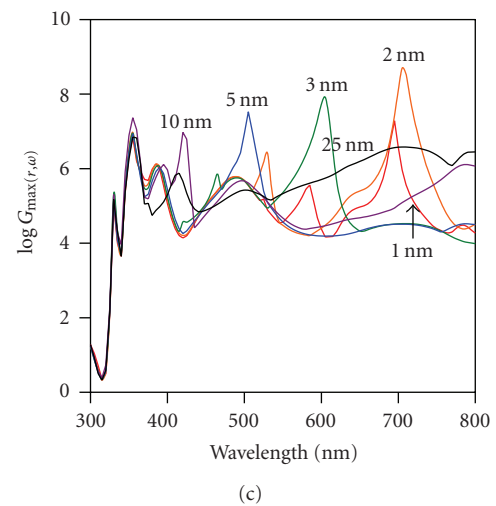
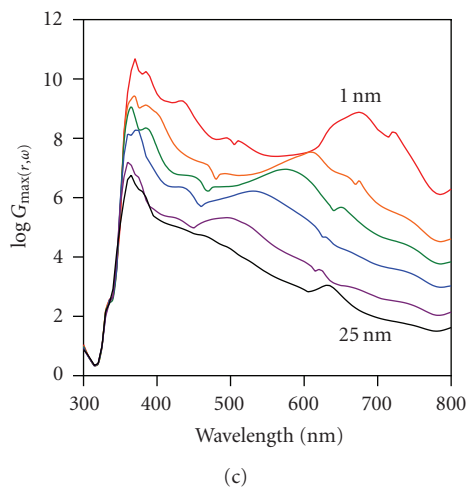
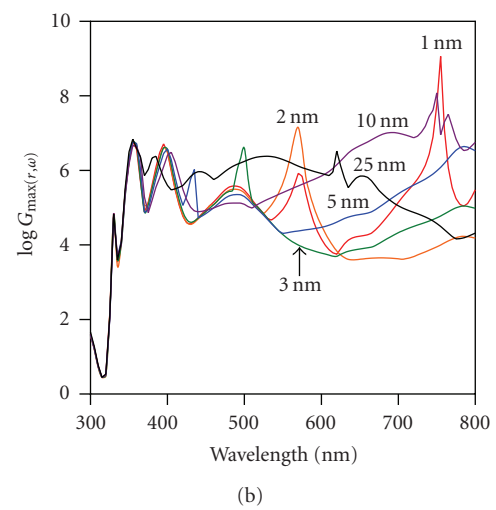
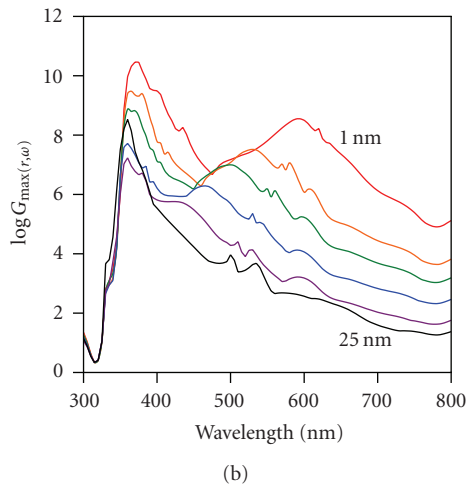
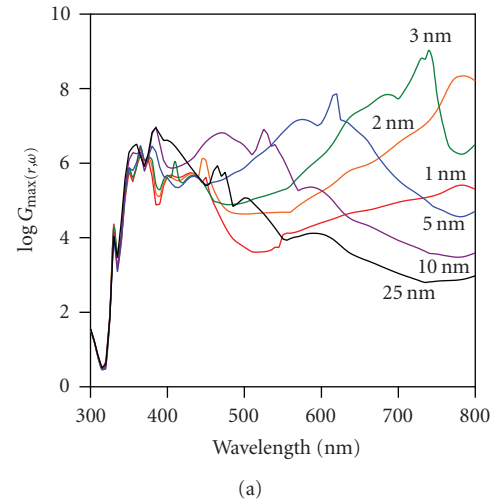
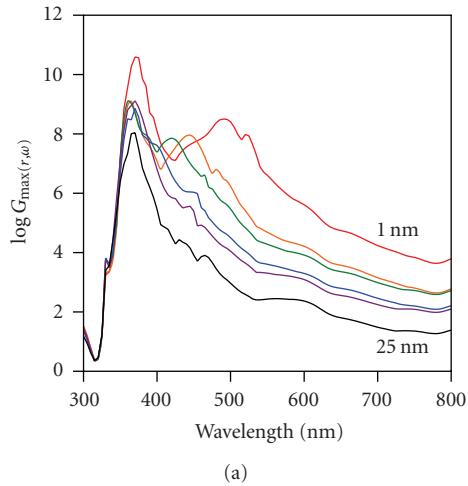


FIGURE 11: Modelled wavelength dependence of the maximum Raman enhancement from a structured silver surface with silver hemispherical features, as shown in Figure 3, with radii r of: (a), 25 nm, (b), 50 nm, and (c), 75 nm; on a flat silver surface. In each case, the separations of the hemispherical features are: 1 nm (top curve at long wavelengths), 2 nm, 3 nm, 5 nm, 10 nm, and 25 nm (bottom curve at long wavelengths).

FIGURE 12: Modelled wavelength dependence of the maximum Raman enhancement from a structured silver surface with silver cuboid features, as shown in Figure 4, with radii r of: (a), 25 nm, (b), 50 nm, and (c), 75 nm; on a flat silver surface. In each case the separations of the cuboid features are: 1 nm, 2 nm, 3 nm, 5 nm, 10 nm, and 25 nm.

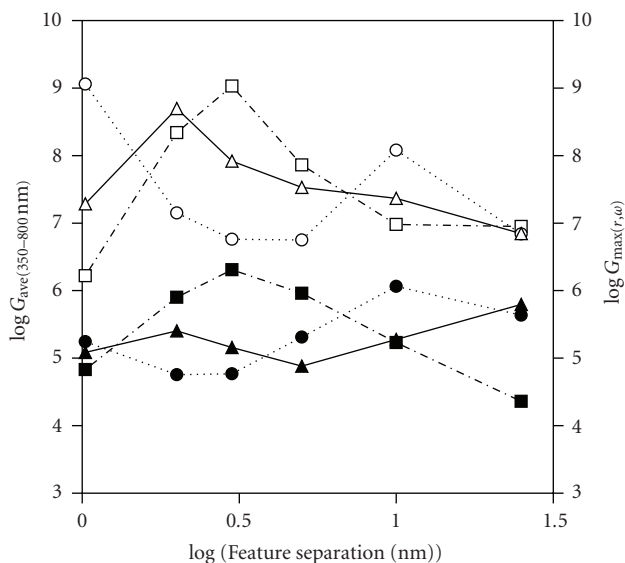


FIGURE 13: Relationship between the average predicted Raman enhancement (between 350 and 800 nm) and the separation of the cuboid features on the structured surface with half-width r of: 25 nm (■), 50 nm (●), and 75 nm (▲); and between the average maximum predicted Raman enhancement the separation of the cuboid features on the structured surface with half-width r of: 25 nm (□); 50 nm (○); and 75 nm (△).

observed for the two nanoparticles at longer wavelengths. The predicted enhancements from the structured surfaces with hemispherical features show a more complex dependence on wavelength than that observed for the two nanoparticles. The maximum enhancements predicted are less sensitive to feature separation than that for the two nanoparticles. Average enhancements from 350 to 800 nm drop off rapidly with increasing feature separation, but are generally an order of magnitude higher than for the two nanoparticles. The enhancements predicted correspond well with those observed in experimental studies for metal film over nanosphere (MFON) [34] and nanoembossed substrates [35].

The enhancement characteristics of the structured surface with cuboid features show a complex dependence on separation and wavelength (Figure 12). Most strikingly the predicted enhancements do not decrease monotonically with increasing wavelength, and with increasing feature separations. In many cases, the highest predicted enhancements are at longer wavelengths than for the other substrates, and for structures that do not have the smallest feature separations. The modelling predicts a slight decrease in the predicted enhancement with increasing feature separation, but very little change in average enhancement levels. Moreover, the enhancement levels predicted are not inconsistent with those observed from similar surfaces in experimental studies [36, 37] and from other modelling investigations [38]. These observations are illustrated by the relationship between the predicted enhancements and feature separation shown in Figure 13.

3.3. Tip surface

The results of modelling the wavelength dependence of the maximum Raman enhancement for the different tip-surface separations (Figure 5) are shown in Figure 14.

The enhancements observed from the tip-surface substrate show similar levels and wavelength trends to those predicted for the two nanoparticles. However, as the incident wavelength increases, the predicted enhancement shows a more complex wavelength dependence. Rather than a monotonic decrease in predicted enhancement from short to long wavelengths, at longer wavelengths the maximum enhancement actually shows an increase (particularly for the larger tip-surface separations). As the size of the tip radius increases there is a small increase in predicted overall enhancement levels. The tip-surface substrate shows very similar average and maximum predicted enhancements across the wavelengths as seen with the two nanoparticles. The predicted enhancements for the tip-surface substrate agree well with experimental data in the literature [39].

3.4. Comparison of the four generic substrate types

The four generic substrate types are compared in Figure 15 for features of $r = 50$ nm and separations of 1 nm. The trends observed for 75 nm feature sizes best illustrate the relationships between the four substrates, however the trends for feature sizes of 50 nm and 25 nm are similar.

As can be seen in Figure 15(a), enhancements decrease as feature separations increase for all four substrates. In general, the structured surfaces produce larger enhancements across all feature separations, whilst the predicted enhancement from the tip surface and the two nanoparticles decreases sharply with increasing feature separation. The structured surfaces remain very efficient Raman enhancers, even at larger feature separations. Figure 15(b) shows that the average Raman enhancement decreases with increasing feature separation for all substrates except the structured surface with cuboid features. For this substrate, the average enhancement is relatively low but remains constant even up to feature separations of 25 nm.

Figure 16 shows how the wavelength at which the maximum Raman enhancement is predicted varies with feature separation for the four substrates. In general, the wavelength of maximum predicted enhancement decreases as the feature separation increases, with all four substrates displaying a wavelength of maximum enhancement between 375 and 400 nm at a feature separation of 25 nm. However, the rate at which this decrease occurs increases in the following order: structured surface with hemispherical features < tip surface < two nanoparticles \ll structured surface with cuboid features.

4. CONCLUSIONS

The relative SERS performance of four generic substrate types that are commonly used in SERS have been modelled and their predicted Raman enhancements compared. Whilst the substrates modelled here only represent simplified

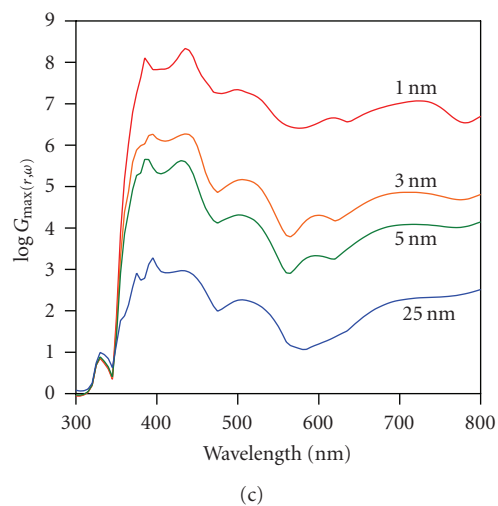
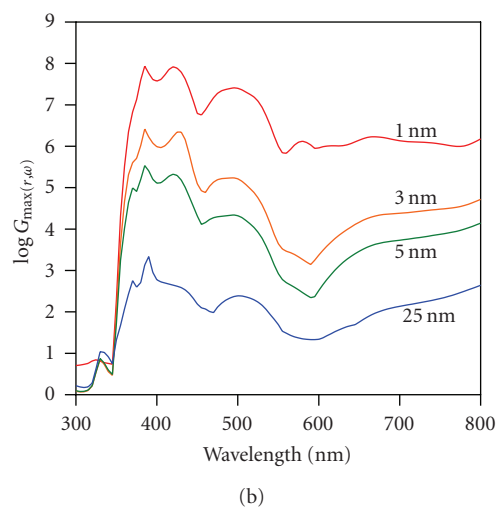
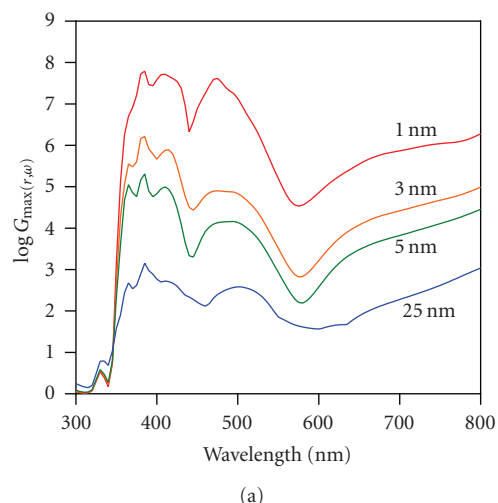


FIGURE 14: Modelled wavelength dependence of the maximum Raman enhancement predicted from silver tips and a silver surface, as shown in Figure 5, of end radii r of: (a), 25 nm, (b), 50 nm, and (c), 75 nm; in close proximity to a silver surface. In each case the separations of the tip and the surface that have been modelled are: 1 nm, 3 nm, 5 nm, and 25 nm.

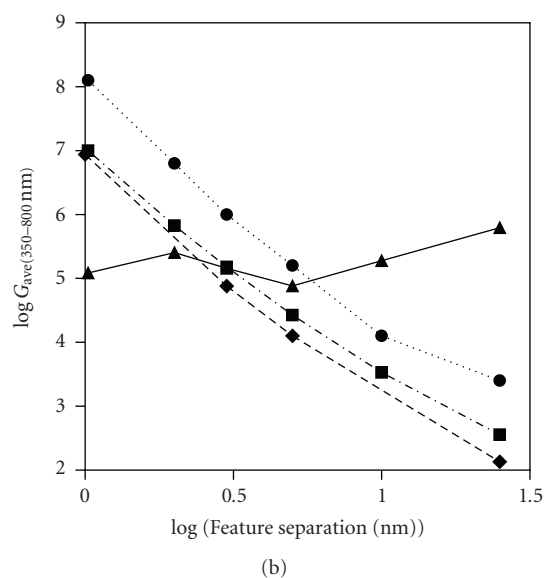
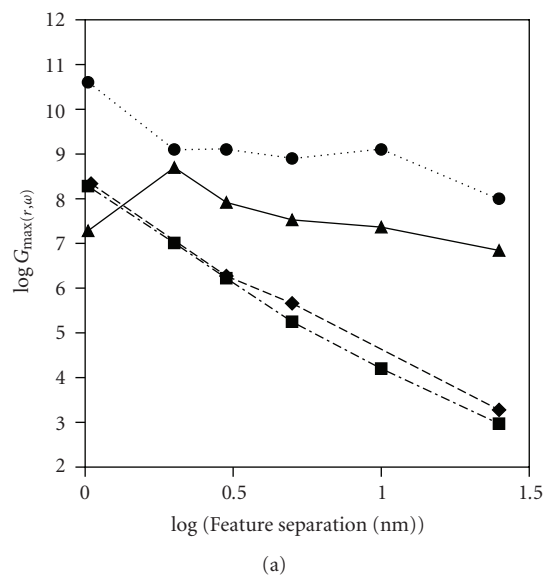


FIGURE 15: Maximum (Figure 15(a)) and average (between 350 and 800 nm) (Figure 15(b)) predicted Raman enhancements, against feature separation for: two nanoparticles (■); structured surface with hemispherical features (●); structured surface with cuboid features (▲); and tip-surface (◆), for features of $r = 75$ nm.

approximations of real experimental situations, the levels of enhancement predicted agree, in most cases, within an order of magnitude of what has been observed experimentally in the literature.

The study has shown that the predicted Raman enhancement is very sensitive to substrate feature separation over the range modelled (1 nm and 25 nm). In addition, average enhancements across the wavelength range modelled (300–800 nm) decrease with increasing feature separation, with the exception of the structured surface with cuboid features, which shows little change in average enhancement levels. Comparison of the four different generic substrate types

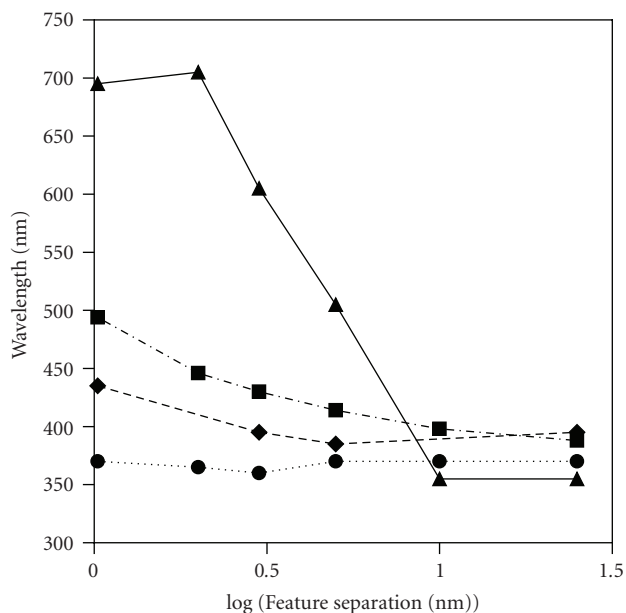


FIGURE 16: Relationship between the wavelength at which the predicted Raman enhancements is at a maximum and feature separation for: two nanoparticles (■); structured surface with hemispherical features (●); structured surface with cuboid features (▲); and tip-surface (◆), for features of $r = 75$ nm.

has revealed that structured surfaces produce larger maximum enhancements than the two nanoparticle or tip-surface substrates. Moreover, the structured surfaces show the most complicated relationships between predicted enhancement and wavelength. The behaviour of two nanoparticle and tip-surface substrates is similar and they produce comparable enhancement levels.

The results presented here predict that a structured surface with hemispherical features produces the largest maximum enhancements at all feature separations and the largest average enhancements at small feature separation. However, the structured surfaces with cuboid features show the most consistent maximum and average enhancements over all feature separations, and the largest average enhancements at large feature separations. An especially important finding of this work is that the average predicted enhancement from a structured surface with cuboid features over the wavelengths modelled shows very little sensitivity to feature size or separation. This suggests that it may not be necessary to manufacture these as precisely as was previously thought, indicating that they could perhaps be prepared to poorer tolerances, with little impact on their efficacy as substrates.

Experimentally, fabrication of structured surface is more time consuming and expensive than the preparation of metal nanoparticles. Tip-surface substrates are even more difficult to implement, but may provide the only way of performing robust SERS mapping of a surface, because the enhancement of the Raman signal is localised at the tip position. Therefore, a balance must be found between performance, reproducibility, and cost effectiveness of these substrates. It is clear that design and modelling of these surfaces prior to manufacture

can save a large amount of experimental effort in this optimisation process. This work has shown that using the techniques presented here, robust and accurate model of SERS substrates is possible that can contribute to improving the efficiency of the research and development process in SERS.

REFERENCES

- [1] R. Petry, M. Schmitt, and J. Popp, "Raman spectroscopy—a prospective tool in the life sciences," *ChemPhysChem*, vol. 4, no. 1, pp. 14–30, 2003.
- [2] H. G. M. Edwards, "Probing history with Raman spectroscopy," *The Analyst*, vol. 129, no. 10, pp. 870–879, 2004.
- [3] A. J. de Mello, "Seeing single molecules," *Lab on a Chip*, vol. 3, no. 2, pp. 29N–34N, 2003.
- [4] A. M. Michaels, M. Nirmal, and L. E. Brus, "Surface enhanced Raman spectroscopy of individual rhodamine 6G molecules on large Ag nanocrystals," *Journal of the American Chemical Society*, vol. 121, no. 43, pp. 9932–9939, 1999.
- [5] S. R. Emory and S. Nie, "Near-field surface-enhanced Raman spectroscopy on single silver nanoparticles," *Analytical Chemistry*, vol. 69, no. 14, pp. 2631–2635, 1997.
- [6] D. Zeisel, V. Deckert, R. Zenobi, and T. Vo-Dinh, "Near-field surface-enhanced Raman spectroscopy of dye molecules adsorbed on silver island films," *Chemical Physics Letters*, vol. 283, no. 5-6, pp. 381–385, 1998.
- [7] P. Etchegoin, H. Liem, R. C. Maher, et al., "A novel amplification mechanism for surface enhanced Raman scattering," *Chemical Physics Letters*, vol. 366, no. 1-2, pp. 115–121, 2002.
- [8] C. Rodger, V. Rutherford, P. C. White, and W. E. Smith, "Towards quantitative surface enhanced resonance Raman scattering (SERRS): a study of aggregation and concentration for two rhodamine dyes," *Journal of Raman Spectroscopy*, vol. 29, no. 7, pp. 601–606, 1998.
- [9] K. Kneipp, E. Roth, C. Engert, and W. Kiefer, "Near-infrared excited surface-enhanced Raman spectroscopy of rhodamine 6G on colloidal silver," *Chemical Physics Letters*, vol. 207, no. 4–6, pp. 450–454, 1993.
- [10] P. Etchegoin, H. Liem, R. C. Maher, et al., "Observation of dynamic oxygen release in hemoglobin using surface enhanced Raman scattering," *Chemical Physics Letters*, vol. 367, no. 1-2, pp. 223–229, 2003.
- [11] P. Etchegoin, R. C. Maher, L. F. Cohen, et al., "New limits in ultrasensitive trace detection by surface enhanced Raman scattering (SERS)," *Chemical Physics Letters*, vol. 375, no. 1-2, pp. 84–90, 2003.
- [12] R. J. C. Brown and M. J. T. Milton, "Analytical techniques for trace element analysis: an overview," *Trends in Analytical Chemistry*, vol. 24, no. 3, pp. 266–274, 2005.
- [13] M. Moskovits, "Surface-enhanced spectroscopy," *Reviews of Modern Physics*, vol. 57, no. 3, pp. 783–826, 1985.
- [14] W. E. Doering and S. Nie, "Single-molecule and single-nanoparticle SERS: examining the roles of surface active sites and chemical enhancement," *Journal of Physical Chemistry B*, vol. 106, no. 2, pp. 311–317, 2002.
- [15] C. H. Munro, W. E. Smith, M. Garner, J. Clarkson, and P. C. White, "Characterization of the surface of a citrate-reduced colloid optimized for use as a substrate for surface-enhanced resonance Raman scattering," *Langmuir*, vol. 11, no. 10, pp. 3712–3720, 1995.

- [16] R. J. C. Brown, J. Wang, R. Tantra, R. E. Yardley, and M. J. T. Milton, "Electromagnetic modelling of Raman enhancement from nanoscale substrates: a route to estimation of the magnitude of the chemical enhancement mechanism in SERS," *Faraday Discussions*, vol. 132, pp. 201–213, 2006.
- [17] R. C. Maher, L. F. Cohen, and P. Etchegoin, "Single molecule photo-bleaching observed by surface enhanced resonant Raman scattering (SERRS)," *Chemical Physics Letters*, vol. 352, no. 5–6, pp. 378–384, 2002.
- [18] M. Brust, D. Bethell, C. J. Kiely, and D. J. Schiffrin, "Self-assembled gold nanoparticle thin films with nonmetallic optical and electronic properties," *Langmuir*, vol. 14, no. 19, pp. 5425–5429, 1998.
- [19] D. Roy, J. Wang, and M. E. Welland, "Nanoscale imaging of carbon nanotubes using tip enhanced Raman spectroscopy in reflection mode," *Faraday Discussions*, vol. 132, pp. 215–225, 2006.
- [20] M. I. Mishchenko, L. D. Travis, and A. A. Lacis, *Scattering, Absorption, and Emission of Light by Small Particles*, Cambridge University Press, Cambridge, UK, 2002.
- [21] H. C. van de Hulst, *Light Scattering by Small Particles*, Dover, New York, NY, USA, 1981.
- [22] I. Romero, J. Aizpurua, G. W. Bryant, and F. J. García de Abajo, "Plasmons in nearly touching metallic nanoparticles: singular response in the limit of touching dimers," *Optics Express*, vol. 14, no. 21, pp. 9988–9999, 2006.
- [23] P. B. Johnson and R. W. Christy, "Optical constants of the noble metals," *Physical Review B*, vol. 6, no. 12, pp. 4370–4379, 1972.
- [24] <http://www.comsol.com/products/multiphysics/>.
- [25] M. Micic, N. Klymyshyn, and H. P. Lu, "Finite element method simulations of the near-field enhancement at the vicinity of fractal rough metallic surfaces," *Journal of Physical Chemistry B*, vol. 108, no. 9, pp. 2939–2947, 2004.
- [26] J. P. Kottmann, O. J. F. Martin, D. R. Smith, and S. Schultz, "Spectral response of plasmon resonant nanoparticles with a non-regular shape," *Optics Express*, vol. 6, no. 11, pp. 213–219, 2000.
- [27] J. Jin, *The Finite Element Method in Electromagnetics*, John Wiley & Sons, New York, NY, USA, 2nd edition, 2002.
- [28] A. Otto, "Surface-enhanced Raman scattering: "Classical" and "Chemical" origins," in *Light Scattering in Solids IV*, vol. 54 of *Topics in Applied Physics*, pp. 289–418, Springer, Berlin, Germany, 1984.
- [29] F. J. García-Vidal and J. B. Pendry, "Collective theory for surface enhanced Raman scattering," *Physical Review Letters*, vol. 77, no. 6, pp. 1163–1166, 1996.
- [30] K. Kneipp, Y. Wang, H. Kneipp, et al., "Single molecule detection using surface-enhanced Raman scattering (SERS)," *Physical Review Letters*, vol. 78, no. 9, pp. 1667–1670, 1997.
- [31] H. Xu, J. Aizpurua, M. Käll, and P. Apell, "Electromagnetic contributions to single-molecule sensitivity in surface-enhanced Raman scattering," *Physical Review E*, vol. 62, no. 3, pp. 4318–4324, 2000.
- [32] Z.-Q. Tian and B. Ren, "Adsorption and reaction at electrochemical interfaces as probed by surface-enhanced Raman spectroscopy," *Annual Review of Physical Chemistry*, vol. 55, pp. 197–229, 2004.
- [33] Z.-Q. Tian, B. Ren, and D.-Y. Wu, "Surface-enhanced Raman scattering: from noble to transition metals and from rough surfaces to ordered nanostructures," *Journal of Physical Chemistry B*, vol. 106, no. 37, pp. 9463–9483, 2002.
- [34] L. A. Dick, A. D. McFarland, C. L. Haynes, and R. P. van Duyne, "Metal film over nanosphere (MFON) electrodes for surface-enhanced Raman spectroscopy (SERS): improvements in surface nanostructure stability and suppression of irreversible loss," *Journal of Physical Chemistry B*, vol. 106, no. 4, pp. 853–860, 2002.
- [35] D. Jung, Y. M. Lee, Y. Lee, N. H. Kim, K. Kim, and J.-K. Lee, "Facile fabrication of large area nanostructures for efficient surface-enhanced Raman scattering," *Journal of Materials Chemistry*, vol. 16, no. 30, pp. 3145–3149, 2006.
- [36] M. E. Abdelsalam, P. N. Bartlett, J. J. Baumberg, S. Cintra, T. A. Kelf, and A. E. Russell, "Electrochemical SERS at a structured gold surface," *Electrochemistry Communications*, vol. 7, no. 7, pp. 740–744, 2005.
- [37] J. Lu, D. Chamberlin, D. A. Rider, M. Liu, I. Manners, and T. P. Russell, "Using a ferrocenylsilane-based block copolymer as a template to produce nanotextured Ag surfaces: uniformly enhanced surface enhanced Raman scattering active substrates," *Nanotechnology*, vol. 17, no. 23, pp. 5792–5797, 2006.
- [38] N. M. B. Perney, J. J. Baumberg, M. E. Zoorob, M. D. B. Charlton, S. Mahnkopf, and C. M. Netti, "Tuning localized plasmons in nanostructured substrates for surface-enhanced Raman scattering," *Optics Express*, vol. 14, no. 2, pp. 847–857, 2006.
- [39] R. M. Stockle, Y. D. Suh, V. Deckert, and R. Zenobi, "Nanoscale chemical analysis by tip-enhanced Raman spectroscopy," *Chemical Physics Letters*, vol. 318, no. 1, pp. 131–136, 2000.

Review Article

The AC and DC Conductivity of Nanocomposites

David S. McLachlan^{1,2} and Godfrey Sauti^{1,3}

¹ Department of Chemistry and Polymer Science, University of Stellenbosch, Private Bag X1, Matieland 7602, South Africa

² Materials Physics Research Institute, School of Physics, University of the Witwatersrand, Private Bag 3, Wits 2050, South Africa

³ National Institute of Aerospace, 100 Exploration Way, Hampton, VA 23666, USA

Received 25 April 2007; Accepted 9 August 2007

Recommended by Christian Brosseau

The microstructures of binary (conductor-insulator) composites, containing nanoparticles, will usually have one of two basic structures. The first is the matrix structure where the nanoparticles (granules) are embedded in and always coated by the matrix material and there are no particle-particle contacts. The AC and DC conductivity of this microstructure is usually described by the Maxwell-Wagner/Hashin-Shtrikman or Bricklayer model. The second is a percolation structure, which can be thought to be made up by randomly packing the two types of granules (not necessarily the same size) together. In percolation systems, there exists a critical volume fraction below which the electrical properties are dominated by the insulating component and above which the conducting component dominates. Such percolation systems are best analyzed using the two-exponent phenomenological percolation equation (TEPPE). This paper discusses all of the above and addresses the problem of how to distinguish among the microstructures using electrical measurements.

Copyright © 2007 D. S. McLachlan and G. Sauti. This is an open access article distributed under the Creative Commons Attribution License, which permits unrestricted use, distribution, and reproduction in any medium, provided the original work is properly cited.

1. INTRODUCTION

As it is all but impossible to measure the electrical properties of a single particle, which is three-dimensionally a nanoparticle, its electrical properties will usually have to be deduced from a compact or a composite containing the nanoparticles. A measurement of the electrical properties is also important as it is usually not possible to deduce the connectivity of a composite system from SEM and TEM micrographs alone. This paper will show how to analyze the AC and DC conductivity, or complex dielectric constant, of binary (conductor and insulator) nanocomposites (media, compacts). Most binary and some tertiary media (with some ingenuity, the analysis can be applied to tertiary media), which are found in practice to at least approximate one of the two basic nanostructures, are discussed in this paper. The first are matrix media, where the matrix phase surrounds the granular (particle) phase at all volume fractions and the distance between the conducting particles is greater than the tunneling distance for electrons. This is usually best described using the Maxwell-Wagner effective media equation (also known as the Maxwell-Garnet equation). The Maxwell-Wagner model is formally equivalent to the Hashin-Shtrikman [1] lower bound (insulator host) and up-

per bound (conductor host) [2, 3] and will be referred to here as the Maxwell-Wagner/Hashin-Shtrikman (MW/HS) model. For matrix dominated media, the Bricklayer model (BLM) [4] is also useful. The second nanostructure is where the conducting particles, in a two-phase material, make electrical contact with each other, when the volume fraction of the conducting particles ϕ reaches a certain critical ϕ_c . At this point, a critical or spanning cluster is formed and there is an abrupt (usually many orders of magnitude) change in the DC conductivity. The complex electrical conductivity of these systems is best [5, 6] described by the two-exponent phenomenological percolation equation (TEPPE) (also known as the general effective medium (GEM) equation) [7–17]. The three standard percolation equations are reviewed by Clerc et al. [18], Bergman and Stroud [19], and Nan [20], but it is specifically shown by McLachlan et al. [5, 6] that, while the single TEPPE reduces to the three standard equations in the appropriate limits, it is far superior in the second-order terms (i.e., the imaginary dielectric constant ϵ_{mi} in the conducting media above ϕ_c and the dielectric loss ϵ_{ij} (or σ_{mr}) below ϕ_c). The theory given here applies to nano-, micro-, and macromedia. Note that the word nanostructure is used throughout this paper although most of the existing experimental results are for microstructures. Section 2.1 deals with

the MW/HS equations, the specific nano- (micro-) structure pertaining to the MW/HS equations [2, 21], as well as observations regarding its applicability to nanostructures. The “rectangular” Bricklayer model [4], widely used in microceramics, which could be appropriate for rectilinear nanostructures, is not discussed in this paper. Section 2.2 describes percolation media and some of the nanostructures which give rise to φ_c 's between 0.0005 [22] and 0.56 [23]. The TEPPE, which is widely used to describe percolation systems, is introduced in Section 2.3. This section is widely illustrated by experimental results. Section 2.4 gives a brief discussion of what features in the nanostructure determine the values of the percolation exponents, s and t , as well as discussing charging effects. Ways of differentiating between effective media and percolation media are discussed in Section 3.

2. THEORY AND RESULTS

The AC conductivity of the media (composites) (σ_m) is the sum of the real and imaginary conductivities, which is given by $\sigma_m = \sigma_{mr} + i\sigma_{mi}$. The conductivity of the more conducting component is given by $\sigma_c = \sigma_{cr} + i\sigma_{ci}$ or simply $\sigma_c = \sigma_{cr}$ if ideal conductivity ($\sigma_{cr} \gg \sigma_{ci}$) is assumed. For the insulating component, the conductivity is $\sigma_i = \sigma_{ir} + i\sigma_{ii}$, where $\sigma_{ii} = \omega\varepsilon_0\varepsilon_{ir}$. σ_i is often approximated as $\sigma_i = i\omega\varepsilon_0\varepsilon_{ir}$ (i.e., $\sigma_{ir} \ll i\sigma_{ii}$). In practice, σ_{ir} incorporates both, a usually very small, DC conductivity and the dielectric polarization loss term ($\omega\varepsilon_0\varepsilon_{ii}$). The expressions for σ_c and σ_i can be dispersive and/or temperature-dependant. Although, to the best of the authors' knowledge, it has never been attempted for an experimental system, Nan [20] showed how a granular component can be modeled as consisting of both a core and a coating. The theory given in this paper definitely applies to micro- and macromedia and most nanostructures, but there are some special features regarding nanostructures which must be considered. In nanostructures, the coating matrix component thickness and the interparticle distances will often be 10 nm thick or less. From 10 nm or less, the coatings are below the tunneling distance for electrons, which would mean that the bulk conductivity (σ_{ir}) of the insulating phase cannot be substituted into the expressions given below, but should be obtainable by fitting the results.

2.1. Matrix media

In matrix media, the conductivity results are often presented using both the complex impedance (Z^*) and modulus (M^*) representations. The notations adopted for Z^* and M^* are $Z^* = Z' - iZ''$ and $M^* = M' + iM''$, where $M^* = i\omega Z^*$, and Z' and Z'' are the real and imaginary impedances, respectively, while M' and M'' are the corresponding modulus parameters. This leads to the following equations:

$$M' = \omega Z'', \quad M'' = \omega Z'. \quad (1)$$

Note that the results are often presented as complex plane (Nyquist) plots ($Z'' - Z'$ and $M'' - M'$) or Z'' -frequency and M'' -frequency plots. When the more conducting phase forms the “dominant” matrix, these plots show only a single

arc—the peak frequency of which is determined by the properties of the components and the volume fraction of each [24]. When the insulating phase forms the matrix, there are two arcs, each characterizing the contribution of one component. The peak frequencies for the multiple component arc (above φ_c) and the two single component arcs (below φ_c) are given by

$$f_p = \frac{\sigma_{mr}(\varphi, 0)}{2\pi\varepsilon_0\varepsilon_{mr}(\varphi, 0)} \quad (\varphi < \varphi_c),$$

$$f_p = \frac{\sigma_{cr}(0)}{2\pi\varepsilon_0\varepsilon_{cr}(0)} \quad (\varphi < \varphi_c; \text{high frequency}), \quad (2)$$

$$f_p = \frac{\sigma_{ir}(0)}{2\pi\varepsilon_0\varepsilon_{ir}(0)} \quad (\varphi < \varphi_c; \text{low frequency}),$$

respectively. The subscript “m” refers to the properties of the composite, and “c” and “i” to those of the components. The $\varepsilon_{xr}(0)$ are the static dielectric constants. Above φ_c , the peak frequency (ω_p) increases with φ . Note that in order to observe all these arcs, the experimental apparatus must adequately cover all ω values defined by (2).

The MW/HS equations ([2] and the references therein), derived directly from Maxwell's equations, for the spherical isotropic microstructure shown in Figure 1, are

$$\frac{\sigma_m - \sigma_c}{\sigma_m + 2\sigma_c} = \frac{(1 - \varphi)(\sigma_i - \sigma_c)}{\sigma_i + 2\sigma_c}, \quad (3a)$$

$$\frac{\sigma_m - \sigma_i}{\sigma_m + 2\sigma_i} = \frac{\varphi(\sigma_c - \sigma_i)}{\sigma_c + 2\sigma_i}. \quad (3b)$$

The MW/HS media can be visualized as built up out of a space-filling array of coated spheres, with an infinite range of sizes, as illustrated in Figure 1. In (3a), σ_c is the conductivity of the coating or matrix material, while σ_i is the conductivity of the spherical core. In (3b), σ_c is for the core while σ_i is for the coating (matrix). Note that the model has been widely and successfully applied to systems which differ from the idealized microstructures shown in Figure 1, for instance, the electrical conductivity results and the complex impedance plane plots for sintered polycrystalline yttria stabilized zirconia. With values of φ close to one ($\varphi \approx 0.999$), micron-sized grains (σ_c), and grain boundaries (σ_i), a few nanometers thick (3b) and the BLM are found to successfully fit experimental data provided that suitable dispersive expressions are substituted for $\sigma_c(\omega)$ and $\sigma_i(\omega)$ [25]. Suitable dispersive expressions include the universal dielectric response function [26] and an expression due to León et al. [27].

Other effective media theories are discussed in the feature article by McLachlan et al. [2] and the review article by Meredith and Tobias [28] which gives expressions for the electrical conductivity for a wide variety of other structures.

2.2. Percolation media: critical volume fraction

If conducting spheres (discs), of just sufficient size to touch their nearest neighbors, are placed at random on the sites of 3D (2D) Bravais lattices, it is found that φ_c is 0.16 ± 0.02 (0.50 ± 0.02) [2, 29]. If equally sized conducting and nonconducting spheres are placed at random in a container, φ_c is also

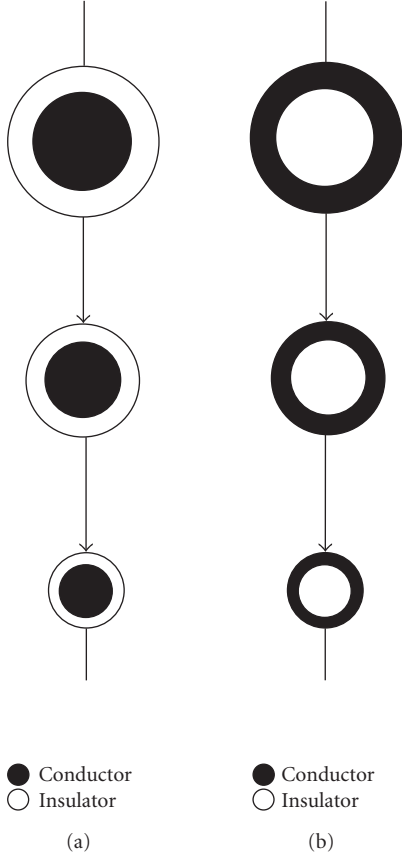


FIGURE 1: The microstructure described by the (a) insulator-host and (b) conductor-host Maxwell-Wagner effective media (MWH/S) theory.

found to be about 0.16. This value of φ_c is often taken to characterize 3D random media but other values of φ_c are permitted [2, 21, 29]. The case, where $\varphi_c > 0.16$, is best illustrated using the grain consolidation model illustrated in Figures 2(a) and 2(b). The model starts with the random nucleation of conducting (white) spheres which grow to form a random close-packed lattice of touching spheres at $\varphi = 0.636$. As the radii of the spheres increase further, the interfacial contact area grows, as illustrated in Figure 2(b), which shows thin layers of insulating material between all the conducting grains. Examining Figure 2(b) shows that the sample becomes conducting when a sufficient number of the barriers, between the conducting grains, have been removed at random for a percolation path to form, which, for thin barriers, can give a high value of φ_c . In the case of nanostructures, the barriers will almost certainly be below the tunneling length so that a conducting critical path, which passes through a series of sufficiently low tunnel barriers, will be formed at φ_c . Below φ_c , the electrons follow a “pseudopercolation” path through a series of barriers with the lowest resistances.

For $\varphi_c < 0.16$, three models can be considered. The first is the grain consolidation model illustrated in Figures 2(c) and 2(d), where insulating spheres have now nucleated and grown sufficiently to confine the conducting material (white)

to intergranular channels (see Figure 2(c)). At a φ value of 0.03 (φ_c), the channels become isolated. In the sintering of ceramics, it is well known that closed porosity is usually achieved at a value of about 3%. The next model is for cellular structures, which is illustrated in Figure 3. Here, a fine conducting powder has been compacted with a coarse insulating one. Calculations, based on there being a percolation path on the surface of the insulating spheres, have been made by Kusy [30]. For instance, when the ratio of the radii of the components is 30, $\varphi_c \approx 0.03$. A series of such cellular systems, which give φ_c 's between 0.012 and 0.065, has been examined in Chiteme and McLachlan [12]. For particles with irregular geometries, especially extended ones (rods, discs), one must use the excluded volume model of Balberg et al. [31]. This has been used in explaining the results for single and multiple wall carbon nanotubes (SWCNT and MWCNT), modeled as random sticks in 3D (McLachlan et al. [22] and the references therein). Figure 4 shows random sticks in 2D and Figure 5 shows φ_c as a function of the aspect ratio of the sticks. According to Figure 5, the SWCNT bundles should have a φ_c higher than that observed [22]. Reasons for this are given by McLachlan et al. [22].

2.3. Percolation media: the TEPPE and experimental results

Note that no experimental details will be given here; for these the reader should consult the original papers. As previously stated, a recent series of papers [7–13, 16, 32] has shown that the TEPPE, which is

$$(1 - \varphi) \frac{\sigma_i^{1/s} - \sigma_m^{1/s}}{\sigma_i^{1/s} + A\sigma_m^{1/s}} + \varphi \frac{\sigma_c^{1/t} - \sigma_m^{1/t}}{\sigma_c^{1/t} + A\sigma_m^{1/t}} = 0, \quad (4)$$

with $A = (1 - \varphi_c)/\varphi_c$ and the exponents s and t , best describes experimental results for percolation systems, especially the second-order terms [10, 11]. When $s = t = 1$ and $\varphi_c = 1/3$, the equation is equivalent to the Bruggeman symmetric media equation [2, 21]. Equation (4) yields the two limits

$$\begin{aligned} |\sigma_c| \rightarrow \infty : \sigma_m &= \sigma_i \left(\frac{\varphi_c}{\varphi_c - \varphi} \right)^s \quad \text{or} \quad \varepsilon_{mr} = \varepsilon_{ir} \left(\frac{\varphi_c}{\varphi_c - \varphi} \right)^s, \\ &\varphi < \varphi_c, \\ &(5) \\ |\sigma_i| \rightarrow 0 : \sigma_m &= \sigma_c \left(\frac{\varphi - \varphi_c}{1 - \varphi_c} \right)^t \quad \text{or} \quad \varepsilon_{mr} = \varepsilon_{ir} \left(\frac{\varphi - \varphi_c}{1 - \varphi_c} \right)^t, \\ &\varphi > \varphi_c. \\ &(6) \end{aligned}$$

These equations are the normalized standard percolation results [18, 19] and characterize the exponents s and t .

In the crossover region, where $\varphi \cong \varphi_c$, and which lies between

$$\begin{aligned} \varphi_c - \left(\frac{\sigma_i}{\sigma_c} \right)^{1/t+s} \quad \text{or} \quad \left(\varphi_c - \frac{\omega \varepsilon_0 \varepsilon_{ir}}{\sigma_{cr}} \right)^{1/t+s} \\ < \varphi < \varphi_c + \left(\frac{\sigma_i}{\sigma_c} \right)^{1/t+s} \quad \text{or} \quad \left(\varphi_c + \frac{\omega \varepsilon_0 \varepsilon_{ir}}{\sigma_{cr}} \right)^{1/t+s}, \end{aligned} \quad (7)$$

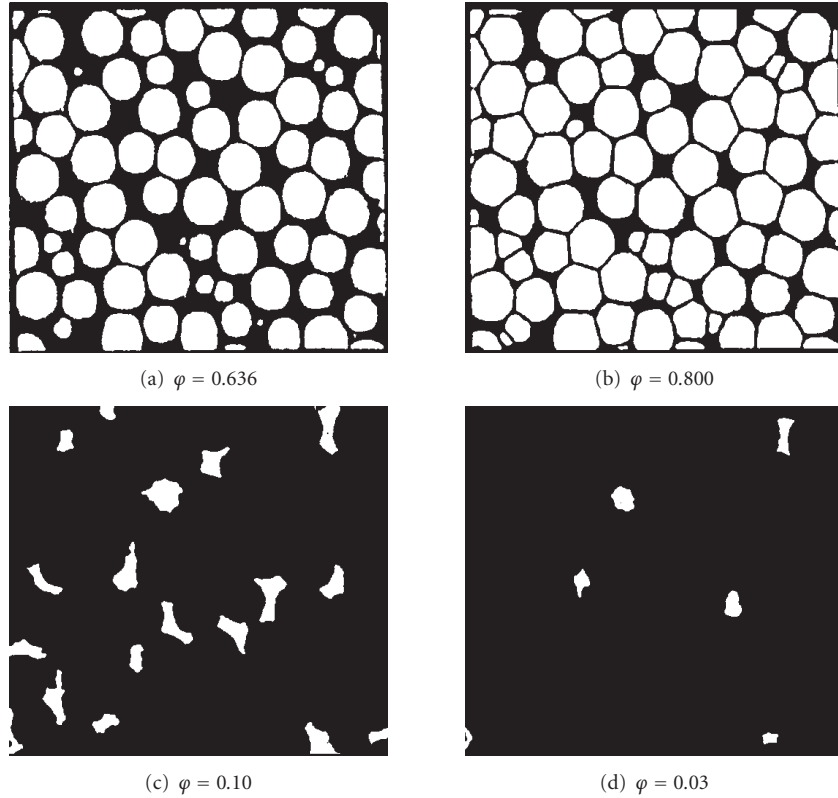
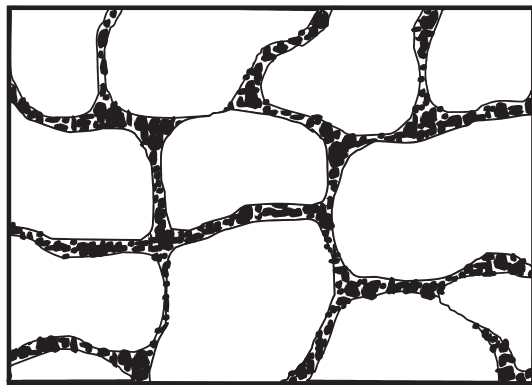


FIGURE 2: The grain consolidation model.



- Conductor
- Insulator

FIGURE 3: Cellular micro-/nanostructure. $\varphi_c = 0.03$, for a radius ratio of about 30.

(4) gives

$$\sigma_m \approx \sigma_i^{t/(s+t)} \sigma_c^{s/(s+t)} \quad \text{or} \quad \left((\omega \epsilon_0 \epsilon_{ir})^{t/(s+t)} \sigma_{cr}^{s/(s+t)} \right), \quad (8)$$

which is in agreement with the theory given in Clerc et al. [18] and Bergman and Stroud [19]. Equation (8) shows that, in the crossover region, the conductivity σ_{mr} should be pro-

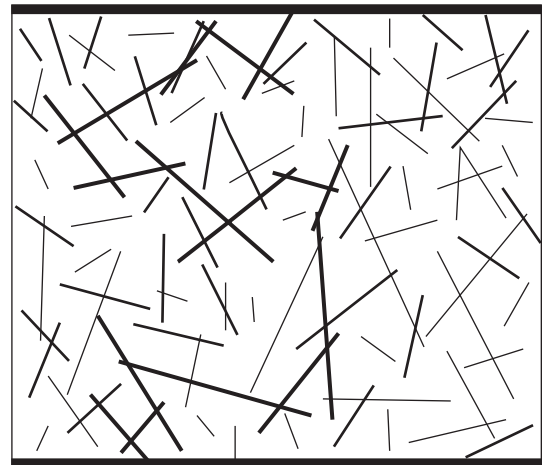


FIGURE 4: Percolation network of random sticks in two dimensions.

portional to $\omega^{t/(s+t)}$ and the dielectric constant ϵ_{mr} (recall that $\epsilon_{xy} = \sigma_{xy}/\omega \epsilon_0$) is proportional to $\omega^{s/(s+t)}$. Note that (5) and (6) are not valid in the crossover region.

The relationship between the DC exponents, s and t , and the high frequency slopes, $u_t = t/(s+t)$, $v_t = s/(s+t)$ and $u_t + v_t = 1$, in the crossover region, is a basic premise for universal behavior, upon which the three standard percolation equations are based ([18–20] and the references therein). In this respect, all AC experimental results ([7–13, 16] and the

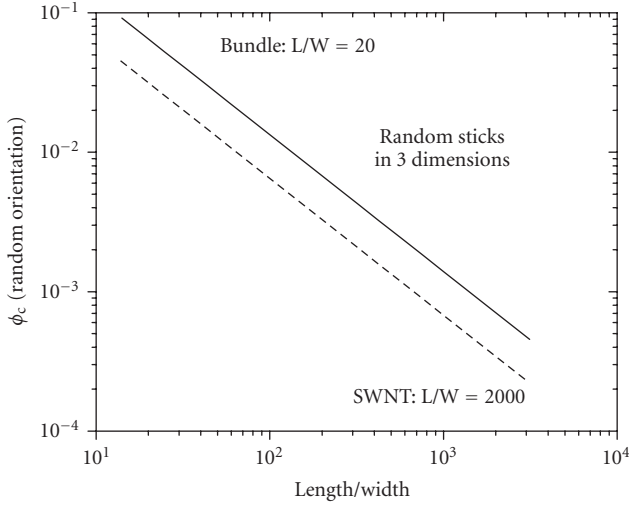
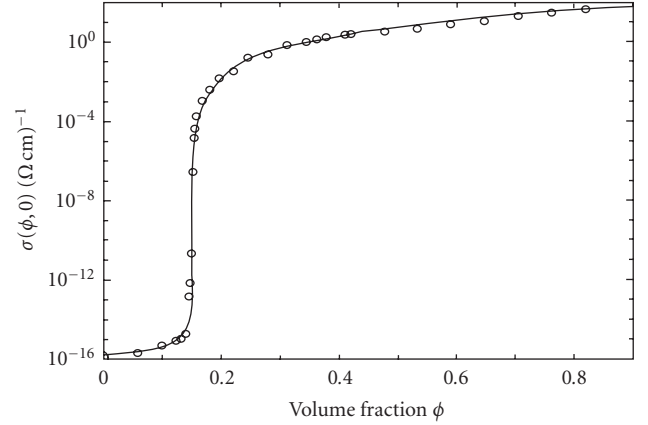
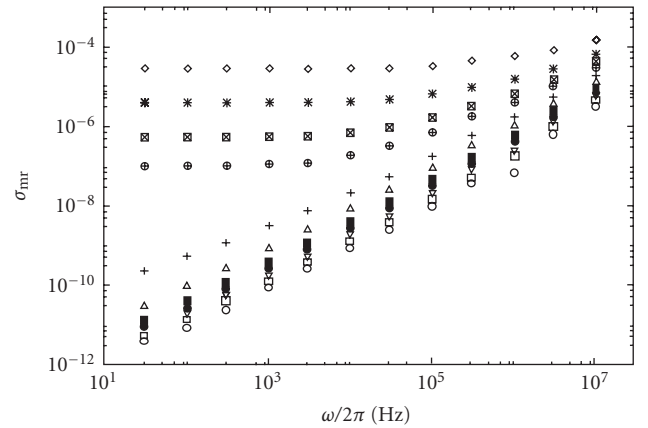


FIGURE 5: The percolation thresholds for random sticks.

references therein) are nonuniversal, with the results in Wu and McLachlan [7, 8] being the closest to universal. Therefore, these results are used to illustrate the first-order results, σ_{mr} above φ_c and ε_{mr} below φ_c , and the second-order results, ε_{mr} above φ_c and σ_{mr} below φ_c . Arguably, the best DC conductivity results, for a percolation system, are those measured on compressed Graphite-hBN discs, which are given in Figure 6, from which φ_c , s , and t can easily be determined using (4). Figure 7 shows the AC conductivity plotted as a function of frequency for a loosely packed Graphite-hBN mixture, and Figure 8 shows the dielectric constant as a function of frequency. These results are presented as they are the only ones where the results below φ_c can be scaled. Note how one can clearly distinguish between samples above and below φ_c in Figure 7. Close to φ_c , the slope in the high-frequency region for a percolation system should be $t/(s+t)$ with s and t being determined from the DC results. Not too much can be determined about the dielectric constant from these plots, except that the linear slope, which should be $s/(s+t)$, is only observed for higher frequencies and very close to φ_c , as it is to be expected from (5). Universality requires that the experimental slopes of such plots be $u_e = t/(s+t)$ and $v_e = s/(s+t)$, using the s and t determined from DC measurements. Note that whereas the slopes in the graphite boron nitride system are close to the universal values, in most systems they are not [12, 16] and $u_e + v_e < 1$. The dielectric constant results shown in Figure 8 are not even qualitatively in accordance with the predictions of the standard equations. Results of this nature can be qualitatively fitted using (4) [10]. However, a more complex algorithm is needed for quantitative fitting [11]. Note that the dielectric constant is frequency dependant below φ_c [12]—something which has never been previously taken into account theoretically, using (4) or any other expression.

Figure 9 shows a further plot of the conductivity as a function of frequency, from a special experiment using loosely packed Graphite-hBN in ultra dry air [10]. The contributions to the conductivity from the insulator (DC and

FIGURE 6: DC percolation results for Graphite-hBN discs. $\varphi_c = 0.150 \pm 0.001$, $s = 1.01 \pm 0.05$, and $t = 2.63 \pm 0.07$.FIGURE 7: AC conductivity plotted against frequency for a loosely packed Graphite-hBN mixture. The range of φ values is between 0.112 and 0.133. A gap occurs between the low-frequency results above and below φ_c .

dielectric loss) and the percolation clusters and their sum are shown by the solid line in the figure (see Wu and McLachlan [8] for further details). To date, the percolation contribution has been only clearly seen in this system, where the insulator is mainly dry air and a little dry BN. In most systems, the percolation contribution is swamped by the contribution from σ_{ii} .

2.4. The exponents s and t

The universal value of the exponent t (t_{un}), which is usually observed in computer simulations and for “ideal” systems, is 2 [18, 19] while $s_{\text{un}} \approx 0.87$. However, values in the ranges of $0.37 < s < 1.28$ and $1 < t < 6.27$ can be found in the literature ([15] and the references therein). Kogut and Straley [33] showed, in computer simulations, that if the low-conductance bonds in the percolation network, or the

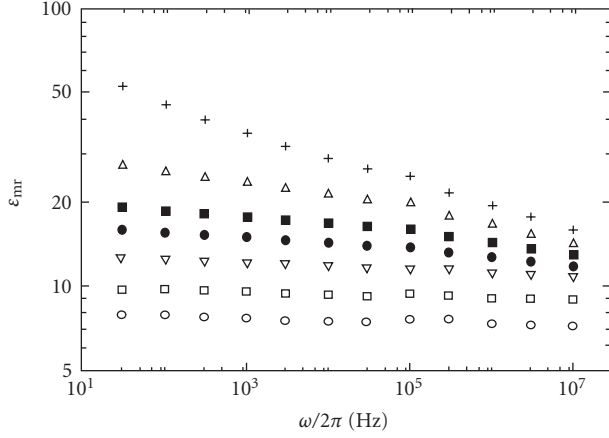


FIGURE 8: Dielectric constant plotted against frequency for a loosely packed Graphite-hBN mixture. The range of ϕ values is between 0.112 and 0.123. The top curve is for a sample marginally above ϕ_c .

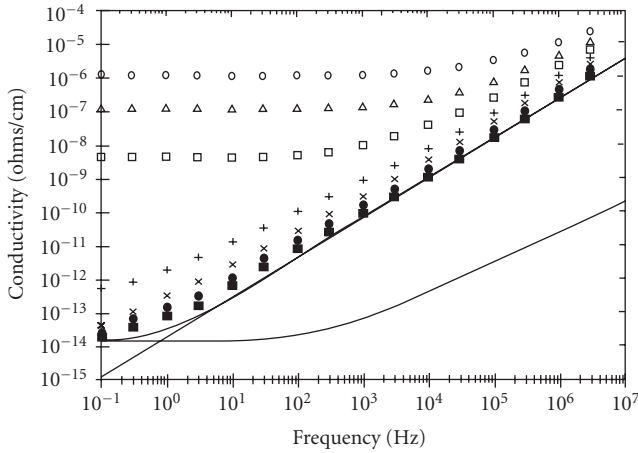


FIGURE 9: AC conductivity of loosely packed Graphite-hBN in ultra dry air. The straight line is the calculated contribution from the percolation clusters and the lowest plot shows the total dielectric loss.

intergranular conductances of the conducting component in a continuum system, have a very wide distribution, then t can be larger than t_{un} . This distribution can be due to a large range of effective geometrical resistivity factors in a continuous homogeneous conducting phase, as occurred in the Swiss Cheese (random void (RV)) model and the inverse Swiss Cheese (inverse random void (IRV)) model [32, 34]. In the Swiss Cheese model, a range of very thin and highly resistive threads of the conductor (Cheese), between the large overlapping voids (air), give rise to a wide distribution in the conductances between the more extended or bulky regions of conductor. These models give values for t in the range of 2–2.5. An extension to the RV model allowing still higher (apparently unlimited) values of t is given by Berg [35]. The links, blobs, and nodes model [36, 37] gives an upper limit of 2.35. Note that all of the above models assume a homoge-

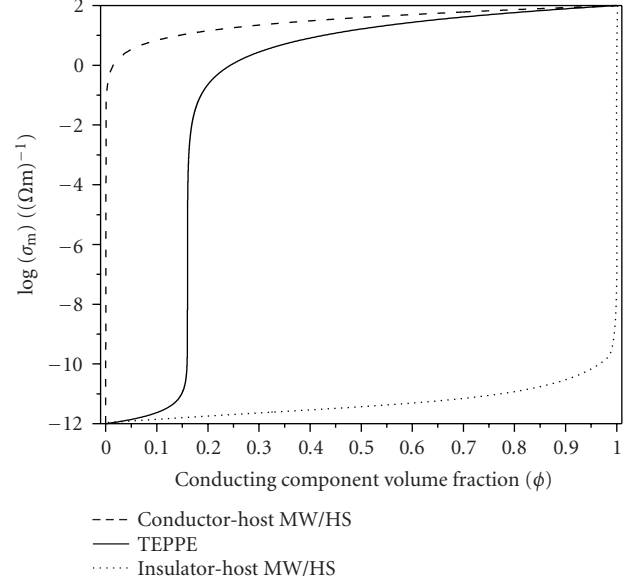


FIGURE 10: DC conductivities for the conductor-host Maxwell-Wagner/Hashin-Shtrikman equation, the TEPPE, and the insulator-host Maxwell-Wagner/Hashin-Shtrikman equation. In the simulation, $\sigma_{cr} = 10^2 (\Omega m)^{-1}$ and $\sigma_{ir} = 10^{-12} (\Omega m)^{-1}$. For the TEPPE, $\phi_c = 0.16$, $s = 0.87$, and $t = 2$.

neous (nongranular) conducting phase. A model for granular conducting systems which gives rise to $t > t_{un}$ was proposed by Balberg [38]. This model is based on the dominant resistances in the current carrying links and blobs (now consisting of a granular conductor) being due to a large range of interparticle tunneling contacts. Due to the characteristic dimensions of nanostructures, the intergranular distances will often be 10 nm thick or less, that is, below the characteristic tunneling distance. This means that the Balberg [38] model will probably be the most appropriate for nanostructures, where values of t greater than two are to be expected.

One might expect the charging effect or coulomb blockage in nanostructures because, for a 100 nm radius (R) sphere carrying charge of one excess electron, the charging energy, which is e^2/C or $e^2/2\pi\epsilon_0 R$, is equal to the thermal energy kT at 300 K. However, this will not affect the conductivity of a bulk sample because, well below ϕ_c , there will be a large number of hopping conductivity paths, with a number of different hopping lengths in each. This, combined with the fact that e^2/C will vary from site to site, will average out any observable effects. Closer to ϕ_c , the hopping occurs between random clusters which have larger and more varied C values, which will again lead to a smearing out of charging effects. It should also be noted that it has been shown by McLachlan et al. [13] that the scaling results for percolation systems and universal conductivity systems, which have been observed in amorphous conductors, ionic conductors, lightly doped semiconductors, and other disordered systems, are very similar. As in some, but not all, universal conductivity systems, coulomb blocking occurs; the presence of coulomb blocking does not necessarily invalidate the TEPPE.

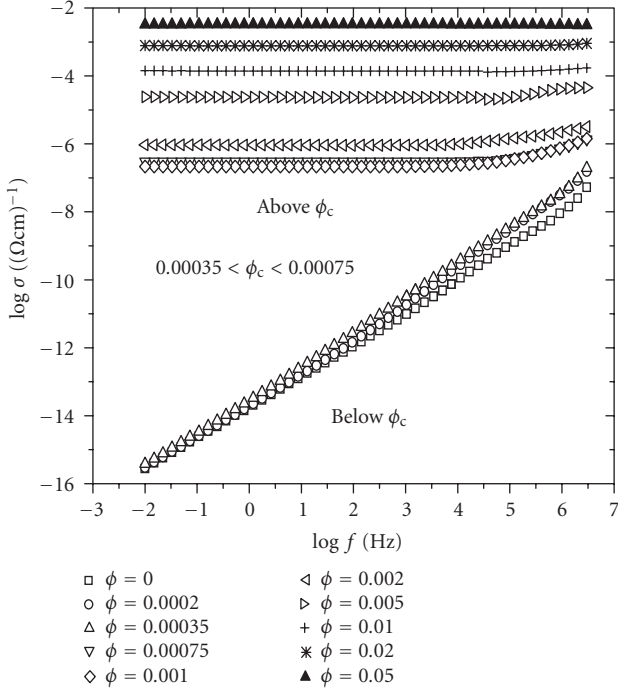


FIGURE 11: The AC conductivity of SWCNT-polymer composites at various ϕ values. Note the big jump in the conductivity around ϕ_c [22].

3. DIFFERENTIATING BETWEEN A MATRIX AND A PERCOLATION NANOSTRUCTURE

Fully fitting DC conductivity measurements, over a wide range of compositions, is the easiest and clearest way of distinguishing nanostructures. Figure 10 shows the DC conductivities for the conductor-host MW/HS equation, TEPPE, and the insulator-host MW/HS equation. It can be clearly seen that over a wide enough range of ϕ 's (on either side of ϕ_c for the percolation system), the three models predict vastly different conductivities.

Equally good, but involving far more work, is a full fit of the AC conductivity data. Youngs [14, 15] describes the use of a genetic algorithm that enables robust fitting of AC conductivity data to the TEPPE (GEM). With sufficient care, and the use of both the AC and DC data, satisfactory results can be obtained, from the TEPPE, for systems with data only on one side of ϕ_c [39]¹. Various algorithms can be used to fit data to the MW/HS equations [25, 39]. Unfortunately, it is not possible to differentiate between the different nanostructures from features of the AC conductivity data, such as the high frequency slope of the conductivity-frequency curves, for a sample of a single composition. These features are in-

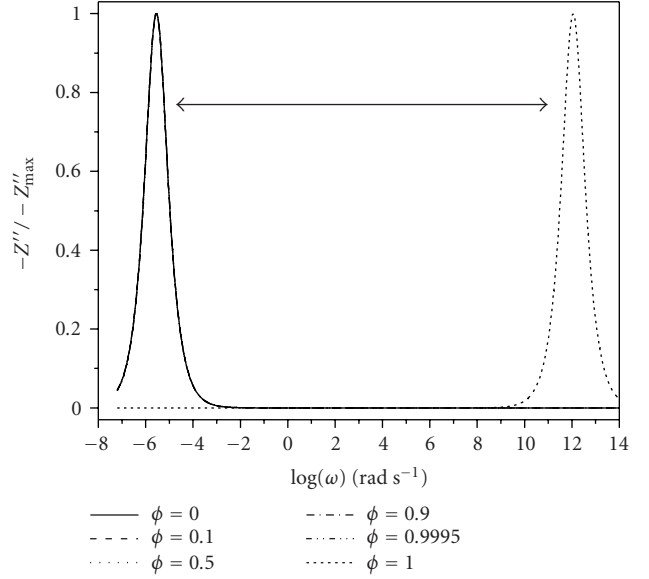


FIGURE 12: The normalized impedance for an insulator-host Maxwell-Wagner/Hashin-Shtrikman system. For the ratio of component conductivities in the simulations, no peaks are observed between those of the insulating and conducting components. The system is dominated either by the insulating or the conducting component. For the simulations, $\sigma_{cr} = 10^2 (\Omega m)^{-1}$, $\epsilon_{cr} = 10$, $\sigma_{ir} = 10^{-16}$, and $\epsilon_{ir} = 4$ (For lower values of σ_{cr}/σ_{ir} two peaks are observed in the spectrum).

fluenced not only by the structure of the composites, but also by the dispersive properties of their components [25].

Where AC conductivity data are available for various compositions, there are various ways of distinguishing between percolation and effective media systems. Percolation and effective media systems can be differentiated by the big changes (usually several orders of magnitude) that occur in the AC conductivities at ϕ_c for the percolation system. Figure 11 shows the AC conductivities, at various ϕ 's for a SWCNT-polymer composite. The samples clearly lie in two groups: one below the percolation threshold and another above. Such a big jump in the AC conductivity, for a relatively small change in ϕ , is not observed for effective media systems, except where $\phi \approx 0$ or 1.

The changes in the positioning of peaks in Z'' -frequency (or $Z' - Z''$) plots can also be used to distinguish between systems described by the different models. For the insulator-host MW/HS, the position of the impedance peak does not change much with increasing ϕ but instead remains under or very close to the $\phi = 0$ peak, until $\phi \approx 1$, as shown in Figure 12.

For a system described by the conductor-host MW/HS, the peaks in Z'' , as shown in Figure 13, remain close to the $\phi = 1$ peak until $\phi \approx 0$.

For a percolation system, Z'' peaks are seen at all frequencies between the characteristic frequencies of the components as shown in Figure 14. Up to ϕ_c , the impedance is dominated by the insulating component and the Z'' peaks

¹ Copies of the fitting and simulation algorithms implemented in MATHEMATICA can be obtained from G. S.

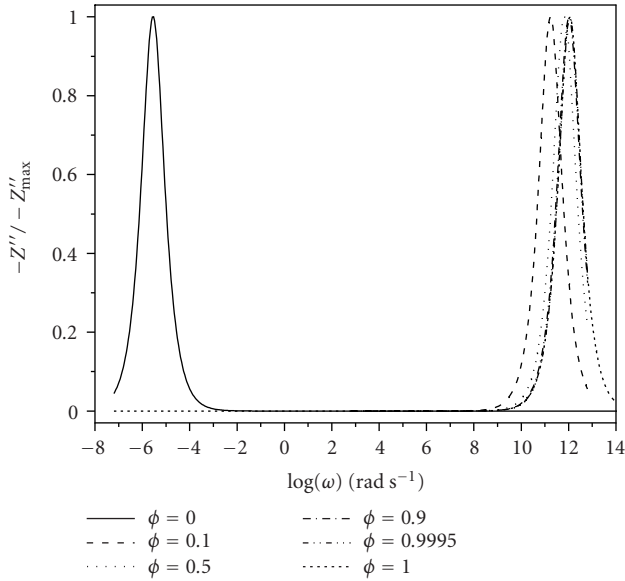


FIGURE 13: Normalized impedance for the conductor-host Maxwell-Wagner/Hashin-Shtrikman model. Note that the single peak starts close to the $\varphi = 1$ peak, even for very low φ and moves to the right, closer to $\varphi = 1$ with increasing φ . For the simulations, $\sigma_{cr} = 10^2(\Omega\text{m})^{-1}$, $\varepsilon_{cr} = 10$, $\sigma_{ir} = 10^{-16}(\Omega\text{m})^{-1}$, and $\varepsilon_{ir} = 4$.

are all superimposed onto the $\varphi = 0$ peak. However, just above φ_c , the peak starts to move towards the $\varphi = 1$ peak with increasing φ .

Similar behavior as seen in Figures 12, 13, and 14 is observed for smaller σ_i/σ_c with the only difference being that the insulator and conductor peaks lie closer together. If $\sigma_i/\sigma_c > 10^{-3}$, the peaks will start to overlap which may cause problems.

4. CONCLUSIONS

This paper has shown how the AC and DC conductivity (dielectric constant) results, for binary composites, with one or more of which having nanodimensions, can be analyzed in terms of either (i) a matrix structure using the Maxwell-Wagner/Hashin-Shtrikman (or Bricklayer) model or (ii) a percolation structure using the two-exponent phenomenological percolation equation (TEPPE). It is also shown how the two structures may be distinguished using electrical measurements. As the actual complex conductivities appear in expressions, it is theoretically possible to determine the dispersive conductivities for both components and, for percolation systems, the critical volume fraction as well as the exponents s and t . Unfortunately, even when a large amount of data, on both sides of the critical volume fraction, are available, this is a formidable task due to the large number of unknown parameters (a dispersive medium has to have two or more). In practice, it will probably be necessary to know an expression to directly measure the conductivity of one of the components. If only one component is nanosized, it should be possible to deduce its dispersive conductivity by fitting the

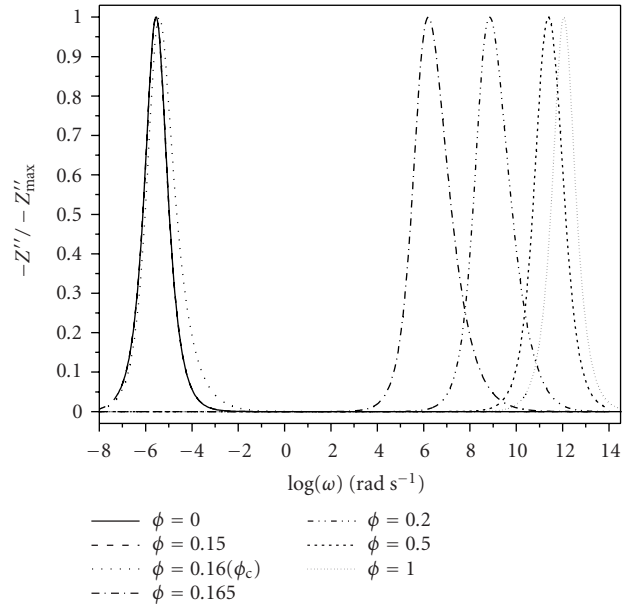


FIGURE 14: The normalized impedance for a percolation system. Note the peaks at frequencies in between those of the insulating and conducting components. For the simulations, $\sigma_{cr} = 10^2(\Omega\text{m})^{-1}$, $\varepsilon_{cr} = 10$, $\sigma_{ir} = 10^{-16}(\Omega\text{m})^{-1}$, $\varepsilon_{ir} = 4$, $s = 1$, $t = 2$, and $\varphi_c = 0.16$.

results for the composite using the MW/HS equations or the TEPPE together with the best expressions for the dispersive conductivity of the other component.

REFERENCES

- [1] Z. Hashin and S. Shtrikman, "A variational approach to the theory of the effective magnetic permeability of multiphase materials," *Journal of Applied Physics*, vol. 33, no. 10, pp. 3125–3131, 1962.
- [2] D. S. McLachlan, M. Blaszkiewicz, and R. E. Newnham, "Electrical resistivity of composites," *Journal of the American Ceramic Society*, vol. 73, no. 8, pp. 2187–2203, 1990.
- [3] M. Campo, L. Woo, T. Mason, and E. Garboczi, "Frequency-dependent electrical mixing law behavior in spherical particle composites," *Journal of Electroceramics*, vol. 9, no. 1, pp. 49–56, 2002.
- [4] J.-H. Hwang, D. S. McLachlan, and T. O. Mason, "Brick layer model analysis of nanoscale-to-microscale cerium dioxide," *Journal of Electroceramics*, vol. 3, no. 1, pp. 7–16, 1999.
- [5] D. S. McLachlan, C. Chiteme, W. D. Heiss, and J. Wu, "The correct modelling of the second order terms of the complex AC conductivity results for continuum percolation media, using a single phenomenological equation," *Physica B*, vol. 338, no. 1–4, pp. 256–260, 2003.
- [6] D. S. McLachlan, C. Chiteme, W. D. Heiss, and J. Wu, "Fitting the DC conductivity and first order AC conductivity results for percolation media, using percolation theory and a single phenomenological equation," *Physica B*, vol. 338, no. 1–4, pp. 261–265, 2003.
- [7] J. Wu and D. S. McLachlan, "Percolation exponents and thresholds obtained from the nearly ideal continuum

- percolation system graphite-boron nitride,” *Physical Review B*, vol. 56, no. 3, pp. 1236–1248, 1997.
- [8] J. Wu and D. S. McLachlan, “Scaling behaviour of the complex conductivity of graphite-boron nitride systems,” *Journal of Physical Review B*, vol. 58, no. 22, pp. 14880–14887, 1998.
- [9] D. S. McLachlan and M. B. Heaney, “Complex ac conductivity of a carbon black composite as a function of frequency, composition, and temperature,” *Physical Review B*, vol. 60, no. 18, pp. 12746–12751, 1999.
- [10] D. S. McLachlan, W. D. Heiss, C. Chiteme, and J. Wu, “Analytic scaling functions applicable to dispersion measurements in percolative metal-insulator systems,” *Physical Review B*, vol. 58, no. 20, pp. 13558–13564, 1998.
- [11] W. D. Heiss, D. S. McLachlan, and C. Chiteme, “Higher-order effects in the dielectric constant of percolative metal-insulator systems above the critical point,” *Physical Review B*, vol. 62, no. 7, pp. 4196–4199, 2000.
- [12] C. Chiteme and D. S. McLachlan, “AC and DC conductivity, magnetoresistance, and scaling in cellular percolation systems,” *Physical Review B*, vol. 67, no. 2, Article ID 024206, 18 pages, 2003.
- [13] D. S. McLachlan, G. Sauti, and C. Chiteme, “Static dielectric function and scaling of the ac conductivity for universal and nonuniversal percolation systems,” *Physical Review B*, vol. 76, no. 1, Article ID 014201, 13 pages, 2007.
- [14] I. J. Youngs, *Electrical percolation and the design of functional electromagnetic materials*, Ph.D. thesis, Electronic and Electrical Engineering, University College, London, UK, 2001.
- [15] I. J. Youngs, “Exploring the universal nature of electrical percolation exponents by genetic algorithm fitting with general effective medium theory,” *Journal of Physics D*, vol. 35, no. 23, pp. 3127–3137, 2002.
- [16] C. Chiteme, D. S. McLachlan, and G. Sauti, “AC and DC percolative conductivity of magnetite-cellulose acetate composites,” *Physical Review B*, vol. 75, no. 9, Article ID 094202, 13 pages, 2007.
- [17] C. Brosseau, “Generalized effective medium theory and dielectric relaxation in particle-filled polymeric resins,” *Journal of Applied Physics*, vol. 91, no. 5, pp. 3197–3204, 2002.
- [18] J. P. Clerc, G. Giraud, J. M. Laugier, and J. M. Luck, “The electrical conductivity of binary disordered systems, percolation clusters, fractals and related models,” *Advances in Physics*, vol. 39, no. 3, pp. 191–309, 1990.
- [19] D. J. Bergman and D. Stroud, “The physical properties of macroscopically inhomogeneous media,” *Solid State Physics*, vol. 46, pp. 148–270, 1992.
- [20] C.-W. Nan, “Physics of inhomogeneous inorganic materials,” *Progress in Materials Science*, vol. 37, pp. 1–116, 1993.
- [21] D. S. McLachlan, “Analytical functions for the DC and AC conductivity of conductor-insulator composites,” *Journal of Electroceramics*, vol. 5, no. 2, pp. 93–110, 2000.
- [22] D. S. McLachlan, C. Chiteme, C. Park, et al., “AC and DC percolative conductivity of single wall carbon nanotube polymer composites,” *Journal of Polymer Science Part B*, vol. 43, no. 22, pp. 3273–3287, 2005.
- [23] D. S. McLachlan, R. Rosenbaum, A. Albers, et al., “The temperature and volume fraction dependence of the resistivity of granular Al-Ge near the percolation threshold,” *Journal of Physics: Condensed Matter*, vol. 5, no. 27, pp. 4829–4842, 1993.
- [24] D. S. McLachlan, J.-H. Hwang, and T. O. Mason, “Evaluating dielectric impedance spectra using effective media theories,” *Journal of Electroceramics*, vol. 5, no. 1, pp. 37–51, 2000.
- [25] G. Sauti, *Electrical Conductivity and Permittivity of Ceramics and other Composites*, Ph.D. thesis, Physics, University of the Witwatersrand, Johannesburg, South Africa, 2005.
- [26] A. K. Jonscher, “The ‘universal’ dielectric response,” *Nature*, vol. 267, no. 5613, pp. 673–679, 1977.
- [27] C. León, M. L. Lucía, and J. Santamaría, “Correlated ion hopping in single-crystal yttria-stabilized zirconia,” *Physical Review B*, vol. 55, no. 2, pp. 882–887, 1997.
- [28] R. E. Meredith and C. W. Tobias, “Conduction in heterogeneous systems,” in *Advances in Electrochemistry and Electrochemical Engineering*, C. Tobias, Ed., vol. 2, pp. 15–47, John Wiley & Sons, New York, NY, USA, 1962.
- [29] R. Zallen, *The Physics of Amorphous Solids*, John Wiley & Sons, New York, NY, USA, 1983.
- [30] R. P. Kusy, “Influence of particle size ratio on the continuity of aggregates,” *Journal of Applied Physics*, vol. 48, no. 12, pp. 5301–5305, 1977.
- [31] I. Balberg, C. H. Anderson, S. Alexander, and N. Wagner, “Excluded volume and its relation to the onset of percolation,” *Physical Review B*, vol. 30, no. 7, pp. 3933–3943, 1984.
- [32] B. I. Halperin, S. Feng, and P. N. Sen, “Differences between Lattice and continuum percolation transport exponents,” *Physical Review Letters*, vol. 54, no. 22, pp. 2391–2394, 1985.
- [33] P. M. Kogut and J. P. Straley, “Distribution-induced non-universality of the percolation conductivity exponents,” *Journal of Physics C*, vol. 12, no. 11, pp. 2151–2159, 1979.
- [34] S. Feng, B. I. Halperin, and P. N. Sen, “Transport properties of continuum systems near the percolation threshold,” *Physical Review B*, vol. 35, no. 1, pp. 197–214, 1987.
- [35] I. Balberg, “Limits on the continuum-percolation transport exponents,” *Physical Review B*, vol. 57, no. 21, pp. 13351–13354, 1998.
- [36] H. E. Stanley, “Cluster shapes at the percolation threshold: and effective cluster dimensionality and its connection with critical-point exponents,” *Journal of Physics A*, vol. 10, no. 11, pp. L211–L220, 1977.
- [37] A. Coniglio, “Cluster structure near the percolation threshold,” *Journal of Physics A*, vol. 15, no. 12, pp. 3829–3844, 1982.
- [38] I. Balberg, “Tunneling and nonuniversal conductivity in composite materials,” *Physical Review Letters*, vol. 59, no. 12, pp. 1305–1308, 1987.
- [39] G. Sauti and D. S. McLachlan, “Impedance and modulus spectra of the percolation system silicon-polyester resin and their analysis using the two exponent phenomenological percolation equation,” *Journal of Materials Science*, vol. 42, no. 16, pp. 6477–6488, 2007.